6 Списак објављених научних радова са њиховим копијама

6.1 Радови објављени након претходног избора у звање са њиховим копијама

6.1.1 Радови у изузетним међународним часописима (M21a)

[1] Dejan M. Djokić, Bojan Stojadinović, Dimitrije Stepanenko, and Zorana Dohčević-Mitrović, *Probing Charge Carrier Transport Regimes in $BiFeO_3$ Nanoparticles by Raman Spectroscopy*, Scripta Materialia **181**, 6 (2020). $\mathbf{M_{norm} = 10.00}$

6.1.2 Радови у врхунским међународним часописима (M21)

[2] Dejan M. Djokić, Dimitrije Stepanenko, and Zorana Dohčević-Mitrović, *Extreme Conduction Electron Spin Resonance: $A/B \rightarrow \left(5+3\sqrt{3}\right)/4$, the Universal Limit of Lineshape Asymmetry Ratio*, Journal of Magnetism and Magnetic Materials **491**, 165616 (2019). $\mathbf{M_{norm} = 8.00}$

[3] Bojan Stojadinović, Dejan M. Djokić, Novica Paunović, Ivica Živković, Luka Ćirić, Vladan Kusigerski, and Zorana Dohčević-Mitrović, *Unvailing the Spin–Phonon Coupling in Nanocrystalline $BiFeO_3$ by Resonant Two-Phonon Raman Active Modes*, Materials Science & Engineering **B274**, 115444 (2021). $\mathbf{M_{norm} = 8.00}$

[4] Novica Paunović, Zorana Dohčević-Mitrović, Dejan M. Djokić, Sonja Aškrabić, Saša Lazović, Ann Rose Abraham, Balakrishnan Raneesh, Nandakumar Kalarikkal, and Sabu Thomas, *Revealing Plasmon-Phonon Interaction in Nanocrystalline $MgFe_2O_4$ Spinels by Far-Infrared Reflection Spectroscopy*, Materials Science in Semiconductor Processing **1491**, 106889 (2022). $\mathbf{M_{norm} = 5.71}$

6.1.3 Монографске студије/поглавља у књизи M11 (M13)

[5] Dejan M. Djokić, Novica Paunović, Bojan Stojadinović, Dimitrije Stepanenko, Saša Lazović, and Zorana Dohčević-Mitrović, *Transport Properties of Nanoscopic Solids as Probed by Spectroscopic Techniques*, Chapter 2 in *Fundamentals and Properties of Multifunctional Nanomaterials – Micro and Nano Technologies*, published in Elsevier (2021). $\mathbf{M_{norm} = 7.00}$

[6] Zorana Dohčević-Mitrović, Sonja Aškrabić, Bojan Stojadinović, and Dejan M. Djokić, *Temperature Dependent Raman Spectroscopy for Nanostructured Materials Characterization*, Chapter 2 in *Design, Fabrication, and Characterization of Multifunctional Nanomaterials – Micro and Nano Technologies*, published in Elsevier (2022). $\mathbf{M_{norm} = 7.00}$

6.1.4 Радови у истакнутим међународним часописима (M22)

[7] Zorana Dohčević-Mitrović, Vinicius D. Araujo, Marko Radović, Sonja Aškrabić, Guilherme R. Costa, Maria Ines B. Bernardi, Dejan M. Djokić, Bojan Stojadinović, and Marko G. Nikolić, *Influence of Oxygen Vacancy Defects and Cobalt Doping on Optical, Electronic, and Photocatalytic Properties of Ultrafine $SnO_{2-\delta}$ Nanocrystals*, Processing and Application of Ceramics **181**, 102 (2020). $\mathbf{M_{norm} = 3.57}$

6.1.5 Радови у међународним часописима (M23)

[8] Dejan M. Djokić, *Dry Friction Camouflaged in Viscous Drag*, The Physics Teacher **58**, 340 (2020). $\mathbf{M_{norm} = 3.00}$

6.1.6 Позивна предавања са међународног скупа (M32)

[9] Dejan M. Djokić, *Quantum Yield Computation in Polymer Wrapped Carbon Nanotubes*, 3rd International Meeting on Materials Science for Energy Related Applications, Belgrade (2018). $\mathbf{M_{norm} = 1.50}$

6.1.7 Позивна предавања са скупа националног значаја (M62)

[10] Dejan M. Djokić, Bojan Stojadinović, Dimitrije Stepanenko, Sonja Aškrabić, Zorana Dohčević-Mitrović, *Variable Range Hopping Mechanism of Carrier Transport in $BiFeO_3$ Nano Particles Revealed via Raman Scattering Technique*, 5th Conference of the Serbian Society for Ceramic Materials, Belgrade (2019). $\mathbf{M_{norm} = 1.00}$

6.2 Радови објављени пре претходног избора у звање

6.2.1 Радови у изузетним међународним часописима (M21a)

[1] A. Maisuradze, A. Shengelaya, H. Berger, D. M. Djokić, and H. Keller, *Magnetoelectric Coupling in Single Crystal Cu_2OSeO_3 Studied by a Novel Electron Spin Resonance Technique*, Physical Review Letters **108**, 247211 (2012).

[2] P. Szirmai, E. Horváth, B. Náfrádi, Z. Micković, R. Smajda, D. M. Djokić, K. Schenk, L. Forró, and A. Magrez, *Synthesis of Homogeneous Manganese Doped Titanium Oxide Nanotubes from Titanate Precursors*, The Journal of Physical Chemistry **C117**, 697 (2013).

[3] D. M. Djokić, L. Antognazza, and M. Decroux *Finite Element Method Simulation Study of Heat Propagation in a Novel YBCO-Based Coated Conductor for Resistive Fault Current Limiters*, International Journal of Thermal Sciences **111**, 160 (2017).

6.2.2 Радови у врхунским међународним часописима (M21)

[4] D. M. Djokić, Z. V. Popović, and F. R. Vukajlović, *Influence of Antiferromagnetic Spin Ordering on the Far-Infrared Active Optical Phonon Modes of $\alpha - MnSe$*, Physical Review **B77**, 01430 (2008).

[5] J. M. Todorović, Z. D. Dohčević-Mitrović, D. M. Djokić, D. Mihailović, and Z. V. Popović, *Investigation of Thermostability and Phonon-Phonon Interactions in $Mo_6S_3I_6$ Nanowires by Raman Scattering Spectroscopy*, Journal of Raman Spectroscopy **41**, 978 (2010).

[6] L. Ćirić, D. M. Djokić, J. Jaćimović, A. Sienkiewicz, A. Magrez, M. Lotya, J. N. Coleman, Ž. Šljivančanin, and L. Forró, *Magnetism in Nanoscale Graphite Flakes as Seen Via Electron Spin Resonance*, Physical Review **B85**, 205437 (2012).

[7] Đ. Jovanović, B. Nikolić, T. Radić, D. M. Djokić, and R. Gajić, *Uncoupled Photonic Band Gaps*, Photonics and Nanostructures - Fundamentals and Applications **10**, 657 (2012).

[8] I. Živković, D. M. Djokić, M. Herak, D. Pajić, K. Prša, P. Pattison, D. Dominko, Z. Micković, D. Cinčić, L. Forró, H. Berger, and H. Rønnow, *Site Selective Quantum Correlations Revealed by Magnetic Anisotropy in the Tetramer System $SeCuO_3$*, Physical Review **B86**, 054405 (2012).

[9] D. M. Djokić and A. Goswami, *Quantum Yield in Polymer Wrapped Single Walled Carbon Nanotubes: A Computational Model*, Nanotechnology **28**, 465204 (2017).

6.2.3 Радови у истакнутим међународним часописима (M22)

[10] Z. V. Popović, D. M. Djokić, Z. D. Dohčević-Mitrović, M. Isobe, and Y. Ueda, *Infrared Reflectivity Spectra of $\eta - Na_{1.3}V_2O_5$ in the Charge Disordered and Ordered Phase*, European Physical Journal **B65**, 1 (2008).

[11] L. Ćirić, A. Sienkiewicz, D. M. Djokić, R. Smajda, A. Magrez, T. Kaspar, R. Nesper, and L. Forró, *Size Dependence of the Magnetic Response of Graphite Oxide and Graphene Flakes - an Electron Spin Resonance Study*, Physica Status Solidi **B247**, 2958 (2010).

6.2.4 Радови у међународним часописима (M23)

[12] Đ. Jovanović, R. Gajić, D. M. Djokić, and K. Hingerl, *Waveguiding Effect in GaAs 2D Hexagonal Photonic Crystal Tiling*, Acta Physica Polonica **A116**, 55 (2009).

6.2.5 Рад у часопису националног значаја (M52)

[13] J. M. Todorović, D. M. Djokić, Z. D. Dohčević-Mitrović, D. Mihailović, and Z. V. Popović, *Ispitivanje Termostabilnosti $Mo_6S_3I_6$ Nanožica Metodom Raman Spektroskopije*; Hemijska Industrija **63**, 217 (2009).

[1]

Scripta Materialia 181 (2020) 6–9

Contents lists available at ScienceDirect

Scripta Materialia

journal homepage: www.elsevier.com/locate/scriptamat

Probing charge carrier transport regimes in $BiFeO_3$ nanoparticles by Raman spectroscopy

Dejan M. Djokić*, Bojan Stojadinović, Dimitrije Stepanenko, Zorana Dohčević-Mitrović

Nanostructured Matter Laboratory, Institute of Physics Belgrade, University of Belgrade, Pregrevica 118, Belgrade 11 080, Republic of Serbia

ARTICLE INFO

Article history:
Received 18 October 2019
Revised 29 January 2020
Accepted 4 February 2020

Keywords:
Raman spectroscopy
Electronic background
$BiFeO_3$ nanoparticles
Variable range hopping

ABSTRACT

We report a finding of two transport regimes in multiferroic $BiFeO_3$ nanoparticles, which correspond to variable range hopping (VRH) mechanisms. Switch between the two regimes coincides with the transition between antiferromagnetic (AF) and paramagnetic (PM) phase. At low temperatures, it was found that temperature dependence of indirectly extracted resistivity is consistent with Efros-Shklovskii mechanism. As with high temperatures, data fit favourably to Mott VRH theory. Estimated resistivity value of ~ 350mΩcm violates the Mott-Ioffe-Regel criterion, corroborating that the transport does not proceed through conduction bands. Conductivity was probed noninvasively via Raman contactless setup and studied as a function of temperature.

Introduction. Multiferroic $BiFeO_3$ has recently attracted much attention due to its desirably high ferroelectric Curie temperature of ca 1100K and AF Néel temperature T_N of around 640K, both decreasing only slightly with decreasing crystallite size [1,2]. At nanoscales, $BiFeO_3$ turns out to be rather prospective for industrial applications in photovoltaics, satellite communications, electrically accessed magnetic memory, and novel sensing technologies [3]. Electric resistance of $BiFeO_3$ is one of the crucial parameters that must meet the relevant industrial requirements. In order to avoid leakage of electric charge, achieving high resistivity is one of the main concerns, and using nano-powders is seen as a promising development route.

As a highly informative experimental tool, Raman scattering spectroscopy stands for a local probe also being able to assess the nature and dynamics of charge carriers in conductive systems in a contactless way. On the other hand, it is exceedingly hard to identify the transport mechanism responsible for charge conduction using exclusively the contact probes [4,5]. Raman spectral response of the scattered light in metals with disorder and doped semiconductors is typically composed of several peaks due to the Raman active phonon excitations and a smooth frequency continuum which reflects direct electronic response [6]. This letter focuses on the temperature evolution of this continuous spectral background which is formed by low-energy electronic excitations, and referred to in the literature as the Raman electronic background [7–11]. The charge carrier scattering rate is intimately linked to the electronic background in Raman spectra. This enables us to follow the character of charge transport in $BiFeO_3$ nanoparticles undergoing the AF/PM phase transition at the temperature around 640K.

As the particle size decreases into nanoscale domain, two crucial changes affect the charge transport in semiconductors. Band structures become distorted with decreasing particle size and, eventually, the states change their nature to get localized. Beyond certain scale, there is no conduction band and the commonly adopted picture of the intrinsic semiconductor transport due to the thermal activation via conduction band states breaks down. As the structure becomes more and more disordered, localization centers that can trap carriers appear more prominent with the decreasing particle size. Therefore, hopping varied with distance between the localization centers can be safely hypothesized to be the dominant transport mechanism even at high temperatures due to the evanescence of the conduction band.

Our measurements of temperature dependent electronic Raman background on the multiferroic $BiFeO_3$ nanoparticles of high purity, synthesized via sol-gel method [12], have been interpreted in terms of the VRH transport mechanism, which appears leading even at quite high temperatures. The role of localization centers is played by the surface states localized within particles, and with energies in the vicinity of Fermi level. An exceptionally high value of resistivity has been evidenced which rules out a metallic type of conductivity to make VRH a viable transport mechanism in the $BiFeO_3$ nanoparticles. We communicate a detection of the two different 3*D* VRH charge carrier transport mechanisms in the nanoscaled $BiFeO_3$, as probed by Raman spectroscopy. They correspond to different impact of electron correlations upon the

* Corresponding author.
E-mail address: djokic@ipb.ac.rs (D.M. Djokić).

https://doi.org/10.1016/j.scriptamat.2020.02.008
1359-6462/

transport on the opposite sides of the AF/PM phase transition. In the AF phase, the transport can well be described by the Efros-Shklovskii VRH theory [13], while in the PM phase, the transport follows the original Mott VRH theory [14].

Raman Scattering Spectra. μ-Raman scattering measurements were performed using a Linkam THMSG600 microscope heating-cooling stage in the temperature range from 80K up to 723K. Raman spectra were collected in backscattering configuration on TriVista 557 Raman system equipped with a nitrogen cooled CCD detector. The $\lambda = 532$nm line of solid state Nd:YAG laser was used as an excitation source with sub-mW laser powers on the sample in order to eliminate heating effects. In the μ-Raman spectra of $BiFeO_3$ nanoparticles measured over $80 - 723$K, more than thirteen optical phonon modes of A_1 and E symmetry have been observed. These spectra, deconvoluted using Lorentzian absorption profiles, are shown in Fig. 1 for four representative temperatures.

The total number and frequencies of the observed Raman active phonon modes of $BiFeO_3$ nanoparticles are identical to those detected in temperature dependent Raman scattering spectra carried out on bulk $BiFeO_3$ single crystals [15], apart from the splittings of some of the polar LO+TO phonon modes in the $BiFeO_3$ nanoparticles [16,17]. In bulk, factor group analysis predicts exactly thirteen $(4A_1 + 9E)$ Raman active phonon modes [18]. Unlike the bulk $BiFeO_3$, the Raman active optical modes of the $BiFeO_3$ nanoparticles are seated on a distinctively broad spectroscopic feature (Fig. 1 shaded in light gray), which markedly varies with temperature. A similar spectroscopic background consisting of a non-resonant continuous profile was encountered in metal-oxide thin films [19], but with nearly structureless and of a rather enhanced intensity. This background is associated with a purely electronic Raman response, i.e. electronic scattering contribution independent of phonon bands, as a result of the atomic scale surface roughness. Furthermore, inelastic Raman scattering by particle-hole pair excitations was evidenced to lead to the emergence of electronic background in both metal-island films with adsorbants [20] and in very small metallic particles [21], which was interpreted in terms of the momentum conservation breakdown in the presence of the surface states. In hole-doped manganese perovskites, Liu et al. [22] found out that the broad electronic Raman response, accompanied with the scattering by conduction electrons, exhibits a distinctive change through the phase transition which could be followed quantitatively by the evolution of electron correlation effects.

A theory that describes and quantifies the profiles of Raman electronic background in ″dirty″ conductors was first developed by Falkovsky [7]. The author observed the effects of electronic excitations at low energies via scattering by impurities or phonons to include a finite momentum transfer ($q \neq 0$) caused by the finite penetration depth. Soon afterwards, Zawadowski and Cardona [8] employed a Feynman diagrammatic approach to evaluate the Kubo response function in the ladder approximation [23] for $q = 0$, establishing a close connection with the charge carrier transport lifetime. Feynman diagrams for nonresonant Raman scattering are given in Fig. 2(a). The wavy lines denote photon propagators with initial and final (momentum, energy): $(\vec{k}_i, \omega_i)$ and $(\vec{k}_f, \omega_f)$ up to the reduced Planck's constant. The incoming photon generates an electron-hole pair scattered by a phonon or impurity excitation $(\vec{q} = \vec{k}_i - \vec{k}_f, \omega = \omega_i - \omega_f)$. In the ladder approximation, a phonon or impurity (dashed line in Fig. 2(a)), excited by the electron within the pair, is caught by the counterpart hole and vice versa. Finally, due to the dominating ladder-like diagrams, the approximation leads to the electronic Raman differential cross section [9,11], which can be written down as

$$\frac{\mathrm{d}^2\sigma}{\mathrm{d}\omega\mathrm{d}\Omega} = \mathscr{A}_\tau \times \frac{1}{1 - \exp\left(-\hbar\omega/k_BT\right)} \times \frac{\omega\tau}{1 + (\omega\tau)^2}. \quad (1)$$

The constant $\mathscr{A}_\tau$ depends on several factors varying from one experiment to another [10], which we attach no importance to in the present study. Bose-Einstein thermal correction factor and Drude-like expression are given by the second and third term in the product, respectively. The effective scattering rate, $1/\tau$, includes two terms,

$$1/\tau = \underbrace{1/\tau_0}_{\text{bulk}} + \underbrace{Dq^2}_{\text{nano}}, \quad (2)$$

where $1/\tau_0$ denotes the scattering rate of the charge carrier by impurities in the $q = 0$ limit coming from the bulk channel, and the second term describes the effects of momentum non-conserving processes. The bulk term will be safely disregarded in the present case.

Actually, there is no evidence of the electronic Raman background in bulk semiconductor $BiFeO_3$ crystals [15], as opposed to the present case of $BiFeO_3$ nanocrystals (Fig. 1). The second term in Eq. (2), which originates from the nanoscopic nature of the crystalline $BiFeO_3$ particles is due to the momentum conservation breakdown. Thus, $q = 2\pi/\langle\ell\rangle$, where $\langle\ell\rangle$ represents the characteristic length of the expected nanoparticle size. We can automatically assume that the second term dominantly contributes to the effective scattering rate $1/\tau$. Prefactor D represents the diffusion constant and is intimately related to the electric resistivity ρ by the Einstein relation: $D^{-1} = e^2 g(\epsilon_F)\rho$, where $e = 1.6 \times 10^{-19}$ C, with $g(\epsilon_F)$ as the average value of the density of electronic states that give rise to the conduction in the vicinity of Fermi level [9]. The temperature evolution of the effective scattering rate $1/\tau$ can be followed from Fig. 2(b) delineating a temperature set of the normalized Drude-like $\hbar\omega$-dependences extracted from the measured Raman temperature dependent spectra of the $BiFeO_3$ nanoparticles.

Charge Carrier Transport. Temperature variation of the logarithm of conductivity, $\ln(1/\rho)$, is oftentimes plotted as a function of $(1/T)^n$ in disordered materials, such as nano $BiFeO_3$, and "badly" conducting ceramics [25]. Exponent n imparts information on the DC conduction mechanism. When it is close to 1/4, n bears a signature of 3D Mott VRH transport mechanism [14], whereas an n value close to 1/2 indicates the presence of strong Coulomb correlations in 3D VRH [13]. Both VRH conduction mechanisms are supposed to prevail at low temperatures owing to the localized states around Fermi level in bulk semiconductors with disorder (blue arrow in Fig. 2(c) left). At rather high temperatures, the conduction runs by thermal activation via conduction band of the intrinsic semiconductor (red arrow in Fig. 2(c) left). However, once the particle size reaches nanoscales, the overlaps among the orbitals decrease. As a result, the bands become too sparse to cause splittings by opening up rather large gaps. The bands high in energy, such as conduction band, therefore tend to disappear as often encountered in disordered nanoscale samples, contrary to the corresponding bulk matter. For that reason, it is reasonable to assume that VRH mechanisms are applicable over temperature ranges that may extend up to higher temperatures in disordered nanostructures like $BiFeO_3$, and surely far outweigh the intrinsic thermally activated transport via conduction band which can be ignored, as is given in the right part of Fig. 2(c).

Crystalline $BiFeO_3$ nanoparticles exhibit the phase transition around 640K. At temperatures below it, the Coulomb correlations become sufficiently strong to form the AF phase, while above it the absence of the correlations is manifested through the weakly metallic-like PM state. We postulate the presence of localized surface states with energies close to the Fermi level that mediate the VRH transport over an extended temperature range. Temperature variations of $\ln(1/\tau)$, which is $\propto\ln(1/\rho)$ by Einstein relation, do differ on two sides of the AF/PM phase transition. The n values, which straighten out the $\ln(1/\tau) \propto T^{-n}$ curves are essentially different in the two phases.

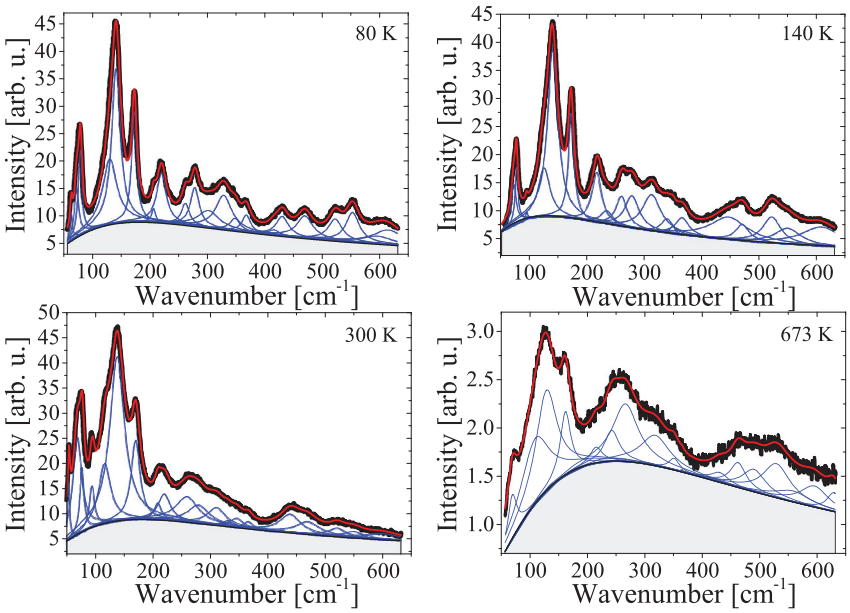

Fig. 1. Raman scattering spectra at four representative temperatures comprising of a smooth electronic background (area shaded in light gray) and more than thirteen phonon peaks (blue lines). The total fitting line is drawn in red, whereas the data points are given in black. (For interpretation of the references to colour in this figure legend, the reader is referred to the web version of this article.)

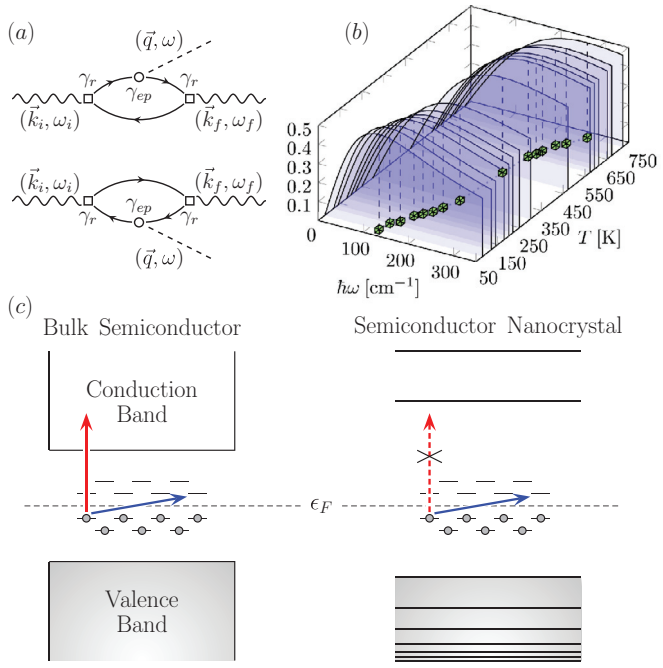

Fig. 2. (*a*) The Feynman diagrams describing the Raman scattering of light (wavy lines) processes by phonons or impurities (dashed lines) with electron-hole formations (solid lines). The processes are of third order in electron or hole scattering by phonons and impurities. Electron and hole contributions are represented by upper and lower diagrams, respectively. γ_r stands for electron-photon interaction (□ vertex), while γ_{ep} stands for electron-phonon interaction (◯ vertex) [24]. (*b*) Temperature dependent Raman electronic Drude-like background of $BiFeO_3$ nanoparticles (Fig. 1) normalized by both Bose-Einstein thermal correction factor and $\mathscr{A}_\tau$ (Eq. (1)). Cubes in green follow the temperature evolution of effective scattering rate $1/\tau$, in temperature (T)-Raman shift ($\hbar\omega$) plane. (*c*) Conduction mechanisms due to the intrinsic activation from valence to conduction band (red arrow) and VRH promoted by localized states around Fermi level (blue arrow) in bulk (left) and nanocrystal (right) semiconductor. (For interpretation of the references to colour in this figure legend, the reader is referred to the web version of this article.)

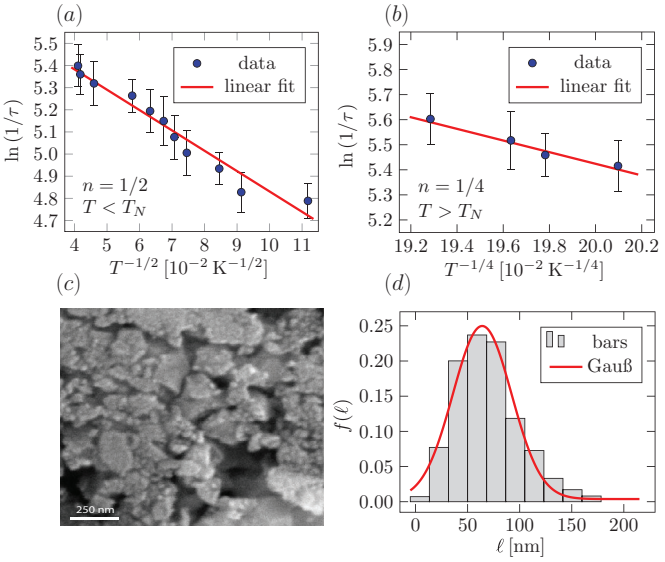

Fig. 3. Temperature (T^{-n}) dependence of the logarithm of the effective scattering rate ($\ln(1/\tau)$) for $T < T_N$ in figure (*a*) with $n = 1/2$ and for $T > T_N$ in figure (*b*) with $n = 1/4$. Linear fits are given in red lines. (*c*) TESCAN SM-300 image of the surface morphology of the $BiFeO_3$ nanoparticle batch and (*d*) the related histogram of the particle diameter distribution (bars in gray) fitted by the normal distribution function (Gauß) given in red line with (64 ± 2) nm as the mean value and (28 ± 2) nm as the standard deviation. $f(\ell)$ stands for the frequency of appearance with respect to the nanoparticle size ℓ. (For interpretation of the references to colour in this figure legend, the reader is referred to the web version of this article.)

The temperature dependences of $\ln(1/\tau)$ are linearized against T^{-n}, with $n = 1/2$ (Fig. 3(*a*)) and $n = 1/4$ (Fig. 3(*b*)) in the strongly correlated AF ($T < T_N$) and PM phase ($T > T_N$), respectively, which is in accordance with the predictions for the applicability of the two VRH mechanisms [13,14]. To be precise, the temperature evolution of $\ln(1/\tau)$ is proportional to $(T_n/T)^n$, with $k_B T_{1/2} \approx e^2/(4\pi\epsilon_0\epsilon_r\xi)$ for $n = 1/2$ [13] and $k_B T_{1/4} \approx 18.1/(g(\epsilon_F)\xi^3)$ for $n = 1/4$ [26], where $k_B = 1.38 \times 10^{-23}$J/K and $\epsilon_0 = 8.85 \times 10^{-12}$F/m. Parameter ξ is the localization length of wave function

of the electronic surface states, while ϵ_r represents the relative permittivity constant, calculated as $\epsilon_r \approx 28$ using the impedance dielectric spectroscopy of nanocrystalline $BiFeO_3$ [27].

Relying on the extracted slopes from the two linear fits in Fig. 3(*a*) & (*b*), we have come up with $\xi \approx 7$nm. This finding proves quite meaningful as a localization length of wave function of the electronic surface states since $\xi < \langle \ell \rangle$, where the average particle size $\langle \ell \rangle$ reaches up nearly to 66nm. This value has been computed as the mean value from the Gaußian particle size distribution obtained from Scanning Electron Microscopy (SEM) image of $BiFeO_3$ nanoparticles at room temperature and using the Scanning Probe Image Processor software (Fig. 3(*c*) & (*d*)). Furthermore, the density of localized states, $g(\epsilon_F)$, can also be determined by manipulating the fitting parameters extracted from Fig. 3(*a*) & (*b*). Namely, $g(\epsilon_F) \approx 2.1 \times 10^{18}$ localized states per (eV $\times$ cm^3) in the high temperature PM phase. This allows us to estimate the resistivity value ρ from Eq. (1) and the Einstein relation. Thus, following Fig. 2(*b*), at high temperatures $h/\tau \approx 250$ cm^{-1}, where $h = 6.626 \times 10^{-34}$Js. Accordingly, $\rho \approx 4\pi^2\tau/(\langle \ell \rangle^2 e^2 g(\epsilon_F)) \approx 350\,\mathrm{m\Omega cm}$ at lowest. Its extraordinarily high value is not possible in conventional metals and exceeds the maximum resistivity value allowed by the Mott-Ioffe-Regel limit of at most $\sim 1\,\mathrm{m\Omega cm}$ [28,29], which classifies nanocrystalline $BiFeO_3$ as a bad conductor. This finding strongly suggests that the conduction band energy sector is likely to fade away to ultimately acquire markedly low electronic density of states, leaving no room for the fixed thermally activated transport to take over 3D VRH. Nevertheless, other reliable experimental tools, such as AC/DC transport measurements, infrared and electron spin resonance spectroscopy on somewhat larger particles, might be a good proposal to uphold the validity of the VRH mechanisms we have put forward.

Conclusions. In summary, here is reported an indirect finding of the two different VRH transport regimes through the analysis of the temperature dependent electronic Raman background of $BiFeO_3$ nanoparticles. The switch between the two strikingly different VRH transport regimes coincides with AF/PM phase transition. The VRH exponent of $n = 1/2$ is associated with the AF strongly correlated phase below T_N implying the presence of correlations, whereas the exponent $n = 1/4$ neatly linearizes the temperature dependence of the logarithm of effective scattering rate in the PM state above T_N. It has been also deduced that the nanoscaled $BiFeO_3$ falls into the family of bad conductors due to its exceptionally high resistivity value. At last, it is worth mentioning that, to the extent of our knowledge, the existence of different conduction VRH regimes in AF and PM phases has never been previously recognized in $BiFeO_3$ nanocrystals.

Declaration of Competing Interest

The authors declare that they have no known competing financial interests or personal relationships that could have appeared to influence the work reported in this paper.

Acknowledgments

We are grateful to Professor László Forró for valuable discussions on the topics of VRH transport mechanism. This work is supported by the Serbian Ministry of Education, Science, and Technological Development through project OI 171032.

References

[1] J. Wang, J.B. Neaton, H. Zheng, V. Nagarajan, B.S.B. Ogale, Liu, D. Viehland, V. Vaithyanathan, D.G. Schlom, U.V. Waghmare, N.A. Spaldin, K.M. Rabe, M. Wuttig, R. Ramesh, Science 299 (2003) 1719–1722, doi:10.1126/science.1080615.
[2] T.J. Park, G.C. Papaefthymiou, A.J. Viescas, A.R. Moodenbaugh, S.S. Wong, Nano Lett. 7 (2007) 766–772, doi:10.1021/nl063039w.
[3] G. Catalan, J.F. Scott, Adv. Mater. 21 (2009) 2463–2485, doi:10.1002/adma.200802849.
[4] A. Mukherjee, M. Banerjee, S. Basu, N.T.K. Thanh, L.A.W. Green, M. Pal, Physica B: Cond. Matt. 448 (2014) 199–203, doi:10.1016/j.physb.2014.03.082.
[5] S. Ruby, S.S.R. Inbanathan, Appl. Surf. Sci. 449 (2018) 10–14, doi:10.1016/j.apsusc.2017.11.231.
[6] L.A. Falkovsky, Phys. Usp. 47 (2004) 249–272, doi:10.1070/pu2004v047n03abeh001735.
[7] L.A. Falkovsky, Sov. Phys. JETP 68 (1989) 661–663.
[8] A. Zawadowski, M. Cardona, Phys. Rev. B 42 (1990) 10732–10734, doi:10.1103/PhysRevB.42.10732.
[9] T.P. Devereaux, Phys. Rev. B 45 (1992) 12965–12975, doi:10.1103/PhysRevB.45.12965.
[10] E.Y. Sherman, O.V. Misochko, J. Phys. Condens. Matter 15 (2003) 3751–3758, doi:10.1088/0953-8984/15/22/309.
[11] T.P. Devereaux, R. Hackl, Rev. Mod. Phys. 79 (2007) 175–233, doi:10.1103/RevModPhys.79.175.
[12] B. Stojadinović, Z. Dohčević-Mitrović, D. Stepanenko, M. Rosić, I. Petronijević, N. Tasić, N. Ilić, B. Matović, B. Stojanović, Ceram Int. 43 (2017) 16531–16538, doi:10.1016/j.ceramint.2017.09.038.
[13] A.L. Efros, B.I. Shklovskii, J. Phys. C Solid State Phys. 8 (1975) L49–L51, doi:10.1088/0022-3719/8/4/003.
[14] N.F. Mott, E.A. Davis, Electronic Processes in Non-Crystalline Materials, Oxford University Press, 1979.
[15] H. Fukumura, H. Harima, K. Kisoda, M. Tamada, Y. Noguchi, M. Miyayama, J. Magn. and Magn. Mat. 310 (2007) e367–e369, doi:10.1016/j.jmmm.2006.10.282.
[16] J. Hlinka, J. Pokorny, S. Karimi, I.M. Reaney, Phys. Rev. B 83 (2011) 020101–020104, doi:10.1103/PhysRevB.83.020101.
[17] J. Bielecki, P. Svedlindh, D.T. Tibebu, S. Cai, S.-G. Eriksson, L. Börjesson, C.S. Knee, Phys. Rev. B 86 (2012) 184422–184437, doi:10.1103/PhysRevB.86.184422.
[18] D.L. Rousseau, R.P. Bauman, S.P.S. Porto, J. Raman Spectrosc. 10 (1981) 253–290, doi:10.1002/jrs.1250100152.
[19] A. Otto, J. Timper, J. Billmann, G. Kovacs, I. Pockrand, Surf. Sci. 92 (1980) L55–L57, doi:10.1016/0039-6028(80)90237-X.
[20] C.Y. Chen, E. Burstein, S. Lundquist, Solid State Commun. 32 (1979) 63–66, doi:10.1016/0038-1098(79)90998-0.
[21] R. Monreal, F. Flores, Y. Gao, T. López-Ríos, Europhys. Lett. 4 (1987) 115–120, doi:10.1209/0295-5075/4/1/019.
[22] H.L. Liu, S. Yoon, S.L. Cooper, S.-W. Cheong, P.D. Han, D.A. Payne, Phys. Rev. B 58 (1998) R10115–R10118, doi:10.1103/PhysRevB.58.R10115.
[23] A.A. Abrikosov, L.P. Gorkov, I.E. Dzyaloshinsky, Quantum Field Theoretical Methods in Statistical Physics, Pergamon Press (Oxford), 1965.
[24] M. Cardona, Light Scattering in Solids I - Introductory Concepts, Springer-Verlag (Berlin), 1983.
[25] L. Zuppiroli, L. Forró, Phys. Lett. A 141 (1989) 181–185, doi:10.1016/0375-9601(89)90785-8.
[26] W.D. Rice, R.T. Weber, P. Nikolaev, S. Arepalli, V. Berka, A.L. Tsai, J. Kono, Phys. Rev. B 88 (2013) 041401–041405, doi:10.1103/PhysRevB.88.041401.
[27] B. Stojadinović, University of Belgrade, 2018 Ph.D. thesis. Faculty of Physics,
[28] O. Gunnarsson, M. Calandra, J.E. Han, Rev. Mod. Phys. 75 (2003) 1085–1099, doi:10.1103/RevModPhys.75.1085.
[29] N.E. Hussey, K. Takenaka, H. Takagi, Philos. Mag. 84 (2004) 2847–2864, doi:10.1080/14786430410001716944.

Journal of Magnetism and Magnetic Materials 491 (2019) 165616

Contents lists available at ScienceDirect

Journal of Magnetism and Magnetic Materials

journal homepage: www.elsevier.com/locate/jmmm

Research articles

Extreme conduction electron spin resonance: $A/B \rightarrow (5 + 3\sqrt{3})/4$, the universal limit of lineshape asymmetry ratio

Dejan M. Djokić[a,b,*], Dimitrije Stepanenko[a], Zorana Dohčević-Mitrović[a]

[a] Nanostructured Matter Laboratory, Institute of Physics Belgrade, University of Belgrade, Pregrevica 118, 11 080 Belgrade, Serbia
[b] Laboratory of Physics of Complex Matter, Ecole Polytechnique Fédérale de Lausanne, Station 3, CH-1015 Lausanne, Switzerland

ARTICLE INFO

Keywords:
Magnetic resonance
Spin relaxation
Microwave absorption
Microcrystalline conductors
Skin depth

ABSTRACT

We derive the Electron Spin Resonance (ESR) lineshape in conducting crystals, relying on the density matrix description. In our approach, lineshape is determined as linear combination of absorptive and dispersive signals with non-negatively real coefficients, corresponding to the NMR limit. The significant points and segments of the total signal at resonance have been systematically quantified, and along that line, we have formulated an alternative fitting strategy consisting of few straightforward steps to obtain the relevant ESR parameters in metallic systems. Finally, by examining different crystal geometries, the universal value, $A/B \rightarrow (5 + 3\sqrt{3})/4$, of the lineshape asymmetry ratio has been derived in the case of metallic particles with extreme conductivity.

1. Introduction

1.1. Past progress in conduction electron spin resonance

Conduction Electron Spin Resonance (CESR) in bulk and micro-sized conducting crystalline materials has captured much scientific attention for its capacity to probe the electric conductivity of materials in a noninvasive way. This makes CESR particularly informative, as there are hardly few experimental techniques able to compete with it in probing conducting systems, where the motion of free carriers has a profound eddy current effect upon the asymmetry of the signal at resonance. The pioneering attempts to tackle the effects of eddy currents in conducting systems, set up by AC field used to excite resonance, date back to the 1950's. As evidenced by Feher and Kip [1], Dyson [2] proposed that asymmetric CESR lines observed in bulk metals arise from a combination of the following two effects. First, the AC field becomes attenuated within a characteristic skin depth. Secondly, the free electrons are capable of diffusing in and out of the skin depth many times between subsequent spin reversals at resonance. The latter fact is particularly important in CESR based on the transmission technique. In this case the magnetization penetrates much farther into the metal as compared to the AC magnetic field, which additionally contributes to asymmetry in resonance signals [3,4]. Chapman et al. [5] soon afterwards developed a theoretical treatment to understand both on- and off-resonance signal for specimens in the shape of flat plates, long cylinders, and spheres, in order to predict the asymmetric nature of the CESR absorption depending on the sample geometry. Dyson was the very first to fully derive such characteristic CESR profiles; thus, these asymmetric lines are referred to as Dysonians. It is often the case that the asymmetry is quantified by the A/B ratio which serves as a reliable indicator of metallicity in experiments. Platzman and Wolf [6] studied spin waves excitations in non-ferromagnetic metals at resonance using the Fermi-liquid theory. The results of their generalized approach in the limit of short momentum relaxation times are equivalent to those of Dyson's. In the meantime, Dyson's theory was further extended to encompass various shapes of crystals and particular resonant field orientations [7–9].

In the early 1980's, however, Kaplan perceived a material discrepancy between the application of Dyson's theory and experiments operating in the reflection mode [10]. This was explained by the fact that CESR signals originate from paramagnetic species on the crystal surface which imposes the inclusion of a dispersion component coming from surface polaritons, unlike CESR signals obtained in the transmission mode. Namely, Kaplan suggested that the resonance in conducting systems is excited rather with electric than with magnetic component of the AC field. The electric field is coupled with the free carrier momentum on the crystal surface through the relativistic spin-orbit interaction that, with application of purely quantum mechanical density matrix method, ultimately leads to the following most general form of the CESR signal: $S(\omega) = \alpha\chi''(\omega) + \beta\chi'(\omega)$ as studied in [11]. Components χ'' and χ' stand for the absorptive and the dispersive part of the signal, while α and β are the sizes of their respective contributions,

* Corresponding author at: Nanostructured Matter Laboratory, Institute of Physics Belgrade, University of Belgrade, Pregrevica 118, 11 080 Belgrade, Serbia.
E-mail address: djokic@ipb.ac.rs (D.M. Djokić).

https://doi.org/10.1016/j.jmmm.2019.165616
Received 27 March 2019; Received in revised form 16 June 2019; Accepted 18 July 2019
Available online 19 July 2019
0304-8853/

which both vanish in the limit of extremely conductive samples and/or short skin depths relative to the size of samples. The notion of complex spin susceptibilities is further elaborated by Siegman [12] who links χ'' to amplifying and χ' to reactive magnetic response near resonance. It is interesting to note that the form $\alpha\chi'' + \beta\chi'$ is indeed a particular form of Dysonian, corresponding to the so-called "NMR limit" [13,14], when electrons diffusion rate is much smaller than the rate of spin relaxation. Kaplan put forward that no other limit is necessary to consider in order to properly understand CESR spectra of ordinary metals. Furthermore, in this case, no particular spin dynamics can lead to Gaussian-profiled absorptions (χ'') due to the dimensionality or motionally narrowed signals [15,16], so that only Lorentzian profiles of the pure absorption are considered.

Over recent years, use of CESR has proven increasingly efficient in studying micrometer-sized crystals in the shape of metallic clusters and/or metallic colloids [17,18]. Baudron et al. [19] employed this probe in order to acquire the resistivity data in a contactless way when working with fragile organic compounds. At nanoscopic scales, CESR finds its practical usefulness in both understanding spin relaxation dynamics and determining the nature of electron transport in fullerenes, carbon nanotubes, and nano-diamond particles [20–22]. Sensitivity of ESR signal shape to the relative length scales of high frequency skin effect, characteristic electron diffusion length, and the spin diffusion lengths make altogether it a useful probe for effects that happen in a thin layer on the surface of conducting sample. Therefore, the lineshape indicates size of particles in micro-structured samples.

1.2. Problem description and structure details

Dyson [2] originally put forward the theory capable to directly associate the onset of asymmetry with the dynamics of charge carriers in metallic samples of different sizes. However, this theory has not proven universally applicable for two reasons. First, ESR techniques may be operating at either transmission or reflection mode, and only former was originally described by Dyson's theory. Second, there are polariton surface modes emerging from the coupling between the electromagnetic wave and electric dipole excitations. These were studied by Kaplan [10] who focused on Dyson's CESR signals that decompose only into a non-negative linear combination of absorption and dispersion. We will rely in this account on this approach in order (i) to analyze the CESR signal, (ii) to quantitatively describe its important lengths and points necessary for simplification of a fitting procedure of CESR lineshape which we establish in this work, as well as, (iii) to explain and derive the geometry independent asymmetry ratio limit ($A/B \to (5 + 3\sqrt{3})/4$) in the case of extreme CESR carried out on highly conducting samples. This limiting value is quite often encountered in literature as 2.55 limit, and yet, to the best of our knowledge, it has never been extracted analytically. The A/B ratio also tends to this universal value once nano- or micro-sized metallic samples start to agglomerate into larger ones. Such a feature makes CESR particularly useful in controlling the degree to which the clustering takes place [23,24].

The present study delves into the theoretical account of the field-dependent CESR signal and its derivative starting with retarded Green's function formalism in angular quasi-frequency space. A method has been set out for properly analyzing the CESR curves, together with their links to geometry and conductivity dependences in terms of sample-dimension-to-skin-depth variable. Our major analytical finding represents the closed-form solution of A/B in the high-conduction limit. Most critically for experimentalists affiliated to the ESR community, this work discusses a scheme to unambiguously resolve the phase emerging in magnetic resonance – an issue particularly essential for CESR measurements at modern-day spectrometers. Owing to the prevalence of paramagnetic measurements, the phases are habitually zeroed out.

2. Theoretical aspects and results

Following the approach by Kaplan [25,10,26], we focus on ESR whose absorption spectral lines are fairly represented by the spectral function $S(q, \omega)$ of a carrier electron spin, which is determined by retarded Green's function $G^R(q, \omega)$, where $\Sigma(q, \omega)$ is retarded self energy [27,28]. In Fourier space, $G^R(q, \omega)$ is specified as follows

$$G^R(q, \omega) = \frac{1}{\omega - \Sigma(q, \omega) - \imath\eta}, \quad \eta \to 0^+, \tag{1}$$

where $\Sigma(q, \omega) \equiv \mathscr{R}e\Sigma(q, \omega) + \imath\mathscr{I}m\Sigma(q, \omega)$ is a complex-valued function. In a CESR experiment, $q \approx 0$, since the microwave wavelength is much longer than the crystal lattice spacing. This approximation does not take into account dynamics of the environment which influences the electron spin. Generally, one has to pay attention to spin diffusion effects in CESR that might drive the physics well beyond long wavelength scales [29–31]. We therefore assume that the spectral function describes local effects by setting $\mathscr{R}e\Sigma(q, \omega) \simeq \mathscr{R}e\Sigma(\omega) = \omega_0$ ($\propto$ the resonant field H_0) and that $\mathscr{I}m\Sigma(q, \omega) \simeq \mathscr{I}m\Sigma(\omega) = -\Delta\omega$ ($\propto$ the linewidth ΔH). The physical meaning of $\mathscr{R}e\Sigma(q, \omega)$ and $\mathscr{I}m\Sigma(q, \omega)$ is grasped at a microscopic level. The resonant condition is translated into $H_0 = \kappa\omega_0$, where ω_0 stands for the resonant angular frequency and $\kappa \equiv \hbar/(g\mu_B\mu_0 S)$. g represents electron Landé factor in the material, $\hbar$ is reduced Planck constant, μ_B is Bohr magneton, μ_0 is vacuum permeability, and electron spin $S = 1/2$. Similarly, $\Delta H = \kappa\Delta\omega$. In SI units, $g{\cdot}\kappa = 1.809792 \times 10^{-5}$ A/(m·Hz), while in *cgs* units, $g{\cdot}\kappa = 2.274252 \times 10^{-7}$ Ørsted·s.

For convenience of notation we stick to the quasi-frequency formalism in which ω is a quasi-frequency, since the externally applied magnetic field H (directly proportional to ω by κ) is actually being swept. In that way, the normalized spectral function (in the case of pure absorption) looks like

$$S(\omega) \equiv -\frac{1}{\pi}\mathscr{I}mG^R(\omega) = \frac{\Delta\omega/\pi}{(\omega - \omega_0)^2 + \Delta\omega^2} \equiv \chi''(\omega). \tag{2}$$

It is necessary to say that $G^R(\omega)$ routinely goes out of phase with the microwave AC stimulus. Root cause of this phase slip is in the effects not taken into account by the bare response function (2). Most prominently, the cavity and electronics of the ESR spectrometer, as well as the dynamics of electron spins in the sample, introduce a correction to the ESR response. For that reason, the ESR signal is derived from Green's function multiplied by a complex function $\rho(\varphi)e^{-\imath\varphi}$, with real both $\rho(\varphi)$ and φ. Consequently, $G^R(\omega) \to G^R(\omega)\rho(\varphi)e^{-\imath\varphi}$, where φ is a free variable and $\rho(\varphi \to 0) \to 1$. Function $\rho(\varphi)$ describes instrumental artifacts arising from phase-mismatched ESR cavities, as well as the effects exerted by intrinsic crystal properties, such as dynamical screening of the AC field at skin depth scales [32]. The analysis of former is often avoided by matching the cavity so that the so-called tangent of loss angle, $\tan\varphi$, becomes minimal. In that case, the quality factor $Q_\varphi \equiv 1/\tan\varphi$ reaches its maximum, especially once $\varphi \to 0$. However, in ESR performed on conducting crystals the aforementioned matching is undesirable because valuable information about the crystal physics could be lost. Therefore, following the line of reasoning from (2), the CESR output now becomes proportional to

$$S(\omega, \varphi) \propto \mathscr{N}\rho(\varphi)(\chi''(\omega)\cos\varphi + \chi'(\omega)\sin\varphi), \tag{3}$$

where term $\chi'(\omega) \equiv \frac{(\omega - \omega_0)/\pi}{(\omega - \omega_0)^2 + \Delta\omega^2}$ stands for dispersive part of the signal, while $\mathscr{N}$ is appended as the number of active spins probed at resonance. $\mathscr{N}$ also reflects on how dynamically susceptible a paramagnetic system is, which will be normalized to 1 for simplicity. Here, we emphasize again that the essence of ω is encapsulated in the scanned magnetic field ($\omega \equiv H/\kappa$). That is why ω is rather a quasi- than a true frequency, except for the case of the true microwave angular frequency $\omega_0 = 2\pi\nu_0$ which is fixed in standard ESR setups [33]. The proportionality factor in (3) is related to ESR spectrometer configuration, not to crystal properties. Moreover, the genuine ESR signal represents the first

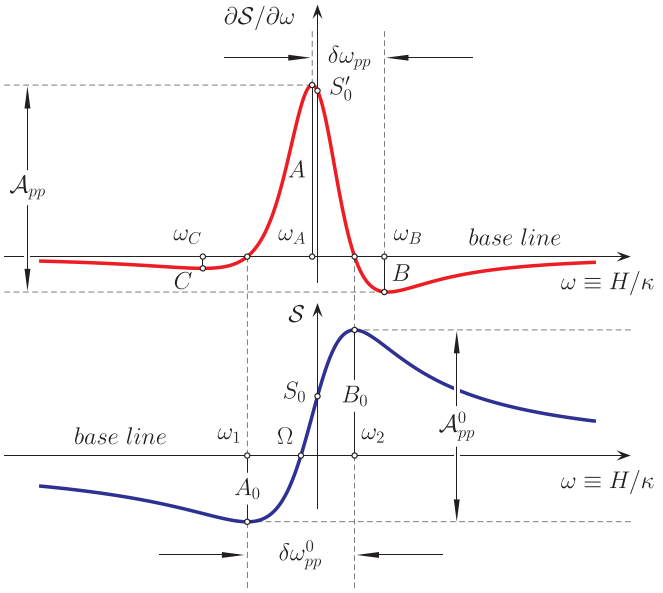

Fig. 1. Lorentzian absorption profile admixed with the associated dispersion (lower in blue) and the related first derivative of the signal with respect to the quasi-frequency (upper in red). The coordinates and lengths of all the relevant points and segments are also given. (For interpretation of the references to colour in this figure legend, the reader is referred to the web version of this article.)

derivative of $S(\omega, \varphi)$, that is $\partial_\omega S(\omega, \varphi)$ or $S'(\omega, \varphi)$, as a result of the deployed lock-in technique. The double integral of $S'(\omega, \varphi)$ is $\mathscr{N}\rho(\varphi)\cos\varphi$. It *does* include the φ dependent contribution, which becomes pure $\mathscr{N}$ only when $\varphi \to 0$.

2.1. Significant points of the spectral lineshape functions

This subsection is devoted to a full description of the characteristic points and segments of CESR signal, both differentiated ($\partial S/\partial\omega$) and non-differentiated (S). Their values depend upon two types of variables. The first type includes φ and $\rho(\varphi)$ that originate from the effects of microwave loss in conducting systems and geometry, whereas the remaining variables come from the spin relaxation processes ($\Delta\omega$), g-factor or H_0 position being identified as $\kappa\omega_0$, and the number of susceptible spins $\mathscr{N}$. For simplicity, we have normalized $\mathscr{N}$ to 1 and shifted ω_0 to 0, without loss of generality.

The significant values of ω are shown in Fig. 1 which features Lorentzian absorption profile admixed with its dispersion $S(\omega)$ (lower, in blue) and the signal first derivative $S'(\omega)$ (upper, in red). Points ω_1 and ω_2 are ω-positions of the two extremal lobes, while Ω stands for the single node of $S(\omega)$. Points ω_A, ω_B, and ω_C are ω-positions of the three extremal lobes of $S'(\omega)$, while there are the two nodes which must coincide with ω_1 and ω_2. In the convention we use, factor of ω_0 needs to be added to all the points of $S(\omega)$ and $S'(\omega)$ lineshape functions. Segments A_0 and B_0 correspond to the depth and height of the two extremal lobes of $S(\omega)$, respectively, while S_0 represents its value at zero ω. Segments A, B, and C are lengths (depths or heights) of the three extremal lobes in $S'(\omega)$, whereas S'_0 measures its height at zero. The lengths of all the segments in both cases, $S(\omega)$ and $S'(\omega)$, should be multiplied with $\mathscr{N}$ for generalization purposes. Table 1 provides a detailed overview of the significant points and lengths whose values are given as functions expressed in a $\mathscr{F}(\varphi, \rho(\varphi), \Delta\omega)$ form for both $S(\omega)$ (left double-column) and $S'(\omega)$ (right double-column). Other relevant values, such as peak-to-peak positions, will be discussed later in the text.

Walmsley and co-workers [13,14] have demonstrated that a Dysonian line exactly coincides with the sum of positively contributed absorptive and dispersive curves in the so-called "NMR-limit", when $0 \leqslant \varphi < \pi/2$. This limit implies that electron diffusion processes are much slower than spin relaxation processes in ordinary metals. On the other hand, it is of practical interest to consider the case when the spectrum is phased not due to the intrinsic physics of the system, but rather owing to the limitations of experimental means. Thus, the real and imaginary part of the measured ESR spectrum do not essentially emerge as the real and imaginary part of the field-differentiated inherent spin susceptibility. In high magnetic field ESR experiments of a few-hundred GHz resonant frequency, such as in a quasi optical high field ESR setup operating in a submillimeter frequency range [34,35], data are usually fitted to an arbitrary combination of absorption and dispersion Lorentzian lines. Even in the case of non-conducting, purely ESR absorptive, crystals which have no intrinsic phase, the combination is present as a sole uncontrollable instrumental consequence to even allow $0 \leqslant \varphi < 2\pi$. The phase with such a range will be henceforth named as ϕ which must not be mistaken for φ that falls into the first quadrant $(+,+)$ only. Therefore, in ESR systems with no tunable cavities, the ESR signal fractions coming from χ'' and χ' can even assume negative values. As a consequence, physically valuable information on the phase inherent to the conducting systems may irreversibly be lost by the inescapable instrumental arrangement. However, it is often the case that samples probed at high frequency ESR contain several ESR active species among which one can be a set of localized defects detected due to the high sensitivity of the probe. One such example is semi-metallic crystalline kagomé compound based on organic tetrathiafulvalene which contains a very low concentration of magnetic defects [19]. Being insulating, these defects may serve as a reference in a high field ESR experiment since they are intrinsically phaseless unlike the major CESR active line. If a spectral component coming from such localized species is present, then the real part is itself purely absorptive and this piece of information can be exploited to (de) phase the spectrum. For that reason, it is of the utmost importance to know the phase difference between the signals of CESR and of localized ESR species, in order to impart the valuable information on the sample conductivity. The two lines are presumably weighted by their instrumental phases which are the same up to the phase period or phase anti-period. Namely, if one has a closer look at $S'(\omega, \phi)$ one notices that there are features of this function which are anti-periodic (and therefore also periodic) in ϕ. For that reason, one has to come up with an irreducible working range of ϕ which is sufficient to reduce the high field ESR signal to a form that is as simple as possible. It turns out that a combination of absorption and dispersion Lorentzian lines with phase $0 \leqslant \phi < 2\pi$, emerging in ESR spectrometers with no controllable cavity, has its unique counterpart in the first quadrant of $0 \leqslant \varphi < \pi/2$. One can notice that $\chi''(\omega)$ and $\chi'(\omega)$ are the even and odd function of ω, respectively. However, the parities of $\partial_\omega\chi''(\omega)$ and $\partial_\omega\chi'(\omega)$ go reverse. Relying on these (anti) symmetry properties of $S'(\omega, \phi)$ each quadrant is covered by the following procedure which makes mapping onto the first quadrant:

$$\begin{aligned}
&\phi \in (+,+) \Rightarrow \quad S'(\omega, \phi) = +S'(+\omega, \varphi), \text{ for} \varphi \in (+,+),\\
&\phi \in (-,+) \Rightarrow \quad S'(\omega, \phi) = +S'(-\omega, \varphi), \text{ for} \varphi \in (+,+),\\
&\phi \in (-,-) \Rightarrow \quad S'(\omega, \phi) = -S'(+\omega, \varphi), \text{ for} \varphi \in (+,+),\\
&\phi \in (+,-) \Rightarrow \quad S'(\omega, \phi) = -S'(-\omega, \varphi), \text{ for} \varphi \in (+,+).
\end{aligned} \tag{4}$$

For simplicity, we have carried out the transformation $\mathscr{H}(\phi)$, which formally translates variable ϕ into $\varphi = \mathscr{H}(\phi)$ in the following manner:

$$\begin{aligned}
&\mathscr{H}(\phi)\\
&= (-1)^{floor\,[2\phi/\pi - 2sgn\,[\phi]]}\\
&\quad \times (\pi + \phi - \pi(quot\,[3 + floor\,[2\phi/\pi - 2sgn\,[\phi]], 2] + sgn\,[\phi])),
\end{aligned} \tag{5}$$

where $floor\,[\phi]$, $sgn\,[\phi]$, and $quot\,[\phi]$ stand for floor, signum, and quotient function in that order. Thus, if there are more than one ESR active species coming from the same sample probed at high frequency ESR

Table 1
Values of the relevant points and segments of the two lineshape functions: S (left) and $\partial S/\partial\omega$ (right) expressed as $\mathscr{F}(\varphi, \rho(\varphi), \Delta\omega)$ dependences.

Points/Segments (S)	$\mathscr{F}(\varphi, \rho(\varphi), \Delta\omega)$	Points/Segments ($\partial S/\partial\omega$)	$\mathscr{F}(\varphi, \rho(\varphi), \Delta\omega)$
ω_1	$\Delta\omega\cot\frac{\varphi}{2}$	ω_A	$\Delta\omega(2\cos\frac{\varphi+\pi}{3} - \cos\varphi)/\sin\varphi$
Ω	$-\Delta\omega\cot\varphi$	ω_B	$\Delta\omega\left(2\cos\frac{\varphi-\pi}{3} - \cos\varphi\right)/\sin\varphi$
ω_2	$\Delta\omega\tan\frac{\varphi}{2}$	ω_C	$\Delta\omega\left(-2\cos\frac{\varphi}{3} - \cos\varphi\right)/\sin\varphi$
$\delta\omega_{pp}^0 \equiv \lvert\omega_2 - \omega_1\rvert$	$2\Delta\omega/\sin\varphi$	$\delta\omega_{pp} \equiv \lvert\omega_B - \omega_A\rvert$	$2\sqrt{3}\Delta\omega\sin\frac{\varphi}{3}/\sin\varphi$
$S_0 \equiv S(0, \varphi)$	$\rho(\varphi)\cos\varphi/(\pi\Delta\omega)$	$S_0' \equiv S'(0, \varphi)$	$\rho(\varphi)\sin\varphi/(\pi\Delta\omega^2)$
$A_0 \equiv \lvert S(\omega_1, \varphi)\rvert$	$\rho(\varphi)\cos^2\frac{\varphi}{2}/(\pi\Delta\omega)$	$C \equiv \lvert S'(\omega_C, \varphi)\rvert$	$\rho(\varphi)\sin^3\frac{\varphi}{3}/(\pi\Delta\omega^2)$
$B_0 \equiv \lvert S(\omega_2, \varphi)\rvert$	$\rho(\varphi)\sin^2\frac{\varphi}{2}/(\pi\Delta\omega)$	$B \equiv \lvert S'(\omega_B, \varphi)$	$\rho(\varphi)\sin^3\varphi(1 - 2\sin\left(\frac{\pi}{6} - \frac{2\varphi}{3}\right))/((-3 + 4\sin\left(\frac{\pi}{6} - \frac{2\varphi}{3}\right) + 2\sin\left(\frac{\pi}{6} + \frac{4\varphi}{3}\right))^2\pi\Delta\omega^2)$
$\mathscr{A}_{pp}^0 \equiv A_0 + B_0$	$\rho(\varphi)/(\pi\Delta\omega)$	$\mathscr{A}_{pp} \equiv A + B$	$3\sqrt{3}\rho(\varphi)\cos\frac{\varphi}{3}/(4\pi\Delta\omega^2)$

systems (let's say two like in the mentioned kagomé compound), we first find their intrinsic phases by employing function $\mathscr{H}(\phi)$ to each, and then subtract their φ values afterwards. In the case when one of the two lines is in fact a CESR line, their phase difference computed in this way reveals the conduction properties of the material.

The antisymmetry of $\omega_A(\phi)$, $\omega_B(\phi)$, and $\omega_C(\phi)$ is outlined in Fig. 2(a). The figure evidently demonstrates the odd parity of the three dependences with respect to $\phi = 180°$. This entails a possibility of halving the entire ϕ domain whereby no property of $S'(\phi)$ is affected. Moreover, this domain can be further dimidiated (cut in half and glued together) on the basis of characteristics of A and B delineated in Fig. 2(b). Namely, it turns out that B and C interchange beyond $\phi = 90°$ so that it is sufficient to map the $S'(\omega, \phi)$ function onto the first quadrant in accordance with the procedure given in (4) and (5). Consequently, all the desired curve features presented in Table 1 can be deduced completely from the dependence on φ. One such parameter is

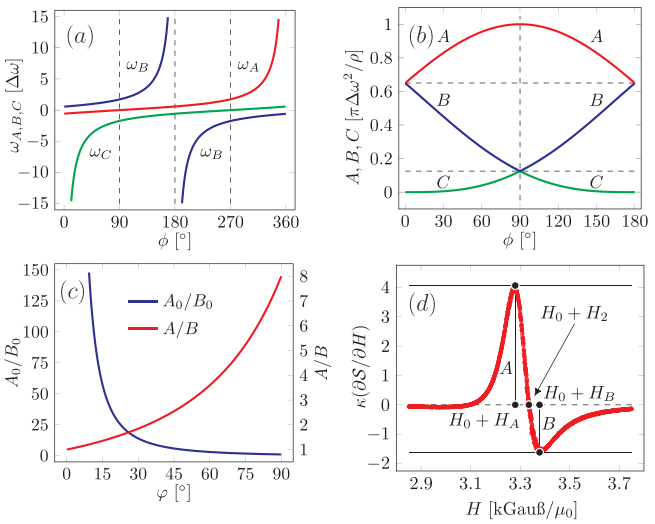

Fig. 2. The odd parity of $\omega_A(\phi)$, $\omega_B(\phi)$, and $\omega_C(\phi)$ over $\phi \in [0, 2\pi)$(a) and the symmetric behaviour of the angular dependent A, B, and C with respect to $\phi = 90°$(b). The φ dependence of asymmetry parameters A/B and A_0/B_0 are given in (c), while (d) delineates arbitrarily simulated CESR data at nearly $\nu_0 = 9.4$ GHz with the representative points meant for fitting shortcuts. First magnetic field derivative of the absorbed power near resonance, $\partial S/\partial H$, must be multiplied by factor κ in order for the spectra to coincide with $\partial S/\partial\omega$ in Fig. 1 (upper in red). External magnetic field strengths H_i are jointly equal to $\kappa\omega_i$ for each $i \in \{1, 2, A, B, C\}$, where ω_i are given in Table 1. External H field is expressed in kGauß/μ_0, which in *cgs* metric converts to the same numbers of kØrsteds ($\mu_0 = 1$ and 1 Gauß = 1 Ørsted), whereas in SI metric the external H field must be expressed in A/m ($\mu_0 = 4\pi \times 10^{-7}$ H/m and 1 T = 10^4 Gauß). (For interpretation of the references to colour in this figure legend, the reader is referred to the web version of this article.)

$A/B \equiv f(\varphi)$, the so-called asymmetry parameter, which measures the ratio between the highest peak height and the lowest dip depth:

$$A/B = \frac{\left(1 + 2\cos\frac{2\varphi}{3}\right)\left(3\cos(\frac{\pi}{6} - \frac{\varphi}{3}) + \sin\varphi\right)}{4\cos(\frac{\pi}{6} - \frac{\varphi}{3})\left(1 + \sin(\frac{\pi}{6} - \frac{2\varphi}{3})\right)^2}, \tag{6}$$

which varies only in the range from 1 to 8, as shown in Fig. 2(c). This property is maintained in the extensions beyond $\phi = \pi/2$, unlike $A_0/B_0 = \cot^2\frac{\varphi}{2}$ in the case of $S(\omega, \phi)$, which may take arbitrary positive values.

2.2. Fitting shortcuts

It is of practical use to experimentalists to have an instructive procedure for fitting CESR spectra in a rather expeditious way. Though exact, algorithms based on the nonlinear least square method, used to refine the fitting parameters by successive iterations, represent slow solution-focused approaches. Here we offer a fitting strategy consisting of few shortcuts towards extracting the relevant CESR parameters, such as phase, microwave loss function, spin relaxation time, and g-factor, immediately from a given lineshape. In Fig. 2(d), the red line represents a single CESR line as recorded in a standard ESR measurement. The first step in interpretation includes tracing the base line (dashed line in Fig. 2) and the three significant points: (*i*) the point with the greatest height ($H_0 + H_A$, A), (*ii*) the point with the greatest depth ($H_0 + H_B$, $-B$), and (*iii*) the spectral node as the crossing point between the spectra and base line ($H_0 + H_2$, 0). By measuring the ratio A/B one finds the phase parameter φ from Eq. (6) as $\varphi = f^{-1}(A/B)$, or alternatively, one can carefully read off the A/B vs φ data from Fig. 2(c). The next steps comprise of measuring the peak-to-peak distances, both horizontal ($\delta H_{pp} = \kappa\delta\omega_{pp}$) and vertical ($\mathscr{A}_{pp} \equiv A + B$). Following Table 1, the ESR linewidth $\Delta H \equiv \kappa\Delta\omega$, which is in direct relationship with spin relaxation time, is obtained as $\Delta H = \frac{\sqrt{3}\sin\varphi}{6\sin(\varphi/3)}\delta H_{pp}$, where $\delta H_{pp} \equiv \kappa\delta\omega_{pp}$. Microwave loss function $\rho(\varphi)$ can be expressed as $\rho(\varphi) = \frac{\pi\sqrt{3}\sin^2\varphi}{27\cos(\varphi/3)\sin^2(\varphi/3)}\delta H_{pp}^2\mathscr{A}_{pp}$, which is based on the results from Table 1 too. Nevertheless, the derivation of $\mathscr{A}_{pp}$ has been made on the assumption that the spin susceptibility is normalized to unity. Consequently, $\mathscr{A}_{pp}$ must be multiplied by factor $\mathscr{N}$. It is therefore necessary to properly calibrate the spectrometer in order to relate the digits displayed on the screen with the actual intensity values related to the authentic number of the active spins ($\mathscr{N}$). ESR reference materials, such as conventionally adopted DPPH solvent complexes [36,37] are frequently used for that point requiring the phase to be set to zero. In conducting systems, however, $\rho(\varphi)$ may well be smaller than 1. This makes such calibrations quite convoluted because they must be cautiously carried out under the strictly same phase-less resonant conditions. Still, in conducting systems φ can purposely be adjusted to zero which automatically leads to the maximum of microwave loss function

($\rho(\varphi) = 1$). To this effect, we resort to (*i*) extra ESR measurements at different crystal orientations with respect to the AC field configuration for which the CESR lineshape asymmetry ratio is drastically moderated down to 1 [19], or simply, (*ii*) extra measurements can be carried out with the sample crushed to a form of powder with ultra-micro-sized crystallites [17,18]. In either way, (*i*) or (*ii*), $\varphi = 0$ so that the microwave loss function obtained at finite phase reads

$$\rho(\varphi) = \frac{\sin^2\varphi}{9\cos(\varphi/3)\sin^2(\varphi/3)} \frac{\delta H^2_{(\varphi)pp}}{\delta H^2_{(0)pp}} \frac{\mathscr{A}_{(\varphi)pp}}{\mathscr{A}_{(0)pp}}, \tag{7}$$

where subscripts (0) and (φ) correspond to the peak-to-peak distances measured at $A/B = 1$ or $\rho(0) = 1$ and $A/B > 1$ or $\rho(\varphi) < 1$, respectively.

Particularly interesting is narrowly locating the resonant magnetic field H_0, as an imperative for a rigorous *g*-factor determination. Ideally, in isotropic highly conducting systems, the *g*-factor attains the free electron value of 2.0023 which is accurate even to five significant figures. Common CESR experiments deal with *g*-factors of rapidly moving electrons scattered by lattice vibrations which deviate only little from this number. This leads to the motional narrowing phenomenon because the CESR linewidth is oftentimes $\propto (g - 2.0023)^2$ [21]. Therefore, requirements for both high precision and reasonable accuracy in finding *g*-factor values are essential in order to trace the origin of the active spins. A cost-effective solution consists of measuring the position of the third significant point, the so-called spectral node $H_0 + H_2$. Value $H_2 = \frac{\sqrt{3}\tan(\varphi/2)\sin\varphi}{6\sin(\varphi/3)}\delta H_{pp}$ must be subtracted from this position to come up with the proper H_0 value. Given that ESR is a highly sensitive probe, omitting this subtraction would have misleading consequences on the interpretation of what the ESR active species are in the system. The most trivial case boils down to $\varphi = 0$ when $H_2 = 0$ so that the subtraction is naturally left out. This common wisdom, nonetheless, cannot be extended to the general $\varphi \neq 0$ case that would otherwise provide an erroneous *g*-factor explanation.

2.3. Geometry independent universality

Following [10] CESR function profile can safely be written down as $x\chi''(\omega) + y\chi'(\omega)$, where x and y are the non-negative absorption and dispersion fractions respectively. Microwave loss function, $\rho(\varphi)$, is thus identified as $\sqrt{x^2 + y^2}$, while φ takes on $\arctan(y/x)$. Along this line, for all absorptions $\chi''(\omega)$ of Lorentzian nature, $A/B \leqslant 8$ must always be fulfilled no matter what the values of $x \geqslant 0$ and $y \geqslant 0$ are in general. This is a restriction imposed on A/B, as there is no limitation on φ within the interval $[0, \pi/2]$. However, concrete response functions in CESR seems not to be as general, and may have further restrictions to φ and thence A/B, which are closely related to crystal properties. In this section we survey three relevant geometries of metallic crystals: infinite plate of thickness *d*, long cylinder of diameter *d*, and sphere of diameter *d*. Using properly defined boundary conditions in Maxwell equations, Chapman et al. [5] explicitly derived the *on-resonance* signal expressions for $x(\eta)$ and $y(\eta)$, where $\eta \equiv d/\delta$ and δ represents the skin depth. AC field acting perpendicularly to the crystal face is screened within this depth which falls off with increasing resonant frequency and, if not anomalous [38], depends on the crystal conductivity explicitly.

Microwave loss function $\rho(\varphi)$ and the asymmetry ratio $A/B \equiv f(\varphi)$ are explicit functions of φ. Moreover, as $\varphi = \arctan(y(\eta)/x(\eta))$, it is rather practical to express the two dependences in terms of η on the log scale for the three considered geometries, as given in Figs. 3 and 4. We observe three local maxima in A/B for the three different geometries: for plate ($\varphi \approx 72.12°$, $A/B \approx 4.86$), for cylinder ($\varphi \approx 55.86°$, $A/B \approx 3.26$), and for sphere ($\varphi \approx 42.18°$, $A/B \approx 2.40$). When $\eta \to 1/2$ the AC field fully penetrates into the crystal, and then $\rho \to 100$ % and $A/B \to 1$, while $\varphi \to 0$ for all the three geometries. This corresponds to the case of insulators or very small metallic particles with the pure absorption and no dispersion for $d/2 \leqslant \delta$. The other limit concerns large or extremely conductive metallic samples when $\eta \to \infty$. The limit leads to

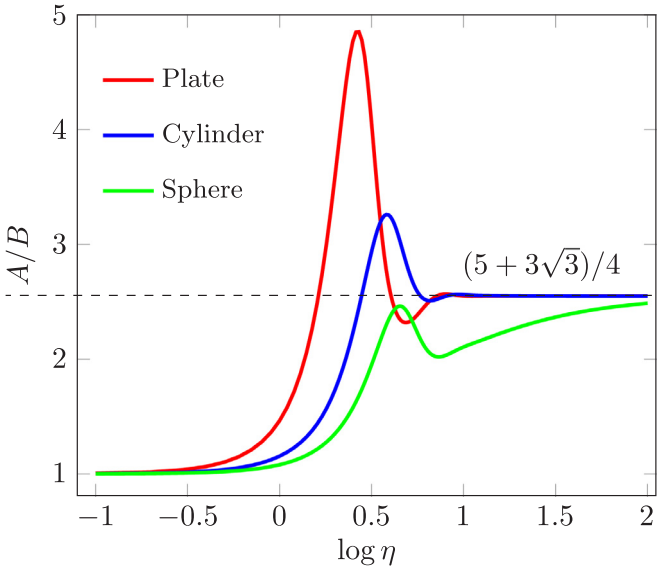

Fig. 3. Evolution of the asymmetry ratio A/B with respect to η for the three geometries considered: infinite plate (red), long cylinder (blue), and sphere (green).

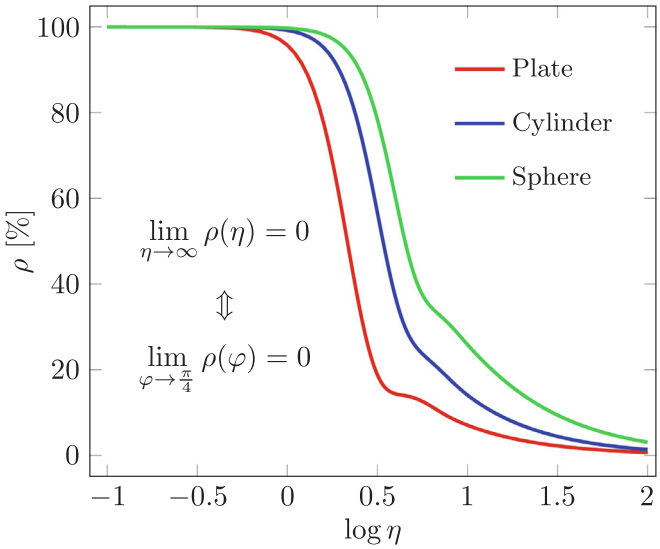

Fig. 4. Evolution of the microwave loss function $\rho(\eta)$ with respect to η for the three geometries considered: infinite plate (red), long cylinder (blue), and sphere (green). (For interpretation of the references to colour in this figure legend, the reader is referred to the web version of this article.)

$\rho \to 0$, $\varphi \to \pi/4$, and $A/B \to f(\pi/4) = (5 + 3\sqrt{3})/4 \approx 2.54904...$, irrespective of geometry. Both fractions $x(\eta \to \infty)$ and $y(\eta \to \infty)$ are in this case infinitesimally small and the total signal is practically lost. It is crucial to note that at $\eta \to \infty$ limit, or alternatively $\varphi \to \pi/4$, each $x(\eta)$ and $y(\eta)$ tends to vanish [10], so that this limit can be treated universally, independent of the assumed geometries. Whatever the analyzed geometry is, both $x(\eta \to \infty)$ and $y(\eta \to \infty)$ tend toward zero at equal asymptotic rates, giving $x/y \to 1$. For this reason $A/B = (5 + 3\sqrt{3})/4$ can safely be considered as the universal value at equal absorption and dispersion contributions to the vanishing CESR spectra. This value can be very often found in literature, yet poorly termed as the 2.55 asymmetry limit without particular analytical derivation. To the extent of our knowledge, this limiting value has not previously been reported in an analytic form.

3. Concluding remarks

In conclusion, we have surveyed the preceding progress in CESR to concentrate on a particular limit of Dyson's theory following a purely quantum mechanical treatment after Kaplan. Known as NMR's, this limit implies that the CESR lineshape is a mixture of absorption and dispersion with non-negative contributions. We have quantitatively analyzed the related CESR profiles by attaching the importance to the applicable points and segments. These have been further implemented in a proposed fitting procedure consisting of few quick shortcuts. Being particularly expeditious and able to keep the relevant information about the sample properties at the same time, the procedure has an advantage over standard ways to fit CESR spectra. At last, it has been demonstrated that the asymmetry ratio limit in the case of highly conducting particles, the so-called extreme CESR, has the universal geometry independent value of $A/B \to (5 + 3\sqrt{3})/4$, which is consistent with a familiar numeric value often seen in literature and nearly equal to 2.55.

Acknowledgments

The authors are profoundly indebted to Professor László Forró for fruitful discussions in the field. Support by the Serbian Ministry of Education, Science, and Technological Development through project OI 171032 is greatly acknowledged.

References

[1] G. Feher, A.F. Kip, Electron spin resonance absorption in metals. I Experimental, Phys. Rev. 98 (1955) 337–348 doi:10.1103/PhysRev. 98.337..
[2] F.J. Dyson, Electron spin resonance absorption in metals. II. Theory of electron diffusion and the skin effect, Phys. Rev. 98 (1955) 349–359 doi:10.1103/PhysRev. 98.349..
[3] M.I. Azbel, V.I. Gerasimenko, I.M. Lifshitz, Paramagnetic resonance and polarization of nuclei in metals, Sov. Phys. JETP 5 (1957) 986–996.
[4] M.I. Azbel, V.I. Gerasimenko, I.M. Lifshitz, On the theory of paramagnetic resonance in metals, Sov. Phys. JETP 8 (1959) 480–487.
[5] A.C. Chapman, P. Rhodes, E.F.W. Seymour, The effect of eddy currents on nuclear magnetic resonance in metals, Proc. Phys. Soc. B 70 (1957) 345–360, https://doi.org/10.1088/0370-1301/70/4/301.
[6] P.M. Platzman, P.A. Wolff, Spin-wave excitation in nonferromagnetic metals, Phys. Rev. Lett. 18 (1967) 280–283, https://doi.org/10.1103/PhysRevLett. 18.280.
[7] H.R. Webb, Electron-spin-resonance line shape in spherical metal particles, Phys. Rev. 158 (1967) 225–233, https://doi.org/10.1103/PhysRev. 158.225.
[8] J.H. Pifer, R. Magno, Conduction-electron spin resonance in a lithium film, Phys. Rev. B 3 (1971) 663–673, https://doi.org/10.1103/PhysRevB.3.663.
[9] A.H. Kahn, Theory of microwave eddy currents and paramagnetic resonance in materials of intermediate conductivity, Phys. Rev. B 16 (1977) 64–72, https://doi.org/10.1103/PhysRevB.16.64.
[10] J.I. Kaplan, J. Reuben, Electron spin resonance line shapes of paramagnetic species on surfaces, J. Phys. Chem. 86 (1982) 4465–4466, https://doi.org/10.1021/j100220a001.
[11] A.G. Marshall, D.C. Roe, Dispersion versus absorption: spectral line shape analysis for radiofrequency and microwave spectrometry, Analyt. Chem. 50 (1978) 756–763, https://doi.org/10.1021/ac50027a023.
[12] A.E. Siegman, Lasers, University Science Books, Mill Valley, California, USA, 1986.
[13] L. Walmsley, G. Ceotto, J.H. Castilho, C. Rettori, Magnetic field modulation frequency, sample size and electromagnetic configuration effects on the spin resonance spectra of graphite intercalation compounds, Synth. Met. 30 (1989) 97–107, https://doi.org/10.1016/0379-6779(89)90645-0.
[14] L. Walmsley, Translating conduction-electron spin-resonance lines into lorentzian lines, J. Magn. Reson. A 122 (1996) 209–213, https://doi.org/10.1006/jmra.1996.0196.
[15] M. Oshikawa, I. Affleck, Electron spin resonance in $s = \frac{1}{2}$ antiferromagnetic chains, Phys. Rev. B 65 (2002) 134410–134437, https://doi.org/10.1103/PhysRevB.65.134410.
[16] J.P. Joshi, S.V. Bhat, On the analysis of broad Dysonian electron paramagnetic resonance spectra, J. Magn. Res. 168 (2004) 284–287, https://doi.org/10.1016/j.jmr.2004.03.018.
[17] F. Beuneu, P. Vajda, Spectroscopic evidence for large ($\gg 1\mu$m) lithium-colloid creation in electron-irradiated li_2o single crystals, Phys. Rev. Lett. 76 (1996) 4544–4547, https://doi.org/10.1103/PhysRevLett. 76.4544.
[18] F. Beuneu, P. Vajda, O.J. Zogal, Magnetic resonance of micrometer size Li-metal colloids in electron-irradiated li_2o crystals, Colloids Surfaces A: Physicochem. Eng. Aspects 158 (1999) 83–87, https://doi.org/10.1016/S0927-7757(99)00134-X.
[19] S.A. Baudron, P. Batail, C. Coulon, R. Clérac, E. Canadell, V. Laukhin, R. Melzi, P. Wzietek, D. Jérome, P. Auban-Senzier, S. Ravy, (EDT-TTF-$CONH_2)_6[Re_6Se_8(CN)_{2005}]$, a metallic kagome-type organic-inorganic hybrid compound: Electronic instability, molecular motion, and charge localization, J. Am. Chem. Soc. 127 (2005) 11785–11797, https://doi.org/10.1021/ja0523385.
[20] A. Janossy, O. Chauvet, S. Pekker, J.R. Cooper, L. Forró, Conduction electron spin resonance in $rb_3\ c_{60}$, Phys. Rev. Lett. 71 (1993) 1091–1094, https://doi.org/10.1103/PhysRevLett. 71.1091.
[21] W.D. Rice, R.T. Weber, P. Nikolaev, S. Arepalli, V. Berka, A.L. Tsai, J. Kono, Spin relaxation times of single-wall carbon nanotubes, Phys. Rev. B 88 (2013) 041401–041405, https://doi.org/10.1103/PhysRevB.88.041401.
[22] P. Szirmai, G. Fábián, J. Koltai, B. Náfrádi, L. Forró, T. Pichler, O.A. Williams, S. Mandal, C. Bäuerle, F. Simon, Observation of conduction electron spin resonance in boron-doped diamond, Phys. Rev. B 87 (2013) 195132, , https://doi.org/10.1103/PhysRevB.87.195132.
[23] K.W. Blazey, K.A. Müller, F. Blatter, E. Schumacher, Conduction electron spin resonance of caesium metallic clusters in zeolite x, Europhys. Lett. 4 (1987) 857–861, https://doi.org/10.1209/0295-5075/4/7/017.
[24] J.J. van der Klink, H.B. Brom, Nmr in metals, metal particles and metal cluster compounds, Prog. Nucl. Magn. Reson. Spectr. 36 (2) (2000) 89–201, https://doi.org/10.1016/S0079-6565(99)00020-5.
[25] J.I. Kaplan, G. Fraenkel, NMR of Chemically Exchanging Systems, Academic Press, 1980.
[26] J.I. Kaplan, Absorption lineshapes modified by an experimentally undetected absorption, J. Magn. Reson. 80 (1988) 340–343, https://doi.org/10.1016/0022-2364(88)90306-X.
[27] D. ter Haar, Fluctuation, Relaxation, and Resonance in Magnetic Systems, Oliver and Boyd, Edinburgh, Schotland, 1962.
[28] T.-K. Ng, Introduction to Classical and Quantum Field Theory, Wiley, Weinheim, Germany, 2009.
[29] P.M. Richards, Proceedings of the International School of Physics, Enrico Fermi, North-Holland, Amsterdam LIX, 1976, p. 539.
[30] T.T.P. Cheung, Z.G. Soos, Theory of exchange narrowing in low-dimensional correlated spin systems, J. Chem. Phys. 69 (8) (1978) 3845–3853, https://doi.org/10.1063/1.437050.
[31] D.L. Huber, Spin diffusion in geometrically frustrated heisenberg ntiferromagnets, J. Phys.: Condens. Matter 15 (2003) L579–L583, https://doi.org/10.1088/0953-8984/15/37/L04.
[32] P. Wölfle, E. Abrahams, Phenomenology of ESR in heavy-fermion systems: Fermi-liquid and non-Fermi-liquid regimes, Phys. Rev. B 80 (2009) 235112–235119, https://doi.org/10.1103/PhysRevB.80.235112.
[33] B. Cowan, Nuclear Magnetic Resonance and Relaxation, Cambridge University Press, Cambridge, UK, 1997 doi: 10.1017/CBO9780511524226.
[34] B. Náfrádi, R. Gaál, T. Fehér, L. Forró, Microwave frequency modulation in continuous-wave far-infrared ESR.
[35] B. Náfrádi, R. Gaál, A. Sienkiewicz, T. Fehér, L. Forró, Continuous-wave far-infrared ESR spectrometer for high-pressure measurements, J. Magn. Res. 195 (2008) 206–210, https://doi.org/10.1016/j.jmr.2008.09.014.
[36] A.M. Prokhorov, V.B. Fedorov, Aniferromagnetism of free radicals, Soviet Phys. JETP 16 (1963) 1489.
[37] F. Teruaki, Magnetic interaction in solvent-free DPPH and DPPH solvent complexes, Bull. Chem. Soc. Jpn. 54 (1981) 3110–3116, https://doi.org/10.1246/bcsj.54.3110.
[38] A.A. Abrikosov, Introduction to the Theory of Normal Metals Solid State Supplement 12, Academic Press, New York, USA, 1972.

[3]

Materials Science and Engineering B 274 (2021) 115444

Contents lists available at ScienceDirect

Materials Science & Engineering B

journal homepage: www.elsevier.com/locate/mseb

Unvailing the spin–phonon coupling in nanocrystalline $BiFeO_3$ by resonant two-phonon Raman active modes

Bojan Stojadinović [a,*], Dejan M. Djokić [a], Novica Paunović [a], Ivica Živković [b], Luka Ćirić [c], Vladan Kusigerski [d], Zorana Dohčević-Mitrović [a,*]

[a] Institute of Physics Belgrade, University of Belgrade, Pregrevica 118, 11080 Belgrade, Serbia
[b] Laboratory for Quantum Magnetism, Institute of Physics, Ecole Polytechnique Féderale de Lausanne, CH-1015 Lausanne, Switzerland
[c] Laboratory of Nanostructures and Novel Electronic Materials, Ecole Polytechnique Féderale de Lausanne, CH-1015 Lausanne, Switzerland
[d] "Vinča" Institute of Nuclear Sciences, University of Belgrade, P.O. Box 522, Belgrade 11001, Serbia

ARTICLE INFO

Keywords:
$BiFeO_3$ nanomaterials
Sol–gel processes
Raman spectroscopy
Magnetic measurements
Spin–phonon interactions

ABSTRACT

We report on temperature dependence of two-phonon Raman spectra in $BiFeO_3$ nanocrystals, above and below the Néel temperature T_N using a resonant laser excitation line (λ = 532 nm). Two-phonon modes exhibited anomalous frequency hardening and deviation from the anharmonic decay below T_N. Such behavior strongly supported the existence of spin-two-phonon interaction, because these modes are known to be very sensitive to the antiferromagnetic ordering. Within the mean-field theory for the nearest-neighbor interaction, the linear relationship between spin–spin correlation function and observed two-phonon frequency shift below T_N was obtained. This approach enabled to quantify the spin–phonon interaction by spin–phonon coupling strength for both two-phonon modes and justified the application of mean-field approach. Magnetic measurements revealed the coexistence of antiferromagnetic and weak ferromagnetic phases below T_N, which were found non competitive, additionally supporting the mean-field approach from which we deduced that the two-phonon modes in $BiFeO_3$ are correlated with antiferromagnetic ordering below T_N.

1. Introduction

Multiferroic materials attract a lot of attention because of their multifunctional properties and interesting fundamental physics [1,2]. Among all the single-phase multiferroic materials studied so far, $BiFeO_3$ takes a prominent place because both ferroelectric (Curie temperature, $T_C \approx 1150$ K) and magnetic (Néel temperature, $T_N \approx 640$ K) transition temperatures are well above room temperature (RT). In bulk phase $BiFeO_3$ has G-type antiferromagnetic ordering (AFM), with a long period cycloidal modulation (62 nm) superimposed below T_N. Above T_N, $BiFeO_3$ becomes paramagnetic (PM) [3]. In nanophased $BiFeO_3$ spin spiral structure can be suppressed [4] and Dzyaloshinskii–Moriya (DM) interaction becomes important. DM interaction induces non-collinear spin states which compete with the exchange interaction that favors anti-parallel spin alignment providing a coexistence of ferromagnetic (FM) and antiferromagnetic ordering [2,5]. Furthermore, the appearance of strong magnetoelectric effect in epitaxial $BiFeO_3$ thin films [6] and nanoparticles [4], positions nanophased $BiFeO_3$ as a leading candidate material for spintronics, magnetic field sensor devices and ferroelectric non-volatile memories [1,5,7–9]. However, the coupling between magnetic and ferroelectric degrees of freedom in $BiFeO_3$ nanostructures still remains an open issue. Therefore, it is of great importance to study the interplay between lattice vibrations and magnetic excitations, because lattice distortion influences the ferroelectric polarization and accordingly affects its coupling to magnetic order. Furthermore, spin–phonon interaction is fundamental for driving relaxation in magnetic materials.

Among the optical spectroscopy methods, Raman spectroscopy proves to be a powerful experimental tool to elucidate spin–phonon (s-ph) interactions, since Raman mode can be sensitive to the spin correlations. In magnetic nanomaterials, such as $BiFeO_3$, optical phonon modes can be influenced by the exchange coupling between magnetic ions at and below the temperatures of magnetic phase transitions. The spin–phonon interaction usually manifests as atypical temperature dependence of Raman phonon frequency, linewidth or integrated intensity. From the deviation of the Raman mode frequency from the anharmonicity at and below the magnetic phase transition, it is possible to estimate the spin–phonon coupling strength in the antiferromagnets or ferromagnets. Being rather phenomenological, the approach developed by Lockwood and Cottam [10] treats the strength of the spin–phonon coupling through the emergence of the AFM order

* Corresponding authors.
E-mail addresses: bojans@ipb.ac.rs (B. Stojadinović), zordoh@ipb.ac.rs (Z. Dohčević-Mitrović).

https://doi.org/10.1016/j.mseb.2021.115444
Received 29 March 2021; Received in revised form 24 August 2021; Accepted 4 September 2021

parameter, that is the sublattice magnetization, but not the net one. Moreover, it turns out that a thorough microscopic treatment due to Djokic et al. [11] further corroborates this fact whereby the majority of the AFM ordering contribution to the phonon spectra is observed through the magnitude of the sublattice magnetization. The influence of any weak FM ordering (canted or so) in the system upon spin–phonon strength is thus greatly overwhelmed by the AFM ordering. Phonon anomalies around and below T_N were observed in the first-order Raman spectra of $BiFeO_3$ single crystal [12,13], ceramics [14] and thin films [15,16] and were ascribed to the influence of spin correlations on the phonon energies. The pioneering works of Cazayous [17] and Ramirez [18] pointed at possible strong spin-two-phonon interaction in $BiFeO_3$ single crystals and thin films, but all above mentioned works were restricted to qualitative description of the effects of spin correlations on the Raman active first and second-order phonons without any deeper analysis of spin–phonon coupling mechanism.

In the light of these facts, to examine more thoroughly the coupling between lattice and spin degrees of freedom in nanocrystalline $BiFeO_3$, we investigated temperature-dependent second-order Raman spectra of $BiFeO_3$ nanocrystals in a wide temperature range below, at and above the Néel temperature using a resonant excitation line. The anomalous phonon hardening and obvious deviation from the anharmonicity of two-phonon Raman modes below Néel temperature was elaborated within a mean-field approach in order to correlate the spin–spin correlation function with observed frequency shift and to estimate the nearest-neighbor spin–phonon coupling constant. Magnetic measurements have shed more light on the nature of spin–phonon coupling mechanism in $BiFeO_3$ nanocrystals.

2. Experimental details

$BiFeO_3$ nanocrystals were synthesized by a sol–gel method and detailed sample preparation and characterization of the crystal structure and phase composition was given in Ref. [19]. $BiFeO_3$ nanoparticles were of spherical shape with average particle size of 64 nm deduced from SEM measurements [19,20]. Raman spectra of $BiFeO_3$ nanocrystals were collected in a backscattering geometry using TriVista 557 triple spectrometer with the spectral resolution of 2 cm^{-1}. Second-order Raman spectra of $BiFeO_3$ nanocrystals pressed into pellets were recorded between 80 and 723 K in the 1000–1500 cm^{-1} frequency range using a Linkam THMSG600 microscope heating stage. The resonant 532 nm line of a solid-state Nd:YAG laser was used as an excitation source, with output laser power low enough (less than 2 mW) to avoid the heating effects and/or sample thermal degradation. The Raman spectra were corrected by thermal occupation factor for the second-order scattering $S(\omega) = S_0(\omega)/(n+1)^2$, where $S_0(\omega)$ is measured intensity and $n = (e^{\hbar\omega/k_B T} - 1)^{-1}$ is the Bose–Einstein thermal occupation factor [21]. Magnetic measurements at and below 300 K were performed on a SQUID-based Quantum Design magnetometers MPMS-5T and MPMS XL-5.

3. Results and discussions

The room-temperature Raman spectrum of $BiFeO_3$ nanocrystalline sample in the range 40–1500 cm^{-1} is shown in Fig. 1.

Factor group analysis for the rhombohedral $R3c$ structure of $BiFeO_3$ predicts 13 Raman active modes ($4A_1 + 9E$), but the assignment of the Raman modes from the literature is somewhat controversial even in the case of $BiFeO_3$ single crystal Raman spectra measured or calculated in different polarizations [22–26]. As shown in Fig. 1, among the first order Γ-point phonons, modes around 79, 146, 175, 219, 261, 282, 332, 367, 435, 480 and 550 cm^{-1} are clearly seen. According to the polarized Raman spectra of $BiFeO_3$ single crystals [23,25], ceramics [27] and thin films [28] we assigned modes around 146, 175 and 219 cm^{-1} to A_1 modes and modes around 79, 261, 282, 332, 367, 435, 480 and 550 cm^{-1} to E modes. Beside these modes, weaker Raman modes at around 575 and 656 cm^{-1} and a stronger mode at ≈630 cm^{-1} are also observed. The 575 and 656 cm^{-1} modes (marked with * in Fig. 1) can be ascribed to the mullite-type ($Bi_2Fe_4O_9$) secondary phase [29], the presence of which has been confirmed from the X-ray diffraction analysis of $BiFeO_3$ nanocrystalline sample [19]. The Raman mode at ≈630 cm^{-1} is not a zone center mode [27,30]. According to Bielecki et al. [30] this mode can be assigned to the Raman inactive A_2 LO phonon mode which appears in $BiFeO_3$ thin films, ceramics and nanoparticles [18,30–33]. As can be seen in Fig. 1, the intense second-order Raman modes were observed above 1000 cm^{-1} and from now on we will focus our attention on the temperature behavior of these Raman modes.

The high-order Raman modes of the ferroelectric materials are usually very weak, but in the spectrum of $BiFeO_3$ from Fig. 1 an intense multiphonon band around 1000–1500 cm^{-1} is observed. This prominent band is already reported in $BiFeO_3$ thin films and single crystals [17,18,25], as well as in $BiFeO_3$ nanoparticles [31,32]. The broad band at 300 K from Fig. 1 was deconvoluted with Lorentzian type profile into four modes: mode at 1090 cm^{-1}, a strong mode at 1252 cm^{-1} and two low-intensity phonon modes at 1150 and 1330 cm^{-1}. The second-order modes at 1090 and 1252 cm^{-1}, labeled as S_1 and S_2 in Fig. 1, are, within the error limits, at the double frequency of the first-order Raman E mode at around 550 cm^{-1} and inactive A_2 mode at around 630 cm^{-1} [22,30]. These modes were ascribed to two-phonon modes in accordance with literature data [13,17,18,30], whereas the remaining two modes can be assigned to $2A_g$ modes of $Bi_2Fe_4O_9$ secondary phase [29]. Yang et al. [34] have investigated the behavior of two-phonon modes in $BiFeO_3$ powders using different excitation lines and reported that the intensity of two-phonon S_1 and S_2 modes are significantly enhanced under the 532 nm excitation. The intensity enhancement of S_1 and S_2 modes was attributed to the resonant enhancement when the excitation energy (532 nm ≈2.34 eV) is close to the absorption edge of $BiFeO_3$. The resonant behavior of these modes was explained by exchange mechanism between Fe^{3+} ions. Weber et al. [35] also reported resonant enhancement of second-order Raman modes in $BiFeO_3$ single crystals using 532 nm excitation, but suggested that in-gap electronic states like defect states from oxygen vacancies can be involved in the resonance process. Accordingly, we used 532 nm laser line in order to track the temperature evolution of S_1 and S_2 Raman modes. Two-phonon S_1 and S_2 modes are related to the Fe–O vibrations, i.e. octahedral rotations [17,18,32] which are very sensitive to the change of magnetic ordering. Moreover, it is well known that any perturbation of spiral spin structure in antiferromagnetic $BiFeO_3$ and distortion of FeO_6 octahedra due to the change of Fe–O–Fe bond angle can lead to the appearance of ferromagnetism [2,4,5]. Therefore, we have analyzed the behavior of S_1 and S_2 modes at temperatures below and above the magnetic phase transition.

In Fig. 2a are presented second-order Raman spectra in the 80–723 K temperature range. With increased temperature S_1 and S_2 modes gradually shift to lower wavenumbers and approaching the 600 K, the wavenumber shift is followed by a pronounced decrease of intensity (Fig. 2a). Similar behavior of S_2 mode was first observed by Ramirez [18] and Cazayous [17] and was ascribed to the coupling of S_2 mode with the magnetic sublattice. The accurate wavenumber change of S_1 and S_2 modes with temperature was obtained by deconvoluting the spectra from Fig. 2a with Lorentzian line shape function and Raman spectra at several representative temperatures together with cumulative fits are presented in Fig. 2b.

In magnetic materials, the change of phonon mode frequency with temperature can be expressed as [36,37]:

$$\omega(T) - \omega_0 \equiv \Delta\omega(T) = \Delta\omega_{lat}(T) + \Delta\omega_{anh}(T) + \Delta\omega_{e-ph}(T) + \Delta\omega_{s-ph}(T), \quad (1)$$

where $\omega(T)$ is measured frequency at temperature T and ω_0 is the harmonic mode frequency at $T = 0$ K. The first term on the right-hand side of the Eq. (1) is the frequency-independent pure-volume contribution due to the lattice expansion/contraction. The second term

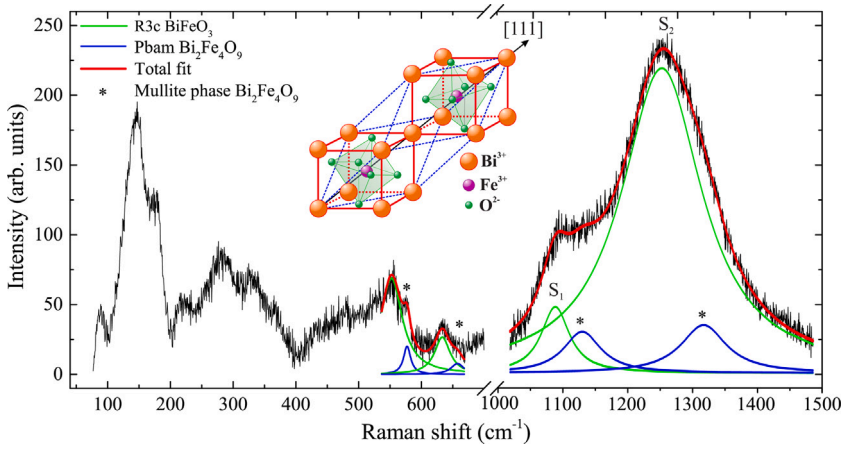

Fig. 1. Room-temperature Raman spectrum of nanocrystalline $BiFeO_3$ with Lorentzian fit (red line) of the first- and second-order phonon regions. The modes of mullite-type secondary phase $Bi_2Fe_4O_9$ are marked with (*). Inset represents the schematic of a pseudocubic unit cell including one formula unit with principle axis of polarization [111].

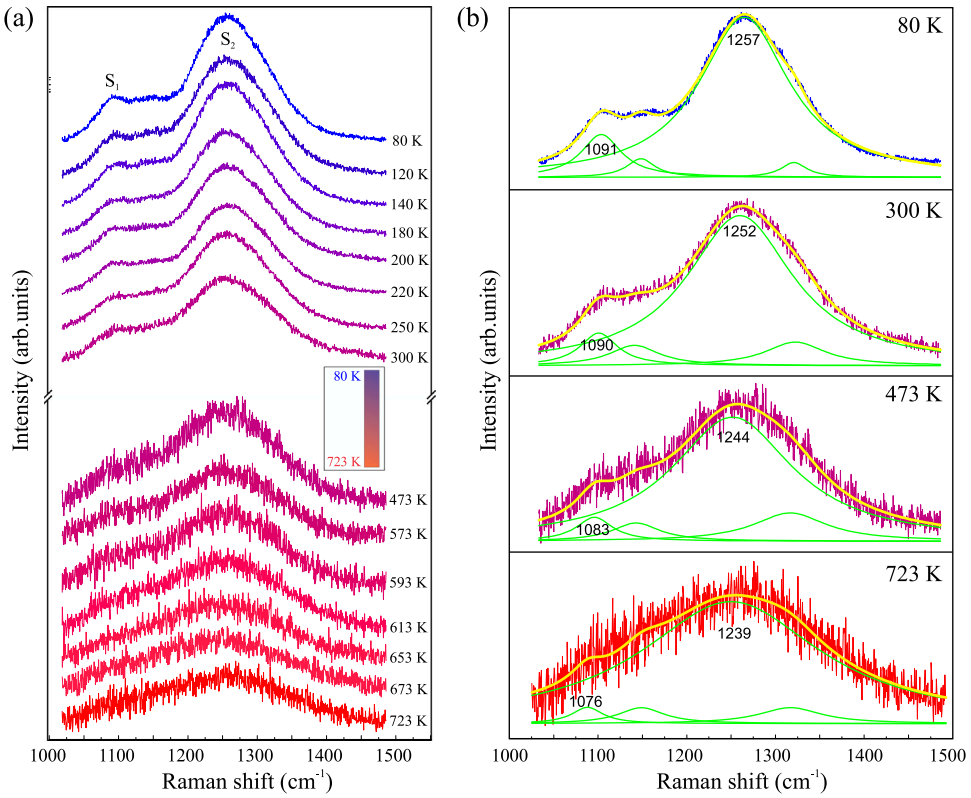

Fig. 2. Second-order Raman spectra of nanocrystalline $BiFeO_3$ (a) in the 80–723 K temperature range and (b) at selected temperatures. The solid lines represent Lorentzian fits of the experimental spectra.

is the anharmonic contribution due to phonon–phonon interactions. The last two terms account for the effects of renormalization of the phonon frequency due to electron–phonon and spin–phonon coupling.

In general, the change of phonon frequency due to pure-volume contribution is much smaller than the intrinsic anharmonic contribution, especially at low temperatures. $BiFeO_3$ in the form of powders or thin films is structurally stable up to 500 °C (773 K) [38] and any phonon frequency change due to lattice distortion is expected to be minimal, hence the first term can be neglected. The anharmonic interactions, significant at elevated temperatures, imply the phonon decay into two or three phonons, with a higher probability of the former. The phonon frequency change due to the decay of the phonon into two lower-energy phonons (three-phonon processes) can be expressed as [39,40]:

$$\Delta\omega_{\mathrm{anh}}(T) = A\left(1 + \frac{2}{e^{\frac{\hbar\omega(T)}{2k_B T}} - 1}\right), \tag{2}$$

where A is the anharmonic constant. In semiconductor materials like $BiFeO_3$, when the carrier concentration is low the third term can be ignored. Finally, the last term in Eq. (1) is the spin–phonon contribution, $\Delta\omega_{s-ph}(T)$, caused by the modulation of the exchange integral by lattice vibration [36]. In magnetic materials such as $BiFeO_3$, the phonon frequencies can be very sensitive to the spin correlations and in a case of Heisenberg model, Baltensberger and Helman [41] derived the relation for the shift of the phonon frequency due to the spin–phonon

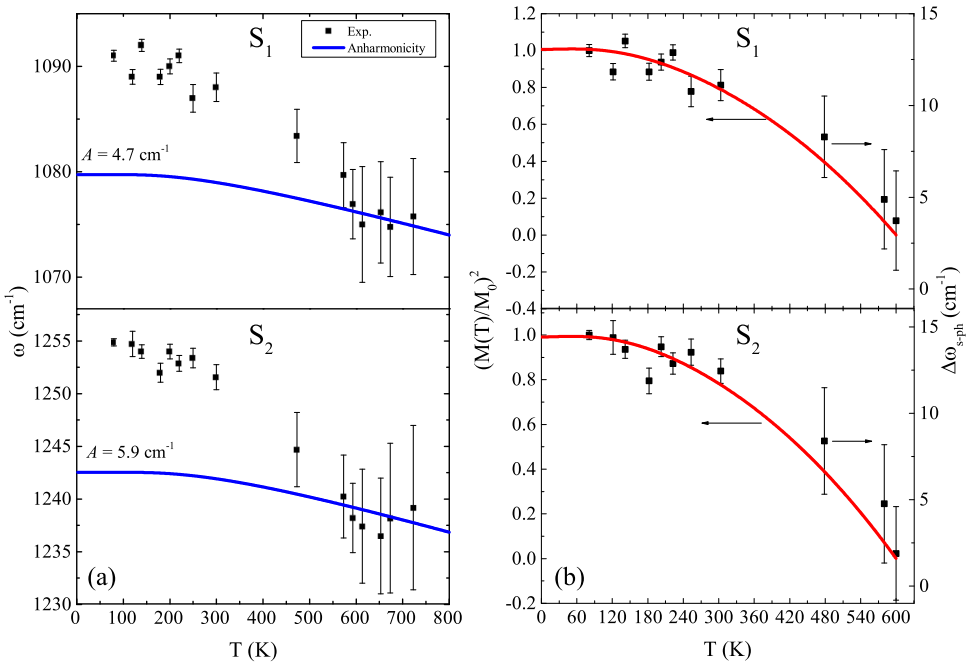

Fig. 3. (a) Temperature dependence of frequencies of the S_1 and S_2 two-phonon modes. The theoretically predicted anharmonic trend is presented by blue line together with the best fit anharmonic parameter (A). (b) Comparison of $(M(T)/M_0)^2$ (left) and $\Delta\omega_{s-ph}(T)$ (right) temperature dependences.

interaction,

$$\Delta\omega_{s-ph}(T) = -\lambda\langle S_i \cdot S_{i+1}\rangle, \quad (3)$$

where λ stands for the spin–phonon coupling constant and $\langle S_i \cdot S_{i+1}\rangle$ is the spin–spin correlation function between adjacent spins.

The temperature dependence of S_1 and S_2 mode frequencies (squares) is shown in Fig. 3a. As can be seen, at lower temperatures (T < 300 K) frequencies of S_1 and S_2 modes exhibit a slower change and at temperature around 600 K display step like anomaly. This temperature should coincide with Néel temperature, since there is no any known structural transition in $BiFeO_3$ at this temperature.

In order to determine the strength of spin–phonon coupling, it is necessary to separate spin–phonon and anharmonic contributions from the change of the phonon frequency with temperature. Knowing that phonon frequencies can be affected by AFM ordering below T_N and that the anharmonic processes should dominate over the spin–phonon coupling at high temperatures ($T > T_N$) for which the $BiFeO_3$ is in the PM state, the data for T > 593 K from Fig. 3a were fitted by Eq. (2) (blue line on Fig. 3a extrapolated to $T = 0$ K) in order to determine the anharmonic contribution to the phonon frequencies change. It is obvious that frequency change of both S_1 and S_2 modes below T_N show distinct deviation away from the expected anharmonic behavior. Similar frequency behavior has been observed in the Raman spectra of other antiferomagnetic [10,36,42–45] and ferromagnetic materials [46,47]. Thus, anomalous frequency hardening of S_1 and S_2 modes below T_N points out at the presence of spin-two-phonon coupling in nanocrystalline $BiFeO_3$. The difference between measured two-phonon frequencies from Fig. 3a and the calculated and extrapolated anharmonic behavior gives us the temperature dependent frequency shift due to spin–phonon interaction, $\Delta\omega_{s-ph}(T) = \omega(T) - \omega_{anh}(T)$. The $\Delta\omega_{s-ph}$ vs T dependence (squares) for S_1 and S_2 two-phonon modes is presented in Fig. 3b.

Within the mean-field approximation introduced by Weiss [48], spin–spin correlation function $\langle S_i \cdot S_{i+1}\rangle$ for adjacent spins at the ith and $(i+1)$th sites is proportional to the square of normalized magnetization, $(M(T)/M_0)^2$, and can be expressed as [49]

$$\frac{\langle S_i \cdot S_{i+1}\rangle}{S^2} = \left(\frac{M(T)}{M_0}\right)^2, \quad (4)$$

where $M(T)$ is in our case sublattice magnetization at temperature T and M_0 is the maximal value of sublattice magnetization. Having a look at Eqs. (3) and (4) it is obvious that $\Delta\omega_{s-ph}(T)$ should scale with $(M(T)/M_0)^2$ curve. The $(M(T)/M_0)^2$ curve was obtained using a numerical solution for Weiss equation in a case of Fe^{3+} ions having spin $S = 5/2$ [50] and then compared with experimentally obtained $\Delta\omega_{s-ph}(T)$ for both two-phonon modes, as presented in Fig. 3b. Obviously, for temperatures $T \leq T_N$, $\Delta\omega_{s-ph}(T)$ scales very good with $(M(T)/M_0)^2$ curve confirming that the significant deviation of S_1 and S_2 phonon frequencies from anharmonic behavior below T_N, i.e. the anomalous hardening, is actually due to spin–phonon interaction.

According to Eq. (3), from the plot $\Delta\omega_{s-ph}(T)$ vs $\langle S_i \cdot S_{i+1}\rangle(T)$ shown in Fig. 4 , the spin–phonon coupling constant λ can be determined for both two-phonon modes S_1 and S_2.

The red solid lines on Fig. 4 present the linear fit of the data from which the spin–phonon coupling constants λ_{S_1}=(2.54 ± 0.10) cm^{-1} and λ_{S_2}=(2.51 ± 0.10) cm^{-1} were determined. The linear behavior of $\Delta\omega_{s-ph}(T)$ vs $\langle S_i \cdot S_{i+1}\rangle(T)$ for the $T \leq T_N$ justifies the application of Eq. (3), implying that in the AFM phase spin–phonon coupling dominates over the anharmonicity and terminates in the paramagnetic phase. Furthermore, the fact that both two-phonon modes exhibit anomalous frequency hardening below magnetic ordering temperature and that the values for λ are very similar, indicates that there is a universal influence of the AFM magnetic ordering upon the two-phonon spectra.

Up to now it is well established that in antiferromagnetic $BiFeO_3$ nanoparticles with particle size close to or less than the period of spin cycloid appear ferromagnetic phase at room temperature [4,51–53]. $BiFeO_3$ nanoparticles can be considered to be composed of AFM core and FM shell giving rise to changes in the magnetic characteristics [53] or to the appearance of exchange bias and training effects [[52], and references within]. Since our $BiFeO_3$ nanoparticles are of the average size close to the spin cycloid period, we performed magnetic measurements in order to get better insight into the two-phonon Raman modes coupling with magnetic ordering below T_N.

Fig. 5a presents room-temperature magnetization (M) vs magnetic field (H) dependence for $BiFeO_3$ nanoparticles. From the M–H loop it can be seen that the magnetization curve (black circles) displays

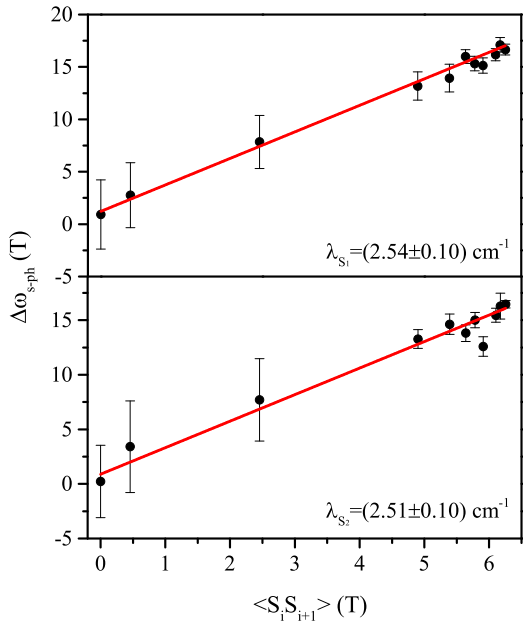

Fig. 4. The plot $\Delta\omega_{s-ph}(T)$ vs $\langle S_i \cdot S_{i+1}\rangle(T)$ for both two-phonon modes S_1 and S_2. The λ values for both modes were determined from the linear fit (red solid line) of the data. (For interpretation of the references to color in this figure legend, the reader is referred to the web version of this article.)

a hysteresis in the low-field region, indicating a presence of weak ferromagnetism. The FM component is superimposed over a linear background from antiferromagnetic $BiFeO_3$ phase and paramagnetic mullite phase. After subtracting the linear background, the ferromagnetic hysteresis curve (red squares) with the saturation magnetization value $M_S = 0.094$ emu/g was obtained. The inset in Fig. 5a displays the magnification of the hysteresis loop in the low-field region. The FM ordering can be considered as genuine one and does not originate from mullite or iron oxide impurity phases. Namely, mullite ($Bi_2Fe_4O_9$) phase is paramagnetic at room temperature and undergoes a transition to an antiferromagnetic state at $T_N \approx 264$ K [54]. Besides, the presence of iron oxides, leads to significantly enhanced ferromagnetism with large values of saturation magnetization [55]. The origin of FM ordering in otherwise antiferromagnetic $BiFeO_3$ is usually ascribed to the suppression of the spiral spin structure in particles with diameter less than the period of spin cycloid (62 nm) and higher distortion of FeO_6 octahedra or to the uncompensated spins on the nanoparticle surface. All of these effects lead to enhanced Dzyaloshinskii–Moriya interaction and appearance of ferromagnetism in nanocrystalline $BiFeO_3$ [2,4,52,56]. In that case $BiFeO_3$ nanoparticles can be considered to be constituted of core/shell structure, i.e. antiferromagnetic core and ferromagnetic shell. As our nanocrystalline $BiFeO_3$ powders are composed of nanoparticles with average particle size of 64 nm [19,20] it can be supposed that the interruption of long-range AFM ordering takes place primarily on the nanoparticle surface. This assumption is supported by a report of Huang et al. [4] who have shown that $BiFeO_3$ nanoparticles of core–shell structure, with size close to the period of spin cycloid, exhibit increased ferromagnetism. It was further argued that FM ordering originates not only from the surface uncompensated spins, but from enhanced distortion of FeO_6 octahedra around the [111] direction. Such enhanced structural distortion can cause suppression of spiral spin structure and strengthening of DM interaction responsible for the appearance of FM. Accordingly, both effects, the suppression of spin cycloid and uncompensated surface spins, can lead to the occurrence of weak ferromagnetism in our sample.

Fig. 5b displays zero field cooled (ZFC) and field cooled (FC) magnetization curves, measured at 1000 Oe. The ZFC and FC curves started to split below 250 K and the divergence became more pronounced with decreasing temperature. The ZFC curve showed a peak around the temperature of spin reorientation transition (200 K) [17,57] at which the Fe^{3+} magnetic moments are canted out of cycloidal plane. Besides, ZFC curve does not tend to $M = 0$ with approaching $T = 0$, as one would expect in a case of the presence of iron oxide impurity phases [58]. The ZFC/FC magnetization curves of our sample are very different from the ZFC/FC magnetization behavior of $BiFeO_3$ single crystal which was ascribed to the spin-glass ordering [59]. Recent ZFC/FC measurements on $BiFeO_3$ nanoparticles with sizes close to or less than the period of spin cycloid [4,7,56] have shown similar pronounced splitting of the ZFC/FC curves when antiferromagnetic and ferromagnetic orderings co-exist. Unlike the $BiFeO_3$ single crystal with antiferromagnetic ordering, those $BiFeO_3$ nanostructures can be considered as core–shell structures composed of antiferromagnetic core and ferromagnetic shell [4,52,56] in which more pronounced ZFC/FC splitting than in bulk $BiFeO_3$ suggests some irreversible effect on magnetic properties like breaking of AFM order and appearance of ferromagnetism [4,7,51,52]. Furthermore, more detailed analysis of ZFC/FC magnetization measurements on nanocrystalline $BiFeO_3$ [53] has shown that pronounced ZFC/FC splitting more likely originates from the changes in the domain structure at low temperatures and eventual antiferromagnetic domain pinning effect [4] than from spin-glass ordering.

In order to justify the use of mean-field theory approximation which does not include magnetic frustrations nor quantum fluctuations apart from the temperature ones [49], we refer to the study of Rao et al. on polycrystalline $BiFeO_3$ [60], where one can infer from that the Curie–Weiss temperature (θ_{CW}) tends to a very large value. Knowing that in bulk $BiFeO_3$ $T_N = 640$ K [1,2] and in nanostructured $BiFeO_3$ T_N slightly decreases with decreasing crystallite size [61], the $BiFeO_3$ is only seemingly frustrated system, since the frustration factor, $f = |\theta_{CW}|/T_N$ can exceed low frustration values [62]. However, we find magnetic frustration inconsequential because of the two noncompeting magnetic interactions: antiferromagnetic and ferromagnetic. These interactions are known to be cooperative in forming the stable Néel phase like in $MnSe_2$ [11]. Therefore, even at low temperatures, the average value of the relevant spin component per site is nearly 5/2, implying the stability of the AFM phase in $BiFeO_3$. Otherwise, spin–phonon coupling would be more complex, the $\Delta\omega_{s-ph}(T)$ would substantially deviate from the mean-field approximation model which we applied [44,47] and a different treatment of the spin–phonon coupling mechanism would be required. The presented magnetic measurements are in favor of the picture in which nothing else, but the AFM magnetic ordering, without the presence of magnetic frustrations, influences the anomalous hardening of two-phonon Raman modes below T_N in nanocrystalline $BiFeO_3$.

4. Concluding remarks

In conclusion, we have investigated the temperature evolution of the resonant Raman two-phonon modes in $BiFeO_3$ nanocrystals, which are known to be very sensitive to magnetic ordering. Temperature studies have shown anomalous hardening and significant deviation of two-phonon frequencies from the anharmonicity below Néel temperature. The anomalous phonon hardening was ascribed to spin-two-phonon coupling. Within the mean-field approach, the spin–spin correlation function was correlated to the two-phonon frequency shift and the spin–phonon coupling strength for two-phonon modes was derived. The linear relation between spin–spin correlation function and frequency shift below Néel temperature confirmed no presence of fluctuations or magnetic frustrations and justified the application of mean-field approach. Magnetic measurements revealed the presence of weak FM phase below T_N. The coexistence of AFM and FM ordering were found not competitive, justifying the conclusion derived from mean-field approach that two-phonon Raman modes below T_N are strongly coupled to AFM ordering.

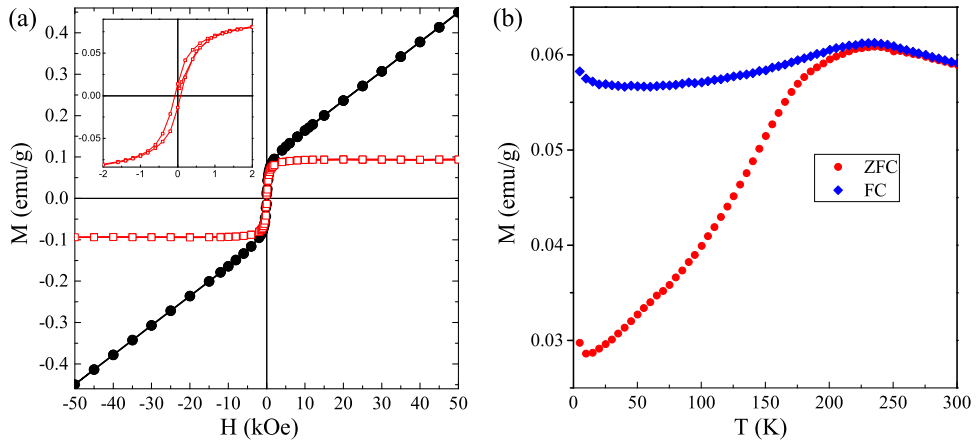

Fig. 5. (a) Room-temperature magnetization (M) vs magnetic field (H) dependence for $BiFeO_3$ nanoparticles, before (circles) and after subtraction (squares) of the linear background component. Inset shows zoom in view of M–H curve. (b) ZFC and FC magnetization curves measured at $H = 1000$ Oe.

Declaration of competing interest

The authors declare that they have no known competing financial interests or personal relationships that could have appeared to influence the work reported in this paper.

Acknowledgments

The authors greatly acknowledge funding provided by the Institute of Physics Belgrade, through the grant by the Ministry of Education, Science, and Technological Development of the Republic of Serbia.

References

[1] N.A. Spaldin, Multiferroics: Past, present, and future, Phys. Today 63 (2010) 38–43, http://dx.doi.org/10.1063/1.3502547.

[2] G. Catalan, J.F. Scott, Physics and applications of Bismuth ferrite, Adv. Mater. 21 (2009) 2463–2485, http://dx.doi.org/10.1002/adma.200802849.

[3] I. Sosnowska, T.P. Neumaier, E. Steichele, Spiral magnetic ordering in bismuth ferrite, J. Phys. C: Solid State 15 (1982) 4835–4846, http://dx.doi.org/10.1088/0022-3719/15/23/020.

[4] F. Huang, Z. Wang, J. Zhang, K. Min, W. Lin, R. Ti, T. Xu, J. He, C. Yue, J. Zhu, Peculiar magnetism of $BiFeO_3$ nanoparticles with size approaching the period of the spiral spin structure, Sci. Rep. 3 (2013) 2907–2913, http://dx.doi.org/10.1038/srep02907.

[5] C.-H. Yang, D. Kan, I. Takeuchi, V. Nagarajan, J. Seidel, Doping $BiFeO_3$: approaches and enhanced functionality, Phys. Chem. Chem. Phys. 14 (2012) 15953–15962, http://dx.doi.org/10.1039/C2CP43082G.

[6] J. Wang, J.B. Neaton, H. Zheng, V. Nagarajan, S.B. Ogale, B. Liu, D. Viehland, V. Vaithyanathan, D.G. Schlom, U.V. Waghmare, N.A. Spaldin, K.M. Rabe, M. Wuttig, R. Ramesh, Epitaxial $BiFeO_3$ multiferroic thin film heterostructures, Science 299 (2003) 1719–1722, http://dx.doi.org/10.1126/science.1080615.

[7] J. Wu, S. Mao, Z.-G. Ye, Z. Xie, L. Zheng, Room-temperature ferromagnetic/ferroelectric $BiFeO_3$ synthesized by a self-catalyzed fast reaction process, J. Mater. Chem. 20 (2010) 6512–6516, http://dx.doi.org/10.1039/c0jm00729c.

[8] J. Ma, J. Hu, Z. Li, C.-W. Nan, Recent progress in multiferroic magnetoelectric composites: from bulk to thin films, Adv. Mater. 23 (2011) 1062–1087, http://dx.doi.org/10.1002/adma.201003636.

[9] R. Ramesh, N.A. Spaldin, Multiferroics: progress and prospects in thin films, Nature Mater. 6 (2007) 21–29, http://dx.doi.org/10.1038/nmat1805.

[10] D.J. Lockwood, M.G. Cottam, The spin-phonon interaction in FeF_2 and MnF_2 studied by Raman spectroscopy, J. Appl. Phys. 64 (1988) 5876–5878, http://dx.doi.org/10.1063/1.342186.

[11] D.M. Djokić, Z.V. Popović, F.R. Vukajlović, Influence of antiferromagnetic spin ordering on the far-infrared active optical phonon modes of αMnSe, Phys. Rev. B 77 (2008) 014305, http://dx.doi.org/10.1103/PhysRevB.77.014305.

[12] C.-S. Chen, C.-S. Tu, P.-Y. Chen, V.H. Schmidt, Z.-R. Xu, Y. Ting, Spin-lattice coupling phase transition and phonon anomalies in bismuth ferrite $BiFeO_3$, J. Alloy. Compd. 687 (2016) 442–450, http://dx.doi.org/10.1016/j.jallcom.2016.06.193.

[13] T.M.H. Nguyen, X.N. Nguyen, X.-B. Chen, X.T. To, S. Lee, T.H. Nguyen, I.-S. Yang, Study of spin-phonon coupling in multiferroic $BiFeO_3$ through Raman spectroscopy, J. Mol. Struct. 1222 (2020) 128884, http://dx.doi.org/10.1016/j.molstruc.2020.128884.

[14] J. Wei, C. Wu, Y. Liu, Y. Guo, T. Yang, D. Wang, Z. Xu, R. Haumont, Structural distortion, spin-phonon coupling, interband electronic transition, and enhanced magnetization in rare-earth-substituted bismuth ferrite, Inorg. Chem. 56 (2017) 8964–8974, http://dx.doi.org/10.1021/acs.inorgchem.7b00914.

[15] M.K. Singh, W. Prellier, H.M. Jang, R.S. Katiyar, Anomalous magnetic ordering induced spin-phonon coupling in $BiFeO_3$ thin films, Solid State Commun. 149 (2009) 1971–1973, http://dx.doi.org/10.1016/j.ssc.2009.07.036.

[16] A. Ahlawat, S. Satapathy, S. Maan, V.G. Sathe, P.K. Gupta, Correlation of structure and spin-phonon coupling in (La, Nd) doped $BiFeO_3$ films, J. Raman Spectrosc. 45 (2014) 958–962, http://dx.doi.org/10.1002/jrs.4573.

[17] M. Cazayous, A. Sacuto, D. Lebeugle, D. Colson, Possible interplay between a two phonon mode and high energy magnetic excitations in $BiFeO_3$, Eur. Phys. J. B 67 (2009) 209–212, http://dx.doi.org/10.1140/epjb/e2009-00033-7.

[18] M.O. Ramirez, M. Krishnamurthi, S. Denev, A. Kumar, S.-Y. Yang, Y.-H. Chu, E. Saiz, J. Seidel, A.P. Pyatakov, A. Bush, D. Viehland, J. Orenstein, R. Ramesh, V. Gopalan, Two-phonon coupling to the antiferromagnetic phase transition in multiferroic $BiFeO_3$, Appl. Phys. Lett. 92 (2008) 022511, http://dx.doi.org/10.1063/1.2829681.

[19] B. Stojadinović, Z. Dohčević-Mitrović, D. Stepanenko, M. Rosić, I. Petronijević, N. Tasić, N. Ilić, B. Matović, B. Stojanović, Dielectric and ferroelectric properties of Ho-doped $BiFeO_3$ nanopowders across the structural phase transition, Ceram. Int. 43 (2017) 16531–16538, http://dx.doi.org/10.1016/j.ceramint.2017.09.038.

[20] D.M. Djokić, B. Stojadinović, D. Stepanenko, Z. Dohčević-Mitrović, Probing charge carrier transport regimes in $BiFeO_3$ nanoparticles by Raman spectroscopy, Scr. Mater. 181 (2020) 6–9, http://dx.doi.org/10.1016/j.scriptamat.2020.02.008.

[21] S.S. Mitra, Infrared and Raman spectra due to lattice vibrations, Springer US, Boston, MA, 1969, pp. 398–400, http://dx.doi.org/10.1007/978-1-4757-1123-3-14.

[22] R. Palai, R.S. Katiyar, H. Schmid, P. Tissot, S.J. Clark, J. Robertson, S.A.T. Redfern, G. Catalan, J.F. Scott, β Phase and γ-β metal-insulator transition in multiferroic $BiFeO_3$, Phys. Rev. B 77 (2008) 014110, http://dx.doi.org/10.1103/PhysRevB.77.014110.

[23] M. Cazayous, D. Malka, D. Lebeugle, D. Colson, Electric field effect on $BiFeO_3$ single crystal investigated by Raman spectroscopy, Appl. Phys. Lett. 91 (2007) 071910, http://dx.doi.org/10.1063/1.2771380.

[24] C. Beekman, A.A. Reijnders, Y.S. Oh, S.W. Cheong, K.S. Burch, Raman study of the phonon symmetries in $BiFeO_3$ single crystals, Phys. Rev. B 86 (2012) 020403, http://dx.doi.org/10.1103/PhysRevB.86.020403.

[25] H. Fukumura, S. Matsui, H. Harima, T. Takahashi, T. Itoh, K. Kisoda, M. Tamada, Y. Noguchi, M. Miyayama, Observation of phonons in multiferroic $BiFeO_3$ single crystals by Raman scattering, J. Phys. Condens. Mat. 19 (2007) 365224, http://dx.doi.org/10.1088/0953-8984/19/36/365224.

[26] P. Hermet, M. Goffinet, J. Kreisel, P. Ghosez, Raman and infrared spectra of multiferroic bismuth ferrite from first principles, Phys. Rev. B 75 (2007) 220102, http://dx.doi.org/10.1103/PhysRevB.75.220102.

[27] J. Hlinka, J. Pokorny, S. Karimi, I.M. Reaney, Angular dispersion of oblique phonon modes in $BiFeO_3$ from micro-Raman scattering, Phys. Rev. B 83 (2011) 020101, http://dx.doi.org/10.1103/PhysRevB.83.020101.

[28] M.K. Singh, H.M. Jang, S. Ryu, M.-H. Jo, Polarized Raman scattering of multiferroic $BiFeO_3$ epitaxial films with rhombohedral $R3c$ symmetry, Appl. Phys. Lett. 88 (2006) 042907, http://dx.doi.org/10.1063/1.2168038.

[29] M.N. Iliev, A.P. Litvinchuk, V.G. Hadjiev, M.M. Gospodinov, V. Skumryev, E. Ressouche, Phonon and magnon scattering of antiferromagnetic $Bi_2Fe_4O_9$, Phys. Rev. B 81 (2010) 024302, http://dx.doi.org/10.1103/PhysRevB.81.024302.

[30] J. Bielecki, P. Svedlindh, D.T. Tibebu, S. Cai, S.-G. Eriksson, L. Börjesson, C.S. Knee, Structural and magnetic properties of isovalently substituted multiferroic $BiFeO_3$: Insights from Raman spectroscopy, Phys. Rev. B 86 (2012) 184422, http://dx.doi.org/10.1103/PhysRevB.86.184422.

[31] S. Chauhan, M. Kumar, P. Pal, Substitution driven structural and magnetic properties and evidence of spin phonon coupling in Sr-doped $BiFeO_3$ nanoparticles, RSC Adv. 6 (2016) 68028–68040, http://dx.doi.org/10.1039/C6RA11021E.

[32] M. Kumar, M. Arora, S. Chauhan, S. Joshi, Raman spectroscopy probed spin-two phonon coupling and improved magnetic and optical properties in Dy and Zr substituted $BiFeO_3$ nanoparticles, J. Alloy. Compd. 692 (2017) 236–242, http://dx.doi.org/10.1016/j.jallcom.2016.09.031.

[33] B. Stojadinović, Z. Dohčević-Mitrović, N. Paunović, N. Ilić, N. Tasić, I. Petronijević, D. Popović, B. Stojanović, Comparative study of structural and electrical properties of Pr and Ce doped $BiFeO_3$ ceramics synthesized by auto-combustion method, J. Alloy. Compd. 657 (2016) 866–872, http://dx.doi.org/10.1016/j.jallcom.2015.09.235.

[34] Y. Yang, J.Y. Sun, K. Zhu, Y.L. Liu, J. Chen, X.R. Xing, Raman study of $BiFeO_3$ with different excitation wavelengths, Physica B 404 (2009) 171–174, http://dx.doi.org/10.1016/j.physb.2008.10.029.

[35] M.C. Weber, M. Guennou, C. Toulouse, M. Cazayous, Y. Gillet, X. Gonze, J. Kreisel, Temperature evolution of the band gap in $BiFeO_3$ traced by resonant Raman scattering, Phys. Rev. B 93 (2016) 125204, http://dx.doi.org/10.1103/PhysRevB.93.125204.

[36] E. Granado, A. Garcí a, J.A. Sanjurjo, C. Rettori, I. Torriani, F. Prado, R.D. Sánchez, A. Caneiro, S.B. Oseroff, Magnetic ordering effects in the Raman spectra of $La_1 - xMn_1 - xO_3$, Phys. Rev. B 60 (1999) 11879–11882, http://dx.doi.org/10.1103/PhysRevB.60.11879.

[37] X.-B. Chen, N.T. Minh Hien, K. Han, J. Chul Sur, N.H. Sung, B.K. Cho, I.-S. Yang, Raman studies of spin-phonon coupling in hexagonal $BaFe_{12}O_{19}$, J. Appl. Phys. 114 (2013) 013912, http://dx.doi.org/10.1063/1.4812575.

[38] J. Ryu, C.-W. Baek, D.-S. Park, D.-Y. Jeong, Multiferroic $BiFeO_3$ thick film fabrication by aerosol deposition, Met. Mater. Int. 16 (2010) 639–642, http://dx.doi.org/10.1007/s12540-010-0818-9.

[39] P.G. Klemens, Anharmonic decay of optical phonons, Phys. Rev. 148 (1966) 845–848, http://dx.doi.org/10.1103/PhysRev.148.845.

[40] M. Balkanski, R.F. Wallis, E. Haro, Anharmonic effects in light scattering due to optical phonons in silicon, Phys. Rev. B 28 (1983) 1928–1934, http://dx.doi.org/10.1103/PhysRevB.28.1928.

[41] W. Baltensperger, J.S. Helman, Influence of magnetic order in insulators on the optical phonon frequency, Helv. Phys. Acta 41 (1968) 668–673, http://dx.doi.org/10.5169/seals-113910.

[42] E. Aytan, B. Debnath, F. Kargar, Y. Barlas, M.M. Lacerda, J. Li, R. Lake, J. Shi, A.A. Balandin, Spin-phonon coupling in antiferromagnetic nickel oxide, Appl. Phys. Lett. 111 (2017) 252402, http://dx.doi.org/10.1063/1.5009598.

[43] P.-H. Shih, C.-L. Cheng, S.Y. Wu, Short-range spin-phonon coupling in in-plane CuO nanowires: a low-temperature Raman investigation, Nanoscale Res. Lett. 8 (2013) 1–6, http://dx.doi.org/10.1186/1556-276X-8-398.

[44] C. Kant, J. Deisenhofer, T. Rudolf, F. Mayr, F. Schrettle, A. Loidl, V. Gnezdilov, D. Wulferding, P. Lemmens, V. Tsurkan, Optical phonons, spin correlations, and spin-phonon coupling in the frustrated pyrochlore magnets $CdCr_2O_4$ and $ZnCr_2O_4$, Phys. Rev. B 80 (2009) 214417–214426, http://dx.doi.org/10.1103/PhysRevB.80.214417.

[45] J. Zhang, Q. Lian, Z. Pan, W. Bai, J. Yang, Y. Zhang, X. Tang, J. Chu, Spin-phonon coupling and two-magnons scattering behaviors in hexagonal NiAs-type antiferromagnetic MnTe epitaxial films, J. Raman Spectrosc. 51 (2020) 1383–1389, http://dx.doi.org/10.1002/jrs.5928.

[46] M.N. Iliev, M.V. Abrashev, A.P. Litvinchuk, V.G. Hadjiev, H. Guo, A. Gupta, Raman spectroscopy of ordered double perovskite La_2CoMnO_6 thin films, Phys. Rev. B 75 (2007) 104118, http://dx.doi.org/10.1103/PhysRevB.75.104118.

[47] R.X. Silva, M.C.C. Júnior, S. Yáñez-Vilar, M.S. Andújar, J. Mira, M.A. Señarís-Rodríguez, C.W.A. Paschoal, Spin-phonon coupling in multiferroic Y_2CoMnO_6, J. Alloy. Compd. 690 (2017) 909–915, http://dx.doi.org/10.1016/j.jallcom.2016.07.010.

[48] B.D. Cullity, C.D. Graham, Introduction to magnetic materials, Second Edition, Wiley-IEEE Press, New Jersey, 2008, pp. 91–99, http://dx.doi.org/10.1002/9780470386323.

[49] K. Yosida, Theory of magnetism, Springer-Verlag Berlin Heidelberg, 1996, pp. 72–74.

[50] V. Barsan, V. Kuncser, Exact and approximate analytical solutions of Weiss equation of ferromagnetism and their experimental relevance, Phil. Mag. Lett. 97 (2017) 359–371, http://dx.doi.org/10.1080/09500839.2017.1366081.

[51] K.P. Remya, D. Prabhu, R.J. Joseyphus, A.C. Bose, C. Viswanathan, N. Ponpandian, Tailoring the morphology and size of perovskite $BiFeO_3$ nanostructures for enhanced magnetic and electrical properties, Mater. Des. 192 (2020) 108694, http://dx.doi.org/10.1016/j.matdes.2020.108694.

[52] F. Huang, X. Xu, X. Lu, M. Zhou, H. Sang, J. Zhu, The exchange bias behavior of $BiFeO_3$ nanoparticles with natural core-shell structure, Sci. Rep.-UK 8 (2018) 2311, http://dx.doi.org/10.1038/s41598-018-19676-5.

[53] S. Vijayanand, M.B. Mahajan, H.S. Potdar, P.A. Joy, Magnetic characteristics of nanocrystalline multiferroic $BiFeO_3$ at low temperatures, Phys. Rev. B 80 (2009) 064423, http://dx.doi.org/10.1103/PhysRevB.80.064423.

[54] N. Shamir, E. Gurewitz, H. Shaked, The magnetic structure of $Bi_2Fe_4O_9$ analysis of neutron diffraction measurements, Acta Crystallogr. A 34 (1978) 662–666, http://dx.doi.org/10.1107/S0567739478001412.

[55] H. Béa, M. Bibes, A. Barthélémy, K. Bouzehouane, E. Jacquet, A. Khodan, J.-P. Contour, S. Fusil, F. Wyczisk, A. Forget, D. Lebeugle, D. Colson, M. Viret, Influence of parasitic phases on the properties of $BiFeO_3$ epitaxial thin films, Appl. Phys. Lett. 87 (2005) 072508, http://dx.doi.org/10.1063/1.2009808.

[56] M. Sakar, S. Balakumar, P. Saravanan, S. Bharathkumar, Particulates Vs. fibers: Dimension featured magnetic and visible light driven photocatalytic properties of Sc modified multiferroic bismuth ferrite nanostructures, Nanoscale 8 (2016) 1147–1160, http://dx.doi.org/10.1039/C5NR06655G.

[57] J.F. Scott, M.K. Singh, R.S. Katiyar, Critical phenomena at the 140 and 200 K magnetic phase transitions in $BiFeO_3$, J. Phys. Condens. Matter 20 (2008) 322203, http://dx.doi.org/10.1088/0953-8984/20/32/322203.

[58] D. Parker, V. Dupuis, F. Ladieu, J.-P. Bouchaud, E. Dubois, R. Perzynski, E. Vincent, Spin-glass behavior in an interacting γ-Fe_2O_3 nanoparticle system, Phys. Rev. B 77 (2008) 104428, http://dx.doi.org/10.1103/PhysRevB.77.104428.

[59] M.K. Singh, W. Prellier, M.P. Singh, R.S. Katiyar, J.F. Scott, Spin-glass transition in single-crystal $BiFeO_3$, Phys. Rev. B 77 (2008) 144403, http://dx.doi.org/10.1103/PhysRevB.77.144403.

[60] T.D. Rao, S. Asthana, Evidence of improved ferroelectric phase stabilization in Nd and Sc co-substituted $BiFeO_3$, J. Appl. Phys. 116 (2014) 164102–164109, http://dx.doi.org/10.1063/1.4898805.

[61] S.M. Selbach, T. Tybell, M.-A. Einarsrud, T. Grande, Size-dependent properties of multiferroic $BiFeO_3$ nanoparticles, Chem. Mater. 19 (2007) 6478–6484, http://dx.doi.org/10.1021/cm071827w.

[62] A.P. Ramirez, Strongly geometrically frustrated magnets, Annu. Rev. Mater. Sci. 24 (1994) 453–480, http://dx.doi.org/10.1146/annurev.ms.24.080194.002321.

[4]

Materials Science in Semiconductor Processing 149 (2022) 106889

Contents lists available at ScienceDirect

Materials Science in Semiconductor Processing

journal homepage: www.elsevier.com/locate/mssp

Revealing plasmon-phonon interaction in nanocrystalline $MgFe_2O_4$ spinels by far-infrared reflection spectroscopy

Novica Paunović [a,*], Zorana Dohčević-Mitrović [a,**], Dejan M. Djokić [a], Sonja Aškrabić [a], Saša Lazović [a], Ann Rose Abraham [b], Balakrishnan Raneesh [c], Nandakumar Kalarikkal [d,e], Sabu Thomas [e,f]

[a] Institute of Physics Belgrade, University of Belgrade, Pregrevica 118, 11080, Belgrade, Serbia
[b] Department of Physics, Sacred Heart College, Kochi, Kerala, 682013, India
[c] Department of Physics, Catholicate College, Pathanamthitta, Kerala, 689645, India
[d] School of Pure and Applied Physics, Mahatma Gandhi University, Kottayam, Kerala, 686560, India
[e] International & Inter University Centre for Nanoscience and Nanotechnology, Mahatma Gandhi University, Kottayam, Kerala, 686560, India
[f] School of Energy Materials, Mahatma Gandhi University, Kottayam, Kerala, 686560, India

ARTICLE INFO

Keywords:
Magnesium ferrite
Inverse spinels
Infrared spectroscopy
Plasmon-phonon interaction

ABSTRACT

Room-temperature far-infrared reflectivity spectra of nanocrystalline, partially inverse $MgFe_2O_4$ were investigated. $MgFe_2O_4$ samples were prepared by sol-gel method and sintered at three different temperatures (400, 600 and 800 °C). Raman spectroscopy was employed to estimate the degree of inversion in the sintered samples. The degree of inversion was found to increase from 0.52 to 0.74 as the sintering temperature increased from 400 °C to 800 °C. The reflectivity spectra, besides the four infrared modes characteristic for spinels (ν_1, ν_2, ν_3, ν_4), revealed the presence of free carriers. Plasmon-longitudinal optical (LO) phonon interaction was analyzed using factorized coupled and decoupled plasmon-phonon models, combined with the Bruggeman effective medium approximation. From these models it was obtained that the ν_1 and ν_3 phonon modes are more strongly coupled with plasmons than the ν_2 mode. A potential mechanism of plasmon-phonon interaction in inverse $MgFe_2O_4$ spinel has been discussed.

1. Introduction

Magnesium ferrite ($MgFe_2O_4$) belongs to the family of spinel ferrites, a very important group of magnetic spinel oxides with a wide range of applications. It is a soft magnetic n-type semiconducting material which received strong attention due its vast uses such as magnetic applications [1,2], catalyst [3,4], metal ion removal [5], water purification [6], water and CO_2 splitting [7,8] or sensors [9]. It is considered as promising candidate for biomedical applications such as hyperthermia and cancer treatment [10–12], targeted drug delivery [13] or magnetic resonance imaging [14]. In recent years $MgFe_2O_4$ has been considered as an anode material for lithium-ion batteries [15–17]. Many properties of $MgFe_2O_4$ depend on the microstructure, grain size and porosity, or preparative methods. Preparation of $MgFe_2O_4$ in nanocrystalline form offers a way to change and tune its optical, electronic, magnetic and other properties [18–20].

Spinel oxides have a general formula AB_2O_4 and belong to the $Fd\bar{3}m$ (O_h^7, No. 227) space group. In normal spinels, A cations occupy only the tetrahedral sites, whereas B cations occupy only the octahedral sites (Fig. 1). In inverse spinels, A cations and half of B cations occupy the octahedral sites while the tetrahedral sites are occupied by the other half of the B cations, which can be represented as $B[AB]O_4$. The intermediate configurations are partially inverse spinels and the structural formula can be written as $(A_{1-\delta}\ B_\delta)_{tetra}[A_\delta B_{2-\delta}]_{octa}O_4$, where δ represents the degree of inversion, which in extreme cases of normal and completely inverse spinels has values $\delta = 0$ and $\delta = 1$, respectively. $MgFe_2O_4$ is a partially inverse spinel for which the degree of inversion δ depends on the synthesis method and thermal treatment. The crystallite size also presents an important factor for adjusting the degree of inversion and fine-tuning of $MgFe_2O_4$ properties.

Far infrared (IR) reflection spectroscopy is a powerful technique

* Corresponding author.
** Corresponding author.
E-mail addresses: paun@ipb.ac.rs (N. Paunović), zordoh@ipb.ac.rs (Z. Dohčević-Mitrović).

https://doi.org/10.1016/j.mssp.2022.106889
Received 17 March 2022; Received in revised form 2 June 2022; Accepted 8 June 2022

which is often used for investigation of crystal structure, phonon and dielectric properties, phase composition, plasmon-fonon interaction, etc., in various types of materials such as oxides, semiconductors, ceramics and many others (e.g., Refs. [21–26]). IR spectroscopy is also commonly used to study normal and inverse spinels. Group theory analysis predicts four active IR modes for spinel structures. Experimental spectra of spinels show at least two strong modes, which, after works of Waldron [27], Hafner [28], and White and DeAngelis [29], are mostly accepted to originate from stretching vibrations of the tetrahedral (octahedral) groups, although it has been argued by Preudhomme and Tarte [30–33] that the actual behavior might be more complex than this. In many spinels, a third, and sometimes a weak forth mode is present at lower frequencies [28,29,32,34–36]. The exact nature of these two modes is not completely clarified yet, but is generally considered that these modes originate from complex vibrations involving both tetrahedral and octahedral groups [27,32,33,35–37]. In most reports, the IR spectra of spinels are presented as transmission or absorption spectra and the IR modes are simply analyzed by the peaks positions (e.g., Refs. [27–30,32,33,35,38–44]). On the other hand, the IR reflectivity spectra of spinels are significantly less often represented in literature (e.g., Refs. [34,36,39,45–49]). To the best of our knowledge, no infrared reflectivity spectra of $MgFe_2O_4$ has been reported. The reflectivity spectra can be more quantitatively analyzed by using an appropriate model for obtaining the values of phonon TO/LO frequencies and dampings. Furthermore, the advantages of reflectivity spectra over the transmittance ones lies in the fact that not only phonon modes but also plasmons and mutual interaction between phonons and plasmons can be analyzed. The knowledge of plasmon-phonon interaction can be important in characterizing transport and optical properties of spinels. Up to date, no infrared reflectivity study of plasmon-LO phonon interaction in $MgFe_2O_4$ has been carried out.

In the present study we have focused on the analysis of far-IR reflectivity spectra of nanocrystalline $MgFe_2O_4$ samples sintered at different temperatures and of varying degrees of inversion. The reflectivity spectra of the samples showed a clear presence of free carriers contribution. The influence of free carriers on the phonon spectra was analyzed employing two different factorized dielectric-function models, from which the coupled (decoupled) LO-phonon modes frequencies and dampings were obtained. Such analysis of reflectivity spectra paves the way for better understanding of the carrier-lattice coupling in inverse nanocrystalline $MgFe_2O_4$.

2. Experimental

Magnesium ferrite ($MgFe_2O_4$) nanocrystalline samples were prepared by sol-gel method and by sintering in air at different temperatures: 400, 600 and 800 °C. The corresponding samples will be further denoted as MFO400, MFO600 and MFO800. Details of the synthesis procedure, structural analysis, as well as various other methods of characterization of these samples have already been published elsewhere [51]. The schematic diagram of the synthesis procedure is given in the Supplementary Information.

The IR reflectivity measurements of the $MgFe_2O_4$ samples in the form of pressed disk-like pellets were carried out at room temperature with a BOMEM DA8 Fourier-transform IR spectrometer. A Hyper beamsplitter and a deuterated triglycine sulfate (DTGS) pyroelectric detector were used to cover the wavenumber region from 90 to 680 cm^{-1}. Micro-Raman spectroscopy was used to estimate the degree of inversion of nanocrystalline $MgFe_2O_4$. Micro-Raman spectra were acquired in the back-scattering configuration using the triple-monochromator Raman system Princeton TriVista 557. Nd:YAG laser line of 532 nm was used as an excitation and the beam was focused onto the samples using 50x objective magnification. Laser power on the sample was 0.08 mW. Raman spectra were deconvoluted using Lorentzian function. More detailed description of infrared and Raman experimental setups is presented in the Supplementary Information.

3. Results and discussion

$MgFe_2O_4$ crystalizes in a cubic spinel structure belonging to the $Fd\bar{3}m$ space group. The full unit cell contains 56 atoms ($Z = 8$), however the smallest Bravais cell, i.e., the primitive cell, has only 14 atoms ($Z = 2$). The factor group analysis for the primitive cell predicts 42 normal modes, three of which are acoustic modes with T_{1u} symmetry, and the remaining 39 Γ-point optical modes are:

$$\Gamma = A_{1g}(R) + E_g(R) + T_{1g} + 3T_{2g}(R) + 2A_{2u} + 2E_u + 4T_{1u}(IR) + 2T_{2u}. \quad (1)$$

Among these modes, four are triply degenerate infrared (IR) modes of T_{1u} symmetry, five are Raman (R) modes, and the remaining modes are silent. Inverse spinels like $NiFe_2O_4$ or $CoFe_2O_4$ show more Raman-active modes than those predicted by factor-group analysis because of inversion of the cations between the tetrahedral and octahedral sites. These spinel structures are characterized by an additional mode in the frequency region where one A_{1g} mode is expected to appear [52,53]. In

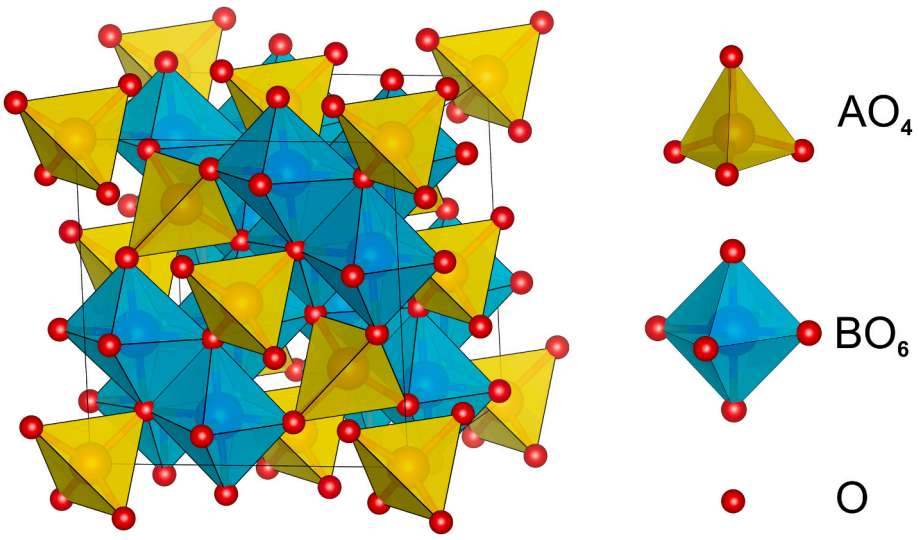

Fig. 1. (Color online) Schematic illustration of normal AB_2O_4 spinel structure with the tetrahedral (AO_4) and octahedral (BO_6) units. The crystal structure visualized by VESTA 3 [50].

the Raman spectra of $MgFe_2O_4$ nanopowders, the A_{1g} mode splits into two modes due to the large difference in mass between Fe^{3+} and Mg^{2+} cations [54–56]. The higher frequency A_{1g} mode corresponds to the vibrations of oxygen anions around Fe^{3+} cations on the tetrahedral sites, whereas the lower frequency mode corresponds to the vibrations of oxygen anions around Mg^{2+} cations on the tetrahedral sites [54,56]. In Fig. 2 are shown deconvoluted room-temperature Raman spectra of MFO400, MFO600 and MFO800 samples, using Lorentzian function. The Raman spectra are presented in the region characteristic for the A_{1g} modes.

Nakagomi et al. [56] have shown that, using corresponding integrated intensities of the two A_{1g} modes, it is possible to quantitatively determine the Mg and Fe content on the tetrahedral sites. Therefore, knowing that the integrated intensities of the two A_{1g} modes are proportional to the concentrations of Mg^{2+} and Fe^{3+} cations on the tetrahedral sites [56], the inversion parameter δ can be calculated from the equation

$$\frac{I\left(A_{1g}^{low}\right)}{I\left(A_{1g}^{high}\right)} = \frac{1-\delta}{\delta} \tag{2}$$

The calculated inversion parameters are 0.52, 0.62 and 0.74 for the MFO400, MFO600 and MFO800 samples, respectively. These data imply that the sample sintered at 400 °C is closer to the normal spinel structure than the sample sintered at 800 °C, which is in complete accordance with the results of positron annihilation analysis of these samples [51]. The inversion parameters obtained from the Raman spectra are also in good agreement with Bloesser et al., who analyzed $MgFe_2O_4$ samples calcined at 400, 600 and 800 °C, and for the sample calcined at 800 °C obtained the inversion degree of 0.72 [18].

The IR reflectivity spectra of $MgFe_2O_4$ nanocrystalline samples are shown in Fig. 3. In the spectra of all samples were found four T_{1u} modes predicted by group theory. Following the seminal work of Waldron [27], most authors label the four T_{1u} modes as ν_1, ν_2, ν_3 and ν_4, indexing them from the highest to the lowest energies. According to Waldron, the highest energy mode ν_1 was attributed to the vibrations of tetrahedra, and the ν_2 mode to the vibrations of octahedra, considering the vibrations of these groups as mostly isolated molecular vibrations [27]. Such conclusions were later also adopted by Hafner [28], and White and DeAngelis [29]. On the other hand, these conclusions were criticized by

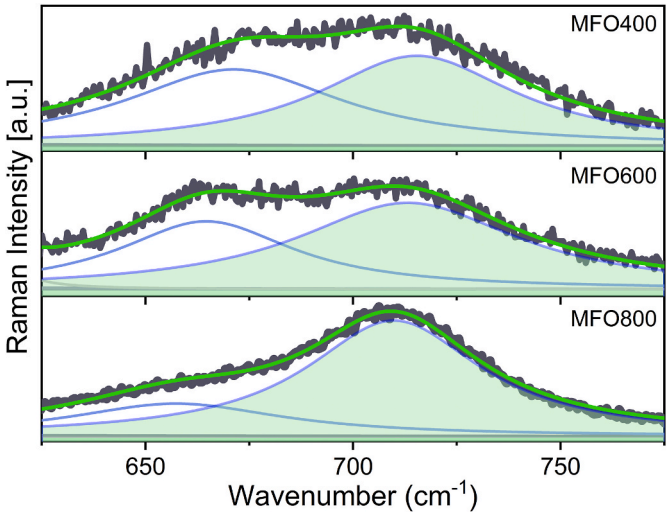

Fig. 2. (Color online) Room-temperature Raman spectra (data in black) of $MgFe_2O_4$ samples sintered at different temperatures, in the region (625–775) cm^{-1}. Experimental curves were deconvoluted with Lorentzian function (blue curves) and cumulative fits are represented by the green curves. The high-frequency A_{1g} mode is shaded for clarity.

Preudhomme and Tarte [30–33] as oversimplified. They argued that, in some cases at least, the observed frequencies cannot be assigned to the vibrations of definite coordinated groups (either tetrahedral or octahedral), but instead are related to complex vibrations of the whole spinel lattice. Nevertheless, many authors still rely mostly on the original Waldron's interpretation of these modes [35,38,42–44,57,58]. It is mostly accepted that the two low frequency modes ν_3 and ν_4 originate from complex vibrations involving both tetrahedral and octahedral groups [27,32,33,35–37].

The MFO400 sample shows two modes ν_1 and ν_2, centered at around 570 and 405 cm^{-1} respectively. These two modes are present in all spinels. For the MFO600 and MFO800 samples, the third mode ν_3 centered at around 330 cm^{-1} is clearly visible. This mode is present in the MFO400 sample too and appears as an asymmetry of the ν_2 mode. In the IR spectra of some spinels a weak forth mode ν_4 appears around 200 cm^{-1} [28,29,32–36,40,49]. This mode can be observed as a small hump centered at around 210 cm^{-1} in the MFO800 sample spectra, and to a lesser extent also in the MFO600 and MFO400 spectra.

In the low frequency region of the IR spectra in Fig. 3, Drude tail appeared and became more pronounced for the MFO600 and MFO800 samples. Its occurrence in the IR spectra is a clear sign of a presence of free carriers. The presence of free carriers in nanocrystalline $MgFe_2O_4$ comes from the presence of vacancies, which introduce electrons as the majority free carriers, making $MgFe_2O_4$ an n-type semiconductor [59]. When free carriers are present in the material, they can interact with phonons. Since plasmons are longitudinal oscillations, they interact with longitudinal-optical (LO) modes, shifting them towards higher frequencies, whereas the transverse-optical (TO) modes remain unaffected. In the analysis of the reflectivity spectra of $MgFe_2O_4$ nanocrystalline samples, two models, both of which include contribution from free carriers, have been applied to investigate the dielectric response. In both models, the factorized form of dielectric function was used. Compared to the classical oscillator model, this factorized form much better describes phonons in strongly polar ionic crystals, where largely split TO/LO modes can have significantly different dampings [60].

The first model, known in literature as the coupled plasmon-phonon model (CPP) [61,62], presents a direct way to characterize plasmon-phonon coupled modes. In this model, the dielectric function has a form:

$$\varepsilon(\omega) = \varepsilon_\infty \frac{\prod_{j=1}^{m+n} \omega^2 + i\gamma_{LOj}\omega - \omega_{LOj}^2}{\omega^m \prod_{j=1}^{m}(\omega + i\gamma_{Pj}) \prod_{j=1}^{n} \omega^2 + i\gamma_{TOj}\omega - \omega_{TOj}^2}, \tag{3}$$

where ε_∞ is the high frequency dielectric constant, $\omega_{TOj}(\omega_{LOj})$ and $\gamma_{TOj}(\gamma_{LOj})$ are the TO(LO) frequencies and dampings of n phonons ($n = 4$ in our case), which can be coupled with m plasmons with dampings γ_{Pj} ($m = 1$ in our case). From this model, the plasma frequency can be obtained indirectly as [61,62]:

$$\omega_P = \frac{\prod_{j=1}^{n+1} \omega_{LOj}^2}{\prod_{j=1}^{n} \omega_{TOj}^2}, \tag{4}$$

and the frequency of the coupled plasmon-phonon mode is given by [61,62]:

$$\Omega_{LOj} = \sqrt{\omega_{LOj}^2 - \frac{1}{4}\gamma_{LOj}^2}. \tag{5}$$

The second model, named as the decoupled plasmon-phonon (DPP) model, is a conventional additive form for dielectric function of pure phonon and plasmon contributions. This model enables to determine the decoupled phonon and plasma frequencies and dampings using

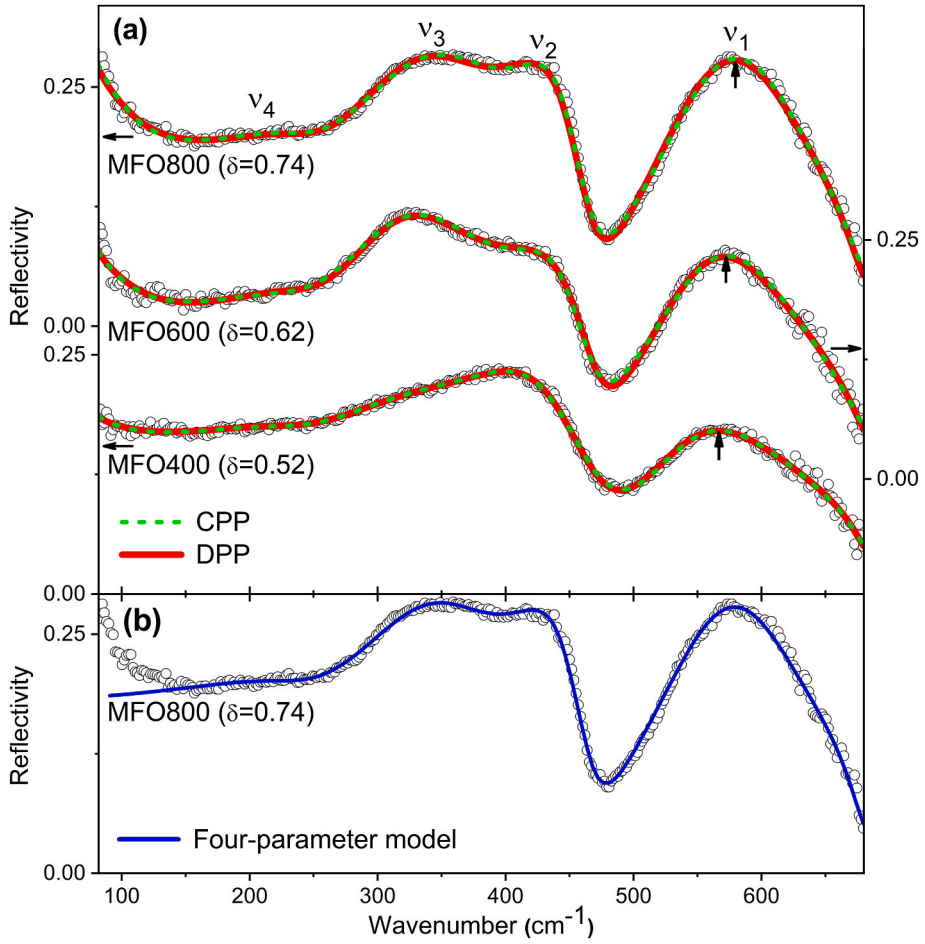

Fig. 3. (Color online) (a) IR reflectivity spectra of $MgFe_2O_4$ nanocrystalline samples sintered at different temperatures together with theoretical fits obtained using the coupled plasmon-phonon (CPP) and decoupled plasmon-phonon (DPP) models. The degree of inversion δ is given in parenthesis. Vertical arrows mark the ν_1 peak (explained in the text). (b) The best fit obtained using the four-parameter model for dielectric function, is also given for the MFO800 sample as an example.

dielectric function in the form [60,63]:

$$\varepsilon\left(\omega\right)=\varepsilon_{\infty}\left(\prod_{j=1}^{n}\frac{\omega_{LOj}^{2}-\omega^{2}-i\gamma_{LOj}\omega}{\omega_{TOj}^{2}-\omega^{2}-i\gamma_{TOj}\omega}-\frac{\omega_{P}^{2}}{\omega(\omega+i\gamma_{P})}\right). \tag{6}$$

The first term in this model represents the phonons contribution, where $\omega_{TOj}(\omega_{LOj})$ and $\gamma_{TOj}(\gamma_{LOj})$ are the TO(LO) frequencies and dampings of phonons. The second term is the Drude term which describes the plasmon mode, where ω_P and γ_P are the frequency and damping of the plasmon mode. In the DPP model, the LO frequencies are actually the frequencies of bare phonons decoupled from plasmon, whereas in the CPP models the LO frequencies are for the coupled plasmon-LO phonon modes. In both models, the TO mode frequencies have the same meaning and are unaffected by free carriers. Without the Drude term, Eq. (6) reduces to the so-called four-parameter model for the dielectric function of phonon spectra [60,63].

In order to properly analyze the IR reflectivity spectra of $MgFe_2O_4$ nanocrystalline samples, the effect of porosity on the IR spectra must be taken into account. In that sense, the Bruggeman effective medium approximation [64,65] is very often used to describe the optical properties of porous nanomaterials. For a homogenous mixture of a material (ε_M) with volume fraction f_M, and air ($\varepsilon = 1$) with fraction ($1\text{-}f_M$), the effective dielectric function ε_{eff} can be obtained from the equation

$$\left(\frac{\varepsilon_{M}-\varepsilon_{eff}}{\varepsilon_{M}+2\varepsilon_{eff}}\right)f_{M}+\left(\frac{1-\varepsilon_{eff}}{1+2\varepsilon_{eff}}\right)(1-f_{M})=0, \tag{7}$$

in which ε_M is described by an appropriate model, in our case by equation (3) or (6). The calculated reflectivity R_{calc} can be obtained using the Fresnel formula

$$R_{calc}=\left|\frac{\sqrt{\varepsilon_{eff}}-1}{\sqrt{\varepsilon_{eff}}+1}\right|^{2}. \tag{8}$$

In the IR spectra fitting procedure, the parameters were automatically tuned until the difference between the experimental ($R_{\exp}$) and calculated (R_{calc}) reflectivity, given by the chi-squared value

$$\chi^{2}=\frac{1}{N}\sum_{i=1}^{N}\left(R_{i,\exp}-R_{i,calc}\right)^{2}, \tag{9}$$

where N is the number of points in spectra, became minimized within the experimental error.

The obtained best fits for both models are shown in Fig. 3(a) (red full and green dashed lines), whereas the best fit parameters are given in Table 1 (CPP model) and Table 2 (DPP model). It can be seen that both models provide satisfactory fits of the experimental spectra. For comparison, the best fit obtained using the four-parameter model for dielectric function, which does not include the free carriers contribution, is also shown in Fig. 3(b) for the MFO800 sample as an example. It is obvious that such a model fails to reproduce experimental spectra at lower frequencies.

Fig. 4 shows the variation of plasma frequency ω_P and damping γ_P for $MgFe_2O_4$ samples sintered at different temperatures, for the both used models. As can be seen, similar behavior of ω_P and γ_P was obtained from the both models. The plasma frequency slightly decreases with sintering

Table 1
Fitting parameters obtained by using the Coupled Plasmon-Phonon (CPP) model, for $MgFe_2O_4$ nanocrystalline samples sintered at different temperatures. Plasma/phonon frequencies and damping values are given in cm^{-1}. The estimated errors are also presented.

Parameters	MFO400	MFO600	MFO800	Est. err.
f_M	0.63	0.7	0.82	±0.02
ω_P	213	200.6	191.1	±5
γ_P	303	188	169	±5
ω_{TO1} (γ_{TO1})	541 (114)	543 (108)	546 (100)	±3 (±5)
ω_{LO1} (γ_{LO1})	684 (48)	679 (45)	677 (50)	±3 (±5)
ω_{TO2} (γ_{TO2})	422 (122)	445 (89)	436 (81)	±5 (±5)
ω_{LO2} (γ_{LO2})	472 (79)	468 (46)	465 (43)	±5 (±5)
ω_{TO3} (γ_{TO3})	321 (192)	317 (123)	338 (131)	±5 (±5)
ω_{LO3} (γ_{LO3})	412 (262)	398 (181)	399 (144)	±5 (±5)
ω_{TO4} (γ_{TO4})	254 (225)	255 (128)	255 (125)	±12 (±12)
ω_{LO4} (γ_{LO4})	266 (166)	256 (98)	258 (99)	±12 (±12)
ω_{LO5} (γ_{LO5})	112 (237)	121 (194)	121 (168)	±5 (±5)

Table 2
Fitting parameters obtained by using the Decoupled Plasmon-Phonon (DPP) model, for $MgFe_2O_4$ nanocrystalline samples sintered at different temperatures. Plasma/phonon frequencies and damping values are given in cm^{-1}. The estimated errors are also presented.

Parameters	MFO400	MFO600	MFO800	Est. err.
f_M	0.62	0.72	0.82	±0.02
ω_P	226	214	194	±5
γ_P	369	231	186	±5
ω_{TO1} (γ_{TO1})	537 (118)	538 (110)	542 (102)	±3 (±5)
ω_{LO1} (γ_{LO1})	663 (36)	663 (47)	662 (47)	±3 (±5)
ω_{TO2} (γ_{TO2})	423 (135)	448 (111)	436 (97)	±5 (±5)
ω_{LO2} (γ_{LO2})	470 (67)	468 (45)	463 (41)	±5 (±5)
ω_{TO3} (γ_{TO3})	323 (204)	315 (111)	332 (122)	±5 (±5)
ω_{LO3} (γ_{LO3})	378 (251)	373 (175)	380 (147)	±5 (±5)
ω_{TO4} (γ_{TO4})	250 (146)	253 (122)	257 (120)	±12 (±12)
ω_{LO4} (γ_{LO4})	252 (125)	256 (99)	258 (98)	±12 (±12)

temperature. On the other hand, the plasma damping decreases significantly for the MFO600 sample, and then further decreases to a lesser extent for the MFO800 sample, resulting in more pronounced Drude tail in the IR spectra of the MFO600 and MFO800 samples. The material volume fraction f_M has increased with increasing sintering temperature (see Tables 1 and 2), indicating that the MFO600 and MFO800 samples became less porous. This is in accordance with previous research on these samples where it was shown that increased sintering temperature leads to larger crystallite sizes and more agglomeration [51]. In samples with larger and more fussed crystallites, with better agglomeration and less pores, the influence of grain boundaries is smaller, having as a consequence the higher electron mobility and longer scattering relaxation time τ. This, in turn, explains the observed significant decrease of plasma dampings, since $\gamma_P = 1/\tau$.

From Tables 1 and 2, it can be seen that in the case of ν_4 mode, the splitting between the TO and LO frequencies is small, meaning that the oscillator strength, being proportional to $(\omega_{LO}^2 - \omega_{TO}^2)$, is also small. The

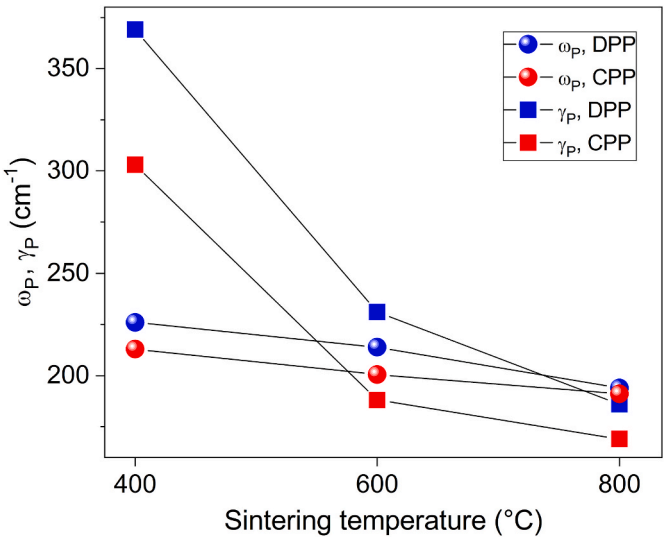

Fig. 4. (Color online) Variation of plasma frequency (ω_P) and damping (γ_P) of $MgFe_2O_4$ nanocrystalline samples sintered at different temperatures, obtained by using the CPP and DPP models.

similar behavior of this mode is found in most other spinels for which this mode is either weak or absent. Other modes exhibit large TO-LO splitting, as common for ionic crystals. The TO frequencies, obtained from both CPP and DPP models, are rather similar for each $MgFe_2O_4$ sample. Such a behavior is expected, as the TO frequencies are not affected by the plasmon-phonon interaction.

In Fig. 5(a) are presented the frequencies of the coupled plasmon-LO phonon modes Ω_{LOj} (obtained from the CPP model, Eq. (3) and Eq. (5)), and the decoupled LO phonon modes ω_{LOj} (from the DPP model, Eq. (6)). It can be seen that for the ν_1 and ν_3 modes, the coupled LO frequencies have higher values than the decoupled ones. The difference between these frequencies is approximately the same for all samples. On the other hand, the coupled/decoupled LO frequencies are quite similar for the ν_2 mode. In the case of ν_4 mode, these frequencies also appear to be similar. However, the ν_4 mode is too weak and broad, whereas the fitting errors are too high, for a definitive conclusion to be drawn. As mentioned before, the LO frequencies obtained from the DPP model are actually the frequencies of bare phonons decoupled from plasmon, whereas the LO frequencies obtained from the CPP model are for the combined plasmon–LO phonon modes. The fact that in the case of ν_1 and ν_3 modes, the LO values obtained by the CPP model are higher than those obtained by the DPP model, implies that these modes are more strongly coupled with free carriers than the ν_2 mode.

The TO frequency behavior for all four IR modes, obtained from the CPP and DPP models (Tables 1 and 2), is presented in Fig. 5(b). In Fig. 3(a), one can notice that the ν_1 peak (marked with vertical arrows), is slightly shifted towards higher frequencies as the sintering temperature and degree of inversion increases, which is also corroborated by the slight increase of ω_{TO1} frequencies obtained from the CPP and DPP models. In the case of $MgFe_2O_4$, the tetrahedral cation-oxygen bonds are of higher force constants and lower bond length than the cation-oxygen octahedral bonds, and the corresponding vibrations of the tetrahedra are of higher frequency [27]. The bonding force between the cation and oxygen also depends on the nature of the cation and its valency [30]. Waldron [27] calculated force constants for some ferrites, and showed for $MgFe_2O_4$ that the force constants of the tetrahedral Fe–O vibrations are higher than the tetrahedral Mg–O vibrations [27]. Therefore, the observed increase of the frequency of the ν_1 mode with the increased degree of inversion is consistent with the tetrahedral origin of this mode, because more Mg^{2+} are replaced with Fe^{3+}. On the other hand, the TO frequency of the ν_2 mode, which mainly originates from the octahedral Fe–O vibrations, shows no consistent shift with the increased sintering

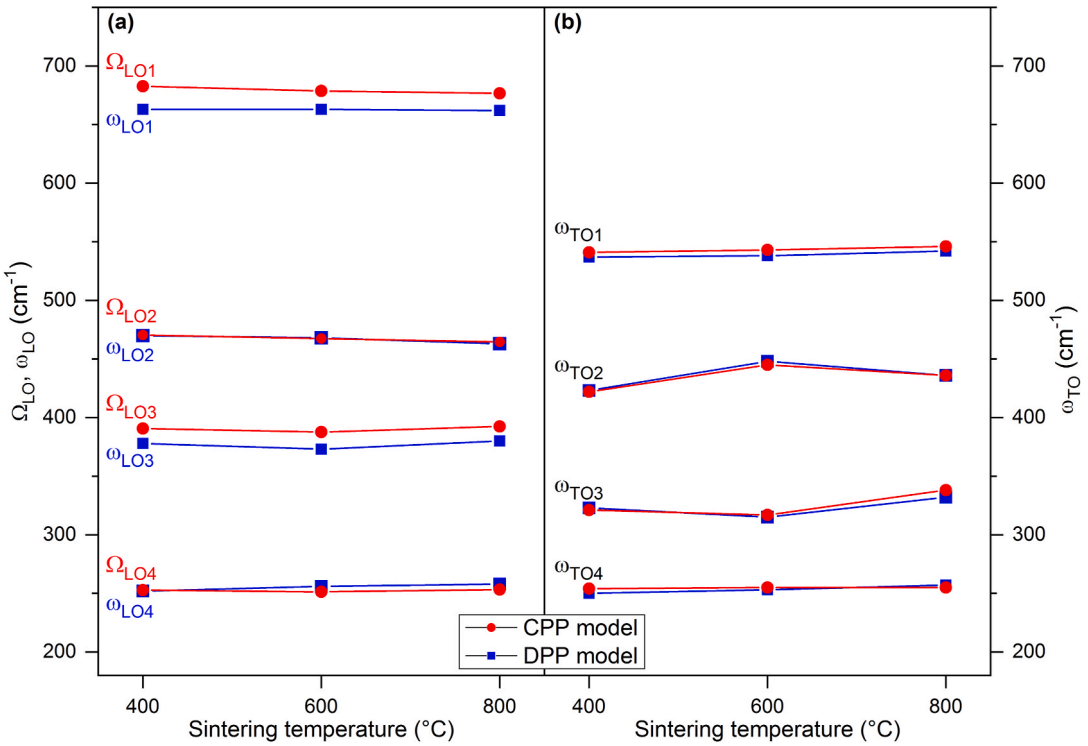

Fig. 5. (Color online) (a) Coupled (Ω_{LOj}) and decoupled (ω_{LOj}) LO phonon frequencies, and (b) the TO phonon frequencies, obtained from the CPP and DPP models, for $MgFe_2O_4$ nanocrystalline samples sintered at different temperatures.

temperature and degree of inversion. It slightly increases for the MFO600 sample, and then slightly decreases for the MFO800 sample. The increase of the TO frequency in the MFO600 sample can be explained by an increasing contribution of the Fe–O tetrahedral vibrations to the ν_2 mode, because with the increasing degree of inversion more Fe^{3+} cations are situated at the tetrahedral sites. With further increase of the degree of inversion (MFO800), one can presume even more complex behavior of the ν_2 mode, where, besides the Fe–O tetrahedral vibrations, the Mg–O octahedral vibrations can participate too. The behavior of the ν_3 mode becomes also more complex with increased

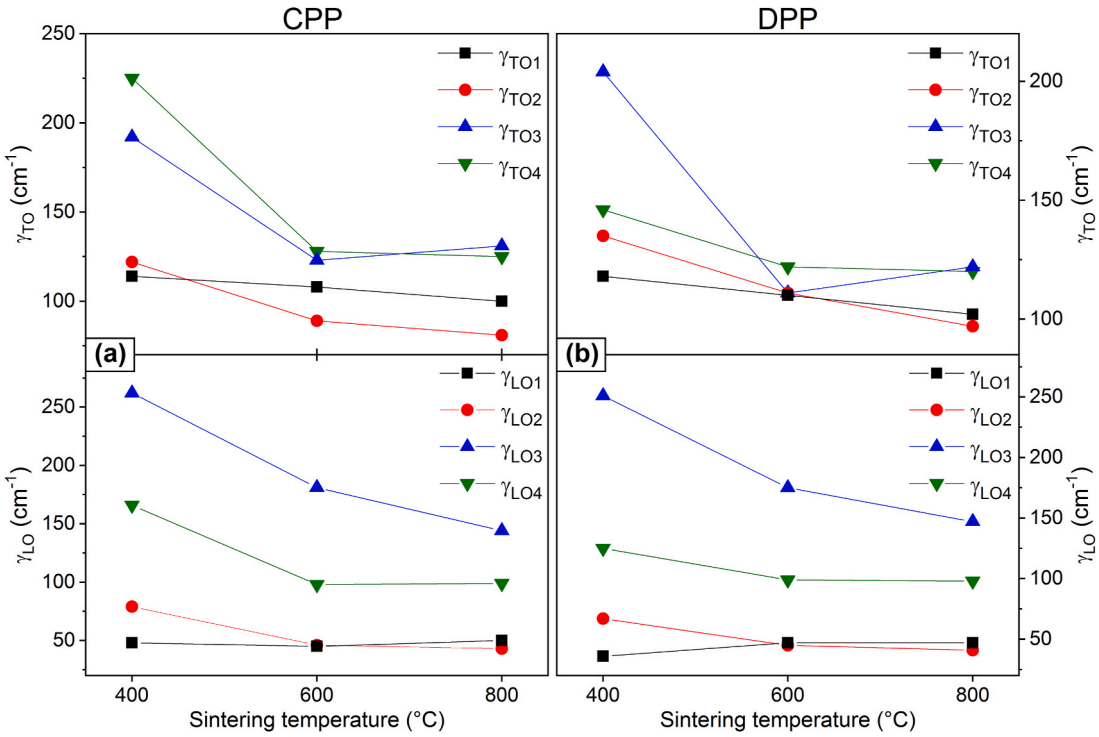

Fig. 6. (Color online) Variation of the TO and LO phonon dampings for $MgFe_2O_4$ nanocrystalline samples sintered at different temperatures, obtained from (a) CPP and (b) DPP models.

degree of inversion. It was already pointed out by Preudhomme and Tarte [31,32] that with higher degree of inversion, coupling between different tetrahedra and octahedra can make infrared vibrations of more complex nature. Consequently, it is no longer realistic to ascribe such vibrations and its frequencies to the localized vibrations of definite coordinated group (tetrahedral or octahedral), but to the vibrations which involve simultaneous participation of different cations (Mg or Fe) and coordinated groups.

The TO and LO phonon dampings obtained from the CPP and DPP models, are shown in Fig. 6. It can be seen that the TO/LO dampings tend to decrease with the increasing sintering temperature. Such a behavior is a consequence of the fact that the increase of sintering temperature produced samples with larger and more fussed crystallites with less pores and smaller influence of grain boundaries. All this in turn can lead to the smaller scattering rates for phonons, which means longer phonon lifetimes and decreased phonon dampings.

From the analysis of the IR spectra based on the CPP and DPP models (Fig. 5(a)), it was obtained that the ν_1 and ν_3 modes are more strongly coupled with free carriers than the ν_2 mode. We propose that this finding may be related to the presence of antisite defects, which are formed in inverse spinels. Namely, when in inverse spinels the trivalent cation replaces the divalent one in tetrahedra, it introduces excess positive charge at this site. Conversely, the octahedral site becomes a site with excess negative charge by introduction of the divalent cation instead of the trivalent one. In inverse $MgFe_2O_4$, positively charged $[Fe^{3+}_{tetra}]^+$ and negatively charged $[Mg^{2+}_{octa}]^-$ antisite defect centers can be formed in tetrahedra and octahedra (presented in Fig. 7), which behave as electron and hole trap centers, respectively [66–68].

If a particular mode has a significant contribution of the Fe–O tetrahedral vibrations, as it is the case for the ν_1 and ν_3 modes, it is quite reasonable to assume that such an infrared mode would be more strongly coupled with free carriers, due to the existence of positively charged $[Fe^{3+}_{tetra}]^+$ antisite defects. In the case of the ν_2 mode, which is mostly of the octahedral origin, the presence of negatively charged $[Mg^{2+}_{octa}]^-$ antisite defects is expected to weaken the plasmon-phonon interaction. With increased degree of inversion, one might expect a stronger plasmon-phonon coupling of the ν_1 and ν_3 modes as more $[Fe^{3+}_{tetra}]^+$ antisite defects should be formed. However, our analysis has shown that the plasmon-phonon coupling strength did not increase with the increased degree of inversion. We suppose that with the increased degree of inversion, when ν_1 and ν_3 vibrations become more complex, a subtle interplay between the tetrahedral Fe–O and octahedral Mg–O vibrations influences the plasmon-phonon coupling, leading to different strength of coupling between particular phonon modes and free carriers. As the exact mechanism of plasmon-phonon coupling in nanosized $MgFe_2O_4$ is not completely clear at the moment, it presents strong motivation for our future research.

4. Conclusions

In summary, we have investigated room-temperature far-IR reflectivity spectra of partially inverse nanocrystalline $MgFe_2O_4$ samples prepared by sol-gel method and sintered at different temperatures (400, 600 and 800 °C). The degree of inversion of $MgFe_2O_4$ samples was estimated from Raman spectra, and was found to increase with the increase of the sintering temperature. The IR spectra exhibited the presence of free carriers (the so-called Drude tail). The plasmon–LO phonon interaction was investigated by using the factorized coupled and decoupled plasmon-phonon models, combined with the Bruggeman effective medium approximation. From the analysis of the IR spectra, the coupled and decoupled phonon frequencies and dampings, as well as plasma frequencies and corresponding dampings of the plasmon mode were obtained. It was shown that with the increased sintering temperature, the phonon and plasmon dampings significantly decreased due to crystallite size increase, smaller porosity, and better connectivity between crystallites. Of particular importance is the finding that the ν_1 and ν_3 modes are more strongly coupled with free carriers than the ν_2 mode. We proposed that in inverse $MgFe_2O_4$ samples, the presence of positively charged $[Fe^{3+}_{tetra}]^+$ and negatively charged $[Mg^{2+}_{octa}]^-$ antisite defects influences the plasmon-phonon interaction. The stronger plasmon-phonon coupling is expected for infrared modes where the contribution of Fe–O tetrahedral vibrations becomes substantial. With the increased degree of inversion, a subtle interplay between the tetrahedral Fe–O and octahedral Mg–O vibrations can lead to different strength of coupling between particular phonon modes and free carriers. Our findings provide a basis for better understanding of plasmon-phonon coupling mechanism in disordered inverse spinels like $MgFe_2O_4$.

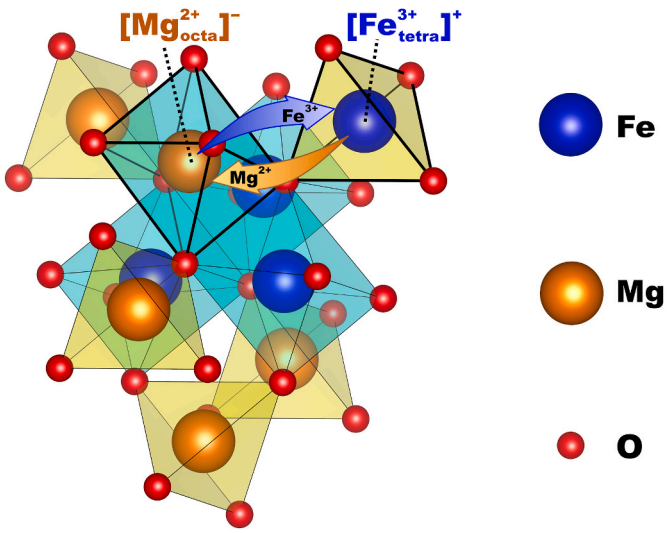

Fig. 7. (Color online) Schematic representation of inversion of trivalent Fe^{3+} and divalent Mg^{2+} cations between octahedra and tetrahedra, and the formation of the $[Fe^{3+}_{tetra}]^+$ and $[Mg^{2+}_{octa}]^-$ antisite defect centers in partially inverse $MgFe_2O_4$. The crystal structure visualized by VESTA 3 [50].

CRediT authorship contribution statement

Novica Paunović: Writing – review & editing, Writing – original draft, Visualization, Software, Methodology, Investigation, Formal analysis, Data curation, Conceptualization. **Zorana Dohčević-Mitrović:** Writing – review & editing, Supervision, Project administration, Methodology, Investigation, Formal analysis, Conceptualization. **Dejan M. Djokić:** Writing – review & editing, Visualization, Project administration, Formal analysis. **Sonja Aškrabić:** Writing – review & editing, Visualization, Investigation, Formal analysis. **Saša Lazović:** Writing – review & editing, Visualization, Investigation. **Ann Rose Abraham:** Writing – review & editing, Resources. **Balakrishnan Raneesh:** Writing – review & editing, Resources. **Nandakumar Kalarikkal:** Writing – review & editing, Project administration, Funding acquisition. **Sabu Thomas:** Writing – review & editing, Supervision.

Declaration of competing interest

The authors declare that they have no known competing financial interests or personal relationships that could have appeared to influence the work reported in this paper.

Data availability

Data will be made available on request.

Acknowledgement

The authors acknowledge funding provided by the Institute of Physics Belgrade, through the grant by the Ministry of Education, Science, and Technological Development of the Republic of Serbia. B. Raneesh acknowledges financial support from the UGC-DAE-Kolkata centre through the CRS project. Parts of the presented research were undertaken through Serbia-India bilateral project (2022–2024, No. 2), within the Program of Cooperation on science and technology between the Ministry of Education, Science and Technological Development of the Republic of Serbia and the Department of Science and Technology of the Ministry of Science and Technology of the Republic of India.

Appendix A. Supplementary data

Supplementary data to this article can be found online at https://doi.org/10.1016/j.mssp.2022.106889.

References

[1] Y.M.Z. Ahmed, E.M.M. Ewais, Z.I. Zaki, In situ synthesis of high density magnetic ferrite spinel ($MgFe_2O_4$) compacts using a mixture of conventional raw materials and waste iron oxide, J. Alloys Compd. 489 (2010) 269–274.
[2] N.M. Deraz, A. Alarifi, Novel preparation and properties of magnesioferrite nanoparticles, J. Anal. Appl. Pyrol. 97 (2012) 55–61.
[3] S.-S. Hong, Catalytic removal of carbon particulates over $MgFe_2O_4$ catalysts, React. Kinet. Catal. Lett. 84 (2005) 311–317.
[4] N. Ma, Y. Yue, W. Hua, Z. Gao, Selective oxidation of styrene over nanosized spinel-type $Mg_xFe_{3-x}O_4$ complex oxide catalysts, Appl. Catal. Gen. 251 (2003) 39–47.
[5] V. Srivastava, Y.C. Sharma, M. Sillanpää, Application of nano-magnesso ferrite (n-$MgFe_2O_4$) for the removal of Co^{2+} ions from synthetic wastewater: kinetic, equilibrium and thermodynamic studies, Appl. Surf. Sci. 338 (2015) 42–54.
[6] D.H.K. Reddy, Y.-S. Yun, Spinel ferrite magnetic adsorbents: alternative future materials for water purification? Coord. Chem. Rev. 315 (2016) 90–111.
[7] R. Dillert, D.H. Taffa, M. Wark, T. Bredow, D.W. Bahnemann, Research Update: photoelectrochemical water splitting and photocatalytic hydrogen production using ferrites (MFe_2O_4) under visible light irradiation, Apl. Mater. 3 (2015), 104001.
[8] G. Takalkar, R.R. Bhosale, F. AlMomani, S. Rashid, R.A. Shakoor, Ni incorporation in $MgFe_2O_4$ for improved CO_2-splitting activity during solar fuel production, J. Mater. Sci. 55 (2020) 11086–11094.
[9] Y. Shimizu, H. Arai, T. Seiyama, Theoretical studies on the impedance-humidity characteristics of ceramic humidity sensors, Sensor. Actuator. 7 (1985) 11–22.
[10] T. Maehara, K. Konishi, T. Kamimori, H. Aono, T. Naohara, H. Kikkawa, Y. Watanabe, K. Kawachi, Heating of ferrite powder by an AC magnetic field for local hyperthermia, Jpn. J. Appl. Phys. 41 (2002) 1620–1621.
[11] K. Konishi, T. Maehara, T. Kamimori, H. Aono, T. Naohara, H. Kikkawa, Y. Watanabe, K. Kawachi, Heating ferrite powder with AC magnetic field for thermal coagulation therapy, J. Magn. Magn Mater. 272–276 (2004) 2428–2429.
[12] S. Kanagesan, M. Hashim, S. Tamilselvan, N.B. Alitheen, I. Ismail, G. Bahmanrokh, Cytotoxic effect of nanocrystalline $MgFe_2O_4$ particles for cancer cure, J. Nanomater. (2013), 865024, 2013.
[13] F. Foroughi, S.A. Hassanzadeh-Tabrizi, A. Bigham, In situ microemulsion synthesis of hydroxyapatite-$MgFe_2O_4$ nanocomposite as a magnetic drug delivery system, Mater. Sci. Eng. C 68 (2016) 774–779.
[14] Q. Chen, Z.J. Zhang, Size-dependent superparamagnetic properties of $MgFe_2O_4$ spinel ferrite nanocrystallites, Appl. Phys. Lett. 73 (1998) 3156–3158.
[15] N. Sivakumar, S.R.P. Gnanakan, K. Karthikeyan, S. Amaresh, W.S. Yoon, G.J. Park, Y.S. Lee, Nanostructured $MgFe_2O_4$ as anode materials for lithium-ion batteries, J. Alloys Compd. 509 (2011) 7038–7041.
[16] Y. Yin, N. Huo, W. Liu, Z. Shi, Q. Wang, Y. Ding, J. Zhang, S. Yang, Hollow spheres of $MgFe_2O_4$ as anode material for lithium-ion batteries, Scripta Mater. 110 (2016) 92–95.
[17] Y. Pan, Y. Zhang, X. Wei, C. Yuan, J. Yin, D. Cao, G. Wang, $MgFe_2O_4$ nanoparticles as anode materials for lithium-ion batteries, Electrochim. Acta 109 (2013) 89–94.
[18] A. Bloesser, H. Kurz, J. Timm, F. Wittkamp, C. Simon, S. Hayama, B. Weber, U.-P. Apfel, R. Marschall, Tailoring the size, inversion parameter, and absorption of phase-pure magnetic $MgFe_2O_4$ nanoparticles for photocatalytic degradations, ACS Appl. Nano Mater. 3 (2020) 11587–11599.
[19] L. Zheng, K. Fang, M. Zhang, Z. Nan, L. Zhao, D. Zhou, M. Zhu, W. Li, Tuning of spinel magnesium ferrite nanoparticles with enhanced magnetic properties, RSC Adv. 8 (2018) 39177–39181.
[20] N. Sivakumar, A. Narayanasamy, J.M. Greneche, R. Murugaraj, Y.S. Lee, Electrical and magnetic behaviour of nanostructured $MgFe_2O_4$ spinel ferrite, J. Alloys Compd. 504 (2010) 395–402.
[21] M. Radović, Z. Dohčević-Mitrović, N. Paunović, S. Bošković, N. Tomić, N. Tadić, I. Belča, Infrared study of plasmon–phonon coupling in pure and Nd-doped CeO_{2-y} nanocrystals, J. Phys. Appl. Phys. 48 (2015), 065301.
[22] Z.V. Popović, M. Grujić-Brojčin, N. Paunović, M.M. Radonjić, V.D. Araújo, M.I. B. Bernardi, M.M. de Lima, A. Cantarero, Far-infrared spectroscopic study of CeO_2 nanocrystals, J. Nanoparticle Res. 17 (2015) 23.
[23] J. Mitric, N. Paunovic, M. Mitric, B. Vasic, U. Ralevic, J. Trajic, M. Romcevic, W. D. Dobrowolski, I.S. Yahia, N. Romcevic, Surface optical phonon – plasmon interaction in nanodimensional CdTe thin films, Phys. E Low-dimens. Syst. Nanostruct. 104 (2018) 64–70.
[24] X. Zhou, L. Liu, J. Sun, N. Zhang, H. Sun, H. Wu, W. Tao, Effects of $(Mg_{1/3}Sb_{2/3})^{4+}$ substitution on the structure and microwave dielectric properties of $Ce_2Zr_3(MoO_4)_9$ ceramics, Journal of Advanced Ceramics 10 (2021) 778–789.
[25] H. Tian, J. Zheng, L. Liu, H. Wu, H. Kimura, Y. Lu, Z. Yue, Structure characteristics and microwave dielectric properties of $Pr_2(Zr_{1-x}Ti_x)_3(MoO_4)_9$ solid solution ceramic with a stable temperature coefficient, J. Mater. Sci. Technol. 116 (2022) 121–129.
[26] L. Huang, Z.F. Li, P.P. Chen, Y.H. Zhang, W. Lu, Far infrared reflection spectra of $InAs_xSb_{1-x}$ ($x = 0$-0.4) thin films, J. Appl. Phys. 113 (2013), 213112.
[27] R.D. Waldron, Infrared spectra of ferrites, Phys. Rev. 99 (1955) 1727–1735.
[28] S. Hafner, Ordnung/Unordnung und Ultrarotabsorption IV. Die Absorption einiger Metalloxyde mit Spinellstruktur, Z. für Kristallogr. - Cryst. Mater. 115 (1961) 331–358.
[29] W.B. White, B.A. DeAngelis, Interpretation of the vibrational spectra of spinels, Spectrochim. Acta Mol. Spectros 23 (1967) 985–995.
[30] J. Preudhomme, P. Tarte, Infrared studies of spinels–I: a critical discussion of the actual interpretations, Spectrochim. Acta Mol. Spectros 27 (1971) 961–968.
[31] J. Preudhomme, P. Tarte, Infrared studies of spinels–II: the experimental bases for solving the assignment problem, Spectrochim. Acta Mol. Spectros 27 (1971) 845–851.
[32] J. Preudhomme, P. Tarte, Infrared studies of spinels–III: the normal II–III spinels, Spectrochim. Acta Mol. Spectros 27 (1971) 1817–1835.
[33] J. Preudhomme, P. Tarte, Infrared studies of spinels–IV: normal spinels with a high-valency tetrahedral cation, Spectrochim. Acta Mol. Spectros 28 (1972) 69–79.
[34] P. Thibaudeau, F. Gervais, Ab initioinvestigation of phonon modes in the $MgAl_2O_4$ spinel, J. Phys. Condens. Matter 14 (2002) 3543–3552.
[35] O.S. Josyulu, J. Sobhanadri, The far-infrared spectra of some mixed cobalt zinc and magnesium zinc ferrites, Phys. Status Solidi 65 (1981) 479–483.
[36] Z.V. Marinković Stanojević, N. Romčević, B. Stojanović, Spectroscopic study of spinel $ZnCr_2O_4$ obtained from mechanically activated ZnO–Cr_2O_3 mixtures, J. Eur. Ceram. Soc. 27 (2007) 903–907.
[37] M. Lenglet, F. Hochu, Correlation between ionic-covalent parameters and infrared spectroscopic data in II-III transition metal spinel-type oxides, Mater. Res. Bull. 32 (1997) 863–872.
[38] A. Pradeep, P. Priyadharsini, G. Chandrasekaran, Sol–gel route of synthesis of nanoparticles of $MgFe_2O_4$ and XRD, FTIR and VSM study, J. Magn. Magn Mater. 320 (2008) 2774–2779.
[39] N.W. Grimes, A.J. Collett, Correlation of infra-red spectra with structural distortions in the spinel series $Mg(Cr_xAl_{2-x})O_4$, Phys. Status Solidi 43 (1971) 591–599.
[40] V.A.M. Brabers, Ionic ordering and infrared spectra of some II-IV spinels, Phys. Status Solidi 12 (1972) 629–636.
[41] M.E. Striefler, G.R. Barsch, S.-I. Akimoto, Infrared absorption spectra of the spinels Fe_2SiO_4 and Co_2SiO_4, Spectrochim. Acta Mol. Spectros 36 (1980) 275–278.
[42] K.A. Mohammed, A.D. Al-Rawas, A.M. Gismelseed, A. Sellai, H.M. Widatallah, A. Yousif, M.E. Elzain, M. Shongwe, Infrared and structural studies of Mg1–xZnxFe2O4 ferrites, Phys. B Condens. Matter 407 (2012) 795–804.
[43] H. Dawoud, L.S.A. Ouda, S. Shaat, FT-IR studies of nickel substituted polycrystalline zinc spinel ferrites for structural and vibrational investigations, Chemical Science Transactions 8 (2017) 179–188.
[44] A. Pradeep, G. Chandrasekaran, FTIR study of Ni, Cu and Zn substituted nano-particles of $MgFe_2O_4$, Mater. Lett. 60 (2006) 371–374.
[45] Z.V. Popović, G. De Marzi, M.J. Konstantinović, A. Cantarero, Z. Dohčević-Mitrović, M. Isobe, Y. Ueda, Phonon properties of the spinel oxide $MgTi_2O_4$ with the S=1/2 pyrochlore lattice, Phys. Rev. B 68 (2003), 224302.
[46] Z.Ž. Lazarević, Č. Jovalekić, A. Rečnik, V.N. Ivanovski, A. Milutinović, M. Romčević, M.B. Pavlović, B. Cekić, N.Ž. Romčević, Preparation and characterization of spinel nickel ferrite obtained by the soft mechanochemically assisted synthesis, Mater. Res. Bull. 48 (2013) 404–415.
[47] Z.V. Marinković Stanojević, N. Romčević, B. Stojanović, Spectroscopic study of spinel ZnCr2O4 obtained from mechanically activated ZnO–Cr2O3 mixtures, J. Eur. Ceram. Soc. 27 (2007) 903–907.
[48] E.Z. Katsnelson, A.G. Karoza, L.A. Meleshchenko, L.A. Bashkirov, IR reflection spectra of manganese-zinc ferrites, Phys. Status Solidi 152 (1989) 657–666.
[49] H.D. Lutz, B. Müller, H.J. Steiner, Lattice vibration spectra. LIX. Single crystal infrared and Raman studies of spinel type oxides, J. Solid State Chem. 90 (1991) 54–60.
[50] K. Momma, F. Izumi, VESTA 3 for three-dimensional visualization of crystal, volumetric and morphology data, J. Appl. Crystallogr. 44 (2011) 1272–1276.
[51] A.R. Abraham, B. Raneesh, P.M.G. Nambissan, D. Sanyal, S. Thomas, N. Kalarikkal, Defects characterisation and studies of structural properties of sol–gel synthesised $MgFe_2O_4$ nanocrystals through positron annihilation and supportive spectroscopic methods, Phil. Mag. 100 (2020) 32–61.
[52] V.G. Ivanov, M.V. Abrashev, M.N. Iliev, M.M. Gospodinov, J. Meen, M.I. Aroyo, Short-range B-site ordering in the inverse spinel ferrite $NiFe_2O_4$, Phys. Rev. B 82 (2010), 024104.
[53] P. Chandramohan, M.P. Srinivasan, S. Velmurugan, S.V. Narasimhan, Cation distribution and particle size effect on Raman spectrum of $CoFe_2O_4$, J. Solid State Chem. 184 (2011) 89–96.

[54] V. D'Ippolito, G.B. Andreozzi, D. Bersani, P.P. Lottici, Raman fingerprint of chromate, aluminate and ferrite spinels, J. Raman Spectrosc. 46 (2015) 1255–1264.
[55] B.D. Hosterman, Raman Spectroscopic Study of Solid Solution Spinel Oxides, University of Nevada, Las Vegas, 2011.
[56] F. Nakagomi, S.W. da Silva, V.K. Garg, A.C. Oliveira, P.C. Morais, A. Franco, Influence of the Mg-content on the cation distribution in cubic $Mg_xFe_{3-x}O_4$ nanoparticles, J. Solid State Chem. 182 (2009) 2423–2429.
[57] A. Sankaramahalingam, J.B. Lawrence, Structural, optical, and magnetic properties of $MgFe_2O_4$ synthesized with addition of copper, synthesis and reactivity in inorganic, metal-organic, Nano-Metal Chemistry 42 (2012) 121–127.
[58] Z.Ž. Lazarević, Č. Jovalekić, V.N. Ivanovski, A. Rečnik, A. Milutinović, B. Cekić, N.Ž. Romčević, Characterization of partially inverse spinel $ZnFe_2O_4$ with high saturation magnetization synthesized via soft mechanochemically assisted route, J. Phys. Chem. Solid. 75 (2014) 869–877.
[59] J. Guo, L. Shi, L. Wu, S. Pan, X. Yuan, J. Zhao, Spin-polarized electron transport in highly reduced $MgFe_2O_{4-\delta}$, Mater. Res. Express 5 (2018), 126301.
[60] F. Gervais, High-temperature infrared reflectivity spectroscopy by scanning interferometry, in: K.J. Button (Ed.), Infrared and Millimeter Waves, Academic Press, New York, 1983, pp. 279–339.
[61] A.A. Kukharskii, Plasmon-phonon coupling in GaAs, Solid State Commun. 13 (1973) 1761–1765.
[62] O.K. Kim, W.G. Spitzer, Study of plasmon–LO-phonon coupling in Te-doped $Ga_{1-x}Al_xAs$, Phys. Rev. B 20 (1979) 3258–3266.
[63] F. Gervais, Optical conductivity of oxides, Mater. Sci. Eng. R Rep. 39 (2002) 29–92.
[64] D.A.G. Bruggeman, Berechnung verschiedener physikalischer Konstanten von heterogenen Substanzen. I. Dielektrizitätskonstanten und Leitfähigkeiten der Mischkörper aus isotropen Substanzen, Ann. Phys. 416 (1935) 636–664.
[65] J.E. Spanier, I.P. Herman, Use of hybrid phenomenological and statistical effective-medium theories of dielectric functions to model the infrared reflectance of porous SiC films, Phys. Rev. B 61 (2000) 10437–10450.
[66] T.A. Bazilevskaya, V.T. Gritsyna, D.V. Orlinski, L.V. Udalova, A.V. Voitsenya, The effect of composition, processing conditions, and irradiation, on lattice defects in spinel ceramics, J. Nucl. Mater. 253 (1998) 133–140.
[67] N. Pathak, B. Sanyal, S.K. Gupta, R.M. Kadam, $MgAl_2O_4$ both as short and long persistent phosphor material: role of antisite defect centers in determining the decay kinetics, Solid State Sci. 88 (2019) 13–19.
[68] N. Matsubara, T. Masese, E. Suard, O.K. Forslund, E. Nocerino, R. Palm, Z. Guguchia, D. Andreica, A. Hardut, M. Ishikado, K. Papadopoulos, Y. Sassa, M. Månsson, Cation distributions and magnetic properties of ferrispinel $MgFeMnO_4$, Inorg. Chem. 59 (2020) 17970–17980.

[5]

CHAPTER 2

Transport properties of nanoscopic solids as probed by spectroscopic techniques

Dejan M. Djokić[1], Novica Paunović[1], Bojan Stojadinović[1], Dimitrije Stepanenko[1], Saša Lazović[2], Zorana Dohčević-Mitrović[1]

[1]Nanostructured Matter Laboratory, Institute of Physics Belgrade, University of Belgrade, Belgrade, Serbia; [2]Biomimetics Laboratory, Institute of Physics Belgrade, University of Belgrade, Belgrade, Serbia

Chapter Outline

1. Introduction

Nanoscale world is at the border between the quantum realm at the smaller dimensions and the classical one at larger. At the quantum side of this divide, systems under consideration consist of few particles and the properties of the sample often do not average into well-behaved quantities with deviations from the mean value much smaller than the mean value itself. So standard assumptions of both the classical physics and the standard statistics can break down within the nanoscale domain. This occurrence impacts the methods for probing the transport at the nanoscale.

Fundamentals and Properties of Multifunctional Nanomaterials. https://doi.org/10.1016/B978-0-12-822352-9.00009-2

[5]

Noncontact measurements of transport can offer distinct advantages. Macroscopic contacts necessary for the standard transport measurements often disturb the system since they are immensely larger than it. The structure of the contacts needs to impact the system as little as possible, requiring cooling to very low temperatures. Thermal noise introduced by contacts is hard to distinguish from the quantum noise that is an interesting property of the probed system.

Experiment is always performed on an object composed of nonidentical units and averaging of the properties does not automatically occur within the measurement apparatus. Moreover, the most interesting properties are often encoded into distribution of the results of measurements, and not exclusively in their mean values. Quantum side of the breakdown is somewhat different. The quantum transport theory deals with universality of the transport. In the quantum limit, as most transparently seen in the Landauer formula for conductivity, the whole variety of the transport behavior boils down to the number and transmitivities of transport channels. The variety of quantum behavior in transport appears due to macroscopic quantum phenomena or lies hidden in the variability of nominally identical nanoscale systems.

To probe the rich variety of transport phenomena at the nanoscale, it is preferable to look at the properties of conducting quasiparticles than to look at the integral characteristics of a collection of them. Quasiparticles are most easily accessed through spectroscopic techniques, like Raman spectroscopy, electron spin resonance (ESR), and infrared reflection (IRR) spectroscopy. Resonant nature of excitations and response detection in spectroscopy offer us a way to discriminate between constituents of the nanoscale system and look exclusively at the processes that are in resonance with the appropriate driving. Therefore the noncontact spectroscopic measurements give us an opportunity to see the nanoscale world in more detail.

This chapter is partitioned in three sections which are organized as follows. In the first section, we provide a short introduction to the Raman scattering technique followed with a review on an indirect finding of the two different variable range hopping (VRH) transport mechanisms based on the analysis of the temperature dependent electronic Raman background of nanocrystalline $BiFeO_3$ [1]. The subsequent section tackles a summary on how both particle size decreased and Nd doping influence the Plasmon−phonon interaction and optical conductivity in CeO_{2-y} nanocrystals investigated by IRR spectroscopy [2]. Finally, in the third section, the main aspects of conduction ESR have been briefly introduced in which terms the temperature evolution and character of transport properties of single-walled carbon nanotubes have been elaborated [3].

2. Raman scattering

2.1 Short introduction to Raman scattering technique

In solid state spectroscopy, the inelastic scattering of photons by lattice vibrations (LVs) is known as Raman effect. The photon energy can be lost or gained in such processes, which

[5]

is accomplished by the phonon creation or annihilation, and termed in literature as Stokes or anti-Stokes Raman excitation, respectively. Brillouin Raman scattering (RS), however, stands for a particular case of RS that concerns the scattering by acoustic phonons of very low frequencies, unlike common Raman which involves optical phonons. The theory of Raman spectroscopy can be found elsewhere. Nevertheless, for a rather comprehensive elaboration the reader is further referred to seminal Mitra's work [4], some of which fragments we will rely on in what follows.

Following the first principles of electromagnetism, the incident electromagnetic field of the photons is coupled with the phonons via dipole moments that are induced by the phonon field. The electronic 3×3 polarizability tensor α_{mn} is modulated by the variation of the lattice due to the normal vibration of frequency ω_p and can be expanded in terms of the time dependent atomic displacement components $u_p = u_p(0)e^{i\omega_p t}$ as

$$\alpha_{mn} = \alpha_{mn}^{(0)} + \sum_p \alpha_{mn,p}^{(1)} u_p + \frac{1}{2}\sum_p \sum_q \alpha_{mn,pq}^{(2)} u_p u_q + \ldots \tag{2.1}$$

where

$$\alpha_{mn,p}^{(1)} = \left(\frac{\partial \alpha_{mn}}{\partial u_p}\right)_{u_p=0}, \; \alpha_{mn,pq}^{(2)} = \left(\frac{\partial^2 \alpha_{mn}}{\partial u_p \partial u_q}\right)_{u_p=0,\, u_q=0} \ldots \tag{2.2}$$

If $\overrightarrow{E}$ denotes the electric field of incident electromagnetic radiation with frequency ω,

$$\overrightarrow{E} = \overrightarrow{E}(0)e^{i\omega t}, \tag{2.3}$$

then the induced dipole moment can be written as

$$\overrightarrow{M} = \widehat{\alpha}\,\overrightarrow{E}, \tag{2.4}$$

which ultimately yields induced dipole moment along p mode

$$\overrightarrow{M}_p = \widehat{\alpha}^{(0)}\overrightarrow{E}_0 e^{i\omega t} + \widehat{\alpha}^{(1)}\overrightarrow{E}_0 e^{i\left(\omega \pm \omega_p\right)t} u_p(0) + \widehat{\alpha}^{(2)}\overrightarrow{E}_0 e^{i\left(\omega \pm 2\omega_p\right)t} u_p^2(0) + \ldots \tag{2.5}$$

First term in Eq. (2.5) represents nothing but elastic Raleigh scattering process. The energy of the electromagnetic radiation remains unchanged in this case. The derivative of the electronic polarizability in the second term in Eq. (2.5) gives rise to the first-order RS processes when incident photon $\left(\hbar\overrightarrow{k}_1, \hbar\omega_1\right)$ is absorbed or created to create or destroy a phonon $\left(\hbar\overrightarrow{k}, \hbar\omega\right)$. The final photon, with both different wave vector and frequency $\left(\hbar\overrightarrow{k}_2, \hbar\omega_2\right)$ from the incident one, gets emitted in such a way that the energy and the momentum are totally conserved. Reduced Planck's constant is denoted as $\hbar$.

[5]

In doped semiconductors and disordered metals, spectral recoil of light in RS consistently comprises a number of distinctive peaks generated by optically active phonons, as well as, an extended frequency continuum which is in direct relationship with electronic response [6]. This continuous spectral background originates from low-energy electronic excitations, which reflects the charge carrier scattering rate, and is familiarly known in literature as the Raman electronic background [1,7–11]. Falkovsky [7] was first to provide a theoretical foundation for the spectral profiles of Raman electronic background in "dirty" metals. The effects of electronic excitations in Raman are usually observed at low-energy scales and are attributed to scattering by phonons or impurities involving finite momentum transfers ($k \neq 0$) as a result of the finite penetration depth of light in materials. Later on, Zawadowski and Cardona [8] proposed a Feynman diagrammatic approach to estimating the Kubo spectral response function within the scope of ladder approximation [12] at $q \approx 0$. Most importantly, these authors were first to recognize an intimately related link between the nonresonant electronic excitations seen in Raman with the carrier transport.

As with nonresonant RS electronic response, the related Feynman diagrams (see Fig. 2.1) are composed of wavy lines denoting photon propagators. Their initial and final (momentum, energy) are respectively $\left(\hbar\vec{k}_1, \hbar\omega_1\right)$ and $\left(\hbar\vec{k}_2, \hbar\omega_2\right)$. An electron-hole pair of (momentum: $\vec{k} = \vec{k}_1 - \vec{k}_2$, energy: $\omega = \omega_1 - \omega_2$), scattered by phonons and/or impurities, become generated by the incoming photon propagator. Phonon propagator, given in dashed line (Fig. 2.1), can be excited by the electron/hole inside a pair and is further captured by its counterpart (hole/electron), as is enforced by the ladder approximation. At last, upon summing up all the dominating ladder-like diagrams, Raman differential cross section due to the purely electronic response [9,11], reads as

$$\frac{d^2\sigma}{d\omega d\Omega} \propto \frac{1}{1-\exp(-\hbar\omega/k_BT)} \times \frac{\omega\tau}{1+(\omega\tau)^2}. \tag{2.6}$$

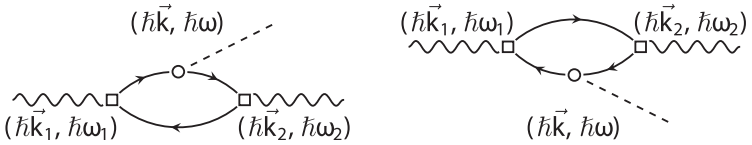

Figure 2.1

Raman scattering of light (*wavy lines*) due to phonons (*dashed lines*). Electron-hole formations (*solid lines*) represented via loops in the Feynman diagrams of third order (first order Raman scattering). Processes involving electron and hole contributions are given in left and right diagrams, respectively. Vertex □ represents electron-photon interaction, while vertex represents electron-phonon interaction as is given in Ref. [5]. *The drawing is adapted from D.M. Djokić, B. Stojadinović, D. Stepanenko, Z. Dohčević-Mitrović, Probing charge carrier transport regimes in $BiFeO_3$ nanoparticles by Raman spectroscopy, Scr. Mater. 181 (2020) 6–9. https://doi.org/10.1016/j.scriptamat.2020.02.008.*

[5]

At a particular value of the effective scattering rate, $1/\tau$, the proportionality factor in Eq. (2.6) is a function of different variables depending on the type of the experimental setup [10]. The temperature-dependent Bose-Einstein factor and expression resembling Drude function are respectively given as the second and third term in the product of Eq. (2.6), while $1/\tau$ involves two terms in the sum as follows

$$1/\tau = 1/\tau_0 + Dq^2. \tag{2.7}$$

$1/\tau_0$ stands for the charge carrier scattering rate due to phonons/impurities in $q \to 0$ limit, which is concerned with nothing but bulk channels. The second term (Dq^2), however, gives rise to the effects of processes nonconserving momenta, very often pronounced in nanocrystals [1]. It is safe to neglect the bulk term ($1/\tau_0$) if there is no experimental evidence for the electronic Raman background in the case of bulk materials. D is the diffusion constant which is, based on the Einstein relation, related to electric conductivity σ in the following manner

$$D = \sigma/\left(g(\varepsilon_F)e^2\right), \tag{2.8}$$

where $e = 1.6 \times 10^{-19}$ C. The average value of the electronic density states close to the Fermi level [9] is denoted with $g(\varepsilon_F)$.

2.2 Multiferroic $BiFeO_3$ nanoparticles

Crystalline bismuth ferrite stands for a multiferroic material increasingly attracting the attention among the researchers and is also one of few materials to provide both ferroelectric ($T_C \approx 1100$ K) and antiferromagnetic ($T_N \approx 643$ K) properties at room temperature [13] and even higher. It is important to know that $BiFeO_3$ has proven undemanding to obtain in ambient conditions. $BiFeO_3$ is classed as rhombohedrally distorted ABO_3 perovskite structure (space group $R3c$) with lattice parameter $a_{rh} = 3.965$ Å, a rhombohedral angle α_{rh} of 89.30−89.48°, and ferroelectric polarization along $[111]_{pseudocubic}$ direction at room temperature [14]. Primitive unit cell consists of two unit formulas and contains 10 atoms. This structure can be represented as two distorted perovskite unit cells, connected along the main pseudocubic diagonal [111] to form a rhombohedral unit cell, as is given in Fig. 2.2A. Bi^{3+} ions are situated at A lattice sites and are surrounded by 12 oxygen atoms. On the other hand side, Fe^{3+} ions are located at B lattice sites, and they are surrounded by six oxygen atoms with which it forms a FeO_6 octahedron. In this configuration, Bi^{3+} and Fe^{3+} ions are shifted along [111] direction, and two oxygen octahedrons are rotated around [111] direction in the opposite directions by 14° that can be seen from the position of the green octahedrons in Fig. 2.2B. This means that the Fe-O-Fe angle deviates from 180° to amount nearly 154−156° [16,17]. The unit cell can also be described in a hexagonal frame of reference, where the hexagonal

[5]

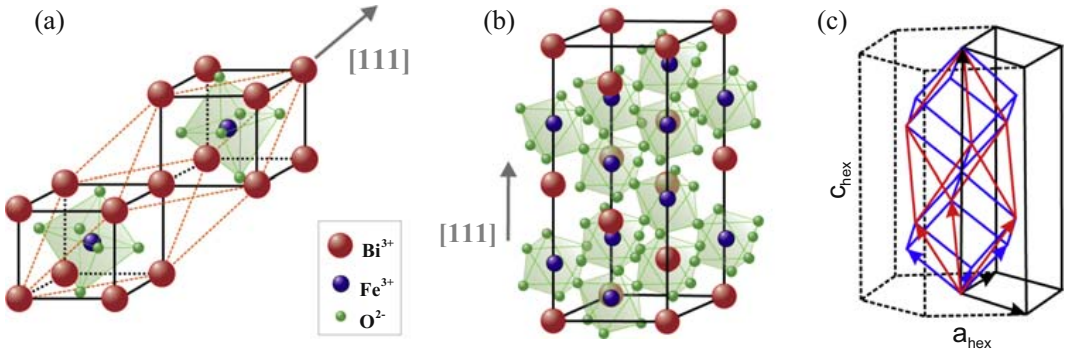

Figure 2.2

Schematic representation of (A) rhombohedral structure framed by orange dashed lines, (B) hexagonal perovskite structure of $BiFeO_3$ with [111] ferroelectric polarization direction given in gray arrow, and (C) hexagonal cell (black), rhombohedral (red), and pseudocubic (blue) unit cell with corresponding unit vectors drawn in *arrows*. *The figure is to a rather large extent reworked from J.-G. Park, M.D. Le, J. Jeong, S. Lee, Structure and spin dynamics of multiferroic $BiFeO_3$, J. Phys. Condens. Mat. 26 (2014) 433202. https://doi.org/10.1088/0953-8984/26/43/433202.*

c-axis is aligned parallel to the diagonals of the perovskite cube. In other terms, $[001]_{\text{hexagonal}} \parallel [111]_{\text{pseudocubic}}$. The corresponding hexagonal lattice parameters (Fig. 2.2C are $a_{\text{hex}} = 5.579$ Å and $c_{\text{hex}} = 13.869$ Å [14,18].

Bulk $BiFeO_3$ is a semiconductor with literature values of the bandgap determined by optical measurements at room temperature in the range from 2.1 to 2.8 eV. Several authors claim that $BiFeO_3$ has a direct bandgap transition at about 2.1−2.8 eV [19−22]. There are, however, published studies in which it has been shown that $BiFeO_3$ has an indirect bandgap transition of about 0.4−1.0 eV, quite smaller as compared to the values obtained for the direct transition [23]. Density functional theory calculations [24,25] have corroborated an indirect energy transition of about 2.1 eV, while in the room temperature absorption spectra recorded on $BiFeO_3$ thin film, the transition at approximately 2.17 eV has been observed [26].

Finally, according to Catalan and some of the references therein [16], based on two-probe DC resistivity measurements carried out on high-quality bulk samples of $BiFeO_3$, the log resistivity value undergoes two slopes in Arrhenius law with increasing temperature. Actually, it has been found that the activation energy of the charge carriers decreases from nearly 1.3 down to nearly 0.6 eV as the material is heated above T_N with the anomaly around it. However, one does not expect such type of conducting behavior when the scale of the crystal moves down to several nanometers. Indeed, in the case of defective nanoparticles with a core/shell structure [1], the nanoparticle shell may have metallic and/or semiconducting features, while the nanoparticle core prominently features insulating properties. This casts a shadow over models that are commonly applied in pristine bulk materials to fit the resistivity data in systems with disorder and/or decreased dimensions.

[5]

At a scale ranging down to nanometers, $BiFeO_3$ has proven very prospective for a potential use in satellite communications, electrically accessed magnetic memory, commercial applications for photovoltaics and alternative sensors [16]. Most essentially, the electric resistance of $BiFeO_3$ is found to be a key parameter that should comply with the prime industrial requirements. Accomplishing high-electric conductivity value in this nanoscopic compound from its powders is one of the major assets and is perceived as a very promising in development of the novelty. Moreover, it proves quite demanding to identify the charge carrier transport, as well as, to distill electric conductivity value using the contact probes themselves invasively [27,28]. On the other hand, RS tool is widely known as a local and highly informative experimental probe capable of assessing the origin and dynamics of charge carriers in conducting materials. This makes Raman technique a reliable, yet noninvasive, means for investigating the transport properties of materials that are treated with utmost delicacy.

Fairly recent temperature-dependent RS study, carried out on the multiferroic $BiFeO_3$ nanoparticles of high purity and relied on the temperature evolution electronic Raman background [1], has explored an exciting prospect of extracting the relevant piece of information about the electric transport in this nanoscopic compound. μ-RS measurements were recorded over the temperature range of 80−723 K, while the related spectra were gathered at the backscattering arrangement with solid state 532 nm Nd:YAG laser as excitation at sub-mW laser powers on the sample itself. There were more than 13 optical phonon modes (symmetry: A_1 and E) detected in the experiment, while the spectra were decomposed with Lorentzian lineshape profiles, as is presented in Fig. 2.3 at four different temperatures. The entire number, together with frequency positions, of the optically active phonon modes of $BiFeO_3$ nanoparticles detected with Raman were found exactly the same with those observed in temperature-dependent RS spectra undertaken for bulk crystalline $BiFeO_3$ [29]. However, the authors [1] properly commented on the emerged splittings of a number of few polar LO+TO phonon modes, which naturally appear in the case of $BiFeO_3$ nanoparticles [30,31]. As with bulk, the prediction based on the factor group analysis turns out to be in accordance with the experiment implying 13 ($4A_1 + 9E$) optically active modes in phonon Raman spectra [32].

In contrast to Raman spectra recorded for on bulk $BiFeO_3$, Raman active optical modes pertinent to $BiFeO_3$ nanoparticles were evidenced to seat on quite a broad spectroscopic profile (Fig. 2.3 shaded in light gray). Such a spectroscopic feature has a pronounced temperature dependence and is familiarly known as Raman electronic background. In literature, indeed there are spectroscopic backgrounds akin to one studied in Ref. [1] such as nonresonant Raman continuous profile observed in metal-oxide thin films [33]. However, the related profile is quite shapeless, moreover with strong intensity, and is ascribed to entirely electronic RS recoil independent of bands due to the phonons. This Raman electronic background emerges as a result of the surface roughness at atomic scale.

[5]

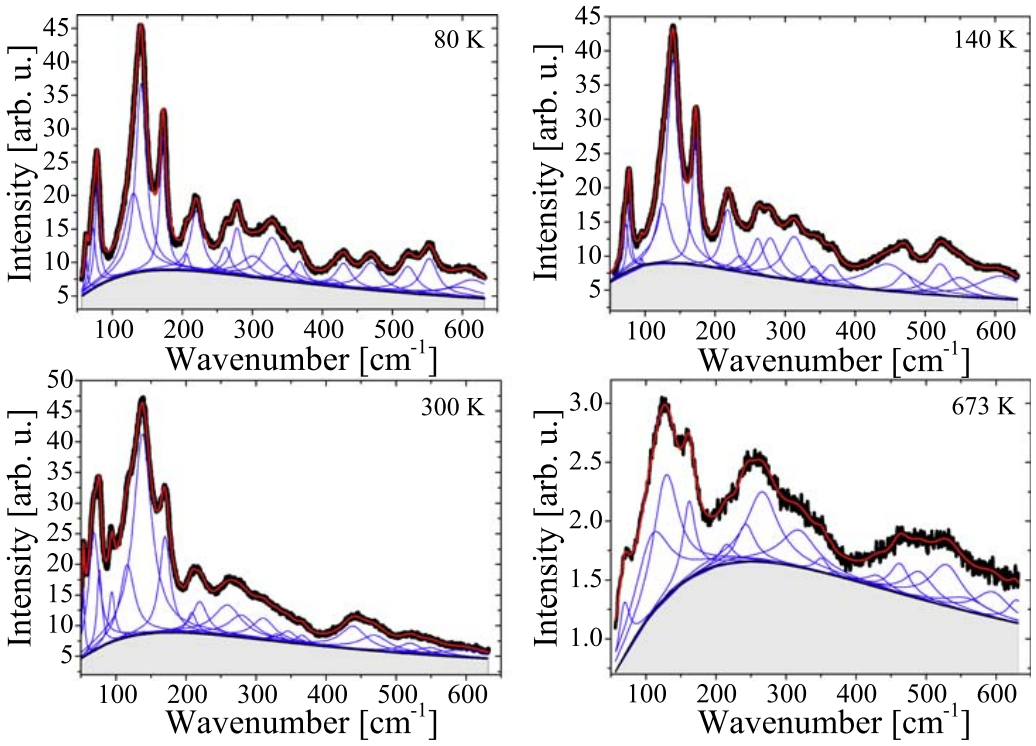

Figure 2.3

Raman scattering spectra given for four representative temperatures (data points presented in black). The spectra are composed of a continuous electronic background (shaded in light gray) and Lorentzian phonon peaks (*lines* in blue). The overall *fitting line* is drawn with *red line*. *The figure is adopted from the published work D.M. Djokić, B. Stojadinović, D. Stepanenko, Z. Dohčević-Mitrović, Probing charge carrier transport regimes in $BiFeO_3$ nanoparticles by Raman spectroscopy, Scr. Mater. 181 (2020) 6–9. https://doi.org/10.1016/j.scriptamat.2020.02.008.*

In addition, it has been reported that, in extremely small metallic particles [34] and metallic thin film islands with adsorbents [35], RS due to the particle-hole pair excitations brings about the emergence of the phononless continuous electronic background. This can be explained in terms of the momentum conservation violation generated in the presence of the electronic states at surface. Furthermore, even in the bulk hole-doped manganese perovskites, the broad electronic Raman response associated with the scattering by conduction electrons has been determined to cause a drastic change at the phase transition, as shown by Liu et al. [36]. The evolution of the effects of electron correlations in this compound could be assessed computably with temperature.

The authors of Ref. [1] have fittingly cast the surface states situated at particle boundaries in the role of localization centers via which the conduction can run efficiently. In terms of energy, these states are located near the vicinity of the Fermi level and they are, in general, unequally distributed to evolve with both spatial and energy gap between them. Therefore, the charge carrier conduction mechanism in which the hopping energy varies

[5]

with the hopping range can be safely modeled for description of the transport over an extended temperature range in disordered semiconductors and/or amorphous solids, such as nanoscaled materials. Commonly, exceptionally high-electric resistivity values are observed in such systems. As such, these values serve as a definite fingerprint to rule out any conventional metallic/semiconducting type of conductivity mechanism intrinsic to (semi)conductors. VRH mechanism, nonetheless [37], stands for a rather viable transport mechanism in nanoparticles with no other alternative acceptable, as was reported in Ref. [1] for $BiFeO_3$ nanoparticles. Two different types of VRH charge carrier transport mechanisms in $3D$ have been probed in a contactless way using temperature-dependent Raman spectroscopy, and it has been evidenced that these two are affected by different degrees of the electron correlation strengths on the opposite sides of the antiferromagnetic phase transition. Below the transition temperature, the transport undergoes the mechanism explained by Efros and Shklovskii [38], whereas at high temperatures, the charge carrier transport adheres to the traditional Mott VRH theory [37].

Here we provide a brief account of the Mott and Efros−Shklovskii laws based on a concise analysis from a seminal paper by Arginskaya and Kozub [39]. The central focus of this study was on a considerable diversity of theoretical results emerging from calculations for the exponential prefactors in various VRH expressions, as well as, the crossover from VRH conductivity of Mott type in which the density of electronic states at Fermi level is $g(\varepsilon \approx \varepsilon_F) = const$ toward VRH conductivity running via states separated by a Coulomb gap when $g(\varepsilon \approx \varepsilon_F) \propto \varepsilon^2$. Aharony et al. [40] have made an attempt to obtain the universal analytic expression for the temperature dependence of conductivity, $\sigma(T)$, in the crossover region from Mott to Efros−Shklovskii law. In general terms, temperature dependence of the VRH conductivity $\sigma(T)$ can be written down as

$$\sigma(T) = \sigma_n \exp\left(-\frac{T_n}{T}\right)^n, \tag{2.9}$$

where n might take on $1/4$ or $1/2$ in $3D$ with respect to the law chosen, Mott's or Efros−Shklovskii's. Constant factors σ_n and T_n depend on the preferred of the two models. However, the common feature of most of the relevant studies in the field of VRH boils down to simplistic approaches in estimating the exponential prefactor σ_n. As a traditional rule, σ_n is generally assumed to have no temperature dependence.

Factors σ_n and T_n, which are given in Eq. (2.9), can be computed straightforwardly by optimizing the correlation linking the energy and spatial separation between the lattice sites. Once an electric field is applied, hopping in the direction of the field is rather preferred at different probabilities with respect to both distance and energy separation. As with the $3D$ free electron case, in original Mott paper [37], it was in a simplified way presented that the hopping energy is inversely proportional to the cube of the hopping distance, while the hopping frequency ν for a given temperature T was found to depend on

[5]

two following parameters: r as the spatial distance between the sites in units of localization length ξ and W as their typical hopping energy separation. Namely,

$$\nu = \nu_0 \exp\left(-\frac{2r}{\xi} - \frac{W}{k_B T} \right), \tag{2.10}$$

where $\nu \equiv \nu_0$ for both $r = 0$ and $W = 0$, whereas $k_B = 1.38 \times 10^{-23}\ \mathrm{J/K}$ stands for Boltzmann constant. The hopping frequency characterizes the relative number of directed charge carrier hops due to the electric field. Indeed, in noncrystalline systems, the variables r and W are not randomly independent so that one can be combined into a single parameter by minimizing the total exponent in (Eq. 2.10). In the actual fact, the hopping from one site to another with a lower energy/distance occurs at high rate. However, reaching both low energy/distance sites at the same time remains utterly impossible. The same reasoning applies for the large energy/distance sites that altogether justifies the application of variation method and thence the term "variable" in VRH.

Variable hopping processes translate a charge carrier by a range r within a time $\sim 1/\nu$, but at a preferred W value that maximizes the electric current via hopping. This proportionality squarely leads to the VRH expression for conductivity which is given in (Eq. 2.9). Yet, to relate r with W or vice versa, one has to further assume that most of the mobile carriers come from a narrow energy window near the Fermi level of width $\sim k_B T$. In such a way, the carrier density n_c of spin $S = 1/2$ which as the other factor prominently figures in the expression for the conductivity and can be computed by integration as

$$n_c = 2 \int_{\varepsilon_F}^{\varepsilon_F + k_B T} g(\varepsilon) \mathrm{d}\varepsilon, \tag{2.11}$$

where $g(\varepsilon)$ measures the total number of states ($\mathrm{d}N$) per both energy ($\mathrm{d}E$) and volume unit (V), each of which is double degenerated ($2S + 1 = 2$).

One must emphasize that the wise choice of $g(\varepsilon)$ leads to the correct expression for the exponent T_n, which differs by switching from $3D$ Mott ($n = 1/4$) to Efros−Shklovskii regime ($n = 1/2$). Experimental measurements in disordered systems do reveal that the electron density of states (DOSs) may strongly vary in the vicinity of Fermi level, and it seems reasonable to suggest that the theoretical concept of uniform DOSs near the Fermi level is certainly insufficient to describe conduction mechanisms which account for the Coulomb gap, as there is a jump in the electron DOSs due to Coulomb interactions between localized states. In general, one can write down

$$k_B T_n = \begin{cases} c_p / \left(g(\varepsilon_F) \xi^3 \right), & \text{for } n = 1/4 \\ e^2 / (4\pi\varepsilon_0 \varepsilon_r \xi), & \text{for } n = 1/2 \end{cases} \tag{2.12}$$

[5]

where $k_B = 1.38 \times 10^{-23}$ J/K and $\varepsilon_0 = 8.85 \times 10^{-12}$ F/m, while ξ stands for the localization length of electron wave function of the surface states. c_p represents the percolation constant varying from 5 to 20. ε_r corresponds to the relative permittivity constant. Nevertheless, even when the DOSs is not constant, the $3D$ Mott VRH conductivity pattern is fully recovered if presented like Eq. (2.9), but is rather referred to as the $3D$ Efros−Shklovskii VRH [38] when n is, in particular, equal to $1/2$. In Ref. [41], a few temperature dependencies of the hopping conductivity, which come under exponent $1/4$ or $1/2$, are presented and the reader is further redirected to this reference to properly infer the validity of use of VRH at high temperatures in disordered materials.

Nanoscaled $BiFeO_3$ puts itself forward as a suitable candidate for exploring the crossover from $1/2$ to $1/4$ exponent VRH conductivity as demonstrated in Ref. [1] based on the Raman spectra. More interesting is the fact that crystalline $BiFeO_3$ nanoparticles do not only undergo a crossover but even a pronounced phase transition at $\sim$640 K below which Coulomb correlations take place to form the antiferromagnetic ordering. Above the transition temperature, however, these correlations become overwhelmed by the temperature fluctuations through the concrete manifestation of the metallic-like paramagnetic state.

There is a presence of localized surface states occupying the energies near the Fermi level in the $BiFeO_3$ nanomaterial. These states through a mediation back the VRH transport even over a broad range of temperature. Temperature variations of $\ln(1/\tau)$, which is proportional to $\ln(\sigma)$ based on the Einstein relation from Eq. (2.8) are linearized against T^{-n} in Fig. 2.4A with $n = 1/2$ and Fig. 2.4B with $n = 1/4$, in the strongly correlated ($T < T_N$) and paramagnetic phase ($T > T_N$), respectively. Relying on the calculation for $\varepsilon_r \approx 28$ from the impedance dielectric spectroscopy of $BiFeO_3$ nanoparticles [42] and following (12) one can find that $\xi \approx 7$ nm, while the DOSs $g(\varepsilon_F)$ in the high-temperature phase nearly amounts 2.1×10^{18} localized states per (eV $\times$ cm^3). The result $\xi \approx 7$ nm is physically meaningful since $\xi < \langle \ell \rangle$, where the average particle size $\langle \ell \rangle \approx 66$ nm has been computed from the Gaußian particle size distribution recorded by Scanning Electron Microscopy at room temperature on $BiFeO_3$ (Fig. 2.4C and D). Finally, $\rho = 1/\sigma \approx 4\pi^2\tau/\left(\langle \ell \rangle^2 e^2 g(\varepsilon_F)\right) \approx 350$ mΩcm, which stands for an extraordinarily high value that is not commonly encountered in conventional metals. This value goes beyond the maximum resistivity value ($\sim$1 mΩcm) limited by the Mott-Ioffe-Regel criterion [43,44], which categorizes crystalline $BiFeO_3$ nanoparticles into a family of bad conductors and ultimately suggests that the conduction bands are vanishing. This eliminates any possibility for the fixed thermally activated transport generic to intrinsic semiconductors to dominate over $3D$ VRH.

[5]

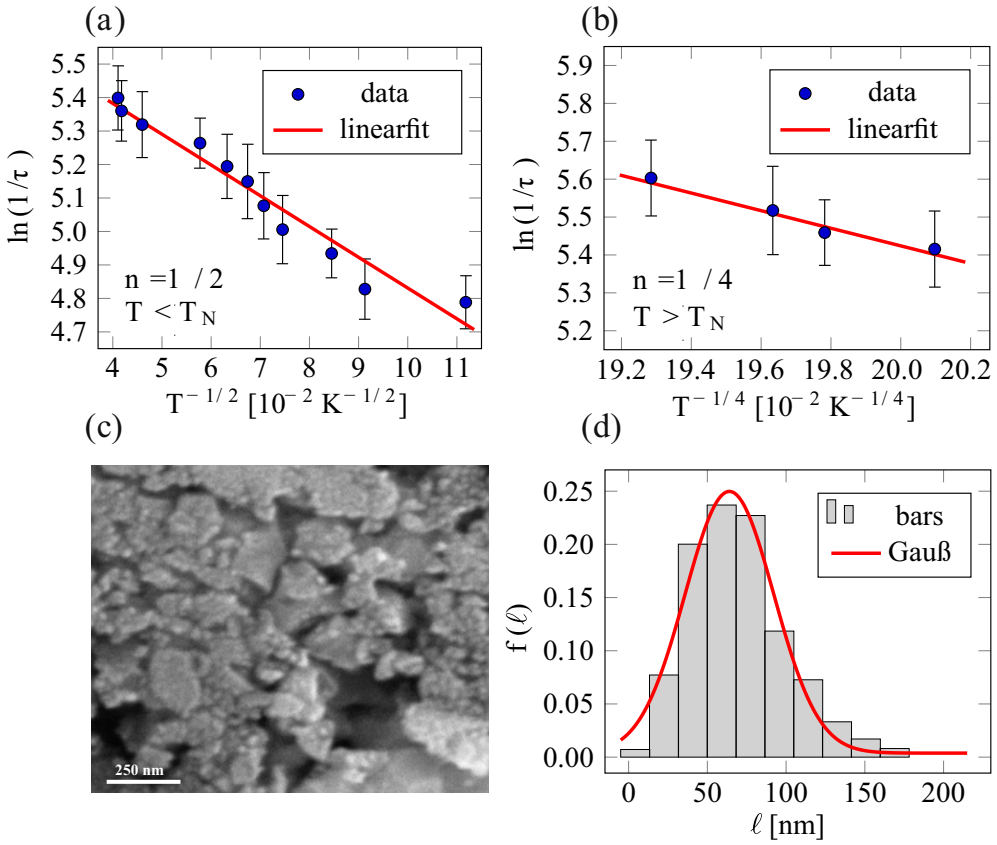

Figure 2.4

The dependence (T^{-n}) versus ($\ln(1/\tau)$) in both paramagnetic phase (subfigure (A), $n = 1/2$) and antiferromagnetic phase (subfigure (B), $n = 1/4$) with the linear fitting curves given in red. The surface morphology of the nanocrystalline $BiFeO_3$ particles made with TESCAN SM-300 (subfigure (C)) and the corresponding histogram of the distribution of the particle size given in gray, fitted by the Gauβ distribution (red line), where (64 ± 2) nm is mean value and (28 ± 2)nm is standard deviation (subfigure (D)). The frequency of occurrence is labeled as $f(\ell)$. *The entire figure is taken from D.M. Djokić, B. Stojadinović, D. Stepanenko, Z. Dohčević-Mitrović, Probing charge carrier transport regimes in $BiFeO_3$ nanoparticles by Raman spectroscopy, Scr. Mater. 181 (2020) 6–9.* https://doi.org/10.1016/j.scriptamat.2020.02.008.

In certain disordered semiconductors, Ioffe and Regel [45], as well as Mott [46], have altogether realized that conduction states pertinent to such systems fail to survive due to the indefinite reduction in free mean path of carriers that scatters by. The key argument is that it can never become shorter than the typical interatomic spacing. In this case, the concept of carrier velocity cannot be properly formulated, and the entire coherent quasiparticle motion is lost. The notion of a minimum metallic conductivity is actually in accordance with a minimum mean free path.

[5]

Generally, the choice of 3*D* VRH ought to be provisionally accepted as an assumption. In the case of $BiFeO_3$ nanoparticles, the existence of the Mott VRH mechanism has already been deduced from the DC/AC measurements. These results are presented in Ref. [27]. Furthermore, the assumption about the validity of VRH is substantiated by the fact that the estimated resistivity value ultimately exceeds the Mott-Ioffe-Regel maximum ($350\ m\Omega cm \gg 1\ m\Omega cm$). This implies that the conduction band energy sector tends to fade away leaving no room for the fixed thermally activated transport to prevail, which typically requires a markedly high density of conduction band states. Therefore, the $BiFeO_3$ nanoparticles are safe to be termed as bad conductors that retain metallic behavior, through qualitative features such as temperature evolution. Quantitatively, however, the bad conductors very much resemble the electric insulators as was observed in Ref. [1]. Specifically, the $BiFeO_3$ nanoparticle shell exhibits metallic behavior whereas the core insulator one, which is a case in defective nanoparticles with a core/shell structure.

3. Infrared reflection

3.1 Short introduction to infrared reflection technique

Infrared solid state spectroscopy stands for one of the most powerful and versatile techniques meant for optically probing a diverse family of materials in a contactless manner. The IRR response can assume either a purely electronic or a purely LV character. The two cases have distinctly different approaches to the quantitative treatment of the interaction processes between the radiation field and matter. The latter has conclusively proven powerful for analyzing propagating vibrations with which crystal structures can be revealed in ionic crystals and polar semiconductors. This analytical probe is highly useful even for systems poor in the degree of crystallinity, which is oftentimes encountered in nanoscopic matter.

In the long-wave limit ($q \approx 0$), optically active vibrations of an ionic bipartite lattice encapsulate the motion of one type of atoms relative to that of the other sublattice, yet both in spatial phase. The natural concomitants of such motions comprise strong electric dipoles of the material that can, accordingly, be directly coupled with the external electric field at a given polarization angle of the incident electromagnetic radiation. The theory of the IRR response originating form the interaction between the radiation field and the matter is purely phenomenological and can be found elsewhere [4,47,48], based on Maxwell's and the macroscopic equations describing the vibrations in a polar material. The reflective IRR spectroscopic recoil begins with a singularity in the dielectric function observed at the transverse optical (TO) frequency of the polar phonon mode. The singularity occurs as the radiation field of the incident electromagnetic wave couples with the TO phonon mode. Coulombic force effects in the polar crystal shift the LO mode to higher energies in contrast to the TO mode. The TO mode has a complex pole of the

complex dielectric response function $\widetilde{\varepsilon}(\omega)$, whereas the LO mode is associated with a complex zero of $\widetilde{\varepsilon}(\omega)$. Consequently, the incident infrared electromagnetic waves at frequencies over the so-called *reststrahlen* TO-LO window are dispersed in such a way that they fail to propagate through the condensed medium, but undergo reflection. In an ideal polar crystal with undamped oscillators, the frequency selective reflectivity amounts exactly 100%, but the reality is rather followed with the oscillator damping. Formally, the reflectivity is given by the Fresnel formula

$$R(\omega) = \left|\frac{\widetilde{n}(\omega) - 1}{\widetilde{n}(\omega) + 1}\right|^2 = \frac{(n(\omega) - 1)^2 + \kappa^2(\omega)}{(n(\omega) + 1)^2 + \kappa^2(\omega)}, \tag{2.13}$$

where $R(\omega)$ is the frequency-dependent fraction of light intensity reflected. Complex frequency dependent index of refraction, $\widetilde{n}(\omega)$, is related to the complex dielectric response as

$$\widetilde{n}(\omega) = n(\omega) - i\kappa(\omega) = \sqrt{\widetilde{\varepsilon}(\omega)}. \tag{2.14}$$

The frequency dependent real part, $n(\omega)$, and imaginary part, $\kappa(\omega)$ as the extinction coefficient, of the complex refractive index $\widetilde{n}(\omega)$ satisfy the following relationships

$$\varepsilon_1(\omega) = n(\omega)^2 - \kappa(\omega)^2 \quad \text{and} \quad \varepsilon_2(\omega) = 2n(\omega)\kappa(\omega), \tag{2.15}$$

where finally

$$\widetilde{\varepsilon}(\omega) \equiv \varepsilon_1(\omega) + i\varepsilon_2(\omega). \tag{2.16}$$

For this reason, it is of uppermost importance to model, as well as, parametrize $\widetilde{n\varepsilon}(\omega)$ that properly describe the system probed by the IRR technique.

IRR signal of poorly conductive ionic crystals with large splitting between TO and LO frequencies is commonly fitted with a complex dielectric function given by the following expression

$$\widetilde{\varepsilon}(\omega) = \varepsilon_\infty \prod_j \frac{\omega_{\mathrm{LO}j}^2 - \omega^2 + i\omega\gamma_{\mathrm{LO}j}}{\omega_{\mathrm{TO}j}^2 - \omega^2 + i\omega\gamma_{\mathrm{TO}j}}, \tag{2.17}$$

where $\omega_{\mathrm{LO}j}$ and $\omega_{\mathrm{TO}j}$ are longitudinal and transverse frequencies of the j-th oscillator, respectively, while $\gamma_{\mathrm{TO}j}$ and $\gamma_{\mathrm{LO}j}$ are their energy dampings, and ε_∞ corresponds to the high-frequency dielectric constant ($\omega \to \infty$). This model presents four tunable parameters for each TO/LO mode and is employed for description of purely phononic spectra. The model is familiarly known as the LV model, or habitually, four-parameter factorized form of the dielectric function. Its major disadvantage consists in the fact that it considers no contribution from the itinerant electronic excitations, neither single particle nor collective [49].

[5]

However, a great deal of semiconductors has a sizable portion of itinerant charge carriers. Accordingly, the full description of the infrared optical reflectivity data of such materials has to allow for both phonon and electronically collective (plasmon) excitations. The cohabitation between the phonons and plasmons brings inexorably about a somewhat pronounced interaction between the plasmons and LO phonons. This effect becomes the most striking if the plasma frequency ω_P lies situated close to the LO phonon energy. In this case, the complex dielectric function [50] can be factorized to read as follows

$$\widetilde{\varepsilon}(\omega) = \varepsilon_\infty \frac{\prod_{j=1}^{m+n}\left(\omega^2 + i\omega\gamma_{\mathrm{LO}j} - \omega_{\mathrm{LO}j}^2\right)}{\omega^m \prod_{j=1}^{m}\left(\omega + i\gamma_{P_j}\right)\prod_{j=1}^{n}\left(\omega^2 + i\omega\gamma_{\mathrm{TO}j} - \omega_{\mathrm{TO}j}^2\right)}, \tag{2.18}$$

where $\omega_{\mathrm{TO}j}$ and $\gamma_{\mathrm{TO}j}$ are frequencies and damping of the TO modes, respectively. γ_P represents the plasma damping rate. The equation directly expresses the coupled plasmon-LO phonon frequencies $\omega_{\mathrm{LO}j}$ and damping rates $\gamma_{\mathrm{LO}j}$. This model is in literature termed as the coupled plasmon-phonon (CPP) model.

In conducting oxides [48], on the other hand side, the Drude model can be employed with no coupling for fitting the infrared reflectivity spectra. The plasmon contribution to the complex dielectric function is expressed through the Drude term so that $\widetilde{\varepsilon}(\omega)$ is composed of two additive terms in the following manner

$$\widetilde{\varepsilon}(\omega) = \varepsilon_\infty \left(\prod_j \frac{\omega_{\mathrm{LO}j}^2 - \omega^2 + i\omega\gamma_{\mathrm{LO}j}}{\omega_{\mathrm{TO}j}^2 - \omega^2 + i\omega\gamma_{\mathrm{TO}j}} - \frac{\omega_P^2}{\omega(\omega - i\gamma_P)} \right). \tag{2.19}$$

The first product term is concerned with the pure phonon contribution, while the second term represents the contributions originating from the collective electronic excitations—plasmons. The $\omega_{(\mathrm{TO/LO})j}$ and $\gamma_{(\mathrm{TO/LO})j}$ are (TO/LO) frequencies and the related damping rates of the decoupled phonon modes. The ω_P and γ_P are the plasma frequency and its daping rate. This model brings us a material advantage in decoupling the phonon from the plasmon contributions, and is called the decoupled plasmon-phonon (DPP) model. Besides the aforementioned "classical" Drude term, sometimes the so-called Double-damped Drude term is used, as is given in

$$\widetilde{\varepsilon}(\omega) = \varepsilon_\infty \left(\prod_j \frac{\omega_{\mathrm{LO}j}^2 - \omega^2 + i\omega\gamma_{\mathrm{LO}j}}{\omega_{\mathrm{TO}j}^2 - \omega^2 + i\omega\gamma_{\mathrm{TO}j}} - \frac{\omega_P^2 + i(\gamma_P - \gamma_0)\omega}{\omega(\omega - i\gamma_0)} \right). \tag{2.20}$$

The difference between the dynamic damping (γ_P) at plasma frequency and the static damping (γ_0) at zero frequency represents particular distinctiveness of this model. The second term in the additive form of $\widetilde{\varepsilon}(\omega)$ turns into the classical Drude term once

[5]

$\gamma_P = \gamma_0$. The use of this model, which is also called DPP, provides more flexibility. In fact, a rather precise description of the parametrized complex dielectric function is offered by the model in numerical fittings based on it.

As with nanomaterials, the related IRR spectra can be properly analyzed using the Bruggeman effective medium approximation [51]. The basic Bruggeman model includes the influence of porosity as

$$\left(\frac{\widetilde{\varepsilon}(\omega) - \widetilde{\varepsilon}_{\text{eff}}\ (\omega)}{\widetilde{\varepsilon}(\omega) + 2\widetilde{\varepsilon}_{\text{eff}}\ (\omega)}\right)\widetilde{f} + \left(\frac{1 - \widetilde{\varepsilon}_{\text{eff}}\ (\omega)}{1 + 2\widetilde{\varepsilon}_{\text{eff}}\ (\omega)}\right)\left(1 - \widetilde{f}\right) = 0. \tag{2.21}$$

A decrease of the powder volume fraction as compared to the ambient air leads to a decrease in the reflectivity values, and thence the IRR features may become significantly broadened if there is a greater air fraction in the powder. For the binary material with a great degree of inhomogeneity, constituted of the material $\widetilde{\varepsilon}(\omega)$ and air ($\varepsilon_{\text{air}} = 1$) with the volume fractions $\widetilde{f}$ and $1 - \widetilde{f}$, respectively, the empirical relation for the complex effective dielectric function $\widetilde{\varepsilon}_{\text{eff}}\ (\omega)$ must obey the above-written equation.

3.2 Doped nanocrystalline CeO_2

As one of the most stable oxide of cerium, cerium dioxide CeO_2 is considered to be highly important functional material with outstanding applications in many various fields. It crystallizes into a fluorite face centered cubic structure with space group F_{m3m} (No. 225) to form a simple cubic oxygen suba lattice where the cerium ions occupy alternate cube centers (see Fig. 2.5A) [52]. In terms of Wyckoff positions, Ce atoms are located at the centers of the tetrahedrons (4a) (0,0,0) of which corners are populated with

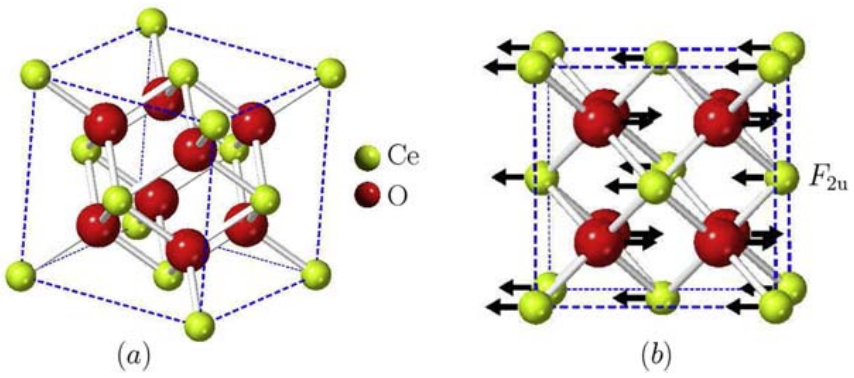

Figure 2.5
The fluorite face centered cubic crystal structure of CeO_2 (A) and its normal mode of the infrared active lattice vibrations of (B). Ce ions are denoted in green, while O ions are denoted in red.

[5]

oxygen ions (8c) (1/4, 1/4, 1/4). Observing the existence of the center of inversion, the structure has exactly one IRR (F_{2u}) and one Raman (F_{2g}) active mode [32], both of which are triple degenerated. As is shown in Fig. 2.5B, the normal mode of the infrared optically active vibrations consist of motions of both Ce and O atoms, but in the opposite directions.

Nanocrystalline CeO_2 is distinguished by its enhanced electric conductivity, size lattice relaxation, as well as, many other advantages to bulk CeO_2. As to what has been reviewed in Ref. [53], decreasing particle size of crystalline CeO_2 particles down to nanoceria dioxide crystals results in the formation of oxygen vacancies which can be further employed as descriptors for determining the valence state of Ce in the nanoparticles. Actually, the large surface to volume ratio, then the inclination toward the oxygen consumption, and basically, freeing Ce because of the reversible transition between Ce^{3+} and Ce^{4+} ions altogether lead to enormous catalytic capacity of this material. Nanoscaled CeO_2 is furthermore found applicable to the active area of research for renewable energy, solid oxide fuel cells, water and air purification, optical glass polishing and decolorizing, UV ray filters, and many others [53].

Doped nanocrystalline CeO_2, however, deserves a special attention as the optimal doping with Cu or Nd has proven efficient in inducing the semiconductor-to-metallic state crossover [2,52] in nanoceria dioxide. Moreover, electrons localized at the vacancies may behave like free charge carriers to contribute drastically to the electrical conductivity [54]. This originates from the presence of free charge carriers, which are numbered in the nanoceria lattice, as the number of oxygen vacancies becomes increased by Nd content [55].

Following Ref. [2], the IRR spectroscopy has been applied to nondestructively investigate the mechanism of the influence of the plasmon due to the enhanced conductivity upon the phonon spectra with increasing Nd content in nanocrystalline CeO_2 This material is a polar semiconductor so that both phonon and plasmon excitations can be registered in the IRR spectra, whereby the plasmon-phonon coupling mechanism can be explored, while the extent to which the system acquires metallicity can be assessed. Radović et al. [2] have recorded the infrared reflectivity spectra on pure and Nd-doped CeO_{2-y} nanopowders at ambient temperature in far-infrared region from 100 up to 700 cm^{-1}.

Fig. 2.6 shows the IRR spectra of undoped and Nd-doped CeO_{2-y} nanopowders fitted with the two models: coupled plasmon-phonon and decoupled plasmon-phonon with double-damped Drude term. The concentration of the dopant is increased from 0% to 25%. The IRR spectra markedly differ from those done on bulk CeO_2, as the bulk reststrahlen region is split into two extended TO-LO modes over 200−550 cm^{-1} range with decreasing crystallite size. The splitting is more pronounced in samples with rather small crystallite sizes and is accompanied with the redshift of the two LO modes, as well. Also, one can

[5]

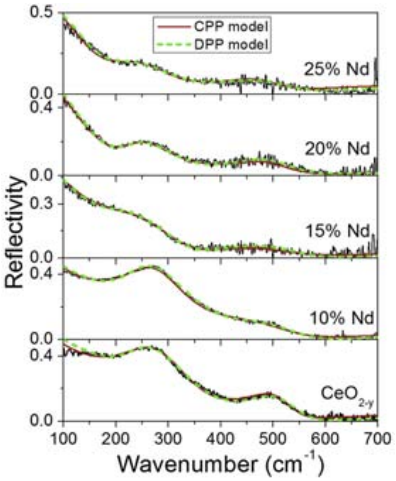

Figure 2.6

Infrared reflectivity spectra of undoped and Nd-doped CeO_{2-y} nanopowders involving the two theoretical fits based on coupled plasmon-phonon and decoupled plasmon-phonon model. *The credits for the figure are given to M. Radović, Z. Dohčević-Mitrović, N. Paunović, S. Bošković, N. Tomić, N. Tadić, I. Belča, Infrared study of plasmon-phonon coupling in pure and Nd-doped CeO_{2-y} nanocrystals, J. Phys. D Appl. Phys. 48 (2015) 065301–065306. https://doi.org/10.1088/0022-3727/48/6/065301.*

notice that with the raise of the dopant concentration, the low energy Drude tail and the screening of the phonon modes became more and more prominent, due to the strong presence of the free charge carriers. In the actual fact, increasing Nd content in the nanoceria dioxide lattice can generate a huge number of oxygen vacancies [2], while the plasmon-phonon interaction in the Nd-doped samples gets stronger.

Following the fits based upon both models applied (Fig. 2.6), all the plasmon modes registered in all nanoceria dioxide samples exhibit a frequency decrease with Nd doping, as can be seen from Fig. 2.7. The shift in the plasma frequency toward lower energies with increasing Nd concentration occurs owing to the weighted effective charge carrier mass, as there is no dopant impact on the free carrier concentration [2]. In fact, the plasma frequency is inversely proportional to the effective electron mass. This feature, together with the enhanced plasmon-phonon coupling with Nd doping, affords us a better insight into the transport properties of crystalline nanoceria based on the infrared-derived optical conductivity [48].

4. Electron spin resonance

4.1 Short introduction to electron spin resonance technique

ESR exemplifies a very sensitive and informative experimental technique, based on the use of magnetic field, which continues to find countless applications not only in solid state and

[5]

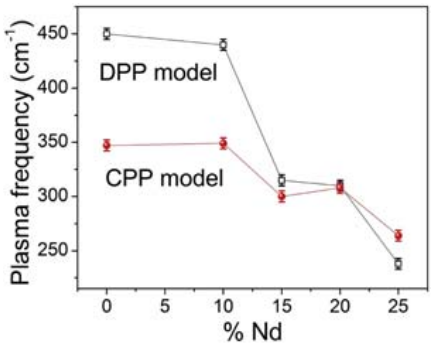

Figure 2.7

Evolution of the plasma frequency with the increased Nd dopant concentration as inferred from the two models: coupled plasmon-phonon and decoupled plasmon-phonon. *The credits for the figure are given to M. Radović, Z. Dohčević-Mitrović, N. Paunović, S. Bošković, N. Tomić, N. Tadić, I. Belča, Infrared study of plasmon-phonon coupling in pure and Nd-doped CeO_{2-y} nanocrystals, J. Phys. D Appl. Phys. 48 (2015) 065301–065306.* https://doi.org/10.1088/0022-3727/48/6/065301.

nano, but also in biomedical and environmental sciences. By means of ESR spectroscopy, one is able to directly probe electron spin response at resonance that certainly makes ESR as one of the most powerful probe to investigate magnetic properties in various compounds. More interestingly, ESR stands for both noninvasive and contactless tool with ability to analyze accurately the nature and dynamics of charge carriers in conductive systems no matter how their geometry welcomes electrical leads and contacts in an electrical circuit.

Familiarly known as CESR in abbreviated term, conduction electron spin resonance has captivated much scientific attention for its capacity to measure the electrical conductivity of systems from bulk over microsized down to nanoscopic conducting materials. In the actual fact, in the conducting systems, the free electron motion exerting eddy current leaves an impact upon the recorded signal at resonance through asymmetry as the definite signature. This was originally recognized by Feher and Kip [56], Dyson [57] who put forward that asymmetric CESR lineshapes originate as linear combinations due to the two facts: (1) the attenuation of the AC field through the skin depth and (2) the capability of itinerant electrons to diffuse backward and forward through the skin depth region in many instances between consecutive spin flips that is only critical to transmission-based CESR techniques. In the case of transmissive CESR, magnetization can penetrate far deeply into metals unlike the AC magnetic field. This gives an extra contribution to enhancing the asymmetry of the signals at resonance [58,59].

Dating back to the 1950′s, Freeman John Dyson is the first in the field to be credited with fully deriving the asymmetric CESR profiles. For the obvious reasons, such CESR lines are referred in literature to as Dysonians of which asymmetry extent is oftentimes quantified using A/B ratio (see the inset in Fig. 2.8), as common signature of metallicity in CESR experiments.

[5]

As with CESR operating in the reflection mode, Chapman et al. [61] developed an approach based on Dyson's theory to grasp both on- and off-resonance signal for the various crystal shapes, such as flat plates, long cylinders, and spheres. This allows the prediction of the asymmetric nature of CESR absorption profiles depending on geometry of the conducting samples with different size. Furthermore, Platzman and Wolf [62] examined spin waves excitations at resonance in paramagnetic metals that are described within the frame of Fermi-liquid theory. Their extended theory boils down to Dyson's in the limit of short momentum relaxation times. Dyson's theory was additionally generalized to involve various shapes of conducting crystals at desirable resonant magnetic field directions [63–65]. Later on, Kaplan pointed out that there is a substantial discrepancy between Dyson's theory and experimental results recorded in CESR based on the reflection mode [66]. Actually, CESR becomes recoiled rather with electric than magnetic component of the frequency-dependent electromagnetic field. The component of electric field is known to get easily coupled with the free electron momentum across the surface via relativistic spin-orbit interaction. This fact finds its application in the quantum mechanical density matrix method, which ultimately brings about the rather general form of CESR signal as [67]:

$$\chi''(\omega)\cos\phi + \chi'(\omega)\sin\phi. \tag{2.22}$$

Terms χ'' and χ' represent the absorptive and dispersive parts of the CESR signal. The magnitudes of their contributions are measured with $\cos\phi$ and $\sin\phi$, respectively, both of which disappear in the limit of highly conductive samples, where ϕ is the signal phase. Eq. (2.22) does represent a particular manifestation of Dysonian, which falls into the range of the so-called "NMR limit" [68,69]. In that case, the electron diffusion rate is considerably slower as compared to the spin relaxation rate, and there is no need to consider other limits so as to reasonably infer CESR spectra of usual metallic samples. Spin dynamics itself as regards this case can lead to nothing but Lorentzian-profiled absorptions (χ''), unlike the situations with reduced dimensionality or motionally narrowed signals [70,71].

In a recent CESR study [60], the authors have favored Kaplan's approach, made for analyzing the CESR lineshape, to impart a valuable piece of information on the conductivity of samples with different geometries. Key lengths and points of CESR lines, necessary for simplification of a fitting procedure of CESR lineshape, have been established in this account to analytically derive, as well as, grasp the geometry independent asymmetry ratio limit $A/B \rightarrow (5+3\sqrt{3})/4$, encountered in literature as universal 2.55 limit, when the CESR is carried out on extremely conducting samples. A/B ratio value markedly evolves once nano- or microsized metallic samples start to agglomerate into larger ones that makes the CESR technique especially helpful in

[5]

monitoring the extent to which the clustering takes place [72,73]. Moreover, in Ref. [60], the phase dependence of the asymmetry ratio A/B is given as

$$A/B = \frac{\left(1+2\cos\frac{2\phi}{3}\right)\left(3\cos\left(\frac{\pi}{6}-\frac{\phi}{3}\right)+\sin\phi\right)}{4\cos\left(\frac{\pi}{6}-\frac{\phi}{3}\right)\left(1+\sin\left(\frac{\pi}{6}-\frac{2\phi}{3}\right)\right)^2}, \tag{2.23}$$

which can be further employed to relate A/B with the conductivity. Namely, Chapman et al. [61] introduced the parameter $\eta \equiv d/\delta$, where d represents the characteristic length od the sample (thickness or diameter), while δ is the skin depth at given resonant frequency. It is exactly this quantity that is in correlation with the sample conductivity. The absorptive and dispersive parts of the CESR signal in Ref. [61] are respectively $x(\eta)$ and $y(\eta)$ so that $y(\eta)/x(\eta)$ exactly corresponds to $\tan\phi$ in Ref. [60]. According to Ref. [61], $x(\eta)$ and $y(\eta)$ for the three relevant geometries look like

$$\text{Plate} \Rightarrow \begin{cases} x(\eta) = \dfrac{\sinh(\eta)+\sin(\eta)}{2\eta(\cosh(\eta)+\cos(\eta))} + \dfrac{1+\cosh(\eta)\cos(\eta)}{(\cosh(\eta)+\cos(\eta))^2}, \\ y(\eta) = \dfrac{\sinh(\eta)-\sin(\eta)}{2\eta(\cosh(\eta)+\cos(\eta))} + \dfrac{\sinh(\eta)\sin(\eta)}{(\cosh(\eta)+\cos(\eta))^2}. \end{cases} \tag{2.24}$$

$$\text{Cylinder} \Rightarrow \begin{cases} x(\eta) = 1 - \dfrac{2(\text{Ber}(\vartheta)\text{Ber}'(\vartheta)+\text{Bei}(\vartheta)\text{Bei}'(\vartheta))(\text{Ber}(\vartheta)\text{Bei}'(\vartheta)-\text{Ber}'(\vartheta)\text{Bei}(\vartheta))}{\left(\text{Ber}^2(\vartheta)+\text{Bei}^2(\vartheta)\right)^2}, \\ y(\eta) = \dfrac{\left(\text{Ber}^2(\vartheta)-\text{Bei}^2(\vartheta)\right)\left(\text{Bei}'^2(\vartheta)-\text{Ber}'^2(\vartheta)\right)-4\text{Ber}(\vartheta)\text{Bei}(\vartheta)\text{Ber}'(\vartheta)\text{Bei}'(\vartheta)}{\left(\text{Ber}^2(\vartheta)+\text{Bei}^2(\vartheta)\right)^2}, \\ \text{where } \vartheta \equiv \eta/\sqrt{2}. \end{cases} \tag{2.25}$$

$$\text{Sphere} \Rightarrow \begin{cases} \dfrac{4}{9}x(\eta) = \dfrac{8+\eta^4}{\eta^4} - \\ \dfrac{8(\sinh(\eta)+\sin(\eta))}{\eta^3(\cosh(\eta)-\cos(\eta))} + \dfrac{8\sinh(\eta)\sin(\eta)}{\eta^2(\cosh(\eta)-\cos(\eta))^2} + \dfrac{\sinh(\eta)-\sin(\eta)}{\eta(\cosh(\eta)-\cos(\eta))} - \dfrac{\sinh^2(\eta)-\sin^2(\eta)}{(\cosh(\eta)-\cos(\eta))^2}, \\ \dfrac{4}{9}y(\eta) = \\ \dfrac{8(\sinh(\eta)-\sin(\eta))}{\eta^3(\cosh(\eta)-\cos(\eta))} - \dfrac{4\left(\sinh^2(\eta)-\sin^2(\eta)\right)}{\eta^2(\cosh(\eta)-\cos(\eta))^2} + \dfrac{\sinh(\eta)+\sin(\eta)}{\eta(\cosh(\eta)-\cos(\eta))} - \dfrac{2\sinh(\eta)\sin(\eta)}{(\cosh(\eta)-\cos(\eta))^2}. \end{cases} \tag{2.26}$$

[5]

This set of the three dependencies allows us to compute A/B versus $\log\eta$ as is presented in Fig. 2.8. Oftentimes, A/B can be expended in the form of the linear approximation with respect to either η or is proportional to the conductivity of the probed spins. The latter approximation works well in the case of the carbon nanotubes [3] of which CESR-based charge carrier transport is going to be discussed in detail throughout the upcoming section.

4.2 Carbon nanotubes

As a building brick that takes fascinating variety of forms such as diamond, fossil fuels, and graphite, together with innumerable compounds derived from it, carbon stands for one of the most impressive elements in the periodic table. Increased focus of renewed scientific interest in carbon has stepped into the realm of novel carbon-based materials, specifically known as the carbon allotropes at nanoscopic level, such as carbon nanotubes. These were first discovered as multiwalled forms by Iijima in 1991 [74] initiating the golden era of the physics and chemistry of carbon nanostructures. Carbon nanotubes are distinguished by their outstanding electronic, mechanical, and transport properties revealing uncorrelated (semi)conducting nature of the tubes in relation to the curvature and chirality. They also prove suitable for various applications which spam from the use as light and electron emitters [75] up to optical biosensors for life sciences and biomedicine [76].

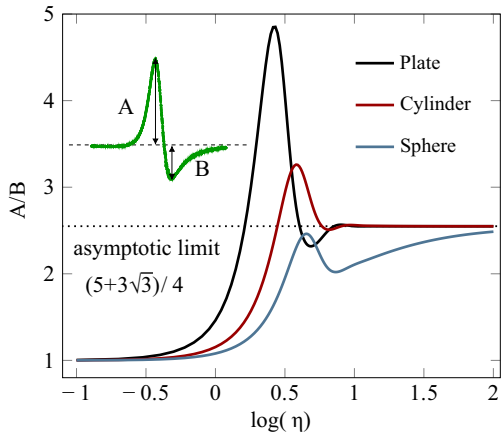

Figure 2.8

Asymmetry ratio A/B dependence on $\log(\eta)$ regarding the three relevant geometries: infinite plate (black), long cylinder (dark red), and sphere (dark blue). All the three curves converge to the asymptotic A/B ratio of $(5+3\sqrt{3})/4$ at $\eta\to\infty$. The inset represents graphically the A/B ratio in an arbitrarily selected CESR line. *The figure is adopted from D.M. Djokić, D. Stepanenko, Z. Dohčević-Mitrović, Extreme conduction electron spin resonance: $A/B\to(5+3\sqrt{3})/4$, the universal limit of lineshape asymmetry ratio, J. Magn. Magn. Mater. 491 (2019) 165616. https://doi.org/10.1016/j.jmmm.2019.165616.*

[5]

Even with the aid of nanoscaled technologies, making ideal electric contacts to adequately probe nanotube conductivity remains a perplexing puzzle. Electron backscattering, imbalanced injection of incident electron modes, and high-ohmic contact resistance are identified as the chief culprits at minuscule dimensions. However, nanotubes with large diameters have the added advantage of favoring low-ohmic contact resistance in a four-probe electric measurement [77]. This made them perfectly suited for the investigation of quantum interference caused by the Aharonov−Bohm effect specific by the pronounced magneto-resistance oscillations as a function of magnetic flux [78].

Despite their short diameters, transport electric properties of multiwalled nanotubes oftentimes remain consistent with theoretical models used to describe disordered conductors in $2D$. This might be explained by the fact that the electron wavelength is quite smaller than the nanotube diameter [79]. On the other hand side, one-dimensional essence of carbon nanotubes becomes already evident through specific heat and thermal lattice conductivity measurements since the phonon wavelength exceeds typical nanotube diameters [80], unlike the before-mentioned electron wavelength. Moreover, according to Ref. [81], it has been demonstrated that the electric transport in single walled carbon nanotubes exhibit a dependence in agreement with Luttinger liquid models.

Temperature and power-dependent CESR on an ensemble of metallic SWCNTs have been performed to infer their transport properties based on the insights into the spin dynamics [3]. The powder-form samples comprised acid-purified laser-oven SWCNTs which were prepared using the standardized annealing procedure, while the related CESR spectra were recorded as a function of temperature from 3.4 K to the ambient temperature at the X-band spectrometer. To yield a rather detailed insight into the transport mechanism, the authors of Ref. [3] studied the temperature evolution of the asymmetry Dysonian line shape parameter, $\alpha \equiv A/B$, which is to the first order approximation proportional to the conductance of the probed electron spins. These can relax by interaction with itinerant electrons that are present in metallic SWCNTs. In addition, the spin dephasing rate at resonance narrows with increasing temperature, which is a signature of the motional narrowing, a phenomenon that is particular to metallic systems.

Temperature dependence of the natural logarithm of conductivity, $\ln(\sigma)$ which in this case boils down to $\ln(\alpha)$, is oftentimes plotted versus n-th root of inverse temperature [41]. Exponent n provides information on the charge carrier transport mechanism and when n approaches $1/4$, it leaves a hallmark of 3D Mott VRH transport mechanism [37].

As shown in Fig. 2.9, the Dysonian asymmetry parameter tends to follow a three-dimensional variable-range hopping behavior at low T. From the scaling relationships in Eq. (2.12), the localization length of the electronic wave function, ξ, is roughly estimated to be $\sim$100 nm, whereas the DOSs $g(\varepsilon_F)$ amounts $\sim 10^{19}$ localized states per (eV $\times$ cm^3)

[5]

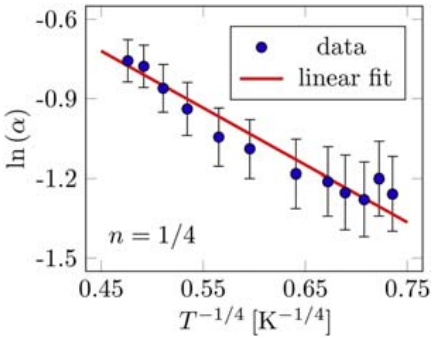

Figure 2.9

Natural logarithm of the asymmetry parameter, $\alpha \equiv A/B$, graphed versus the fourth root of inverse temperature. The logarithm is found to undergo the 3D VRH mechanism. *The data are taken from W.D. Rice, R.T. Weber, P. Nikolaev, S. Arepalli, V. Berka, A.L. Tsai, J. Kono, Spin relaxation times of single-wall carbon nanotubes, Phys. Rev. B 88 (2013) 041401–041405. https://doi.org/10.1103/PhysRevB.88.041401.*

around the Fermi energy. The traditional four-point probe transport measurements on the similarly prepared SWCNT samples [3] have, to some extent, corroborated the present picture of the CESR observed 3D VRH at low *T*.

As with nanoscopic systems such as SWCNTs, one can even venture to state that the VRH conduction mechanism, owing to the localized edge/surface states positioned around Fermi level, may extend even over a wide range of temperatures [1]. At high temperatures, the conduction mechanism in bulk systems commonly runs intrinsically via thermal activation through conduction bands. On the other hand side, there are, as a rule, defect states across the nanotube surface, effectively making its pristine length quite short and comparable to nanoscaled dimensions (Fig. 2.10). In this case, the overlaps between the orbitals decrease to cause the bands to become less dense. This leads to the band splittings to eventually open up wide gaps at rather high energies. Bands that are high in energy have, therefore, tendency to fade away so does the conduction band, as contrary to an ideally pristine SWCNT. It is thus reasonable to adopt that VRH mechanisms may apply up to somewhat higher temperatures in defected nanotubes. Certainly, the intrinsic thermally activated transport via conduction band can be ignored comparing to the VRH due to the evanescent DOSs, as is given in Fig. 2.10.

5. Concluding remarks

In summary, noncontact measurements of transport have been evidenced to offer various advantages to studying novel nanoscopic materials such as: multiferroic crystalline $BiFeO_3$ nanoparticles, doped nanocrystalline CeO_2 used for fuel cell applications, as well as,

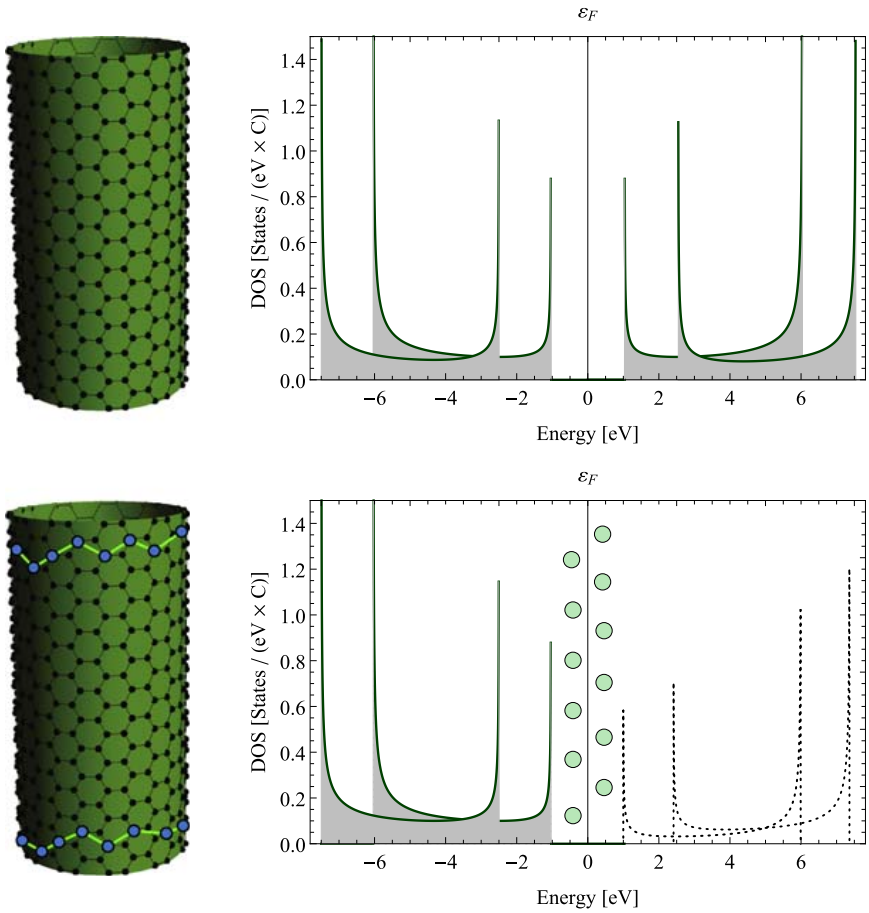

Figure 2.10

Plots of the electronic density of states versus energy for an ideally pristine (upper part) and a defected semiconducting SWCNT (lower part), computed using the tight-binding model. The electronic states of the defects forming the effective SWCNT edges are given in *green circles*. They are distributed around Fermi level at zero energy above which the DOS perishes gradually as the energy goes higher.

single walled carbon nanotubes exploited for molecular electronics and spintronics. The transport properties of these novel multifunctional materials have been reviewed in this chapter in the light of noninvasive spectroscopic techniques which involve: RS, IRR, and ESR. Through brief introductions made at the beginning of each section, these three contactless spectroscopic tools have been described in detail.

Acknowledgments

The authors greatly acknowledge funding provided by the Institute of Physics Belgrade, through the grant by the Ministry of Education, Science, and Technological Development of the Republic of Serbia.

[5]

References

[1] D.M. Djokić, B. Stojadinović, D. Stepanenko, Z. Dohčević-Mitrović, Probing charge carrier transport regimes in $BiFeO^3$ nanoparticles by Raman spectroscopy, Scripta Mater. 181 (2020) 6−9, https://doi.org/10.1016/j.scriptamat.2020.02.008.

[2] M. Radović, Z. Dohčević-Mitrović, N. Paunović, S. Bošković, N. Tomić, N. Tadić, I. Belča, Infrared study of plasmon-phonon coupling in pure and Nd-doped CeO^{2-y} nanocrystals, J. Phys. D Appl. Phys. 48 (2015) 065301−065306, https://doi.org/10.1088/0022-3727/48/6/065301.

[3] W.D. Rice, R.T. Weber, P. Nikolaev, S. Arepalli, V. Berka, A.L. Tsai, J. Kono, Spin relaxation times of single-wall carbon nanotubes, Phys. Rev. B 88 (2013) 041401−041405, https://doi.org/10.1103/PhysRevB.88.041401.

[4] S.S. Mitra, Infrared and Raman Spectra Due to Lattice Vibrations, Springer US, 1969, pp. 333−451, https://doi.org/10.1007/978-1-4757-1123-3_14.

[5] M. Cardona, Light Scattering in Solids I - Introductory Concepts, Springer-Verlag, Berlin), 1983.

[6] L.A. Falkovsky, Investigation of semiconductors with defects using Raman scattering, Phys. Usp. 47 (2004) 249−272, https://doi.org/10.1070/pu2004v047n03abeh001735.

[7] L.A. Falkovsky, Raman scattering of light by electrons in a metal with impurities, Sov. Phys. JETP 68 (1989) 661−663.

[8] A. Zawadowski, M. Cardona, Theory of Raman scattering on normal metals with impurities, Phys. Rev. B 42 (1990) 10732−10734, https://doi.org/10.1103/PhysRevB.42.10732.

[9] T.P. Devereaux, Theory for the effects of impurities on the Raman spectra of superconductors, Phys. Rev. B 45 (1992) 12965−12975, https://doi.org/10.1103/PhysRevB.45.12965.

[10] E.Y. Sherman, O.V. Misochko, Raman scattering in metals with disorder: beyond the zero-momentum approximation, J. Phys. Condens. Matter 15 (2003) 3751−3758, https://doi.org/10.1088/0953-8984/15/22/309.

[11] T.P. Devereaux, R. Hackl, Inelastic light scattering from correlated electrons, Rev. Mod. Phys. 79 (2007) 175−233, https://doi.org/10.1103/RevModPhys.79.175.

[12] A.A. Abrikosov, L.P. Gorkov, I.E. Dzyaloshinsky, Quantum Field Theoretical Methods in Statistical Physics, Pergamon Press, Oxford), 1965.

[13] H. Zhang, K. Kajiyoshi, Hydrothermal synthesis and size-dependent properties of multiferroic bismuth ferrite crystallites, J. Am. Ceram. Soc. 93 (2010) 3842, https://doi.org/10.1111/j.1551-2916.2010.03953.x.

[14] F. Kubel, H. Schmid, Structure of a ferroelectric and ferroelastic monodomain crystal of the perovskite $BiFeO_3$, Acta Crystallogr. B 46 (1990) 698, https://doi.org/10.1107/S0108768190006887.

[15] J.-G. Park, M.D. Le, J. Jeong, S. Lee, Structure and spin dynamics of multiferroic $BiFeO^3$, J. Phys. Condens. Mat. 26 (2014) 433202, https://doi.org/10.1088/0953-8984/26/43/433202.

[16] G. Catalan, J.F. Scott, Physics and applications of bismuth ferrite, Adv. Mater. 21 (2009) 2463−2485, https://doi.org/10.1002/adma.200802849.

[17] C.-H. Yang, D. Kan, I. Takeuchi, V. Nagarajan, J. Seidel, Doping $BiFeO^3$: approaches and enhanced functionality, Phys. Chem. Chem. Phys. 14 (2012) 15953, https://doi.org/10.1039/C2CP43082G.

[18] J.D. Bucci, B.K. Robertson, W.J. James, The precision determination of the lattice parameters and the coefficients of thermal expansion of $BiFeO_3$, J. Appl. Cryst. 5 (1972) 187−191, https://doi.org/10.1107/S0021889872009173.

[19] J.F. Ihlefeld, N.J. Podraza, Z.K. Liu, R.C. Rai, X. Xu, T. Heeg, Y.B. Chen, J. Li, R.W. Collins, J.L. Musfeldt, X.Q. Pan, J. Schubert, R. Ramesh, D.G. Schlom, Optical band gap of $BiFeO^3$ grown by molecular-beam epitaxy, Appl. Phys. Lett. 92 (2008) 142908, https://doi.org/10.1063/1.2901160.

[20] Y. Xu, M. Shen, Structure and optical properties of nanocrystalline $BiFeO^3$ films prepared by chemical solution deposition, Mater. Lett. 62 (2008) 3600, https://doi.org/10.1016/j.matlet.2008.04.006.

[21] A. Kumar, R.C. Rai, N.J. Podraza, S. Denev, M. Ramirez, Y.-H. Chu, L.W. Martin, J. Ihlefeld, T. Heeg, J. Schubert, D.G. Schlom, J. Orenstein, R. Ramesh, R.W. Collins, J.L. Musfeldt, V. Gopalan, Linear and nonlinear optical properties of $BiFeO_3$, Appl. Phys. Lett. 92 (2008) 121915, https://doi.org/10.1063/1.2901168.

[22] J. Allibe, K. Bougot-Robin, E. Jacquet, I.C. Infante, S. Fusil, C. Carrétéro, J.-L. Reverchon, B. Marcilhac, D. Creté, J.-C. Mage, A. Barthélémy, M. Bibes, Optical properties of integrated multiferroic $BiFeO^3$ thin films for microwave applications, Appl. Phys. Lett. 96 (2010) 182902, https://doi.org/10.1063/1.3402763.

[23] M. Shariq, D. Kaur, V.S. Chandel, M.A. Siddiqui, Investigation on multiferroic properties of $BiFeO^3$ ceramics, Mater. Sci. Poland 31 (2013) 471, https://doi.org/10.2478/s13536-013-0128-2.

[24] S.J. Clark, J. Robertson, Band gap and Schottky barrier heights of multiferroic $BiFeO_3$, Appl. Phys. Lett. 90 (2007) 132903, https://doi.org/10.1063/1.2716868.

[25] H. Wang, Y. Zheng, M.-Q. Cai, H. Huang, H.L. Chan, First-principles study on the electronic and optical properties of $BiFeO_3$, Solid State Commun. 149 (2009) 641, https://doi.org/10.1016/j.ssc.2009.01.023.

[26] S.R. Basu, L.W. Martin, Y.H. Chu, M. Gajek, R. Ramesh, R.C. Rai, X. Xu, J.L. Musfeldt, Photoconductivity in $BiFeO^3$ thin films, Appl. Phys. Lett. 92 (2008) 091905, https://doi.org/10.1063/1.2887908.

[27] A. Mukherjee, M. Banerjee, S. Basu, N.T.K. Thanh, L.A.W. Green, M. Pal, Enhanced magnetic and electrical properties of Y and Mn co-doped $BiFeO^3$ nanoparticles, Physica B: Cond. Matt. 448 (2014) 199−203, https://doi.org/10.1016/j.physb.2014.03.082.

[28] S. Ruby, S.S.R. Inbanathan, Structural properties and electrical conduction mechanisms of $Bi^{0.9}Sm^{0.05}Tb^{0.05}FeO^3$ thin film, Appl. Surf. Sci. 449 (2018) 10−14, https://doi.org/10.1016/j.apsusc.2017.11.231.

[29] H. Fukumura, H. Harima, K. Kisoda, M. Tamada, Y. Noguchi, M. Miyayama, Raman scattering study of multiferroic $BiFeO^3$ single crystal, J. Magn. Magn. Mat. 310 (2007) e367−e369, https://doi.org/10.1016/j.jmmm.2006.10.282.

[30] J. Hlinka, J. Pokorny, S. Karimi, I.M. Reaney, Angular dispersion of oblique phonon modes in $BiFeO^3$ from micro-Raman scattering, Phys. Rev. B 83 (2011) 020101−020104, https://doi.org/10.1103/PhysRevB.83.020101.

[31] J. Bielecki, P. Svedlindh, D.T. Tibebu, S. Cai, S.-G. Eriksson, L. Börjesson, C.S. Knee, Structural and magnetic properties of isovalently substituted multiferroic $BiFeO^3$: insights from Raman spectroscopy, Phys. Rev. B 86 (2012) 184422−184437, https://doi.org/10.1103/PhysRevB.86.184422.

[32] D.L. Rousseau, R.P. Bauman, S.P.S. Porto, Normal mode determination in crystals, J. Raman Spectrosc. 10 (1981) 253−290, https://doi.org/10.1002/jrs.1250100152.

[33] A. Otto, J. Timper, J. Billmann, G. Kovacs, I. Pockrand, Surface roughness induced electronic Raman scattering, Surf. Sci. 92 (1980) L55−L57, https://doi.org/10.1016/0039-6028(80)90237-X.

[34] R. Monreal, F. Flores, Y. Gao, T. López-Ríos, Raman scattering by electron-hole pairs at metal surfaces, Europhys. Lett. 4 (1987) 115−120, https://doi.org/10.1209/0295-5075/4/1/019.

[35] C.Y. Chen, E. Burstein, S. Lundquist, Giant Raman scattering by pyridine and cn adsorbed on silver, Solid State Commun. 32 (1979) 63−66, https://doi.org/10.1016/0038-1098(79)90998-0.

[36] H.L. Liu, S. Yoon, S.L. Cooper, S.-W. Cheong, P.D. Han, D.A. Payne, Probing anisotropic magnetotransport in manganese perovskites using Raman spectroscopy, Phys. Rev. B 58 (1998) R10115−R10118, https://doi.org/10.1103/PhysRevB.58.R10115.

[37] N.F. Mott, E.A. Davis, Electronic Processes in Non-crystalline Materials, Oxford University Press, 1979.

[38] A.L. Efros, B.I. Shklovskii, Coulomb gap and low temperature conductivity of disordered systems, J. Phys. C Solid State Phys. 8 (1975) L49−L51, https://doi.org/10.1088/0022-3719/8/4/003.

[39] N.V. Arginskaya, V.I. Kozub, Potential influence of pre-exponential factors on the temperature dependence of variable-range hopping conductivity, Soviet JETP 79 (1994) 466−472.

[40] A. Aharony, Y. Zhang, M.P. Sarachik, Universal crossover in variable range hopping with Coulomb interactions, Phys. Rev. Lett. 68 (1992) 3900−3903, https://doi.org/10.1103/PhysRevLett.68.3900.

[41] L. Zuppiroli, L. Forró, Hopping conductivity in polaronic situations, Phys. Lett. A 141 (1989) 181−185, https://doi.org/10.1016/0375-9601(89)90785-8.
[42] B. Stojadinović, Faculty of Physics, University of Belgrade, 2018 (Ph.D. thesis).
[43] O. Gunnarsson, M. Calandra, J.E. Han, *Colloquium*: saturation of electrical resistivity, Rev. Mod. Phys. 75 (2003) 1085−1099, https://doi.org/10.1103/RevModPhys.75.1085.
[44] N.E. Hussey, K. Takenaka, H. Takagi, Universality of the Mott-Ioffe-Regel limit in metals, Philos. Mag. A 84 (2004) 2847−2864, https://doi.org/10.1080/14786430410001716944.
[45] A. Ioffe, A. Regel, Non-crystalline, amorphous and liquid electronic semiconductors, Prog. Semicond. 4 (1960) 237−291.
[46] N.F. Mott, Conduction in non-crystalline systems IX. The minimum metallic conductivity, Philos. Mag. J. Theor. Exp. Appl. Phys 26 (4) (1972) 1015−1026, https://doi.org/10.1080/14786437208226973.
[47] F. Gervais, Infrared dispersion in several polar-mode crystals, Opt. Commun. 22 (1977) 116−118, https://doi.org/10.1016/0030-4018(77)90260-7.
[48] F. Gervais, Optical conductivity of oxides, Mater. Sci. Eng. R Rep. 39 (2002) 29−92, https://doi.org/10.1016/S0927-796X(02)00073-6.
[49] R.F. Wallis, M. Balkanski, Many-body Aspects of Solid State Spectroscopy, Elsevier Science Ltd, Amsterdam, the Netherlands, 1986.
[50] A.A. Kukharskii, Plasmon-phonon coupling in GaAs, Solid State Commun. 13 (1973) 1761−1765, https://doi.org/10.1016/0038-1098(73)90724-2.
[51] D.A.G. Bruggeman, Berechnung verschiedener physikalischer Konstanten von heterogenen substanzen. I. Dielektrizitatskonstanten und Leitfahigkeiten der Mischkorper aus isotropen Substanzen, Ann. Phys. 416 (7) (1935) 636−664, https://doi.org/10.1002/andp.19354160705.
[52] Z.V. Popović, M. Grujić-Brojčin, N. Paunović, M.M. Radonjić, V.D. Araújo, M.I.B. Bernardi, M.M. de Lima, A. Cantarero, Far-infrared spectroscopic study of CeO^2 nanocrystals, J. Nanopart. Res. 17 (2015) 23−30, https://doi.org/10.1007/s11051-015-2859-y.
[53] A. Younis, D. Chu, S. Li, Cerium oxide nanostructures and their applications, in: Functionalized Nanomaterials, 2016, pp. 52−68, https://doi.org/10.5772/65937. Ch. 3.
[54] P. Jasinski, T. Suzuki, H.U. Anderson, Nanocrystalline undoped ceria oxygen sensor, Sensor. Actuator. B Chem. 95 (2003) 73−77, https://doi.org/10.1016/S0925-4005(03)00407-6.
[55] X. Han, J. Lee, H.-I. Yoo, Oxygen-vacancy-induced ferromagnetism in CeO^2 from first principles, Phys. Rev. B 79 (2009) 100403−100406, https://doi.org/10.1103/PhysRevB.79.100403.
[56] G. Feher, A.F. Kip, Electron spin resonance absorption in metals. I Experimental, Phys. Rev. 98 (1955) 337−348, https://doi.org/10.1103/PhysRev.98.337.
[57] F.J. Dyson, Electron spin resonance absorption in metals. II. Theory of electron diffusion and the skin effect, Phys. Rev. 98 (1955) 349−359, https://doi.org/10.1103/PhysRev.98.349.
[58] M.I. Azbel, V.I. Gerasimenko, I.M. Lifshitz, Paramagnetic resonance and polarization of nuclei in metals, Sov. Phys. JETP 5 (1957) 986−996.
[59] M.I. Azbel, V.I. Gerasimenko, I.M. Lifshitz, On the theory of paramagnetic resonance in metals, Sov. Phys. JETP 8 (1959) 480−487.
[60] D.M. Djokić, D. Stepanenko, Z. Dohčević-Mitrović, Extreme conduction electron spin resonance: $A/B \rightarrow^{(5+3\sqrt{3})/4}$, the universal limit of lineshape asymmetry ratio, J. Magn. Magn. Mater. 491 (2019) 165616, https://doi.org/10.1016/j.jmmm.2019.165616.
[61] A.C. Chapman, P. Rhodes, E.F.W. Seymour, The effect of eddy currents on nuclear magnetic resonance in metals, Proc. Phys. Soc. B 70 (1957) 345−360, https://doi.org/10.1088/0370-1301/70/4/301.
[62] P.M. Platzman, P.A. Wolff, Spin-wave excitation in nonferromagnetic metals, Phys. Rev. Lett. 18 (1967) 280−283, https://doi.org/10.1103/PhysRevLett.18.280.
[63] H.R. Webb, Electron-spin-resonance line shape in spherical metal particles, Phys. Rev. 158 (1967) 225−233, https://doi.org/10.1103/PhysRev.158.225.
[64] J.H. Pifer, R. Magno, Conduction-electron spin resonance in a lithium film, Phys. Rev. B 3 (1971) 663−673, https://doi.org/10.1103/PhysRevB.3.663.

[65] A.H. Kahn, Theory of microwave eddy currents and paramagnetic resonance in materials of intermediate conductivity, Phys. Rev. B 16 (1977) 64−72, https://doi.org/10.1103/PhysRevB.16.64.
[66] J.I. Kaplan, J. Reuben, Electron spin resonance line shapes of paramagnetic species on surfaces, J. Phys. Chem. 86 (1982) 4465−4466, https://doi.org/10.1021/j100220a001.
[67] A.G. Marshall, D.C. Roe, Dispersion versus absorption: spectral line shape analysis for radiofrequency and microwave spectrometry, Analyt. Chem. 50 (1978) 756−763, https://doi.org/10.1021/ac50027a023.
[68] L. Walmsley, G. Ceotto, J.H. Castilho, C. Rettori, Magnetic field modulation frequency, sample size and electromagnetic configuration effects on the spin resonance spectra of graphite intercalation compounds, Synth. Met. 30 (1989) 97−107, https://doi.org/10.1016/0379-6779(89)90645-0.
[69] L. Walmsley, Translating conduction-electron spin-resonance lines into lorentzian lines, J. Magn. Reson. A 122 (1996) 209−213, https://doi.org/10.1006/jmra.1996.0196.
[70] M. Oshikawa, I. Affleck, Electron spin resonance in S=½ antiferromagnetic chains, Phys. Rev. B 65 (2002) 134410−134437, https://doi.org/10.1103/PhysRevB.65.134410.
[71] J.P. Joshi, S.V. Bhat, On the analysis of broad Dysonian electron paramagnetic resonance spectra, J. Magn. Res. 168 (2004) 284−287, https://doi.org/10.1016/j.jmr.2004.03.018.
[72] K.W. Blazey, K.A. Müller, F. Blatter, E. Schumacher, Conduction electron spin resonance of Caesium metallic clusters in zeolite X, Europhys. Lett. 4 (1987) 857−861, https://doi.org/10.1209/0295-5075/4/7/017.
[73] J.J. van der Klink, H.B. Brom, NMR in metals, metal particles and metal cluster compounds, Prog. Nucl. Magn. Reson. Spectr. 36 (2) (2000) 89−201, https://doi.org/10.1016/S0079-6565(99)00020-5.
[74] S. Iijima, Helical microtubules of graphitic carbon, Nature 354 (1991) 56−58, https://doi.org/10.1038/354056a0.
[75] L. Forró, C. Schönenberger, Physical Properties of Multi-Wall Nanotubes, Springer Berlin Heidelberg, Berlin, Heidelberg, 2001, pp. 329−391, https://doi.org/10.1007/3-540-39947-X_13.
[76] D.M. Djokić, A. Goswami, Quantum yield in polymer wrapped single walled carbon nanotubes: a computational model, Nanotechnology 28 (2017) 465204, https://doi.org/10.1088/1361-6528/aa8f38.
[77] A. Bachtold, M. Henny, C. Terrier, C. Strunk, C. Schönenberger, J.-P. Salvetat, J.-M. Bonard, L. Forró, Contacting carbon nanotubes selectively with low-ohmic contacts for four-probe electric measurements, Appl. Phys. Lett. 73 (1998) 274−276, https://doi.org/10.1063/1.121778.
[78] A. Bachtold, C. Strunk, J.-P. Salvetat, J.-M. Bonard, L. Forró, T. Nussbaumer, C. Schönenberger, Aharonov-Bohm oscillations in carbon nanotubes, Nature 397 (1999) 673−675, https://doi.org/10.1038/17755.
[79] L. Langer, V. Bayot, E. Grivei, J.-P. Issi, J.P. Heremans, C.H. Olk, L. Stockman, C. Van Haesendonck, Y. Bruynseraede, Quantum transport in a multiwalled carbon nanotube, Phys. Rev. Lett. 76 (1996) 479−482, https://doi.org/10.1103/PhysRevLett.76.479.
[80] W. Yi, L. Lu, Z. Dian-lin, Z.W. Pan, S.S. Xie, Linear specific heat of carbon nanotubes, Phys. Rev. B 59 (1999) R9015−R9018, https://doi.org/10.1103/PhysRevB.59.R9015.
[81] M. Bockrath, D.H. Cobden, J. Lu, A.G. Rinzler, R.E. Smalley, L. Balents, P.L. McEuen, Luttinger-liquid behaviour in carbon nanotubes, Nature 998 (1999) 598−601, https://doi.org/10.1038/17569.

[6]

CHAPTER 2

Temperature-dependent Raman spectroscopy for nanostructured materials characterization

Zorana D. Dohčević-Mitrović, Sonja Aškrabić, Bojan S. Stojadinović, Dejan M. Djokić

Nanostructured Matter Laboratory, Institute of Physics Belgrade, University of Belgrade, Belgrade, Serbia

Chapter Outline

1. Introduction

Raman spectroscopy (RS) is one of the most important nondestructive and noncontact vibrational spectroscopy method providing primarily an information on the vibrational and electronic properties in confined systems [1]. The beauty and the power of RS (conventional and micro-Raman) can be summarized as follows: no sample preparation or damage; high spatial resolution (submicron resolution when combined with a microscopic tool), sensitivity, and easy use. It is powerful and handy analytical tool for the

Design, Fabrication, and Characterization of Multifunctional Nanomaterials. https://doi.org/10.1016/B978-0-12-820558-7.00001-7

[6]

characterization of great variety of nanomaterials such as quantum dots, quantum wells, nanowires, nanopowders, nanocomposites and advanced ceramics, thin films, and biomaterials [1].

In nanostructured confined materials, due to the violation of the $q \approx 0$ selection rule, phonons over the entire Brillouin-zone contribute to the Raman line shape causing a shift and asymmetrical broadening of Raman optical or acoustic modes [2,3]. Proper analysis of temperature dependent changes of the phonon mode line shape in nanostructures is of fundamental importance to understand the changes in phonon dynamics. Significant information regarding the phonon-phonon interactions in nanomaterials, i.e., anharmonicity in the lattice potential energy can be obtained. Decay dynamics of the optical/acoustic phonon modes can be complex and dependent not only on anharmonic phonon-phonon decay mechanisms, but on other parameters like particle size and shape, size distribution, type and magnitude of the strain (compressed or tensile) and lattice disorder, structural anisotropy, or surface states. From the temperature dependence of Raman spectra it is possible to deduce about their influence on other nanomaterials properties like thermal expansion, specific heat, or thermal conductivity.

RS, as a complementary technique to X-ray diffraction, has proved to be a useful tool to identify structural stability of nanomaterials. Raman scattering is sensitive to the changes in crystal structure and can be applied for detecting new phases and/or phase transitions in investigated nanomaterials at elevated temperatures.

RS has been extensively employed for investigation the interplay between charge, spin, and lattice degrees of freedom in nanocrystalline materials. Understanding of electron-phonon interaction is of great importance, as this interaction plays a significant role in thermal conduction, charge carrier mobility, and recently discovered superconductivity in nanoparticles [4,5]. Information about the electron-phonon interaction can be obtained from the phonon shift and linewidth of Raman modes, or through the appearance of new modes in heterostructures of 2D materials [6]. The temperature-dependent variation of charge coupled Raman modes enables to deduce about the strength of electron-phonon coupling.

In magnetic nanomaterials, magnetic ordering has a well pronounced effect on the phonon frequencies near magnetic ordering temperature because the exchange coupling between magnetic ions influences Raman mode position, linewidth and integrated intensity. The subtle interplay between the spin and lattice degrees of freedom may be pivotal mechanism for understanding the superconductivity in nanocomposite structures known as nanosuperconductors [7] or can mediate magnetoelectric coupling in type-II multiferroic materials. In composite multiferroic nanostructures spin and phonons can be strongly coupled to the lattice strain as well, and this type of coupling is important aspect in manipulating the magnetic or ferroelectric properties of these materials [8]. An intense spin-phonon interaction manifests as hardening or softening of the phonon frequency or as

[6]

nontrivial behavior of optical phonon linewidth and integrated intensity near the magnetic ordering temperature. Due to the complexity of magnetic interactions in nanomaterials, the coupling between the lattice and spin degrees of freedom (spin-phonon coupling) can be different for different phonon modes, and the coupling strength may vary even in the case of the same spin-spin interaction. Electron-phonon and spin-phonon coupling strength in low-dimensional materials are size-dependent [9–11], and temperature-dependent RS offers a unique opportunity of probing the temperature evolution of electron-phonon and/or spin-phonon coupling in low-dimensional materials. Since electron-phonon and spin-phonon interactions in nanoscaled materials can be notably modified with respect to bulk materials, it is of great importance to get much better insight into these phenomena having a large impact on the electronic device engineering based on novel nanosized materials [5,6,8].

In this chapter we give a brief overview of the state-of-the-art applications of temperature-dependent RS for analyzing diverse fundamental physical processes in low-dimensional materials. Understanding of these processes enables to predict many novel thermophysical, optical, electric, magnetic, and superconducting nanomaterials features.

2. Anharmonicity in nanostructured materials

Anharmonic effects at elevated temperatures (T) and pressures (p), strongly affect a number of processes in nanostructured materials including thermal and electronic transport properties, structural phase transformation or optical properties. Although theory predicts that heat transport is performed mainly by lower frequency acoustic phonons, the anharmonic decay of optical phonons into acoustic phonons can also contribute to the thermal conductivity [12,13]. Information on phonon scattering processes is therefore important for further improvement of functionality of the nanointegrated devices. RS provides a great deal of information about the phonon vibrations and lattice anharmonicity and the following section will be dedicated to the research of anharmonic interactions in nanomaterials by using temperature-dependent RS.

2.1 Basic theory of phonon-phonon interactions

Anharmonicity in the interatomic potentials (vibrational potential energy), induced by temperature variations, causes the changes of the Raman normal modes frequency (ω), linewidth (Γ), and mode intensity. Because of the anharmonicity of the lattice forces, an optical mode can interchange energy with other lattice modes and decays into phonons of lower energies or is scattered by thermal phonons into modes of different higher energies. The phonon-phonon interactions are characterized by the complex quantity, *phonon self-energy* [14].

$$\Delta(\omega) - i\Gamma(\omega) \tag{2.1}$$

[6]

For a phonon of frequency ω and wave vector q in the jth branch, the real part $\Delta_j(\omega, q)$ represents the frequency shift due to anharmonicity, whereas the imaginary part $\Gamma_j(\omega, q)$ corresponds to reciprocal of the phonon lifetime τ ($\tau^{-1} = 2\Gamma$, 2Γ is the full width at half maximum [FWHM] of the Raman peak) [14].

In nonmagnetic, insulating, or semiconductor nanomaterials, the variation of the frequency of the jth normal mode with temperature at constant pressure arises from two contributions: frequency-independent pure-volume contribution ($\Delta_j^E(q)$), emerging from thermal expansion of the crystal and frequency-dependent, pure-temperature contribution ($\Delta_j^A(\omega, q)$), which results from cubic ($\Delta_{j3}(\omega, q)$), and quartic ($\Delta_{j4}(\omega, q)$) anharmonic terms in the vibrational potential energy. The real part of phonon self-energy $\Delta(\omega)$ can be presented as a sum of these two contributions [15].

$$\Delta_j(\omega, q) = \Delta_j^E(q) + \Delta_j^A(\omega, q) = \Delta_j^E(q) + \Delta_{j3}(\omega, q) + \Delta_{j4}(\omega, q) \tag{2.2}$$

Both $\Delta_j^E(q)$ and $\Delta_j^A(\omega, q)$ give rise to temperature-dependent frequency shift from the harmonic mode frequency ω_0. The Raman mode frequency ω_j, as a function of temperature, can be expressed as

$$\omega_j(T) = \omega_0 + \Delta_j^E(q) + \Delta_{j3}(\omega, q) + \Delta_{j4}(\omega, q) \tag{2.3}$$

In most solids $\Delta_j^E(q) < 0$, i.e., lattice dilation results in phonon mode softening. Frequency shift due to thermal expansion can be evaluated from the following equation [16]:

$$\Delta^E = \omega_0 \left(e^{-3\gamma_i \int_0^T \alpha(T')dT'} - 1 \right) \tag{2.4}$$

where $\alpha(T)$ is the coefficient of linear thermal expansion and γ_i is the mode-Gruneisen parameter. The multiphonon processes associated with the cubic terms represent the three-phonon decay (scattering) processes. The low-order perturbation calculations show that frequency shift and broadening of the jth Raman mode due to these processes should be linearly dependent on T [17–19].

$$\Delta_{j3}\left(\vec{0}, j; \omega\right) = -\frac{18}{\hbar^2} \sum_{\vec{q_1}, j_1} \sum_{\vec{q_2}, j_2} \left| V\left(\vec{0}, j; \vec{q_1}, j_1; \vec{q_2}, j_2\right) \right|^2 \times \mathscr{P}\left[\frac{n_1 + n_2 + 1}{\omega + \omega_1 + \omega_2} - \frac{n_1 + n_2 + 1}{\omega - \omega_1 - \omega_2} + \frac{n_1 - n_2}{\omega - \omega_1 + \omega_2} - \frac{n_1 - n_2}{\omega + \omega_1 - \omega_2} \right] \tag{2.5}$$

$$\Gamma_{j3}\left(\vec{0}, j; \omega\right) = \frac{18\pi}{\hbar^2} \sum_{\vec{q_1}, j_1} \sum_{\vec{q_2}, j_2} \left| V\left(\vec{0}, j; \vec{q_1}, j_1; \vec{q_2}, j_2\right) \right|^2 \times \{(n_1 + n_2 + 1) \times [\delta(\omega - \omega_1 - \omega_2) - \delta(\omega + \omega_1 + \omega_2)] + (n_1 - n_2)[\delta(\omega + \omega_1 - \omega_2) - \delta(\omega - \omega_1 + \omega_2)]\} \tag{2.6}$$

[6]

The first two terms in Δ_{j3} and Γ_{j3} present the contribution from phonon decay into two phonons of lower energy (*down-conversion* three-phonon processes). The last two terms describe the processes in which a nonequilibrium phonon is destroyed by a thermal phonon and a phonon of higher energy is created (*up-conversion* three-phonon processes). Up-conversion processes contribute at higher temperatures and vanish as T approaches zero, whereas the down-conversion processes always have a finite contribution even at $T = 0$ K [20]. From Eq. (2.5) is obvious that cubic contribution is negative ($\Delta_{j3} < 0$), giving rise to a negative frequency shift. The quartic terms correspond to four-phonon processes and vary linearly, but also quadratically with T [19].

$$\Delta_{j4a}\left(\overrightarrow{0},j;\omega\right) = \frac{24}{\hbar}\sum_{\overrightarrow{q_1},j_1} V\left(\overrightarrow{0},j;\overrightarrow{0},j;\overrightarrow{q_1},j_1;-\overrightarrow{q_1},j_1\right)\left(n_1+\frac{1}{2}\right) \tag{2.7}$$

$$\begin{aligned}\Delta_{j4b}\left(\overrightarrow{0},j;\omega\right) &= -\frac{96}{\hbar^2}\sum_{\overrightarrow{q_1},j_1}\sum_{\overrightarrow{q_2},j_2}\sum_{\overrightarrow{q_3},j_3}\left|V\left(\overrightarrow{0},j;\overrightarrow{q_1},j_1;\overrightarrow{q_2},j_2;\overrightarrow{q_3},j_3\right)\right|^2 \\ &\times \mathscr{P}\left\{[(n_1+1)(n_2+1)(n_3+1)-n_1n_2n_3]\times\left[\frac{1}{\omega+\omega_1+\omega_2+\omega_3}-\frac{1}{\omega-\omega_1-\omega_2-\omega_3}\right]\right. \\ &\left.+3[n_1(n_2+1)(n_3+1)-(n_1+1)n_2n_3]\times\left[\frac{1}{\omega-\omega_1+\omega_2+\omega_3}-\frac{1}{\omega+\omega_1-\omega_2-\omega_3}\right]\right\}\end{aligned} \tag{2.8}$$

$$\begin{aligned}\Delta_{j4c}\left(\overrightarrow{0},j;\omega\right) &= -\frac{576}{\hbar^2}\sum_{\overrightarrow{q_1},j_1}\sum_{j_2}\sum_{\overrightarrow{q_3},j_3} V\left(\overrightarrow{0},j;\overrightarrow{0},j_1;-\overrightarrow{q_1},j_1;\overrightarrow{q_1},j_2\right)V\left(\overrightarrow{q_1},j_1;-\overrightarrow{q_1},j_2;\overrightarrow{q_3},j_3;-\overrightarrow{q_3},j_3\right) \\ &\times \mathscr{P}\left[\frac{n_1+n_2+1}{\omega_1+\omega_2}-\frac{n_1-n_2}{\omega_1-\omega_2}\right]\left(n_3+\frac{1}{2}\right)\end{aligned} \tag{2.9}$$

$$\begin{aligned}\Gamma^{(4)}\left(\overrightarrow{0},j;\omega\right) &= \frac{96\pi}{\hbar^2}\sum_{\overrightarrow{q_1},j_1}\sum_{\overrightarrow{q_2},j_2}\sum_{\overrightarrow{q_3},j_3}\left|V\left(\overrightarrow{0},j;\overrightarrow{q_1},j_1;\overrightarrow{q_2},j_2;\overrightarrow{q_3},j_3\right)\right|^2 \\ &\times\{[(n_1+1)(n_2+1)(n_3+1)-n_1n_2n_3][\delta(\omega-\omega_1-\omega_2-\omega_3)-\delta(\omega+\omega_1+\omega_2+\omega_3)] \\ &+3[n_1(n_2+1)(n_3+1)-(n_1+1)n_2n_3]\times[\delta(\omega+\omega_1-\omega_2-\omega_3)-\delta(\omega-\omega_1+\omega_2+\omega_3)]\}\end{aligned} \tag{2.10}$$

In the aforementioned equations $n_j(\omega_j) = \left[\exp\left(\frac{\hbar\omega_j}{k_BT}\right)-1\right]^{-1}$ is the thermal (Bose-Einstein) population factor of the jth phonon mode with wave vector q and frequency ω_j. The quartic terms (Eqs. 2.7–2.9) may be positive or negative. Accordingly, the resultant frequency shift due to phonon-phonon interaction may be either positive or negative depending on the relative magnitudes of the anharmonic terms in the interatomic potential. The *up* and *down-conversion* three (four)-phonon processes are shown diagrammatically in Fig. 2.1A.

[6]

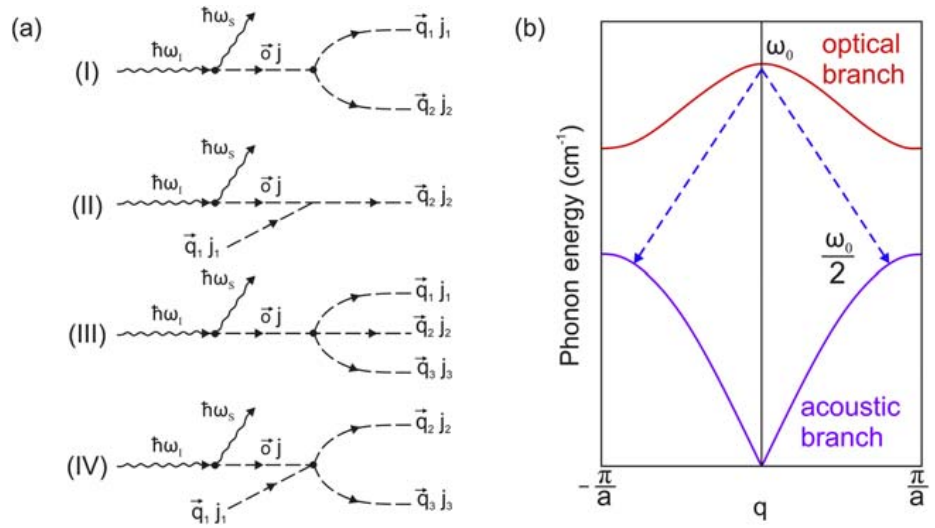

Figure 2.1
Three and four-phonon anharmonic processes (A) (I), (III) down-conversion and (II), (IV) up-conversion processes. (B) three-phonon processes according to Klemens model. *Based on M. Balkanski, R.F. Wallis, E. Haro, Anharmonic effects in light scattering due to optical phonons in silicon. Phys. Rev. B 28 (1983) 1928–1934.*

Following the approach of Klemens, [21], if the optical phonon decays into two or three acoustical phonons of lower mutually equal energies and opposite momenta, the temperature variation of the Raman phonon frequency and linewidth can be simplified:

$$\omega_j(T) = \omega_0 + C\left[1 + \frac{2}{e^x - 1}\right] + D\left[1 + \frac{3}{e^y - 1} + \frac{3}{(e^y - 1)^2}\right] = \omega_0 + \Delta\omega(T) \tag{2.11}$$

$$\Gamma(T) = \Gamma_0 + A\left[1 + \frac{2}{e^x - 1}\right] + B\left[1 + \frac{3}{e^y - 1} + \frac{3}{(e^y - 1)^2}\right] = \Gamma_0 + \Delta\Gamma \tag{2.12}$$

where ω_0 is the harmonic frequency, $x = \frac{\hbar\omega_0}{2k_BT}$, $y = \frac{\hbar\omega_0}{3k_BT}$, A, B, C, D are anharmonic constants and Γ_0 is the intrinsic mode linewidth (temperature-independent broadening). In Fig. 2.1B is presented a three-phonon decay process according to Klemens model. This model, although too simplistic, is generally accepted especially after the work of Hart et al. on Si [22].

2.2 Phonon-phonon interactions in nanomaterials

For many crystalline semiconductor or insulator materials, due to increased temperature, the anharmonic frequency shift and broadening of the Raman modes follow down or up-conversion three-phonon processes, [14,20], but at higher temperatures ($T > 300$ K) four-phonon processes begin to dominate [19]. In nanocrystalline materials, beside the anharmonic effects, temperature induced changes of the Raman line profile depend on several other factors like phonon confinement, strain, disorder/defects. Consequently,

[6]

anharmonic processes in nanomaterials can show quite distinct behavior from those of bulk counterparts. For more precise determination of influence of these factors on the Raman line profile, the temperature-dependent Raman spectra can be well modeled using phonon confinement model (PCM) [23,24] for spherical nanoparticles in which are incorporated size, inhomogenous strain and anharmonicity [25,26].

$$I(\omega,T)\propto\sum_{i=1}^{n}\int_{0}^{\infty}\rho(L)dL\int_{BZ}\frac{\exp\left(\frac{-q^2L^2}{8\beta}\right)d^3q}{[\omega-(\omega_i(q)+\Delta\omega)]^2+\left(\frac{\Gamma(T)}{2}\right)^2} \tag{2.13}$$

In the above equation, the frequency shift $\Delta\omega=\Delta\omega_i(q,L)+\Delta\omega(T)$, where the first term presents strain contribution and the second one originates from anharmonicity; $\rho(L)$ is Gaussian distribution of particle size, q-wave vector expressed in units of $2\pi/a$ (a-lattice cell parameter), L-particle diameter, β-confinement strength and $\Gamma(T)$ is a phonon linewidth, which encompasses broadening due to confinement, strain, and anharmonicity [25]. The integration is performed along all optical dispersion branches within first Brillouin-zone characteristic for certain material. As an example, in Fig. 2.2A are shown

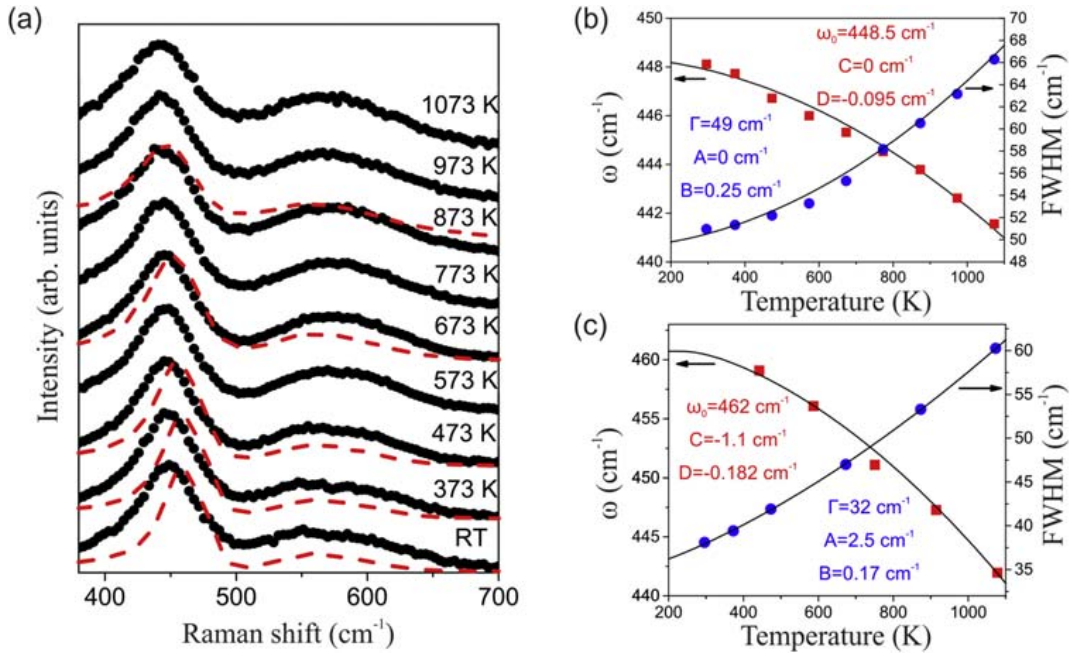

Figure 2.2

(A) Raman spectra of $Ce_{0.75}Nd_{0.25}O_{2-\delta}$ sample upon heating (*circles*) and cooling (*dashed lines*). The variation of frequency and linewidth of F_{2g} mode during (B) heating and (C) cooling. Full lines present calculated values for the peak position and linewidth using the PCM model with Klemens anzats. The best fit anharmonic parameters are given as well. *Reprinted from Z.D. Dohčević-Mitrović, M. Radović, M. Šćepanović, M. Grujić-Brojčin, Z.V. Popović, B. Matović, S. Bošković, Temperature-dependent Raman study of $Ce_{0.75}Nd_{0.25}O_{2-\delta}$ nanocrystals, Appl. Phys. Lett. 91 (2007) 203118, with the permission of AIP Publishing.*

[6]

Raman spectra of cerium dioxide nanocrystals doped with 25% of Nd ($Ce_{0.75}Nd_{0.25}O_{2-\delta}$) upon heating over the temperature range of 293−1073 K (circles) and gradual cooling down to room temperature (dashed lines) [25]. During the heating, the most intense F_{2g} Raman mode, positioned at ~450 cm^{-1} at room temperature (RT), shifts to lower frequencies, whereas its linewidth increases as presented in Fig. 2.2B. These spectra are fitted using the PCM model (Eq. 2.13) with Klemens anzats (Eqs. 2.11 and 2.12). The best fits of the peak position and linewidth of F_{2g} mode (full lines in Fig. 2.2B) upon heating were obtained including only four-phonon anharmonic processes (D, $B > 0$, $A = C = 0$), contrary to the bulk materials for which three-phonon anharmonic processes are dominant. Such a behavior implies that phonon decay channels are different in nanocrystalline particles. During the cooling process that followed annealing to 1073 K (Fig. 2.2C), anharmonic interactions in $Ce_{0.75}Nd_{0.25}O_{2-\delta}$ nanocrystals are similar to the ones in polycrystalline CeO_2 [25]. Namely, three-phonon anharmonic processes dominated over the four-phonon processes (constants A and C are much higher than B and D), designating that after the heat treatment the particle size increased enough, so that the anharmonic interactions are more similar to bulk materials.

Phonon-phonon interactions were investigated in $Ce_{0.85}Gd_{0.15}O_{2-\delta}$ nanocrystals [27] by following the changes of the F_{2g} Raman mode at elevated temperatures (293−1073 K). High-temperature Raman spectra were analyzed by PCM model (Eq. 2.13) in which are incorporated size, strain and anharmonic phonon decay processes which dominated over the thermal expansion [27]. The temperature variation of F_{2g} Raman mode position and linewidth is presented in Fig. 2.3A and B.

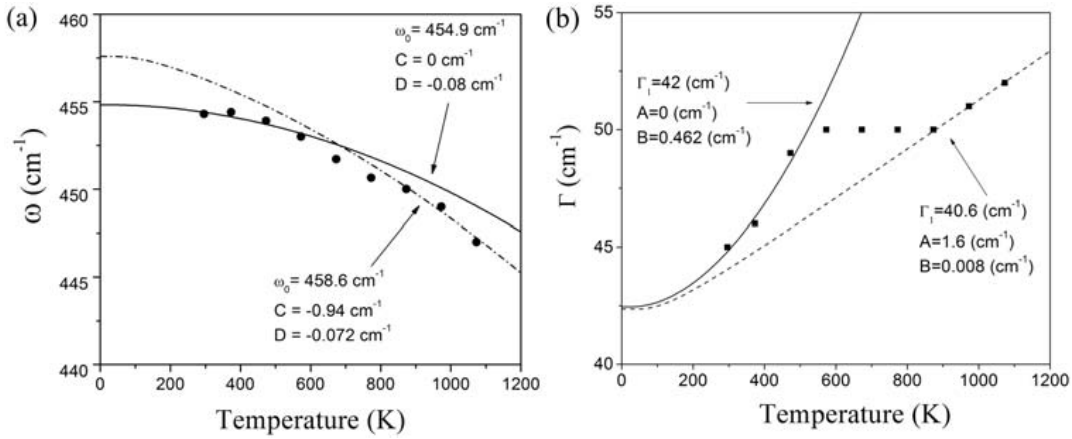

Figure 2.3

Temperature dependence of (A) frequency and (B) linewidth of the F_{2g} Raman mode in $Ce_{0.85}Gd_{0.15}O_{2-\delta}$ nanopowders. The anharmonic parameters of the best fits are also presented. *Reprinted from S. Askrabić, Z.D. Dohcević-Mitrović, M. Radović, M. Sćepanović, Z.V. Popović, Phonon-phonon interactions in $Ce_{0.85}Gd_{0.15}O_{2-\delta}$ nanocrystals studied by Raman spectroscopy, J. Raman Spectrosc. 40 (2009) 650−655 with the permission of John Wiley & Sons.*

[6]

As can be seen from Fig. 2.3A, F_{2g} Raman mode position over the whole temperature range was not possible to fit with a single curve based on three or four-phonon anharmonic processes. The best fit of the experimental values in the 293−573 K temperature range was obtained using only four-phonon anharmonic processes (full line), whereas in the 873−1073 K temperature range three-phonon coupling prevailed (dotted line). It was concluded that anharmonic processes were different in two temperature ranges. The F_{2g} mode linewidth dependency on temperature showed even more distinct behavior, as illustrated in Fig. 2.3B. The $\Gamma(T)$ firstly increased with annealing, then experienced a plateau-like behavior between 573 and 873 K and after that increased again. Such a behavior was ascribed to the effect of increased average particle size which was estimated from the PCM. As the particle size increased with annealing, nanoparticles started to take on the bulk properties and the three-phonon processes became dominant, which was confirmed from the experiment on cooling down the $Ce_{0.85}Gd_{0.15}O_{2-\delta}$ nanocrystals to RT [27]. This study obviously points to subtle interplay between size and anharmonic effects in nanostructured materials, which have to be taken into account.

In the temperature-dependent Raman spectra of ZnO nanopowders [28] it was found that E_2 (low) phonon mode linewidth exhibited anomalous behavior with temperature. In Fig. 2.4A and B are presented frequency (circles) and linewidth (squares) dependence on temperature for two Raman modes, E_2 (high) and E_2 (low) modes. As can be seen from Fig. 2.4A and B, the nonpolar optical phonon (E_2 (high)) has shown expected frequency redshift and increased broadening with increasing temperature (Fig. 2.4A) which is in good accordance with cubic and quartic anharmonicity. On the contrary, the E_2 (low) mode experienced an anomalous linewidth decrease with increasing temperature. This anomaly was ascribed to the increased interference of acoustic and surface modes with E_2 (low) optical phonon mode [28].

Optical phonon modes in most nanostructures experience frequency redshift (softening) with increasing temperature due to the cumulative effect of thermal expansion contribution and three-phonon processes (Eqs. 2.4 and 2.5), which give rise to a negative frequency shift. Contrary to this, the most intense E_g mode (positioned at ~144 cm^{-1} under ambient conditions) of nanophase anatase TiO_2 shifts to higher frequency (blueshift) with temperature rise, whereas the other anatase modes exhibit expected softening [29−32]. Although the blueshift and broadening of this mode with regard to bulk counterpart can be ascribed to the phonon confinement, oxygen nonstoichiometry and surface defects, [29,31], the main contribution originates from the anharmonic interactions that generate positive frequency shift, i.e., four-phonon anharmonic processes (Eq. 2.7) [32].

3. Size/microstrain effects and phase separation

Changes of the wavenumber and the linewidth of the Raman modes at elevated temperatures carry important information about the particle size and shape or about

[6]

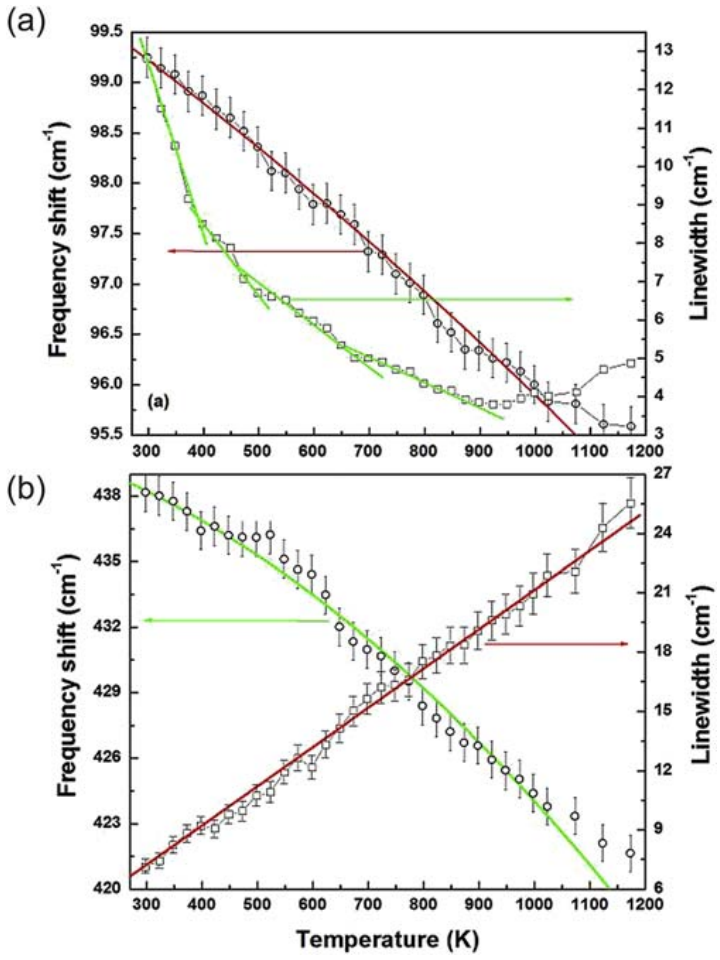

Figure 2.4

Frequency and linewidth dependence on temperature for (A) E_2 (low) and (B) E_2 (high) Raman modes of ZnO nanopowders. The *solid lines* (excluding the linewidth of E_2 (low) mode) are the best theoretical fits using Klemens model. *Reprinted from H.K. Yadav, R.S. Katiyar, V. Gupta, Temperature-dependent dynamics of ZnO nanoparticles probed by Raman scattering: A big divergence in the functional areas of nanoparticles and bulk material. Appl. Phys. Lett. 100 (2012) 051906 with the permission of AIP Publishing.*

structural phase transition which manifests itself through the appearance of new Raman modes. The PCM, described in Section 1.2, is often used to model a Raman mode intensity distribution in nanostructured materials where the size and strain effects lead to significant phonon shift and asymmetric broadening [2,3,23,24]. Using the PCM, effects of particle size, size distribution and microstrain can be disentangled. For example, in related study, oxygen deficient $CeO_{2-\delta}$ nanopowders were annealed in the air in the temperature range (200−500 °C) in order to study structural and vibrational properties of nanophase $CeO_{2-\delta}$ at elevated temperatures [33]. Raman spectra of the annealed samples (S2−S5) are presented in Fig. 2.5A together with as-synthesized $CeO_{2-\delta}$. The most intense F_{2g} mode

[6]

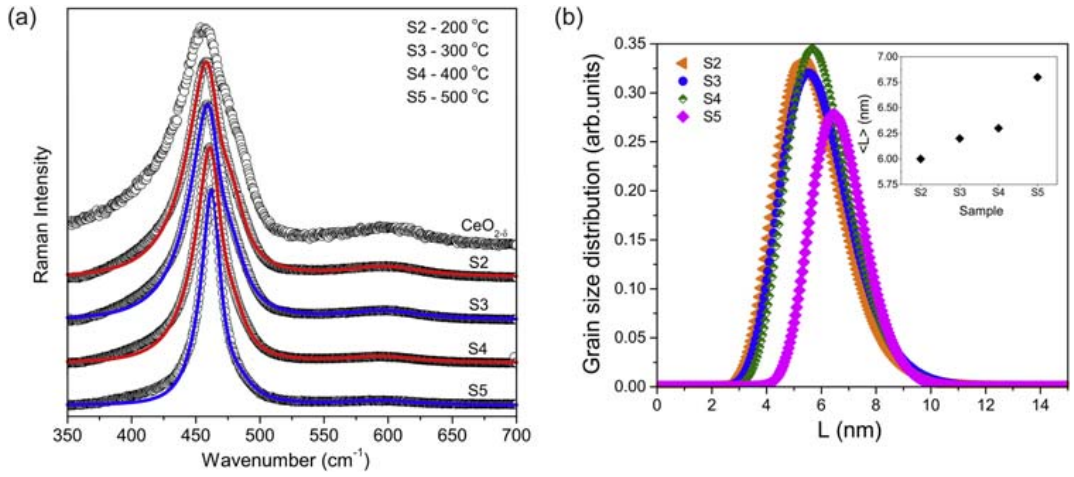

Figure 2.5

(A) Raman spectra of F_{2g} mode for the $CeO_{2-\delta}$ nanopowders at RT and annealed at different temperatures (*circles*), fitted by PCM (*full lines*). (B) Nanocrystalline particle size distribution deduced from the PCM. Samples S2–S5 represent powders annealed at different temperatures 200–500 °C. The inset presents the average particle size increase with annealing, obtained from PCM. *Reprinted from S. Aškrabić, Z. Dohčević-Mitrović, A. Kremenović, N. Lazarević, V. Kahlenberg, Z.V. Popović, Oxygen vacancy-induced microstructural changes of annealed CeO_{2-x} nanocrystals, J. Raman Spectrosc. 43 (2012) 76–81 with the permission of John Wiley & Sons.*

(~458 cm^{-1}) was shifted to higher wavenumbers and became more symmetric for the samples annealed at higher temperatures (>300 °C). Another mode which was ascribed to the intrinsic oxygen vacancies defect mode (around 600 cm^{-1}) became less intensive in the samples annealed above 300 °C. This implies that with annealing the concentration of oxygen vacancies decreased. PCM was employed [25,33] to model the changes of F_{2g} mode from Fig. 2.5A. The average lattice parameters were determined by Rietveld analysis of X-ray diffraction spectra [33] and the empirical relation between lattice parameter and particle size, $a = a_0 + k_1 \cdot \exp(-k_2/L)$, was used in PCM, where k_1 and k_2 are fitting parameters. Combined XRD and Raman analysis showed that during the thermal treatment average particle size distribution (Fig. 2.5B) and particle size (inset of Fig. 2.5B) haven't changed much, but the average microstrain was significantly reduced, almost three times in samples annealed at 400 °C and 500 °C. As content of oxygen vacancies decreased too, it was deduced that relaxation of microstrain due to the improved stoichiometry dominantly contributed to the changes seen in the Raman spectra [33].

Another temperature-dependent study of MoO_3 nanoribbons [34] by Raman spectroscopy have shown anomalies in wavenumber and linewidth behavior in the 150–400 °C temperature range. As shown in Fig. 2.6A and B, in $\omega(T)$ and $\Gamma(T)$ dependences (black circles and squares) of 155 cm^{-1} Raman mode, a plateau was observed. The $\omega(T)$ and $\Gamma(T)$ dependences departed from the anharmonic decay model in bulk MoO_3, for which the Raman mode frequency/linewidth monotonously decreased/increased with the

[6]

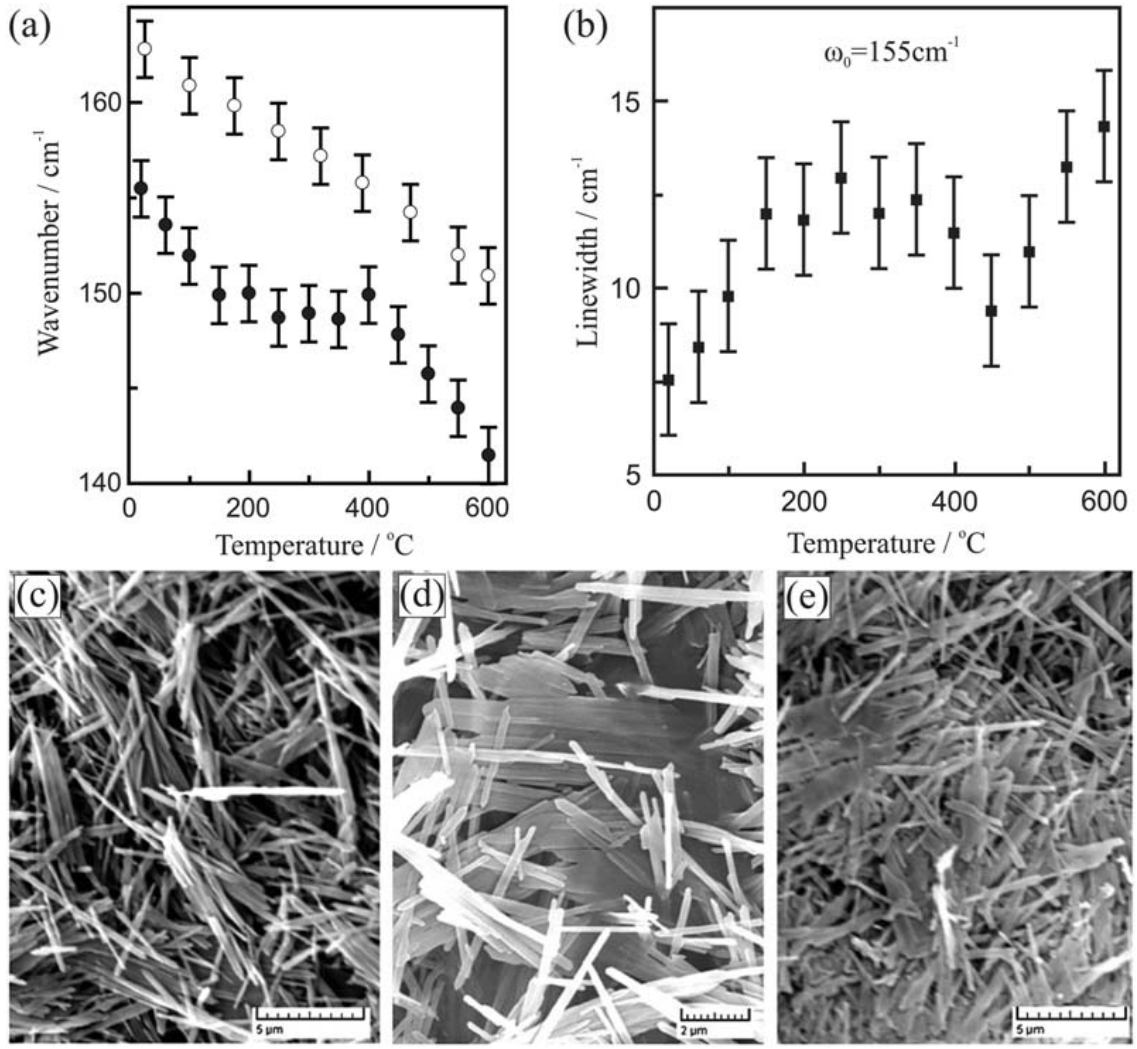

Figure 2.6

Temperature dependence of (A) frequency (*black circles*) and (B) linewidth of 155 cm^{-1} Raman mode of MoO_3 nanoribbons. Open circles present frequency versus temperature plot for bulk counterpart. SEM images at different temperatures: (C) T = 25 °C, (D) T = 150 °C and (E) T = 350 °C. *Reprinted from J.V. Silveira, L.L. Vieira, J.M. Filho, A.J.C. Sampaio, O.L. Alvesc, A.G. Souza Filho, Temperature-dependent Raman spectroscopy study in MoO_3 nanoribbons, J. Raman Spectrosc. 43 (2012) 1407–1412 with the permission of John Wiley & Sons.*

temperature rise. Such a behavior could not be ascribed to a structural phase transition, as MoO_3 nanoribbons are structurally stable up to 650 °C, but can be a consequence of size-induced effects. During the thermal treatment, the crystallite size of MoO_3 nanoribbons increased. In the 150–400 °C temperature range, the anharmonic interactions and the coalescence process are competing processes that lead to the departure from the optical phonon anharmonic decay model and appearance of a plateau [34]. Above 400 °C nanoribbons adopted bulk properties. SEM images of MoO_3 nanoribbons treated at

[6]

different temperatures (Fig. 2.6C–E) confirmed morphological changes. Namely, in the temperature regime between 150 °C and 400 °C, besides the isolated nanoribbons, large slab structures have been formed due to the coalescence of nanoribbons. At temperatures above 400 °C the nanoribbons were almost totally converted into large slabs behaving more like the bulk counterpart.

A similar appearance of a plateau-like behavior in the F_{2g} mode linewidth dependence on temperature was observed in the case of $Ce_{0.85}Gd_{0.15}O_{2-\delta}$ nanopowders from Fig. 2.3B [27]. From the PCM model it was deduced that anomalous behavior of the F_{2g} mode linewidth in the temperature range 573–873 K can be ascribed to the particle size increase and change of the particle size distribution with annealing when nanomaterials begin to resemble the bulk crystals [27].

RS has a potential to detect the presence of other phases through the appearance of the peaks characteristic for a certain crystalline structure, present even in small concentrations, and particularly in the case when two phases are very similar and cannot be resolved through X-ray diffraction spectra [35,36]. An illustration of phase separation can be found in the Raman spectra of $Ce_{0.85}Gd_{0.15}O_{2-\delta}$ nanopowders which are gradually cooled down from 1073 K to RT [27]. During the cooling process, in the Raman spectra at 473 K a new mode appeared at ~483 cm^{-1}. This new mode presented one of the strongest Raman modes of Gd_2O_3 phase, confirming that phase separation took place [27]. Another example concerns $BaTiO_3$ which has the property of forming four structural phases depending on the temperature [37]. At low temperatures, it has rhombohedral (R) structure and the phase transition to orthorombic (O), tetragonal (T), and cubic (C) phase occurs approximately at 180, 275 and 400 K [37]. Temperature-dependent Raman spectra of $BaTiO_3$ nanoparticles, with a 300 nm average particle size, are a good example how to follow the structural phase transitions in this ferroelectric material [37]. In Fig. 2.7A and B are shown Raman spectra of 300 nm $BaTiO_3$ nanoparticles recorded at two different temperatures (83 and 503 K).

The changes in the polar A_1 (TO) mode position with increasing temperatures were found to be a very good indicator of the onset of each of four phases for 300 nm nanoparticles, as presented in Fig. 2.7C. Namely, the redshift of this mode with temperature signifies the presence of one phase, whereas the temperature at which this mode starts to shift to higher wavenumbers (blueshift) points to the onset of a phase transition. In Fig. 2.7C are also indicated the temperatures of the structural phase transitions of the corresponding phases (R, O, T, C).

4. Raman thermometry

Less known application of RS concerns its use in thermometry. RS as a noncontact method of high spatial resolution can be used to measure the local temperature of the

[6]

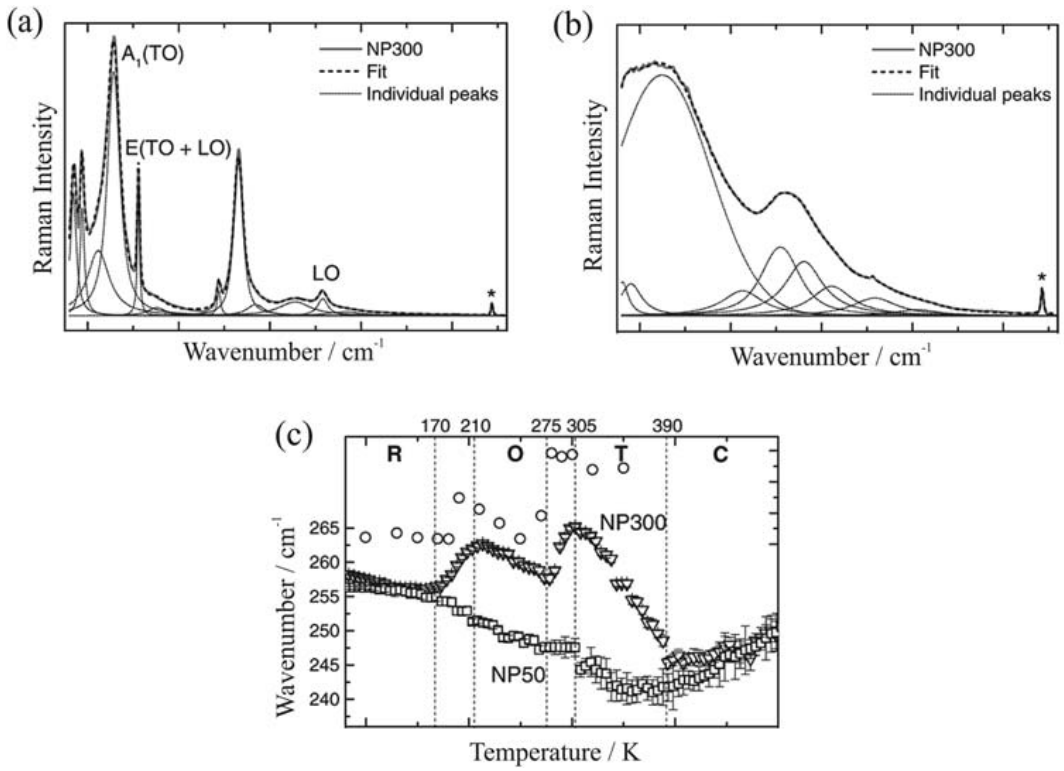

Figure 2.7

Raman spectra of $BaTiO_3$ nanoparticles at (A) 83 K and (B) 503 K; (C) wavenumber shift of the A_1(TO) mode versus temperature for nanoparticles of 300 and 50 nm average sizes. *Adapted from M. Sendova, B.D. Hosterman, R. Raud, T. Hartmann, D. Koury, Temperature-dependent, micro-Raman spectroscopic study of barium titanate nanoparticles, J. Raman Spectrosc. 46 (2015) 25–31 with the permission of John Wiley & Sons.*

material. It is known that Raman mode position will shift with temperature increase/decrease due to the change of the bond length and anharmonic effects. From the peak shift dependence on temperature a calibration curve can be formed and used for material's temperature estimation, but caution should be taken to accurately control the reference material's temperature. It is of great importance to use extremely low excitation powers in order to prevent additional heating due to the excitation power absorption by the sample. Another way to determine the temperature is to measure intensities of a Raman band at the Stokes (I_S) and anti-Stokes (I_{AS}) positions and calculate the temperature from the formula based on the Placzek's approximation

$$\frac{I_{AS}}{I_S} = \frac{(\omega_I + \omega_S)^4}{(\omega_I - \omega_S)^4} \, e^{-\frac{\hbar\omega_S}{k_B T}} \tag{2.14}$$

where ω_I and ω_S are wavenumbers of laser excitation line and a Stokes line, respectively. RS is nowadays readily used to determine the temperature or temperature sensitivity of various nanocrystalline materials.

[6]

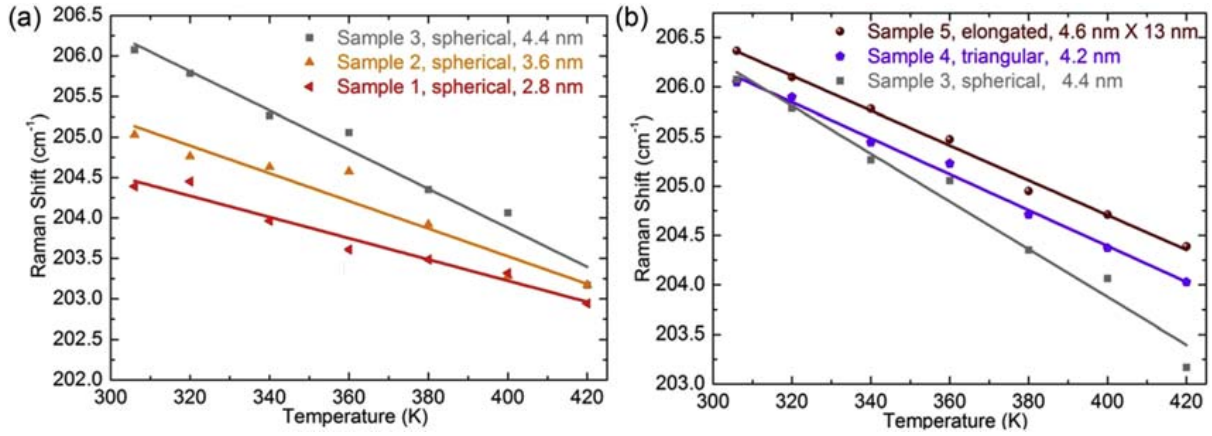

Figure 2.8

A_1(LO) frequency shift as a function of temperature for (A) spherical CdSe NCs of different size, and (B) various shaped CdSe NCs of similar size. *Reprinted from L. Chen, K. Rickey, Q. Zhao, C. Robinson, X. Ruan, Effects of nanocrystal shape and size on the temperature sensitivity in Raman thermometry, Appl. Phys. Lett. 103 (2013) 083107 with the permission of AIP Publishing.*

A study by Chen and coworkers [38] dealt with the effects of different size and shape of CdSe nanocrystals (NCs) on the temperature sensitivity of the A_1(LO) Raman mode shift. This study was performed in the temperature range 300−420 K. In Fig. 2.8 is shown the A_1(LO) mode position dependency on temperature for CdSe NCs of different sizes and shapes.

In the case of CdSe spherical NCs of different size (Fig. 2.8A), it was shown that temperature sensitivity is higher for larger nanocrystals. From the fitting of frequency shift (full lines) based on a model which incorporates thermal expansion and anharmonic effects, it was deduced that in larger nanocrystals anharmonic phonon processes dominate over the decreasing thermal expansion coefficient. In nanocrystals of different shape (triangular and elongated from Fig. 2.8B), the temperature sensitivity decreased because the effect of reduced thermal expansion coefficient overwhelms the anharmonic processes [38]. Since the temperature sensitivity is dependent on crystal size and morphology, this study points to the necessity of finding a balance between nanometric size and morphology for the application of nanomaterials in noncontact thermometry.

Raman thermometry can be also employed for thermal conductivity measurements [39,40]. This is relatively simple method with an advantage of avoiding the influence of thermal contact resistance on the intrinsic thermal conductivity. Applying the Raman shift method, heat is generated by a laser spot and the detected Raman mode shift carries an information on the induced average temperature change. The measured dependence of the peak position on the power dissipated in the material $(\partial\omega/\partial P)$ can be later used to estimate thermal conductivity using the premise of radial or plane wave heat propagation away from the laser spot position on the sample [39,40].

[6]

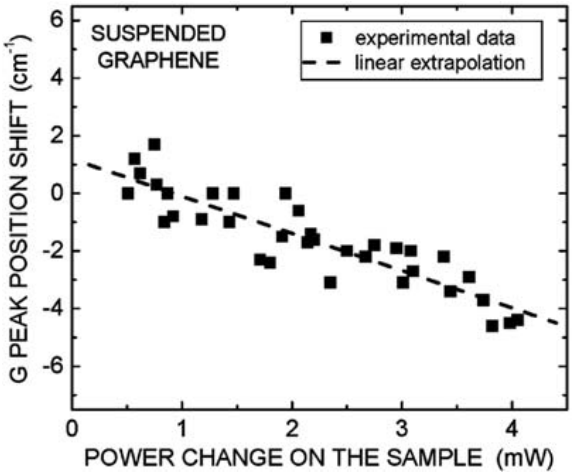

Figure 2.9

G mode position shift as a function of total dissipated power for single-layer graphene. The spectra are collected at RT using 488 nm laser excitation line. *Reprinted with permission from A.A. Balandin, S. Ghosh, W.Z. Bao, I. Calizo, D. Teweldebrhan, F. Miao, C.N. Lau, Superior thermal conductivity of single-layer graphene, Nano Lett. 8 (2008) 902−907. Copyright (2008) American Chemical Society.*

In the case of a graphene flakes placed over a trench made in Si/SiO_2 substrate, [39], and supposing that the G mode position linearly depends on the sample temperature ($\omega = \omega_0 + \chi_G T$), thermal conductivity can be expressed as [39,41].

$$K = \frac{L}{2aW}\chi\left(\frac{\partial\omega}{\partial P}\right)^{-1} \tag{2.15}$$

where L is the lateral dimension of the sample along which the wave propagates, W is the sample width, a, the sample thickness and $\partial\omega$ is a shift of G peak position due to the variation in the heating power ∂P on the sample surface. Fig. 2.9 shows the G mode position shift dependence on the total dissipated power change, from which the slope value, $\partial\omega/\partial P$, can be extracted. The temperature coefficient χ_G can be obtained by explicit Raman measurements of the G mode shift dependency on temperature change in a separate experiment when temperature is changed in a controlled way, i.e., heating of the entire sample in a heating stage.

Using Raman thermometry, thermal conductivity of a single-layer graphene flake was deduced to be ~5300 W/(mK) [39]. This value is much larger compared to other carbon materials which is of significance for this material application. In a similar way, thermal conductivities of individual single-wall and multiwall carbon nanotubes were estimated to be 2400 W/(mK) and 1400 W/(mK) [40].

5. Temperature behavior of acoustic vibrations in nanocrystalline materials studied by low-frequency Raman spectroscopy

Low-frequency Raman acoustic modes have been observed in nanocrystalline materials of various morphologies (spheres, ellipsoids, rods, etc.) and of crystallite size less than tens

[6]

of nanometers [42–45]. The appearance of these modes in the spectra of nanocrystals results from the geometrical confinement and coupling of longitudinal and transversal acoustic modes within a nanocrystalline particle [46,47]. According to the theory of Lamb, [48], the frequencies of acoustic vibrations are inversely proportional to the particle diameter: $\omega_{ln} = \beta_{ln}/D$, where ω_{ln} is the mode frequency, D is particle diameter and β_{ln} nondimensional eigensolutions of the Navier equation for homogenous elastic sphere. According to the selection rules, only the spheroidal modes with angular quantum numbers $l = 0$ and $l = 2$ are Raman active [46]. The strongest modes in the low-frequency region of the Raman spectra can be used to determine the particle diameter. Intensity of the Raman modes enables the determination of the nanocrystalline size distribution and can be described by the relation [45,49].

$$I(\omega) = \frac{n(\omega) + 1}{\omega} C(\omega) g(\omega) \tag{2.16}$$

where $n(\omega)$ is Bose-Einstein factor, $C(\omega)$ is the mode-radiation coupling factor, $g(\omega)$ is the density of vibrational states. The $l = 0$ and $l = 2$ modes are usually of the highest intensity from which the size distribution can be estimated. Taking the relation between mode frequency and particle diameter into account, in off-resonant conditions, $C(\omega) \sim \mathrm{D} \sim 1/\omega$ and the density of states $g(\omega)$ reflects the particle size distribution $N(D) \sim g(\omega_{ln} = \beta_{ln}/D)$. The simple relation can then be used to determine the particle size distribution $N(D)$ [45]:

$$N(D) \sim g(\omega) = \frac{I(\omega)\omega^2}{n(\omega) + 1} \tag{2.17}$$

Therefore, temperature dependent study of low-frequency acoustic modes in nanomaterials can potentially contribute to the pool of noncontact methods for the estimation of nanocrystalline size and/or size distribution change with temperature variation.

Although there is a huge number of papers in the literature dedicated to the temperature-dependent behavior of optical phonons in various nanostructures, little is known about the acoustic phonons dynamics as a function of temperature, despite their relevance in nonradiative relaxation processes or exciton decoherence and dephasing in nanocrystalline solids [50]. Temperature-dependent acoustic mode dynamics can be complex and dependent not only on anharmonicity, but on other parameters like particle size, structural anisotropy, morphology, surface states, or interactions with the charge carriers and therefore deserves more profound investigation.

One of rare studies on temperature dependence of breathing-mode acoustic vibrations in CdSe nanocrystals was presented in the work of Mork et al. [50] The temperature evolution of low-frequency Raman modes of CdSe NCs of several sizes is presented in Fig. 2.10A. All low-frequency Raman modes have shown the expected phonon

[6]

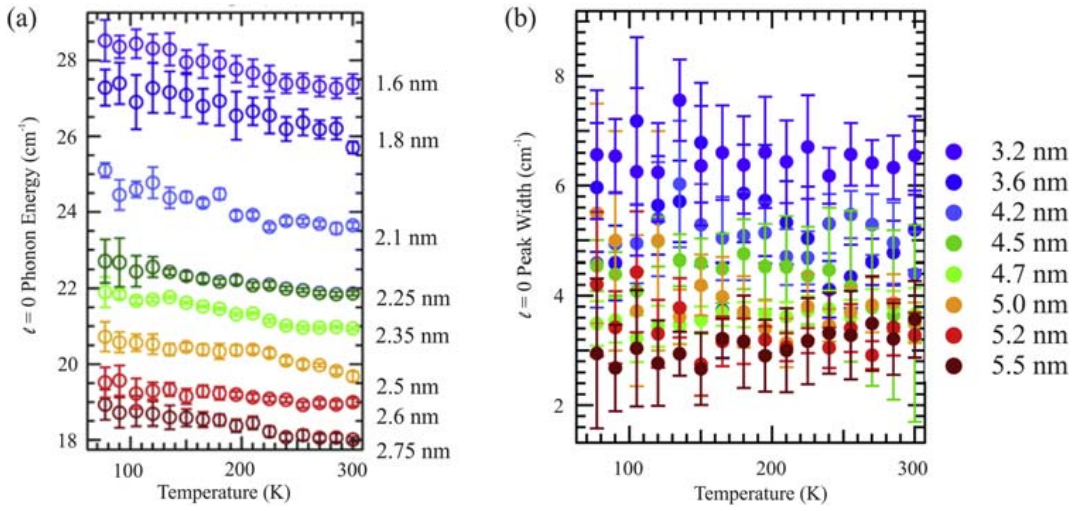

Figure 2.10

Temperature dependence of (A) acoustic phonon energy and (B) linewidth for CdSe NCs of different diameters. *Adapted from A.J. Mork, E.M.Y. Lee, W.A. Tisdale, Temperature dependence of acoustic vibrations of CdSe and CdSe—CdS core-shell nanocrystals measured by low-frequency Raman spectroscopy, Phys. Chem. Chem. Phys. 18 (2016) 28797—28801. Published by the PCCP Owner Societies.*

softening, regardless the particle size, but the magnitude of observed phonon softening could not be explained by Lamb's model only. Since, the acoustic vibrations are dependent not only on size, but also on bulk modulus, density, and transverse and longitudinal sound velocities, their change with temperature has to be taken into account. In the case of CdSe NCs, it was shown that the bulk modulus and density changes in the investigated temperature range were less than 5%, which was insufficient to explain the observed frequency change. It was concluded that organic ligands on the nanoparticle surface, with different elastic modulus, can significantly contribute to the acoustic phonon shift [50]. The linewidth (Fig. 2.10B) has shown no expected change with temperature. Such a temperature-independent behavior of linewidth was ascribed to the strong environmental damping and inhomogenous contribution of different nanocrystalline sizes to the linewidth [50].

A complex temperature-dependent behavior of acoustic phonons was observed in ZnO nanoparticles too [51]. Fig. 2.11 shows the low-frequency Raman spectra of ZnO nanoparticles recorded at elevated temperatures (300—600 K). The prominent mode (around 22/cm) at 300 K, ascribed to spheroidal acoustic mode, shifted toward lower wavenumbers with temperature increase and after 600 K disappeared under the Rayleigh wing. Analyzing the temperature induced shift of the acoustic mode from Fig. 2.11B (open circles), it was deduced that at lower temperatures under 500 K, anharmonic decay processes and bond strength weakening were responsible for mode softening. At higher temperatures (>500 K), fast exponential decrease of peak frequency was attributed to the

[6]

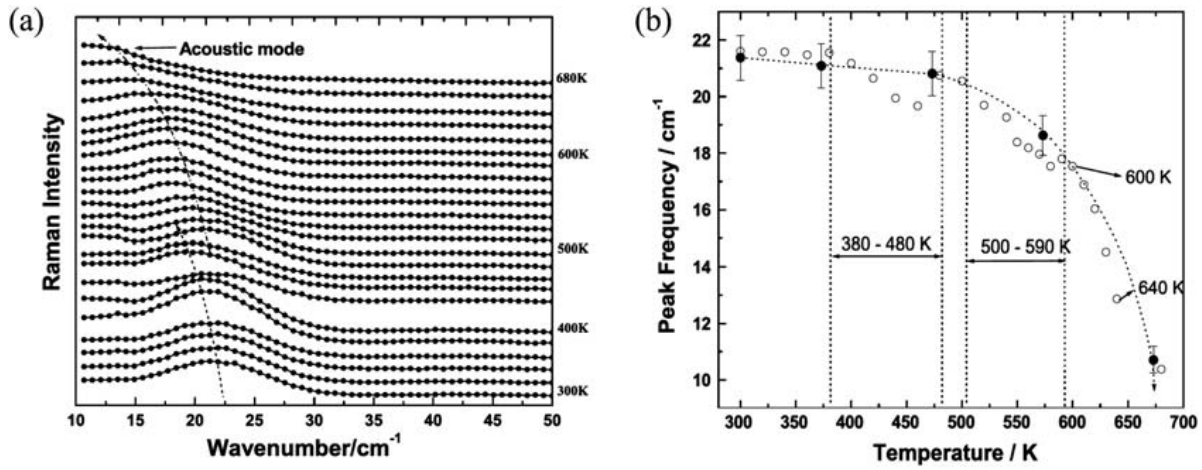

Figure 2.11

Temperature-dependent (A) low-frequency Raman spectra of ZnO nanoparticles and (B) acoustic mode frequency (*open circles*) obtained from the fitting of the acoustic mode [51]. *Black circles* are the calculated values of the peak frequency [51] and dotted line presents expected frequency behavior including anharmonic and size effects. *Reprinted from H.K. Yadav, K. Sreenivas, R.S. Katiyar, V. Gupta, Softening behavior of acoustic phonon mode in ZnO nanoparticles: the effect of impurities and particle size variation with temperature, J. Raman Spectrosc. 42 (2011) 1620–1625 with the permission of John Wiley & Sons.*

increased particle growth and coalescence process. Evident anomalous softening in the temperature ranges 380–480 K and 500–580 K originated from the impurities and reaction byproducts present on the surface of ZnO nanoparticles, the presence of which was proved by thermogravimetric analysis and differential scanning calorimetry measurements [51].

6. Electron-phonon interaction

Investigation of the interaction between electrons and lattice vibrations in nanocrystalline materials is an important topic because it has substantial influence on electronic and thermal transport, optical properties, or superconductivity. RS is convenient method for studying the electron-phonon (*e*-ph) interaction and enables to quantitatively determine the electron-phonon coupling constant. In metallic and polar or heavily doped semiconductor nanomaterials, the interaction of phonons with the conduction electrons or electron-hole pairs reflects in the Raman spectra as the asymmetric mode shift and broadening. Asymmetric line shapes of the Raman phonon spectra originate from a Fano-type interference effect between the discrete one-phonon states and a continuum of electronic transitions and can be well described with the Fano line shape [52,53].

[6]

$$I(\omega) = \sum_i I_{0i} \frac{(\varepsilon_i + q_i)^2}{1 + \varepsilon_i^2} \tag{2.18}$$

where $\varepsilon_i = 2(\omega - \omega_i)/\Gamma_i$, I_{0i}, ω_i and Γ_i are the intensity, bare phonon frequency and linewidth of the ith phonon mode and q_i is the Fano asymmetric parameter for the ith mode. The parameter q controls the asymmetry of the Raman mode with respect to a standard Lorentzian profile, whereas the value $1/q$ serves as a measure of electron-phonon coupling strength. The increase of $1/q$ value indicates stronger coupling and in the limit $|1/q| \rightarrow 0$ the Fano profile reduces to the Lorentzian line shape [53].

The electron-phonon coupling strength can also be estimated from the Allen formula [54] which connects the linewidth γ_i of the ith phonon mode with electron-phonon coupling constant λ_i [54,55]

$$\lambda_i = \frac{2 g_i \gamma_i}{\pi N_{\varepsilon_f} \omega_{bi}^2} \tag{2.19}$$

where N_{ε_f} is the electronic density of states at the Fermi surface per spin per unit cell, g_i is the mode degeneracy, and ω_{bi} is the bare phonon frequency in the absence of electron-phonon interaction. In the framework of Allen's theory, the electronic density of states N_{ε_f} can be estimated from the relation [55,56].

$$\gamma_i = -\frac{\pi}{2} N_{\varepsilon_f} \omega_{bi} \Delta\omega \tag{2.20}$$

where $\Delta\omega$ presents the difference between the bare phonon frequency and the observed frequency.

A good example of e-ph coupling in nanophase materials presents the Raman temperature study on $LiTi_2O_4$ superconducting thin films [57]. In Fig. 2.12A are presented temperature-dependent Raman spectra of three T_{2g} modes (342.2 cm^{-1}, 433.3 cm^{-1}, and 495.2 cm^{-1}) of $LiTi_2O_4$. All T_{2g} modes had asymmetric Fano line shape in the whole temperature range 5−300 K and were well fitted with the Fano function (full lines on Fig. 2.12A). The parameters q, obtained from the fitting of T_{2g} modes from Fig. 2.12A, are displayed in Fig. 2.12B. There is an obvious anomaly in the asymmetry parameters around the temperature of 50 K, where the negative to positive magnetoresistance transition takes place [57]. This anomaly was ascribed to the onset of other competing order like orbital-related state, which can suppress the e-ph coupling by modifying the electron density of states [57].

Electron-phonon interactions can be responsible for some anomalous behavior of phonon linewidths and intensities as a function of temperature. As an example, calculations from first principles [58] have proven that the anomalous decrease of E_{2g} (G band) phonon linewidth in graphene is dominated by e-ph interactions. In Fig. 2.13 is shown the total

[6]

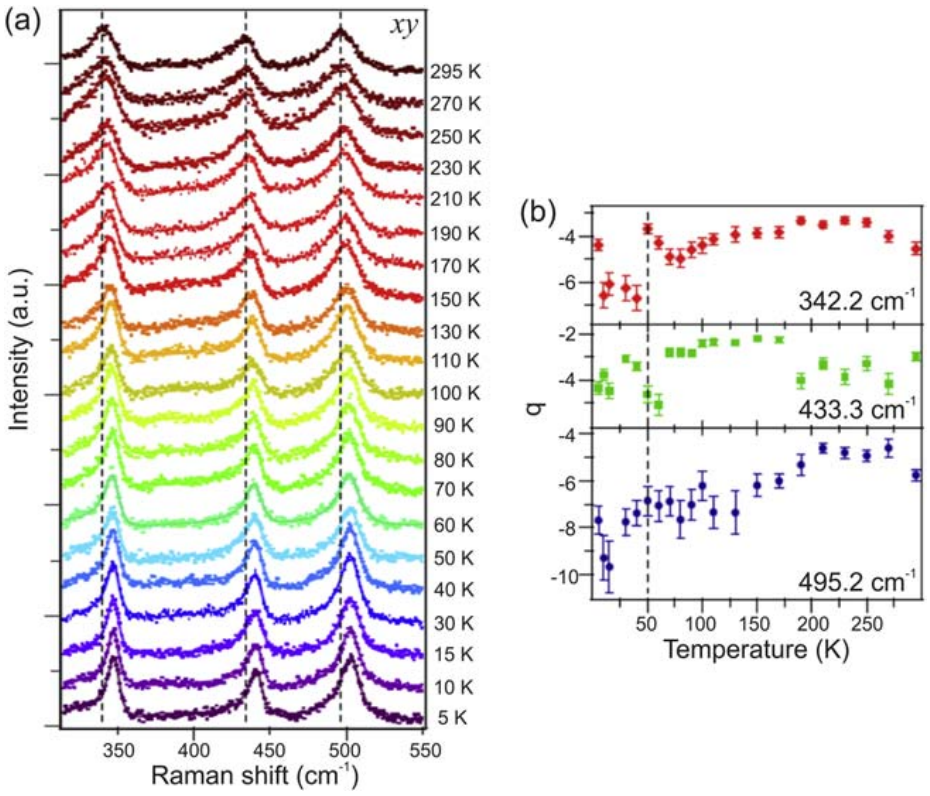

Figure 2.12

Temperature-dependent (A) Raman spectra of three T_{2g} modes of $LiTi_2O_4$ thin films and (B) Fano asymmetry factor q of the T_{2g} modes. *Reprinted figure with permission from D. Chen, Y.-L. Jia, T.-T. Zhang, Z. Fang, K. Jin, P. Richard, H. Ding, Raman study of electron-phonon coupling in thin films of the spinel oxide superconductor $LiTi_2O_4$, Phys. Rev. B 96 (2017) 094501. Copyright (2017) by the American Physical Society.*

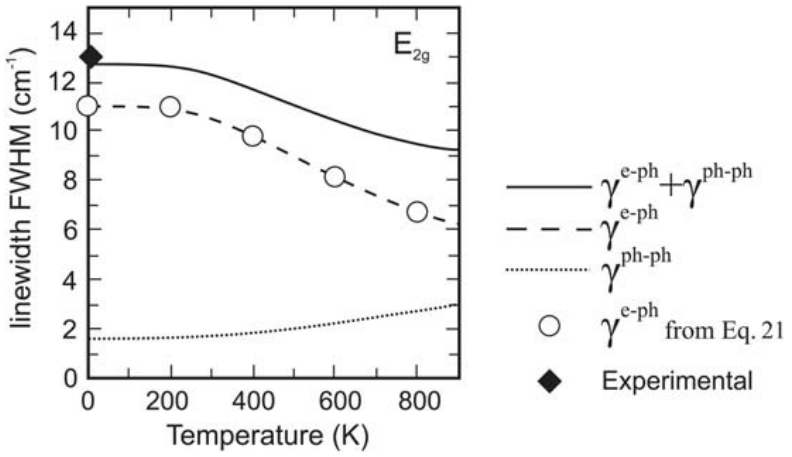

Figure 2.13

Calculated temperature dependence of the total E_{2g} mode linewidth of graphene (*full line*), *e*-ph (*dashed line*), and ph-ph (*dotted line*) contributions, from first principles together with experimental results and the results (*open circles*) based on Eq. (2.21). *Reprinted figure with permission from N. Bonini, M. Lazzeri, N. Marzari, F. Mauri, Phonon anharmonicities in graphite and graphene, Phys. Rev. B 99 (2007) 176802. Copyright (2007) by the American Physical Society.*

[6]

linewidth of E_{2g} mode (full line) computed from first principles, whereas dashed and dotted lines present *e*-ph and ph-ph contributions. These calculations are in very good agreement with respect to measurements [58] and have shown that the *e*-ph coupling has dominant role in the temperature dependence of E_{2g} mode linewidth. Furthermore, these calculations are compared with the results (open circles in Fig. 2.13) obtained from the simplified model for temperature dependence of E_{2g} phonon linewidth due to *e*-ph coupling [58,59].

$$\gamma^{e-ph}(T) = \gamma^{e-ph}(0)\left[f\left(-\frac{\hbar\omega_0}{2k_BT}\right) - f\left(\frac{\hbar\omega_0}{2k_BT}\right)\right] \tag{2.21}$$

where $f(x) = [\exp(x)+1]^{-1}$, k_B is the Boltzmann constant and $\hbar\omega_0$ is the E_{2g} phonon energy. As can be seen from Fig. 2.13, the simplified model very well reproduces the calculations for the linewidth behavior of E_{2g} phonon with temperature confirming the dominant role of *e*-ph coupling.

Another temperature-dependent Raman study on nanostructured cuprous oxide (Cu_2O) film (Fig. 2.14), revealed the anomalous temperature behavior of the LO components of

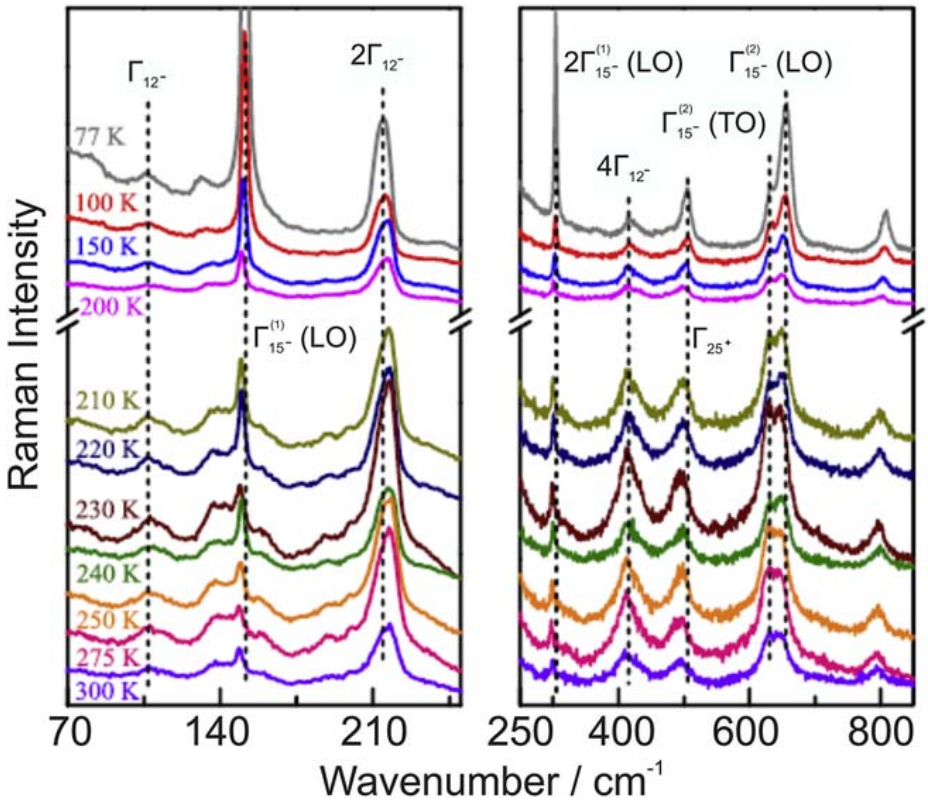

Figure 2.14

Temperature-dependent Raman spectra of Cu_2O film. *Dashed lines* present the guides to the eye of the Raman modes shift with temperature. *Reprinted from W. Yu, M. Han, K. Jiang, Z. Duan, Y. Li, Z. Hu, J. Chu, Enhanced Fröhlich interaction of semiconductor cuprous oxide films determined by temperature-dependent Raman scattering and spectral transmittance, J. Raman Spectrosc. 44 (2013) 142–146 with the permission of John Wiley & Sons.*

[6]

the infrared-active polar $\Gamma_{15-}^{(1)}$ and $\Gamma_{15-}^{(2)}$ modes [60]. Namely, an appearance of $\Gamma_{15-}^{(1)}$ and $\Gamma_{15-}^{(2)}$ modes at 151 and 655 cm^{-1} in the Raman spectra from Fig. 2.14 indicated the presence of strong *e*-ph coupling mediated by Fröhlich interaction. At lowest temperature of 77 K, these modes were sharp and of high intensity. With temperature increase, their intensity decreased and after 200 K intensities of both modes were significantly reduced. This study pointed to much stronger Fröhlich interaction at temperatures lower than 200 K. The larger TO-LO splitting of $\Gamma_{15-}^{(2)}$ mode at temperatures below 200 K imply that Fröhlich interaction is very sensitive to temperature [60].

It is worth to mention that Raman studies on nanocrystalline materials [9,61] suggest that the strength of *e*-ph interaction is dependent on nanocrystalline size. Therefore, analyzing the temperature-dependent Raman spectra of nanostructured materials it is important to correctly estimate the contributions from size effects, anharmonicity and *e*-ph coupling on the Raman line profile.

7. Electromagnons in cycloidal multiferroic nanostructures

Raman scattering is an efficient tool for studying the mutual and complex coupling between the magnetic (magnons) and lattice (phonons) excitations. One such example are the single-magnon spin waves with an electric dipole activity, called electromagnons, which can be excited by the electric component of electromagnetic waves and are consequently much stronger coupled to the light than ordinary magnons which interact through magnetic dipole excitations. Up to date, electromagnons were registered in a variety of crystalline antiferromagnets like $CuFe_{1-x}Ga_xO_2$, [62], garnets, [63], multiferroics like RMn_2O_5 (R = Y, Tb, Eu), [64], $Ba_2CoGe_2O_7$, [65], manganites [66].

The presence of electromagnons was first discovered in the low-temperature Raman spectra of cycloidal multiferroic $BiFeO_3$ single crystals [67,68] and recently in $BiFeO_3$ thin films [69]. In Fig. 2.15A is presented the electromagnon Raman spectra of $BiFeO_3$ crystal measured at 7 K in parallel and crossed polarizations in (010) plane.

Two types of electromagnon excitations were registered in the Raman spectra of $BiFeO_3$ crystal, which lie in (cyclon modes, φ) and out (extra-cyclon modes, ψ) of (-12-1) cycloidal plane [67]. The cycloidal plane is formed by the vector of spontaneous polarization *P* along [111] direction and cycloid propagation defined by the wavevector *q* along [10-1] direction, as sketched in Fig. 2.15B. These low-energy Raman modes show sudden increase of intensity at temperatures close to the spin reorientation phase transition (140 K) which is additional confirmation of their magnetic nature [67].

In the framework of simple Landau-Ginzburg model for cycloidal multiferroics, Sousa and Moore [70] have shown that the modes which propagate along the cycloidal plane

[6]

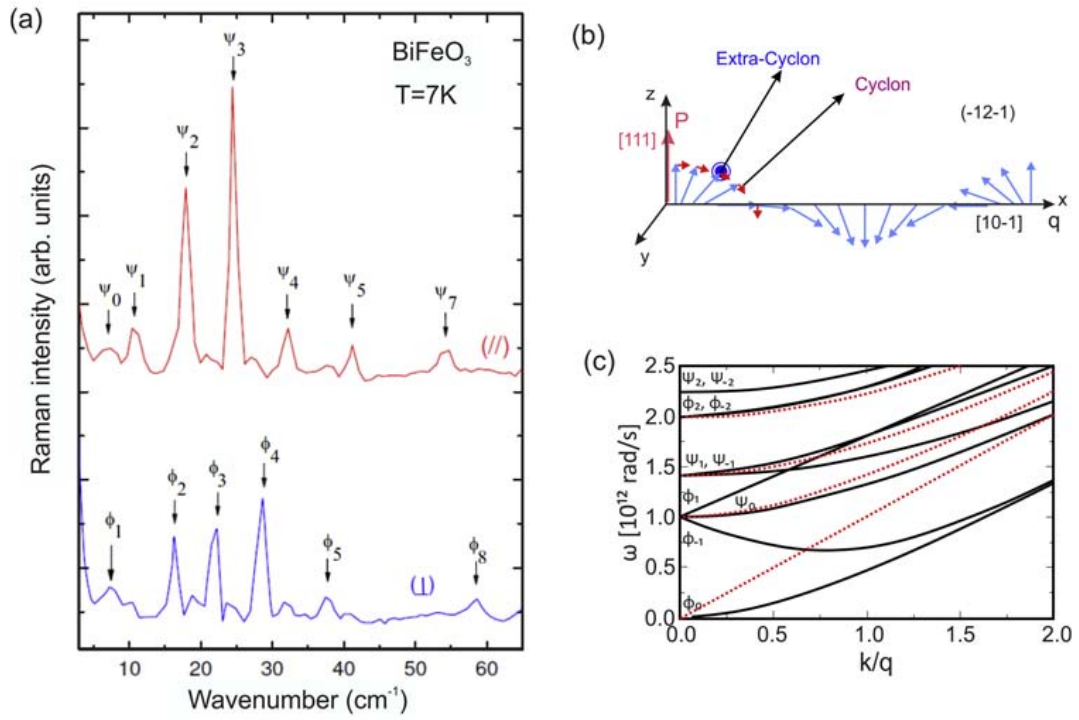

Figure 2.15

(A) Electromagnon Raman spectra of $BiFeO_3$ single crystal obtained using parallel (//) and crossed ($\perp$) polarizations in the (010) plane; (B) schematic representation of cycloidal magnetic order in $BiFeO_3$ and (C) dispersion curves of cyclon (φ) and extra-cyclon (ψ) modes in the direction perpendicular to (-12-1) cycloidal plane (*full lines*), and along [111] direction (*dashed lines*). *Reprinted figure with permission from M. Cazayous, Y. Gallais, A. Sacuto, R. de Sousa, D. Lebeugle, D. Colson, Possible observation of cycloidal electromagnons in $BiFeO_3$, Phys. Rev. Lett. 101 (2008) 037601. Copyright (2008) by the American Physical Society, R. De Sousa, J.E. Moore, Optical coupling to spin waves in the cycloidal multiferroic $BiFeO_3$, Phys. Rev. B 77 (2008) 012406. Copyright (2008) by the American Physical Society.*

$(k_y = 0)$, are simple plane waves with different dispersions depending on their coupling to electrical polarization

$$\omega'^2 = c\tilde{k}^2 (\varphi \text{ modes}) \tag{2.22}$$

$$\omega'^2 = c\left(\tilde{k}^2 + q^2\right)(\Psi \text{ modes}) \tag{2.23}$$

with $\tilde{k} = (k_x + nq)^2 + k_y^2 + k_z^2$ and n as integer. The propagation along the k_y direction leads to the appearance of small gaps in the propagation frequency due to the pinning of the cycloidal plane by the electrical polarization. The numerical solutions of spin waves propagation [70] in the direction perpendicular to (-12-1) cycloidal plane (full lines) and along [111] direction (dashed lines) are shown in Fig. 2.15C.

[6]

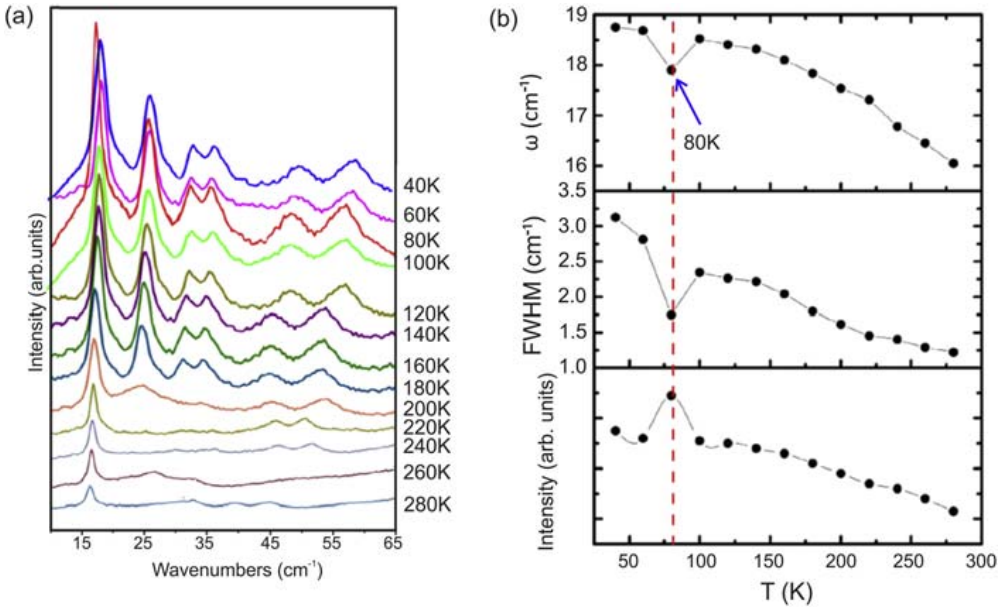

Figure 2.16

Temperature dependence of (A) electromagnon spectra of $BiFeO_3$ thin films in normal configuration (B) wavenumber, linewidth (FWHM), and intensity of electromagnon mode at 18.75 cm^{-1}. *Reprinted from W. Azeem, S. Riaz, A. Bukhtiar, S.S. Hussain, Y. Xu, S. Naseem, Ferromagnetic ordering and electromagnons in microwave synthesized $BiFeO_3$ thin films, J. Magnet. Magnet. Mater. 475 (2019) 60–69, Copyright (2019) with permission from Elsevier.*

Recently, electromagnons have been found in the low-frequency Raman spectra of $BiFeO_3$ thin films [69]. The temperature-dependent electromagnon spectra is shown in Fig. 2.16A. Two intense modes (at 18.75 cm^{-1} and 25.8 cm^{-1}) together with four other modes of lower intensity were observed at 40 K. These two low-energy electromagnon modes are strongly affected by temperature. In Fig. 2.16B is presented the temperature variation of the wavenumber, linewidth and intensity of 18.75 cm^{-1} electromagnon mode. As can be seen, neither frequency, linewidth nor intensity exhibit monotonic behavior. Instead, there is an anomaly at around 80 K. Such a behavior can be correlated with changes in the cycloid spin arrangements at low temperatures like spin reorientation transition in $BiFeO_3$ single crystal [68] or in orthoferrites like $TmFeO_3$ [71].

From these studies, it can be concluded that RS is a suitable optical method not only for detection of electromagnons, but for revealing more about the anharmonicity in magnetic order of cycloidal multiferroic nanostructures.

8. Spin-phonon interaction

RS is a useful tool to elucidate spin-phonon (*s*-ph) coupling mechanism, because the Raman modes in magnetic materials can be sensitive to the magnetic ordering.

Spin-phonon interaction manifests as nontypical temperature dependence of optical phonon frequency, linewidth and integrated intensity, since all these phonon features can be influenced by the exchange coupling between magnetic ions at and below the temperatures of magnetic phase transitions. It is expected that the coupling between the lattice and spin degrees of freedom (spin-phonon coupling) is different for different phonon modes because the magnetic interactions can be complex and the spin-phonon coupling constant may vary even in the case of the same spin-spin interaction [72].

In magnetic materials, the change of a jth phonon mode frequency with temperature can be expressed as:

$$\omega_j(T) - \omega_j(T_0) = \Delta\omega_j(T) = \Delta\omega_{\text{latt}} + \Delta\omega_{\text{anh}} + \Delta\omega_{e-\text{ph}} + \Delta\omega_{s-\text{ph}} \tag{2.24}$$

The first three terms present the change of the phonon frequency due to the lattice expansion/contraction, intrinsic anharmonicity and electron-phonon coupling, whereas the fourth term accounts for the effect of the s-ph contribution. The frequency shift due to s-ph coupling can be expressed as [73,74].

$$\Delta\omega_{s-\text{ph}} = \omega - \omega_0 = -\lambda_{s-\text{ph}}\langle S_i S_j\rangle \tag{2.25}$$

where ω_0 is the eigenfrequency in the absence of s-ph coupling; S_iS_j denotes the spin-spin correlation function for adjacent spins localized at the ith and jth sites and $\lambda_{s-\text{ph}}$ is the s-ph coupling constant which is different for each phonon and may have positive or negative sign [73]. From the mean field theory and considering nearest neighbor interaction it follows that

$$\langle S_i S_j\rangle = S^2\phi(T) \tag{2.26}$$

where $\phi(T)$ is the normalized short-range order parameter which is estimated from the mean field theory [73] and defined as $\phi(T) = \left|S_iS_j\right|/S^2$. According to the mean field theory, $\phi(T)$ decreases with temperature from 1 at $T = 0$ K and falling to 0 at temperature of magnetic phase transition (either T_N or T_C). The $\Delta\omega_{s\text{-ph}}$ can be now expressed as

$$\Delta\omega_{s-\text{ph}} = -\lambda_{s-\text{ph}}S^2\phi(T) \tag{2.27}$$

On the other hand, according to the mean field approximation the $S_iS_j \propto \left(\frac{M(T)}{M_S}\right)^2$, where $M(T)$ is the temperature-dependent average magnetization per magnetic ion and M_S is the saturation magnetization [75–77]. Therefore, the shift of the Raman mode due to s-ph coupling is $\omega_{s-\text{ph}} \propto \left(\frac{M(T)}{M_S}\right)^2$. In antiferromagnetic (AF) and ferromagnetic (FM) materials spin correlation function S_iS_{i+1} approaches zero for $T > T_N$, T_C and the spin-phonon coupling usually terminates in the paramagnetic phase.

[6]

Raman spectroscopy has been utilized to study spin-phonon coupling in various magnetic nanomaterials [11,78–80] through the temperature-dependent variation of the one-phonon or two-phonon Raman spectra. CuO nanowires are a good example to study spin-phonon interaction and the effect of size decrease on the spin-phonon coupling constant [11]. In Fig. 2.17A are presented Raman spectra of in-plane CuO nanowires, with the mean diameter of 120 nm, at different temperatures across the Néel temperature, T_N (~143 K).

Two well-defined modes at around 300 and 348 cm^{-1} of A_g and B_g^1 symmetries were registered at 193 K. With temperature decrease an additional mode at ~231 cm^{-1}

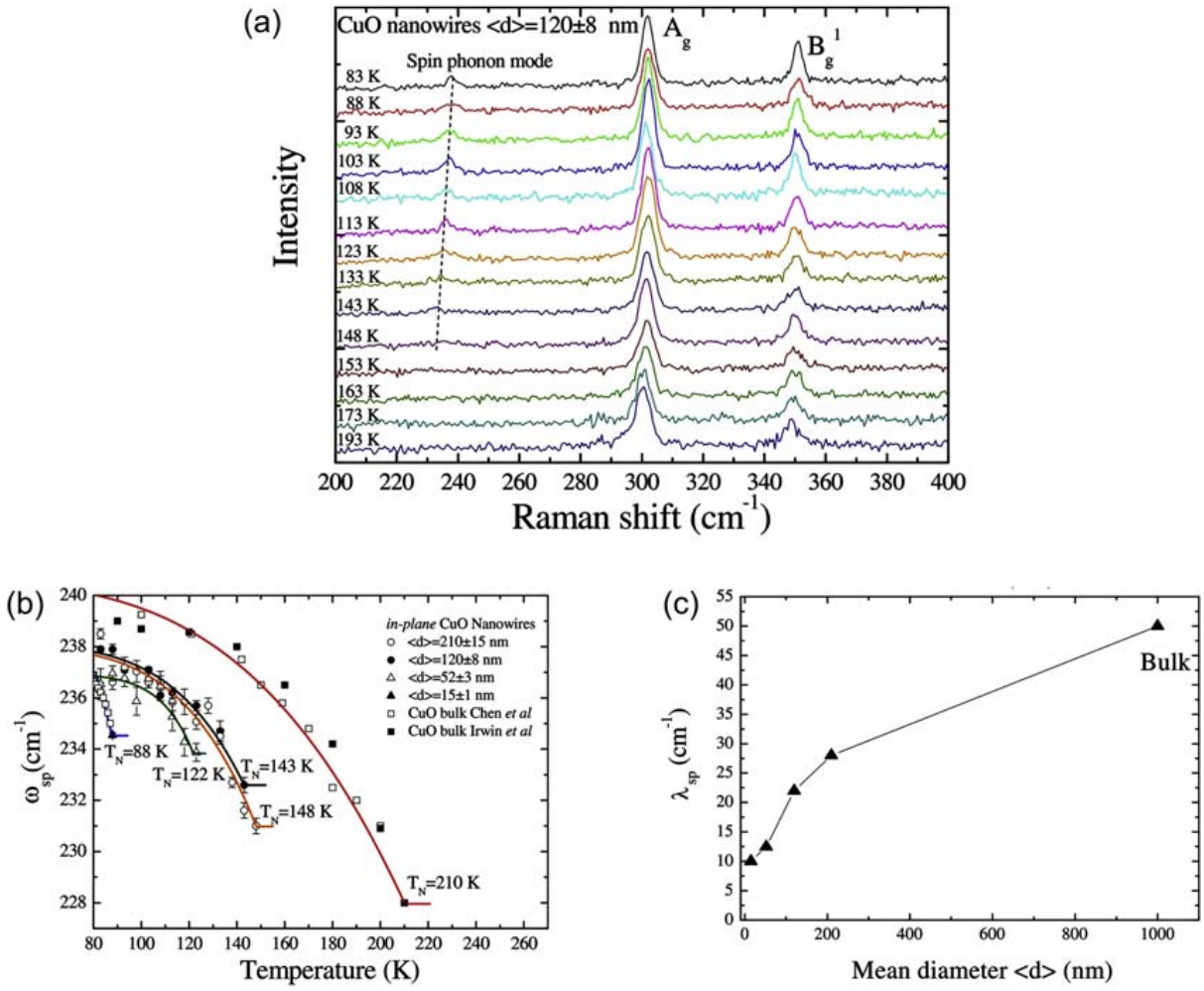

Figure 2.17

(A) Raman spectra of CuO nanowires with mean diameter $<d> = 120 \pm 8$ nm at various temperatures across the T_N; (B) temperature variation of spin-phonon mode frequency and (C) change of spin-phonon coupling constant on nanowires mean diameter. *Reprinted from P.-H. Shih, C.-L. Cheng, S.Y. Wu, Short-range spin-phonon coupling in in-plane CuO nanowires: a low-temperature Raman investigation, Nanoscale Res. Lett. 8 (398) (2013) 1–6 with the permission of SpringerNature.*

[6]

appeared. This mode is ascribed to the zone-folded LA phonon from the Z′ point of the Brillouin-zone boundary, which can appear in the Raman spectra below T_N as a consequence of the onset of long-range AF magnetic order and phonon modulation of the exchange constant [72]. This mode exhibits unusual variation both in intensity and frequency with decreasing temperature below T_N. Namely, intensity of this mode abruptly increases, whereas the frequency significantly hardens below T_N. This anomalous behavior results from a strong spin-phonon interaction [72]. The temperature variation of spin-phonon mode frequency for CuO nanowires of different mean diameter and bulk counterpart is shown Fig. 2.17B. The spin-phonon mode temperature variation can be well described by Eq. (2.27) (solid lines) for $S^2 \sim 1/4$[73] using empirical formula for $\phi(T) = 1-(T/T_N)^{\gamma}$ (solid lines) [79]. In such a way T_N and spin-phonon coupling constant $\lambda_{s\text{-ph}}$ can be estimated. As can be seen from Fig. 2.17B and C, with decreasing diameter, T_N and $\lambda_{s\text{-ph}}$ tend to decrease. This implies that the size effect weakens the strong spin-phonon interaction, favorizing the short-range AF ordering [11].

Another example of strong spin-phonon interaction was reported in multiferroic $BiFeO_3$ thin films [80] evidenced through the temperature behavior of the two-phonon Raman modes, $2A_4$, $2E_8$ and $2E_9$. These modes are positioned at around 968, 1110, and 1265 cm^{-1} at RT. Upon heating, as shown in Fig. 2.18A, all Raman modes slightly shift to

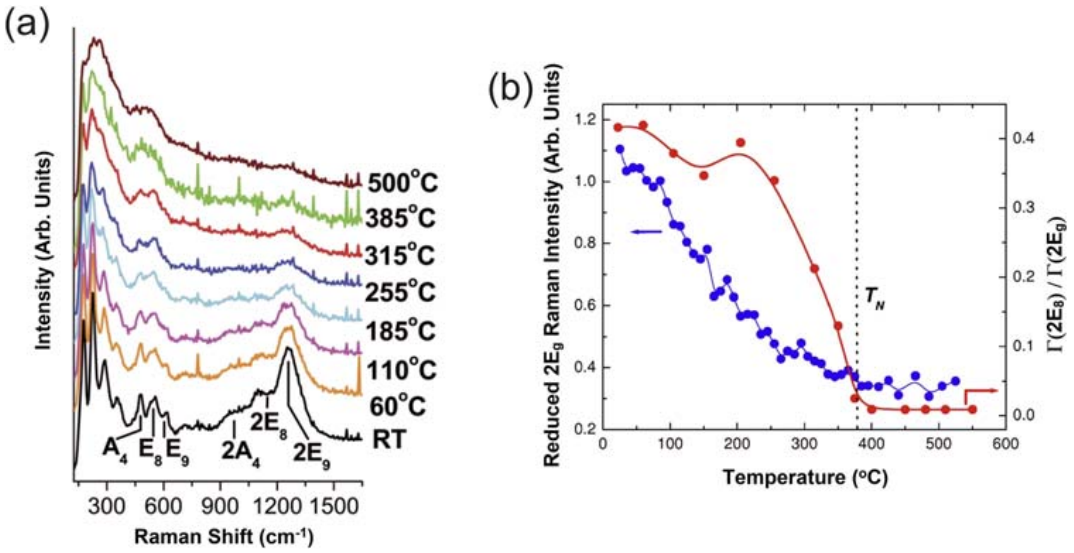

Figure 2.18

(A) Temperature dependence of unpolarized Raman spectra of $BiFeO_3$ film and (B) reduced integrated intensity of 1260 cm^{-1} two-phonon Raman mode (*blue dots*). Temperature dependence of the integrated intensity ratio between 2*E*8 and 2*E*9 two-phonon modes is presented with *red circles*. The *solid lines* are guide to the eye. *Reprinted from M.O. Ramirez, M. Krishnamurthi, S. Denev, A. Kumar, S.-Y. Yang, Y.-H. Chu, E. Saiz, J. Seidel, A.P. Pyatakov, A. Bush, D. Viehland, J. Orenstein, R. Ramesh, V. Gopalan, Two-phonon coupling to the antiferromagnetic phase transition in multiferroic $BiFeO_3$, Appl. Phys. Lett. 92 (2008) 022511 with the permission of AIP Publishing.*

[6]

lower frequency and broaden due to anharmonicity, but the integrated intensity of two-phonon modes drastically decrease, particularly of two-phonon mode $2E_9$. Above the Néel temperature, this mode almost disappeared. Eliminating the contribution from Bose-Einstein population, the reduced intensity of $2E_9$ mode is presented in Fig. 2.18B (blue circles) and compared to the reduced intensity of $2E_8$ mode (red circles). As can be seen, a remarkable decrease of the integrated intensity of $2E_9$ mode is seen when approaching T_N, and above the temperature of magnetic phase transition it is almost constant. The integrated intensity ratio, $\Gamma(2E_8)/\Gamma(2E_9)$, is almost constant up to 200 °C and abruptly decreases in the vicinity of Néel temperature, indicating strong spin-two-phonon coupling in $BiFeO_3$ [80].

9. Summary

This chapter presents a brief review how temperature-dependent RS comes to be of significant importance for investigating various phenomena in nanostructured materials. Raman spectra of diverse nanomaterials in the form of metal-oxide nanopowders, quantum dots, nanowires, nanoribbons, carbon-based, and multiferroic nanostructures were analyzed as examples.

It was shown that the application of RS at elevated temperatures is a very convenient method to study the anharmonic interactions through the evolution of optical phonon modes in nanophase materials. The temperature evolution of the Raman modes can be successfully modeled by PCM which incorporates size, strain, and anharmonic effects and enables to estimate the contribution of each of these effects. It was shown that the size, morphology, and size distribution largely determine which of the anharmonic processes (three or four-phonon anharmonic interaction) will be dominant, pointing out that phonon-phonon interactions can be different in nanomaterials compared to their bulk counterpart. Low-frequency RS provided the information about the acoustic phonons dynamics as a function of temperature in nanocrystalline solids as well. It was demonstrated that the decay dynamics of the acoustic phonons was complex and dependent not only on different size and size distribution, i.e., coalescence process at higher temperatures, but also on organic ligands with different elastic modulus and impurities bound to the nanoparticle surface.

Temperature-dependent Raman scattering has a potential to detect the formation of other structural phases, present even in small concentrations, through the appearance of new peaks characteristic for a certain crystalline structure. As a noncontact method of high spatial resolution, RS can be used in thermometry for the measurements of the local temperature or thermal conductivity of nanomaterials.

RS is a suitable optical method for probing lattice and charge excitations, as well as interplay between them. In the Raman spectra of low-dimensional materials electron-phonon interaction manifests itself by an asymmetric Fano line shape of the phonon modes. The electron-phonon coupling strength can be estimated directly from the fitting of the Raman spectra at different temperatures with the Fano function or from the linewidth of the phonon modes using Allen's formula. Besides, in nanophase materials, the electron-phonon interaction is sensitive to temperature and nanocrystallite size.

Special class of nanomaterials present magnetic and multiferroic nanomaterials. In these materials, it was shown that phonon frequency, linewidth, and integrated intensity may all be influenced by the exchange coupling between magnetic ions and from their temperature dependence it is possible to investigate both spin-ordering and spin-reorientation transitions, revealing more about the complexity of magnetic interactions in nanophase materials.

In summary, from the temperature induced changes of the Raman features (peak position, intensity, or linewidth) it is possible to predict many new thermophysical, electric, and magnetic nanomaterials properties.

Acknowledgment

The authors acknowledge funding by the Institute of Physics Belgrade, through the grant by the Serbian Ministry of Education, Science and Technological Development.

References

[1] C.S.S.R. Kumar, Raman Spectroscopy for Nanomaterials Characterization, Springer-Verlag Berlin Heidelberg, 2012.
[2] H. Richter, Z.P. Wang, L. Ley, The one phonon Raman spectrum in microcrystalline silicon, Solid State Commun. 39 (1981) 625−629.
[3] I.H. Campbell, P.M. Fauchet, The effects of microcrystal size and shape on the one phonon Raman spectra of crystalline semiconductors, Solid State Commun. 58 (1986) 739−741.
[4] L. Donetti, F. Gámiz, N. Rodriguez, F. Jimenez, C. Sampedro, Influence of acoustic phonon confinement on electron mobility in ultrathin silicon on insulator layers, Appl. Phys. Lett. 88 (2006) 122108.
[5] A.C. Gandhi, S.S. Gaikwad, J.-C. Peng, C.-W. Wang, T.S. Chan, S.Y. Wu, Strong electron-phonon coupling in superconducting bismuth nanoparticles, APL Mater. 7 (2019) 031111.
[6] G.S.N. Eliel, M.V.O. Moutinho, A.C. Gadelha, A. Righi, L.C. Campos, H.B. Ribeiro, P.-W. Chiu, K. Watanabe, T. Taniguchi, P. Puech, M. Paillet, T. Michel, P. Venezuela, M.A. Pimenta, Intralayer and interlayer electron−phonon interactions in twisted graphene heterostructures, Nat. Commun. 9 (2018) 1221.
[7] H. Rijckaert, P. Cayado, R. Nast, J.D. Sierra, M. Erbe, P.L. Dominguez, J. Hänisch, K. De Buysser, B. Holzapfel, I. Van Driessche, Superconducting HfO_2-$YBa_2Cu_3O_{7-\delta}$ nanocomposite films deposited using ink-jet printing of colloidal solutions, Coatings 10 (2020) 17.
[8] C.Y. Tsai, H.M. Cheng, H.R. Chen, K.F. Huang, L.N. Tsai, Y.H. Chu, C.H. Lai, W.F. Hsieh, Spin and phonon anomalies in epitaxial self-assembled $CoFe_2O_4$-$BaTiO_3$ multiferroic nanostructures, Appl. Phys. Lett. 104 (2014) 252905.

[9] D.M. Sagar, J.M. Atkin, P.K.B. Palomaki, N.R. Neale, J.L. Blackburn, J.C. Johnson, A.J. Nozik, M.B. Raschke, M.C. Beard, Quantum confined electron-phonon interaction in silicon nanocrystals, Nano Lett. 15 (2015) 1511−1516.
[10] D. Paramanik, S. Varma, Raman scattering characterization and electron phonon coupling strength for MeV implanted InP (111), J. Appl. Phys. 101 (2007) 023528.
[11] P.-H. Shih, C.-L. Cheng, S.Y. Wu, Short-range spin-phonon coupling in in-plane CuO nanowires: a low-temperature Raman investigation, Nanoscale Res. Lett. 8 (2013) 398.
[12] G.S. Doerk, C. Carraro, R. Maboudian, Temperature dependence of Raman spectra for individual silicon nanowires, Phys. Rev. B 80 (2009) 073306.
[13] M. Kazan, S. Pereira, M.R. Correia, P. Masri, Contribution of the decay of optical phonons into acoustic phonons to the thermal conductivity of AlN, Phys. Rev. B 77 (2008) 180302.
[14] J. Kulda, A. Debernardi, M. Cardona, F. de Geuser, E.E. Haller, Self-energy of zone-boundary phonons in germanium: ab initio calculations versus neutron spin-echo measurements, Phys. Rev. B 69 (2004) 045209.
[15] Z. Dohčević-Mitrović, Z.V. Popović, M. Šćepanović, Anharmonicity effects in nanocrystals studied by Raman scattering spectroscopy, Acta Phys. Pol. A 116 (2009) 36−41.
[16] G. Lucazeau, Effect of pressure and temperature on Raman spectra of solids: anharmonicity, J. Raman Spectrosc. 34 (2003) 478−496.
[17] A.A. Maradudin, A.E. Fein, Scattering of neutrons by an anharmonic crystal, Phys. Rev. B 128 (1962) 2589−2608.
[18] R.P. Lowndes, Anharmonic self-energy of a soft mode, Phys. Rev. Lett. 27 (1971) 1134−1136.
[19] M. Balkanski, R.F. Wallis, E. Haro, Anharmonic effects in light scattering due to optical phonons in silicon, Phys. Rev. B 28 (1983) 1928−1934.
[20] G. Morell, W. Pérez, E. Ching-Prado, R.S. Katiyar, Anharmonic interactions in beryllium oxide, Phys. Rev. B 53 (1996) 5388−5395.
[21] P.G. Klemens, Anharmonic decay of optical phonons, Phys. Rev. 148 (1966) 845−848.
[22] T.R. Hart, R.L. Aggarwal, B. Lax, Temperature dependence of Raman scattering in silicon, Phys. Rev. B 1 (1970) 638−642.
[23] Z. Dohčević-Mitrović, M. Grujić-Brojčin, M. Šćepanović, Z.V. Popović, S. Bošković, B. Matović, M. Zinkevich, F. Aldinger, The size and strain effects on the Raman spectra of $Ce_{1-x}Nd_xO_{2-\delta}$ ($0 \leq x \leq 0.25$) nanopowders, Solid State Commun. 137 (2006) 387−390.
[24] Z. Dohčević-Mitrović, M. Grujić-Brojčin, M. Šćepanović, Z.V. Popović, S. Bošković, B. Matović, M. Zinkevich, F. Aldinger, $Ce_{1-x}Y(Nd)_xO_{2-\delta}$ nanopowders: potential materials for intermediate temperature solid oxide fuel cells, J. Phys. Condens. Matter 18 (2006) S2061−S2068.
[25] Z.D. Dohčević-Mitrović, M. Radović, M. Šćepanović, M. Grujić-Brojčin, Z.V. Popović, B. Matović, S. Bošković, Temperature-dependent Raman study of $Ce_{0.75}Nd_{0.25}O_{2-\delta}$ nanocrystals, Appl. Phys. Lett. 91 (2007) 203118.
[26] J. Spanier, R. Robinson, F. Zhang, S.-W. Chan, I. Herman, Size-dependent properties of CeO_{2-y} nanoparticles as studied by Raman scattering, Phys. Rev. B 64 (2001) 245407.
[27] S. Askrabić, Z.D. Dohcević-Mitrović, M. Radović, M. Scepanović, Z.V. Popović, Phonon-phonon interactions in $Ce_{0.85}Gd_{0.15}O_{2-\delta}$ nanocrystals studied by Raman spectroscopy, J. Raman Spectrosc. 40 (2009) 650−655.
[28] H.K. Yadav, R.S. Katiyar, V. Gupta, Temperature dependent dynamics of ZnO nanoparticles probed by Raman scattering: a big divergence in the functional areas of nanoparticles and bulk material, Appl. Phys. Lett. 100 (2012) 051906.
[29] Y.L. Du, Y. Deng, M.S. Zhang, Variable-temperature Raman scattering study on anatase titanium dioxide nanocrystals, J. Phys. Chem. Solid. 67 (2006) 2405−2408.
[30] K. Gao, Strong anharmonicity and phonon confinement on the lowest-frequency Raman mode of nanocrystalline anatase TiO_2, Phys. Status Solidi 244 (2007) 2597−2604.

[31] M.J. Šćepanović, M. Grujić-Brojčin, Z.D. Dohčević-Mitrović, Z.V. Popović, Temperature dependence of the lowest frequency E_g Raman mode in laser-synthesized anatase TiO_2 nanopowder, Appl. Phys. A 86 (2007) 365−371.
[32] G.R. Hearne, J. Zhao, A.M. Dawe, V. Pischedda, M. Maaza, M.K. Nieuwoudt, P. Kibasomba, O. Nemraoui, J.D. Comins, M.J. Witcomb, Effect of grain size on structural transitions in anatase TiO_2: a Raman spectroscopy study at high pressure, Phys. Rev. B 70 (2004) 134102.
[33] S. Aškrabić, Z. Dohčević-Mitrović, A. Kremenović, N. Lazarević, V. Kahlenberg, Z.V. Popović, Oxygen vacancy-induced microstructural changes of annealed CeO_{2-x} nanocrystals, J. Raman Spectrosc. 43 (2012) 76−81.
[34] J.V. Silveira, L.L. Vieira, J.M. Filho, A.J.C. Sampaio, O.L. Alvesc, A.G. Souza Filho, Temperature-dependent Raman spectroscopy study in MoO_3 nanoribbons, J. Raman Spectrosc. 43 (2012) 1407−1412.
[35] J.M. Todorović, Z.D. Dohčević-Mitrović, D.M. Đokić, D. Mihailović, Z.V. Popović, Investigation of thermostability and phonon-phonon interactions in $Mo_6S_3I_6$ nanowires by Raman scattering spectroscopy, J. Raman Spectrosc. 41 (2010) 978−982.
[36] M. Testa-Anta, M.A. Ramos-Docampo, M. Comesaña-Hermo, B. Rivas-Murias, V. Salgueiriño, Raman spectroscopy to unravel the magnetic properties of iron oxide nanocrystals for bio-related applications, Nanoscale Adv. 1 (2019) 2086−2103.
[37] M. Sendova, B.D. Hosterman, R. Raud, T. Hartmann, D. Koury, Temperature-dependent, micro-Raman spectroscopic study of barium titanate nanoparticles, J. Raman Spectrosc. 46 (2015) 25−31.
[38] L. Chen, K. Rickey, Q. Zhao, C. Robinson, X. Ruan, Effects of nanocrystal shape and size on the temperature sensitivity in Raman thermometry, Appl. Phys. Lett. 103 (2013) 083107.
[39] A.A. Balandin, S. Ghosh, W.Z. Bao, I. Calizo, D. Teweldebrhan, F. Miao, C.N. Lau, Superior thermal conductivity of single-layer graphene, Nano Lett. 8 (2008) 902−907.
[40] Q. Li, C. Liu, X. Wang, S. Fan, Measuring the thermal conductivity of individual carbon nanotubes by the Raman shift method, Nanotechnology 20 (2009) 145702.
[41] S. Ghosh, I. Calizo, D. Teweldebrhan, E.P. Pokatilov, D.L. Nika, A.A. Balandin, W. Bao, F. Miao, C.N. Lau, Extremely high thermal conductivity of graphene: prospects for thermal management applications in nanoelectronic circuits, Appl. Phys. Lett. 92 (2008) 151911.
[42] M. Fujii, T. Nagareda, S. Hayashi, K. Yamamoto, Low-frequency Raman scattering from small silver particles embedded in SiO_2 thin films, Phys. Rev. B 44 (1991) 6243−6248.
[43] L. Saviot, B. Champagnon, E. Duval, A.I. Ekimov, I.A. Kudriavtsev, Size dependence of acoustic and optical vibrational modes of CdSe nanocrystals in glasses, J. Non-Cryst. Solids 197 (1996) 238−246.
[44] A. Diéguez, A. Romano-Rodríguez, Nondestructive assessment of the grain size distribution of SnO nanoparticles by low-frequency Raman spectroscopy, Appl. Phys. Lett. 71 (1997) 1957−1959.
[45] M. Ivanda, K. Furić, S. Musić, M. Ristić, M. Gotić, D. Ristić, A.M. Tonejc, I. Djerdj, M. Mattarelli, M. Montagna, F. Rossi, M. Ferrari, A. Chiasera, Y. Jestin, G.C. Righini, W. Kiefer, R.R. Gonçalves, Low wavenumber Raman scattering of nanoparticles and nanocomposite materials, J. Raman Spectrosc. 38 (2007) 647−659.
[46] E. Duval, Far-infrared and Raman vibrational transitions of a solid sphere: selection rules, Phys. Rev. B 46 (1992) 5795−5797.
[47] M. Montagna, R. Dusi, Raman scattering from small spherical particles, Phys. Rev. B 52 (1995) 10080−10089.
[48] H. Lamb, On the vibrations of an elastic sphere, Proc. Lond. Math. Soc. 13 (1882) 189−212.
[49] R. Shuker, W. Gammon, Raman-scattering selection-rule breaking and the density of states in amorphous materials, Phys. Rev. Lett. 25 (1970) 222−225.
[50] A.J. Mork, E.M.Y. Lee, W.A. Tisdale, Temperature dependence of acoustic vibrations of CdSe and CdSe-CdS core-shell nanocrystals measured by low-frequency Raman spectroscopy, Phys. Chem. Chem. Phys. 18 (2016) 28797−28801.

[51] H.K. Yadav, K. Sreenivas, R.S. Katiyar, V. Gupta, Softening behavior of acoustic phonon mode in ZnO nanoparticles: the effect of impurities and particle size variation with temperature, J. Raman Spectrosc. 42 (2011) 1620−1625.
[52] U. Fano, Effects of configuration interaction on intensities and phase shifts, Phys. Rev. 124 (1961) 1866−1878.
[53] W.-L. Zhang, H. Li, D. Xia, H.W. Liu, Y.-G. Shi, J.L. Luo, J. Hu, P. Richard, H. Ding, Observation of a Raman-active phonon with Fano line shape in the quasi-one-dimensional superconductor $K_2Cr_3As_3$, Phys. Rev. B 92 (2015) 060502.
[54] P.B. Allen, Neutron spectroscopy of superconductors, Phys. Rev. B 6 (1972) 2577−2579.
[55] J. Winter, H. Kuzmany, Landau damping and lifting of vibrational degeneracy in metallic potassium fulleride, Phys. Rev. B 53 (1996) 655−661.
[56] Z.V. Popović, Z.D. Dohčević-Mitrović, N. Paunović, M. Radović, Evidence of charge delocalization in $Ce_{1-x}Fe_x^{2+(3+)}O_{2-y}$ nanocrystals (x=0, 0.06, 0.12), Phys. Rev. B 85 (2012) 014302.
[57] D. Chen, Y.-L. Jia, T.-T. Zhang, Z. Fang, K. Jin, P. Richard, H. Ding, Raman study of electron-phonon coupling in thin films of the spinel oxide superconductor $LiTi_2O_4$, Phys. Rev. B 96 (2017) 094501.
[58] N. Bonini, M. Lazzeri, N. Marzari, F. Mauri, Phonon Anharmonicities in graphite and graphene, Phys. Rev. B 99 (2007) 176802.
[59] M. Lazzeri, S. Piscanec, F. Mauri, A.C. Ferrari, J. Robertson, Phonon linewidths and electron-phonon coupling in graphite and nanotubes, Phys. Rev. Lett. 73 (2006) 155426.
[60] W. Yu, M. Han, K. Jiang, Z. Duan, Y. Li, Z. Hu, J. Chu, Enhanced Fröhlich interaction of semiconductor cuprous oxide films determined by temperature-dependent Raman scattering and spectral transmittance, J. Raman Spectrosc. 44 (2013) 142−146.
[61] H.-M. Cheng, K.-F. Lin, H.-C. Hsu, C.-J. Lin, L.-J. Lin, W.-F. Hsieh, Enhanced resonant Raman scattering and electron-phonon coupling from self-assembled secondary ZnO nanoparticles, J. Phys. Chem. B 109 (2005) 18385−18390.
[62] S. Seki, N. Kida, S. Kumakura, R. Shimano, Y. Tokura, Electromagnons in the spin collinear state of a triangular lattice antiferromagnet, Phys. Rev. Lett. 105 (2010) 097207.
[63] D. Rogers, Y.J. Choi, E.C. Standard, T.D. Kang, K.H. Ahn, A. Dubroka, P. Marsik, C. Wang, C. Bernhard, S. Park, S.-W. Cheong, M. Kotelyanskii, A.A. Sirenko, Adjusted oscillator strength matching for hybrid magnetic and electric excitations in $Dy_3Fe_5O_{12}$ garnet, Phys. Rev. B 83 (2011) 174407.
[64] A.B. Sushkov, R. Valdés Aguilar, S. Park, S.-W. Cheong, H.D. Drew, Electromagnons in multiferroic YMn_2O_5 and $TbMn_2O_5$, Phys. Rev. Lett. 98 (2007) 027202.
[65] I. Kézsmárki, N. Kida, H. Murakawa, S. Bordács, Y. Onose, Y. Tokura, Enhanced directional dichroism of terahertz light in resonance with magnetic excitations of the multiferroic $Ba_2CoGe_2O_7$ oxide compound, Phys. Rev. Lett. 106 (2011) 057403.
[66] A. Pimenov, A.A. Mukhin, V.Y. Ivanov, V.D. Travkin, A.M. Balbashov, A. Loidl, Possible evidence for electromagnons in multiferroic manganites, Nat. Phys. 2 (2006) 97−100.
[67] M. Cazayous, Y. Gallais, A. Sacuto, R. de Sousa, D. Lebeugle, D. Colson, Possible observation of cycloidal electromagnons in $BiFeO_3$, Phys. Rev. Lett. 101 (2008) 037601.
[68] M.K. Singh, R.S. Katiyar, J.F. Scott, New magnetic phase transitions in $BiFeO_3$, J. Phys. Condens. Matter 20 (2008) 252203.
[69] W. Azeem, S. Riaz, A. Bukhtiar, S.S. Hussain, Y. Xu, S. Naseem, Ferromagnetic ordering and electromagnons in microwave synthesized $BiFeO_3$ thin films, J. Magn. Magn Mater. 475 (2019) 60−69.
[70] R. De Sousa, J.E. Moore, Optical coupling to spin waves in the cycloidal multiferroic $BiFeO_3$, Phys. Rev. B 77 (2008) 012406.
[71] S. Venugopalan, M. Dutta, A.K. Ramdas, J.P. Remeika, Magnetic and vibrational excitations in rare-earth orthoferrites: a Raman scattering study, Phys. Rev. B 31 (1985) 1490−1497.
[72] X.K. Chen, J.C. Irwin, J.P. Franck, Evidence for a strong spin-phonon interaction in cupric oxide, Phys. Rev. B 52 (1995) R13130−R13133.

[6]

[73] D.J. Lockwood, Spin-phonon interaction and mode softening in NiF_2, Low Temp. Phys. 28 (2002) 505−509.
[74] X.-B. Chen, N.T.M. Hien, K. Han, J.C. Sur, N.H. Sung, B.K. Cho, I.-S. Yang, Raman studies of spin-phonon coupling in hexagonal $BaFe_{12}O_{19}$, J. Appl. Phys. 114 (2013) 013912.
[75] E. Granado, A. García, J.A. Sanjurjo, C. Rettori, I. Torriani, F. Prado, R.D. Sánchez, A. Caneiro, S.B. Oseroff, Magnetic ordering effects in the Raman spectra of $La_{1-x}Mn_{1-x}O_3$, Phys. Rev. B 60 (1999) 11879−11882.
[76] J. Laverdière, S. Jandl, A.A. Mukhin, I.V. Yu, V.G. Ivanov, M.N. Iliev, Spin-phonon coupling in orthorhombic $RMnO_3$ (R=Pr, Nd, Sm, Eu, Gd, Tb, Dy, Ho, Y): a Raman Study, Phys. Rev. B 73 (2006) 214301.
[77] R. Katoch, C.D. Sekhar, V. Adyam, J.F. Scott, R. Gupta, A. Garg, Spin phonon interactions and magnetodielectric effects in multiferroic $BiFeO_3$−$PbTiO_3$, J. Phys. Condens. Matter 28 (2016) 075901.
[78] A. Jaiswal, R. Das, T. Maity, K. Vivekanand, S. Adyanthaya, P. Poddar, Temperature-dependent Raman and dielectric spectroscopy of $BiFeO_3$ nanoparticles: signatures of spin-phonon and magnetoelectric coupling, J. Phys. Chem. C 114 (2010) 12432−12439.
[79] C.-H. Hung, P.-H. Shih, F.-Y. Wu, W.-H. Li, S.Y. Wu, T.S. Chan, H.-S. Sheu, Spin-phonon coupling effects in antiferromagnetic Cr_2O_3 nanoparticles, J. Nanosci. Nanotechnol. 10 (2010) 4596−4601.
[80] M.O. Ramirez, M. Krishnamurthi, S. Denev, A. Kumar, S.-Y. Yang, Y.-H. Chu, E. Saiz, J. Seidel, A.P. Pyatakov, A. Bush, D. Viehland, J. Orenstein, R. Ramesh, V. Gopalan, Two-phonon coupling to the antiferromagnetic phase transition in multiferroic $BiFeO_3$, Appl. Phys. Lett. 92 (2008) 022511.

Processing and Application of Ceramics 14 [2] (2020) 102–112
https://doi.org/10.2298/PAC2002102D

Influence of oxygen vacancy defects and cobalt doping on optical, electronic and photocatalytic properties of ultrafine $SnO_{2-\delta}$ nanocrystals

Zorana D. Dohčević-Mitrović[1,*], Vinicius D. Araújo[2], Marko Radović[3], Sonja Aškrabić[1], Guilherme R. Costa[4], Maria Ines B. Bernardi[4], Dejan M. Djokić[1], Bojan Stojadinović[1], Marko G. Nikolić[5]

[1]*Nanostructured Matter Laboratory, Institute of Physics Belgrade, University of Belgrade, Pregrevica 118, 11080 Belgrade, Serbia*
[2]*NanoA-UACSA, Universidade Federal Rural de Pernambuco, UFRPE, Cabo de Santo Agostinho, PE, Brazil*
[3]*University of Novi Sad, Group for Nano and Microelectronics, Biosense Institute, Novi Sad, Serbia*
[4]*Instituto de Física de São Carlos, Universidade de São Paulo, USP, 13560-970, São Carlos – SP, Brasil*
[5]*Institute of Physics Belgrade, University of Belgrade, P.O. Box 68, Pregrevica 118, 11080 Belgrade, Serbia*

Received 12 November 2019; Received in revised form 21 February 2020; Accepted 15 March 2020

Abstract

Ultrafine pure and cobalt doped $SnO_{2-\delta}$ nanocrystals ($Sn_{1-x}Co_xO_{2-\delta}$, $0 \leq x \leq 0.05$) were synthesized by microwave-assisted hydrothermal method. The as-prepared nanocrystals have single phase tetragonal rutile structure. With increase of Co content ($x > 0.01$), Co entered into SnO_2 lattice in mixed Co^{2+}/Co^{3+} state. Pronounced blue shift of the band gap with cobalt doping originated from the combined effect of quantum confinement and Burnstain-Moss shift. Raman and photoluminescence study revealed oxygen deficient structure of $SnO_{2-\delta}$ for which the prevalent defects are in the form of in-plane oxygen vacancies. Co-doping induced decrease of in-plane oxygen vacancy concentration and luminescence quenching. $SnO_{2-\delta}$ exhibited significantly better photocatalytic activity under UV light irradiation, than Co-doped samples due to better UV light absorption and increased concentration of in-plane oxygen vacancies which, as shallow donors, enable better electron-hole separation and faster charge transport.

Keywords: *SnO_2 nanopowders, wet-chemical synthesis, defects, optical properties, photocatalysis*

I. Introduction

Tin oxide (SnO_2) is an n-type semiconductor with large band gap (3.6 eV) at room temperature. Because of its unique electronic, optical and electrochemical properties, SnO_2 is widely used in dye-sensitized solar cells, transparent conductive electrodes, solid state sensors, lithium-ion batteries and catalysis [1–7]. During the past decade, SnO_2 nanostructures have become one of the most important oxide nanostructures due to their exceptional properties and potential applications which are strongly influenced by size effects and morphology [8].

In the past decade various efforts were devoted to the synthesis of SnO_2 nanostructures with controlled size and morphology. SnO_2 nanostructures like thin films, nanobelts, nanotubes or nanowires, nanodisks and nanocrystals have been prepared using different methods, such as carbothermal reduction process, hydrothermal and solvothermal, chemical vapour condensation, laser ablation, sol-gel and molten salt techniques [9–18]. However, for most of these methods relatively high temperatures are required during the synthesis process and the samples are usually subjected to additional thermal treatment in order to achieve good crystallinity. In recent years hydrothermal approaches appeared to be widely applied as SnO_2 nanostructures can be obtained with different morphologies and tunable size at mild temperatures [8,19]. Microwave-assisted hydrothermal

*Corresponding author: tel: +381 113713024,
e-mail: *zordoh@ipb.ac.rs*

[7]

synthesis (MAH) became a very promising method for obtaining size and morphology controllable oxide nanostructures due to the unique advantages, such as fast heating rate and uniform heating without superheating of the solvent, which results in small particle size, narrow size distribution and high purity of the obtained nanopowders. Therefore, MAH appeared to be very convenient method for obtaining ultrafine SnO_2 nanopowders [19,20].

SnO_2 nanostructures are generally less studied as potential photocatalysts compared to TiO_2 and ZnO, despite its crystalline structure being similar to TiO_2 and good properties such as high photochemical stability, non-toxic nature, strong oxidizing power, and low-cost [21]. In order to improve the photocatalytic efficiency of SnO2, selective doping with metal ions, transition metals (gold, manganese, silver and iron) and rare–earth elements (Ce, Sm, Gd) was performed and well presented in the review paper by Al-Hamdi *et al.* [21]. Among the transition metals, cobalt is rarely applied as dopant. In fact, there are only few papers dedicated to potential applicability of Co-doped SnO_2 nanostructures as photocatalysts [22–24], but none of them investigated the synergic influence of defective nature and Co-doping on photocatalytic properties of very fine SnO_2 nanocrystals. It is well known that photocatalytic efficiency of metal oxide nanostructures can be influenced by the presence of intrinsic defects such as oxygen vacancies [25–28]. The presence of oxygen vacancies strongly influences the charge recombination process and the band gap structure. Namely, oxygen vacancies introduce the defect levels (near conduction or valence band) inside the gap and behave as trapping centres for photogenerated carriers preventing the fast recombination. Besides, oxygen vacancies can facilitate the transferring of charge carriers to adsorbed species (OH^- or water molecules and dissolved oxygen present on the surface of the catalyst) and enhance the formation of reactive radicals which are responsible for improved photocatalytic activity of oxide nanostructures [26,27]. Moreover, the formation of defect states inside the gap reduces the band gap and extends the absorption to visible light [25,27]. The prominent intrinsic defects in SnO_2 nanostructures are oxygen vacancies as well, which form donor/acceptor states inside the SnO_2 gap, influencing its electronic structure and making it conductive [4]. As oxygen vacancies play a critical role in many new physical phenomena, it is important to investigate associated changes in the optical and electronic properties of pure and Co-doped SnO_2 nanomaterials which can have a strong impact on photocatalytic activity of these materials.

In the work presented here, ultrafine, nonstoichiometric pristine and Co-doped $SnO_{2-\delta}$ nanopowders were synthesized via simple and cost effective microwave-assisted hydrothermal method. This paper intends to explore how defective structure and Co-doping provoke changes of optical and electronic properties of $SnO_{2-\delta}$ nanocrystals influencing the photocatalytic performances.

II. Experimental procedure

2.1. Materials preparation

$Sn_{1-x}Co_xO_{2-\delta}$ (where x = 0, 1, 3 and 5 mol%) nanopowders were synthesized by microwave-assisted hydrothermal method using $SnCl_4 \cdot 5\,H_2O$ (98%, Aldrich), $CoCl_2 \cdot 6\,H_2O$, NaOH and HCl as starting precursors. Initially, 1 ml of hydrochloric acid was added to 10 ml of distilled water at 50 °C resulting in a solution with pH between 0 and 1. Next, 17.529 g of $SnCl_4 \cdot 5\,H_2O$ was added and the mixed solution was homogenized under stirring with simultaneous increasing of the water amount to approximately 50 ml. In a case of the doped samples, 0.119 g, 0.357 g and 0.595 g of $CoCl_2 \cdot 6\,H_2O$ were added to obtain 1, 3 and 5 mol% Co-doped samples, respectively. NaOH was added dropwise under vigorous stirring until the pH of the solution was adjusted to 8. The mixed solution was placed in a 110 ml sealed Teflon autoclave and subjected to microwave heating, applying 2.45 GHz of microwave radiation at a maximum power of 800 W. The as-prepared solution was heated at 140 °C for 10 min using heating rate of 14 °C/min and then air-cooled to room temperature. The as-prepared undoped and Co-doped $SnO_{2-\delta}$ nanopowders were submitted to dialysis in order to be separated from the solution and then dried at 80 °C for 12 h.

2.2. Materials characterization

The crystalline structure and average crystallite size of the $Sn_{1-x}Co_xO_{2-\delta}$ samples were evaluated using X-ray diffraction (XRD) measurements. The measurements were carried out using an automatic X-ray diffractometer (Rigaku, Rotaflex RU200B) with CuKα radiation (50 kV, 100 mA, λ = 1.5405 Å) in a θ–2θ configuration using a graphite monochromator. The 2θ scanning range was between 20 and 70°, with a step size of 0.02°. Microstructural analysis was made by transmission electron microscopy (TEM) FEI Titan 60-300 operating at voltages between 60 and 300 kV, using a field emission gun (FEG) with an objective lens (Super Twin) and a corrector that allows resolution of 0.08 nm.

Micro-Raman scattering measurements were performed at room temperature in the backscattering configuration on Tri Vista 557 Raman system equipped with a nitrogen-cooled CCD detector, using 532 nm laser line of optically pumped semiconductor laser (Coherent Verdi G) as an excitation source. UV-visible diffuse reflectance spectra were acquired with a Cary 5G spectrophotometer in the 200–800 nm range. Diffuse reflectance spectra were transformed into the absorbance spectra by the Kubelka-Munk method. The ellipsometric measurements were performed using high resolution variable angle spectroscopic ellipsometer (SOPRA GES5E-IRSE) of the rotating polarizer type. The data

[7]

were collected at room temperature in the UV-Vis spectral range with a resolution of 0.02 eV, for the incidence angle of 70°. Photoluminescence emission measurements were performed at room temperature using Spex Fluorolog spectrofluorometer with C31034 cooled photomultiplier under Xenon lamp excitation at 380 nm.

2.3. Photocatalytic experiments

The photocatalytic activity of the $Sn_{1-x}Co_xO_{2-\delta}$ samples, for the degradation of methylene blue (MB) as model pollutant, was tested under UV illumination. The different samples with the same photocatalyst amount (150 mg/l) were immersed in 20 ml of an aqueous solution of methylene blue (5.0 mg/l). The beakers were placed in a photo-reactor at controlled temperature (15 °C), under magnetic stirring, and were illuminated by six 15 W UV lamps (TUV Philips, maximum intensity at 254 nm). The solution was placed in the dark for 60 min to reach the adsorption/desorption equilibrium before UV light exposure. Blank experiment without UV irradiation demonstrated no adsorption of MB dye on the surface of the $Sn_{1-x}Co_xO_{2-\delta}$ samples. The photocatalytic experiments were conducted at the natural pH = 6 of MB dye. At regular time intervals 2 ml aliquots were taken, centrifuged to remove any catalyst particles and the concentration of the dye was determined by UV-Vis absorption spectrophotometer (Shimadzu-UV-1601 PC) monitoring the variation of absorbance at 663 nm.

The formation of hydroxyl radicals ($OH^{\bullet}$) on the surface of the $SnO_{2-\delta}$ sample under the UV light illumination was examined by photoluminescence (PL) technique using terephthalic acid (TA) as a probe molecule. The detailed experimental procedure was described in reference [29]. TA is known to react with $OH^{\bullet}$ radicals induced on the photocatalyst's surface where it produces highly fluorescent 2-hydroxyterephthalic acid which shows an intense PL peak at around 425 nm. The intensity of this peak is proportional to the amount of $OH^{\bullet}$ radicals [30,31] produced in the photocatalytic process. The changes of the 425 nm PL peak intensity were measured at room temperature using 315 nm excitation.

III. Results and discussion

3.1. Crystal structure and morphology

Figure 1a shows XRD patterns of the $Sn_{1-x}Co_xO_{2-\delta}$ ($0 \le x \le 0.05$) nanopowders, whereas the Rietveld refined XRD spectra of the $SnO_{2-\delta}$ and $Sn_{0.95}Co_{0.05}O_{2-\delta}$ samples are presented in Figs. 1b and 1c. The XRD patterns of all the samples revealed single phase tetragonal structure (cassiterite phase). The XRD peaks at 26.6, 33.8, 51.9 and 65.8° can be assigned to (110), (101), (211) and (301) planes, which are in good agreement with literature data (ICDS № 9163). No secondary phases like Co oxides, Co clusters or other tin oxide phases were observed. Moreover, broad diffraction peaks of low intensities compared to those of bulk SnO_2, point to low crystallinity and small crystallite size of the SnO_2 nanoparticles.

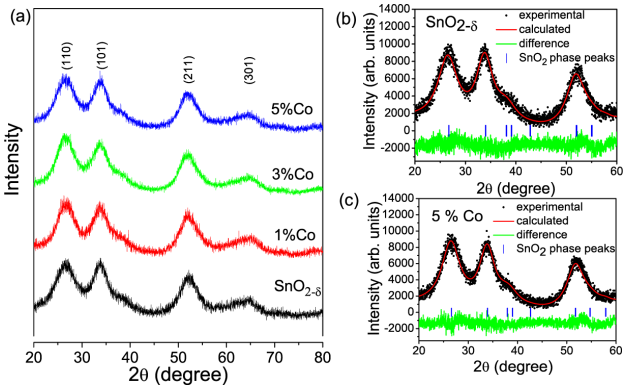

Figure 1. XRD patterns of $Sn_{1-x}Co_xO_{2-\delta}$ nanocrystals ($0 \le x \le 0.05$) indexed to tetragonal rutile structure of SnO_2 (a), Rietveld refined XRD spectra of $SnO_{2-\delta}$ (b) and $Sn_{0.95}Co_{0.05}O_{2-\delta}$ (c) nanoparticles

The average lattice parameters and unit cell volume obtained from the Rietveld refinement data are given in Table 1. These results showed an expansion of the SnO_2 unit cell with increasing cobalt content up to 5%. This variation originates from the substitution of smaller Sn^{4+} cations (0.83 Å) with larger Co^{2+} cations in high spin state (0.89 Å) [32]. The slight shrinkage of the unit cell observed for the 5% Co-doped sample can be related to the presence of increased amount of smaller Co^{3+} cations (*ls*: 0.68 Å or *hs*: 0.75 Å). The average crystallite size (D) of the $Sn_{1-x}Co_xO_{2-\delta}$ nanocrystals was calculated with the Scherrer formula using the 110 reflection and their values are reported in Table 1. Obviously, the mean crystallite sizes of the undoped and Co-doped samples are less than Bohr exciton radius (2.7 nm for SnO_2) [33] and with increased Co-doping the crystallite size of the $Sn_{1-x}Co_xO_{2-\delta}$ nanocrystals decreases. Such a trend implies that Co-doping has an inhibiting effect on the crystal growth. This inhibiting effect of Co on the crystal grains growth was already confirmed in the work of Babu *et al.* [34].

TEM images of the undoped and Co-doped $SnO_{2-\delta}$ samples are presented in Fig. 2. TEM images revealed

Table 1. Lattice parameters (a, c), unit cell volume (V) and average crystallite size (D) of the $Sn_{1-x}Co_xO_{2-\delta}$ nanocrystals

Sample	$a = b$ [Å]	c [Å]	V [Å^3]	D [nm]
$SnO_{2-\delta}$	4.722 ± 0.002	3.180 ± 0.003	70.905	2.5
$Sn_{0.99}Co_{0.01}O_{2-\delta}$	4.747 ± 0.002	3.201 ± 0.003	72.131	2.4
$Sn_{0.97}Co_{0.03}O_{2-\delta}$	4.759 ± 0.002	3.206 ± 0.002	72.609	2.3
$Sn_{0.95}Co_{0.05}O_{2-\delta}$	4.744 ± 0.002	3.186 ± 0.002	71.703	2.2

[7]

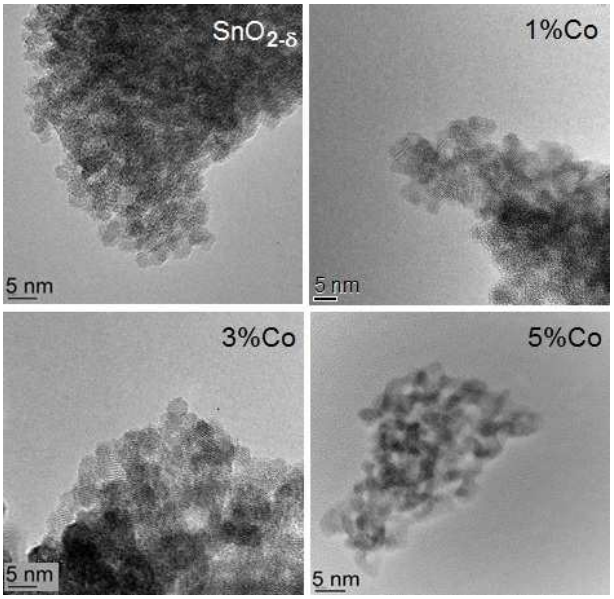

Figure 2. TEM images of $Sn_{1-x}Co_xO_{2-\delta}$ ($0 \le x \le 0.05$) nanoparticles

that the undoped $SnO_{2-\delta}$ sample is composed of single crystalline nanoparticles of very small size and quasi-spherical shape. The morphology of the $Sn_{1-x}Co_xO_{2-\delta}$ nanoparticles remained the same with Co-doping. The particles are of spherical shape with the size less than 3 nm, which is in good agreement with the results obtained from XRD data. The observed agglomeration of the $Sn_{1-x}Co_xO_{2-\delta}$ nanoparticles can be ascribed to small crystallite sizes.

3.2. Raman analysis

SnO_2 tetragonal rutile crystalline structure (space group $P4_2/mnm$) has four active Raman modes (non-degenerate A_{1g}, B_{1g}, B_{2g} modes, and a doubly degenerated E_g mode), two active infrared modes (A_{2u} and E_u) and two silent modes (A_{2g}, B_{1u}) [35]. The positions of A_{1g}, B_{1g}, B_{2g} and E_g Raman modes in SnO_2 single crystal under ambient conditions are 634, 123, 776 and 475 cm^{-1}, respectively, and the A_{1g} and E_g modes are of much higher intensity compared to B_{1g} and B_{2g} modes [35].

The Raman spectra of nanocrystalline, non-stoichiometric $SnO_{2-\delta}$ are modified in comparison with single-crystal or polycrystalline SnO_2, because Raman spectroscopy is more sensitive to intrinsic defects and confinement effect than conventional XRD technique. Namely, the position, bandwidth and intensity of Raman modes are size dependent, i.e. Raman modes are broadened, of lower intensity and shifted towards lower or higher energies depending on phonon dispersion curves. Besides, new modes of defect origin can appear [36,37]. The room temperature Raman spectra of the $Sn_{1-x}Co_xO_{2-\delta}$ nanocrystals are presented in Fig. 3 and they are deconvoluted using Lorentzian profiles (full lines in Fig. 3).

In the Raman spectrum of the pure $SnO_{2-\delta}$, the most prominent mode is located at ~574 cm^{-1}. This mode

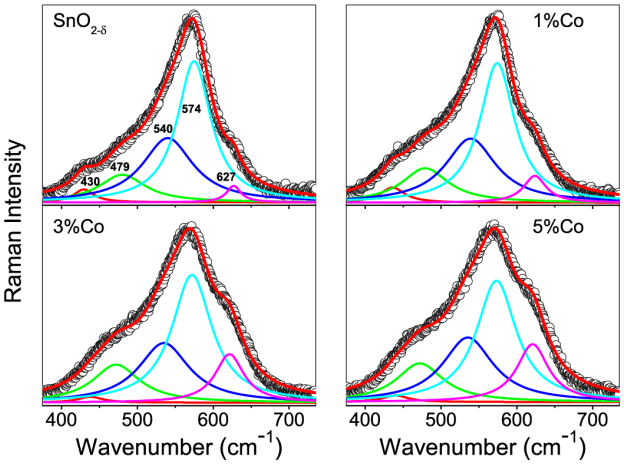

Figure 3. Deconvoluted room-temperature Raman spectra of $Sn_{1-x}Co_xO_{2-\delta}$ nanoparticles

is characteristic for non-stoichiometric $SnO_{2-\delta}$ and it is not present in the Raman spectra of SnO_2 single-crystal [35]. Density functional calculations performed by Liu *et al.* [38] have shown that this mode arises from in-plane oxygen vacancies (V_{Oin}) in the surface region of $SnO_{2-\delta}$ nanoparticles, intensity of which is proportional to their concentration. In very fine nanoparticles this mode has the highest intensity due to the increased concentration of oxygen vacancies. Raman mode at ~627 cm^{-1} can be ascribed to the A_{1g} mode of rutile SnO_2 structure. This mode is of lower intensity, broadened and shifted to lower wave numbers compared to the bulk counterpart, due to the phonon confinement effect [37]. As the crystallite size of the undoped $SnO_{2-\delta}$ is smaller than the Bohr exciton radius, the size effect can be very pronounced in this sample. Another broad Raman mode at ~479 cm^{-1} is assigned to E_g mode and it is shifted to higher wavenumbers with size decrease of $SnO_{2-\delta}$ nanocrystals [37]. Besides these modes, additional modes at around 430 and 540 cm^{-1} appear. These new modes are usually seen in very fine SnO_2 nanoparticles [37–39], nanotubes [40] or nanoribbons [41] because of the increased degree of local disorder, i.e. loss in long-range order due to the large number of lattice vacant positions, especially at the surface of nanoparticles. These modes are of high intensity in small nanoparticles and disappear with particle size increase. According to some literature data, due to the relaxation of the selection rules in nanostructured SnO_2, the mode at 540 cm^{-1} is assigned to the Raman forbidden mode (B_{1u}) [40,41], whereas the new mode at around 430 cm^{-1} can be assigned to the oxygen vacancy clusters (V_C) [39]. The A_{1g} and E_g modes exhibited redshift and broadening with Co-doping. The redshift and broadening of these modes are expected with substitution of Sn^{4+} ions with larger Co^{2+} ions and decreased crystallite size due to the phonon confinement effect. The positions and intensities of the A_{1g}, E_g and oxygen vacancy related modes (V_{Oin} and V_C) are presented in Fig. 4. As it can be seen from Fig. 4, the intensity of A_{1g} mode increases with increased Co concentration, whereas the intensity of E_g

[7]

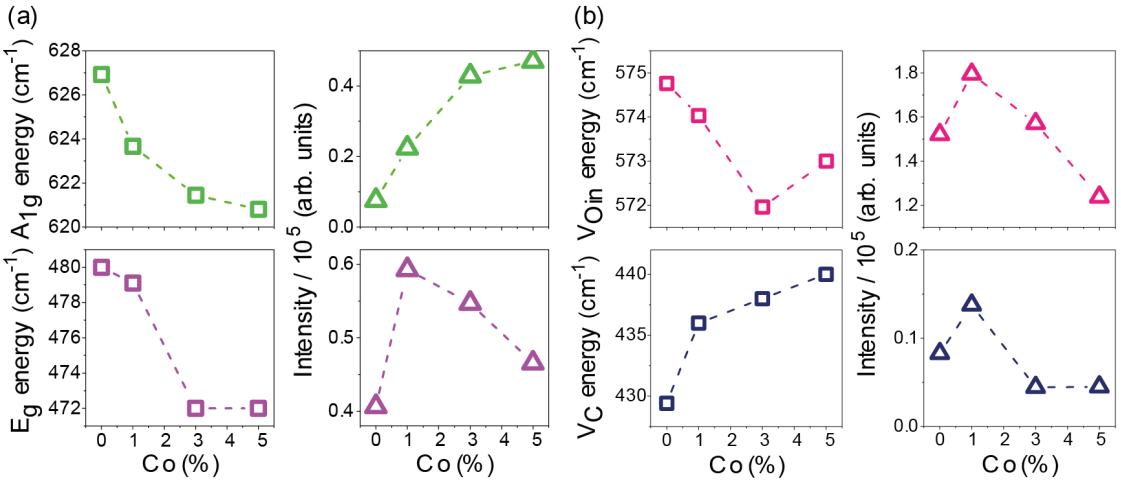

Figure 4. Positions and intensities of A_{1g} and E_g (a) and vacancy (V_{Oin} and V_C) (b) Raman modes

mode is higher in the Co-doped samples compared to the undoped $SnO_{2-\delta}$. The E_g mode intensity slightly decreased in samples doped with higher Co content, as a consequence of lattice distortion and reduction in lattice space symmetry. The position of the Raman mode ascribed to in-plane oxygen vacancies (574 cm^{-1}) did not change significantly, whereas the Raman mode related to vacancy clusters (430 cm^{-1}) shifts to higher energies with Co-doping. The intensity of both modes decreased in the $Sn_{0.97}Co_{0.03}O_{2-\delta}$ sample and this trend is more evident for the $Sn_{0.95}Co_{0.05}O_{2-\delta}$ sample. The intensity reduction of oxygen vacancy related modes in these samples implies that the concentration of oxygen vacancies decreased. The decrease of the oxygen vacancy concentration is expected if the part of Co cations were in Co^{3+} state or if some Co cations were interstitially incorporated in $SnO_{2-\delta}$ lattice [33,42].

In order to see if Co cations substituted Sn^{4+} in Co^{2+} state or the part of them was in Co^{3+} state, UV-Vis absorption measurements were performed and the absorption spectra of the $Sn_{1-x}Co_xO_{2-\delta}$ samples are presented in Fig. 5. In the UV range, the absorption spectrum of $SnO_{2-\delta}$ displays a strong absorption due to

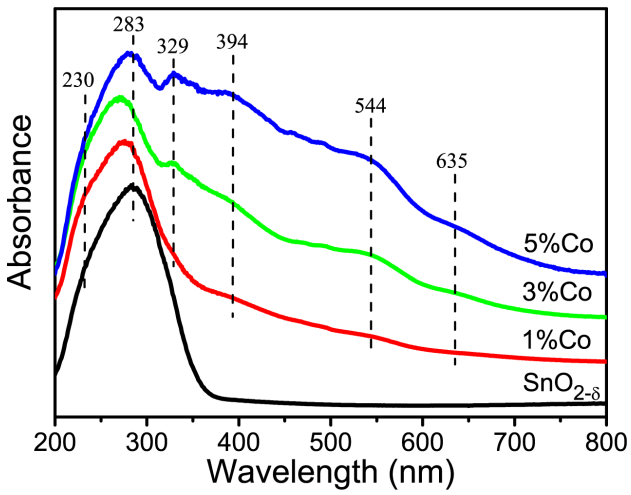

Figure 5. UV-Vis spectra of $Sn_{1-x}Co_xO_{2-\delta}$ nanoparticles

the SnO_2 interband transition. Two peaks at 230 and 283 nm are superimposed giving the broad band which might correspond to the surface Sn^{4+} species and to the $Sn^{4+} \rightarrow Sn^{2+}$ intervalence charge transfer, respectively [43]. In Co-doped samples the broad band is shifted to lower wavelength implying the band gap increase with Co-doping. In the absorption spectra of the $Sn_{0.97}Co_{0.03}O_{2-\delta}$ and $Sn_{0.95}Co_{0.05}O_{2-\delta}$ samples, new bands appear. The band around 329 nm can be assigned to the partial change of oxidation state of Co^{2+} to Co^{3+} [44], whereas the broad band around 400 nm can be ascribed to $^1A_{1g} \xrightarrow{\nu_2} {}^1T_{2g}$ transition of low spin Co^{3+} ions in octahedral environment [45]. The intensity of these bands increased in the $Sn_{0.95}Co_{0.05}O_{2-\delta}$ sample pointing to the increased concentration of Co^{3+} ions. The bands around 544 and 635 nm can be related to $^4A_2(F) \xrightarrow{\nu_2} {}^4T_1(P)$ transition of tetrahedral Co^{2+} species [45]. Therefore, from the absorption spectra of the $Sn_{0.97}Co_{0.03}O_{2-\delta}$ and $Sn_{0.95}Co_{0.05}O_{2-\delta}$ samples it can be deduced that part of Co cations entered into SnO_2 lattice in Co^{3+} state, concentration of which increased with the increased dopant content. This result supports the finding obtained from the refined XRD spectrum of the $Sn_{0.95}Co_{0.05}O_{2-\delta}$ sample, since the shrinkage of the unit cell was ascribed to the increased amount of Co^{3+} cations.

Our conclusions derived from absorption measurements are well-supported by recently published work of Roy *et al.* [46] concerning Co-doped SnO_2 nanocrystals. From the XPS study, Roy *et al.* [46] confirmed the mixed valence nature of Co ions in the host lattice and they have found that the relative concentration of Co^{3+} exceeds that of Co^{2+} with the increase of dopant content. This study also showed that Co incorporation into SnO_2 leads to the reduction of oxygen vacancies which is consistent with our Raman study.

3.3. Optical and electronic properties

The investigation of complex dielectric function by spectroscopic ellipsometry offers an insight into the

[7]

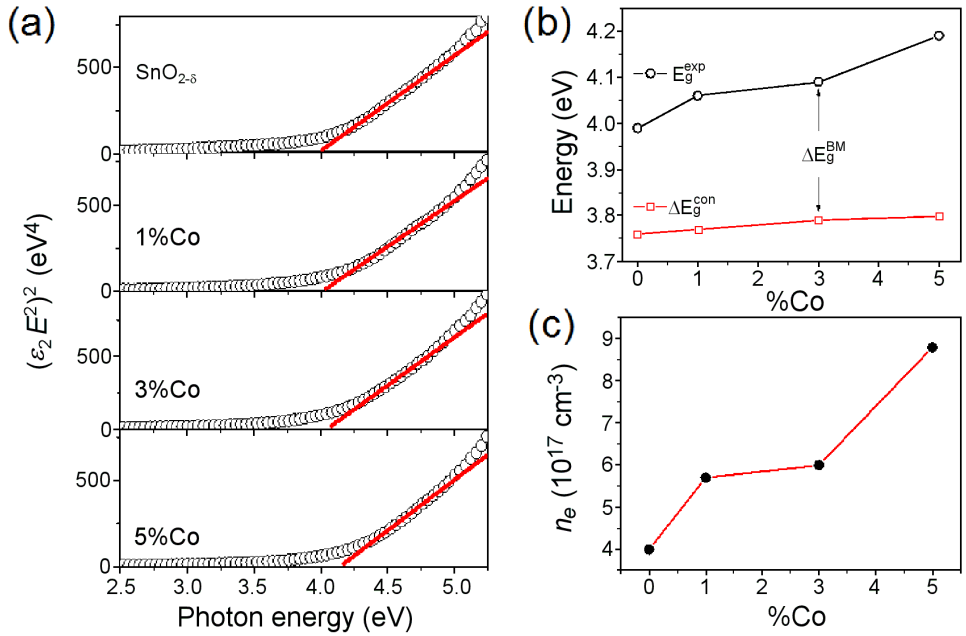

Figure 6. Determination of the direct band gap for $Sn_{1-x}Co_xO_{2-\delta}$ nanoparticles using Tauc law(a); variation of the band gap energy obtained from ellipsometric measurements (E_g^{exp}) and from quantum confinement model (ΔE_g^{con}) (b) and concentration of charge carriers n_e for $Sn_{1-x}Co_xO_{2-\delta}$ samples (c)

most important optical properties of the nanomaterials, such as, optical band gap, interband and intraband transitions, defect electronic states. The imaginary part of dielectric function is directly related to the electronic density of states and in a case of nanopowders it can be deduced from the ellipsometric measurements by applying two-phase model approximation (in our case: $SnO_{2-\delta}$ nanocrystals/air). In order to investigate the optical band gap behaviour and the influence of Co dopant on the absorption edge in $SnO_{2-\delta}$ nanocrystals we applied the Tauc model for direct band gap transition [47], knowing that SnO_2 is a direct band gap material [48]. In this case general expression for $\varepsilon_2(E)$ is:

$$(\varepsilon_2 \cdot E^2)^2 = a(E - E_g) \tag{1}$$

where E is the photon energy, E_g is the band gap and a is the constant related to the density of states for the conduction band. The Tauc plots of the $Sn_{1-x}Co_xO_{2-\delta}$ samples obtained from ellipsometric measurements are presented in Fig. 6a. Linear extrapolation to zero absorption (straight lines in Fig. 6a) gives the band gap energy values of the $Sn_{1-x}Co_xO_{2-\delta}$ samples.

In Fig. 6b, the dependence of the band gap energy (from Fig. 6a) on dopant content for the $Sn_{1-x}Co_xO_{2-\delta}$ samples is represented with open circles. It is obvious that Co-doping induces an increase of the E_g. Also, it is important to notice that all investigated samples have the band gap values higher than that for bulk SnO_2. Such changes in electronic properties of SnO_2 nanomaterials can be a consequence of the quantum confinement effect. This effect causes an increase of the band gap value due to the stronger localization of electronic states inside the volume of nanocrystals. The band gap energy shift, caused by this effect, can be calculated according to the following relation [49]:

$$\Delta E_g^{con} = E_g + \frac{\hbar^2 \pi^2}{2\mu \cdot D^2} \tag{2}$$

where E_g is the band gap value for the bulk SnO_2 (3.6 eV), D is the crystallite radius and μ is the reduced effective mass of the electron-hole pair. From the XRD results it was obtained that the average crystallite size of the undoped $SnO_{2-\delta}$ nanocrystals is lower than Bohr exciton radius, and that it has a tendency of further decrease with Co-doping. Therefore, it is reasonable to take into account the quantum confinement effect in order to properly analyse the band gap behaviour of the $Sn_{1-x}Co_xO_{2-\delta}$ samples. Taking the D values from Table 1 and knowing that $\mu = 0.38m_0$ [48], the band gap values (ΔE_g^{con}) that arise from the quantum confinement effect were calculated using Eq. 2. The ΔE_g^{con} values are presented in Fig. 6b with open squares. Comparing the ΔE_g^{con} values with E_g^{exp} ones it is obvious that observed band gap increase of the $Sn_{1-x}Co_xO_{2-\delta}$ samples cannot be ascribed only to the quantum confinement effect.

Another effect that can cause a shift of optical absorption edge to higher energies is the Burstein-Moss effect, which becomes more relevant in doped semiconductors (like transparent conducting oxides) with high charge carrier concentration. The Burstein-Moss effect is already registered in doped SnO_2 thin films [50,51]. According to this effect, the widening of the optical gap is caused by metallic doping and increase of carrier density which leads to the filling of empty semiconductor electronic states in the vicinity of Fermi level and its shift to higher energies. Assuming parabolic bands and

[7]

spherical Fermi surface the band gap shift due to the Burstein-Moss effect can be calculated by simple relation [4]:

$$\Delta E_g^{BM} = \frac{h^2}{2\mu}\left(3\pi^2 \cdot n_e\right)^{2/3} \quad (3)$$

where h is Planck constant, μ is the reduced effective mass and n_e is the carrier concentration.

Additional charge, i.e. increased charge carrier density in pure and doped $SnO_{2-\delta}$ nanocrystals, can originate from the donor type defects like oxygen vacancies and Co-dopants. Raman spectra have already evidenced defective structure of $SnO_{2-\delta}$, whereas Co^{2+} dopants bring additional charge when substituting Sn^{4+} ions. Hence, the observed increase of the E_g from Fig. 6b can be ascribed to the Burstein-Moss shift (ΔE_g^{BM}). Combining Eqs. 2 and 3 it is possible to estimate the concentration of charge carriers (n_e) in the $Sn_{1-x}Co_xO_{2-\delta}$ samples and the obtained values are presented in Fig. 6c. These calculated values are in good agreement with literature data for SnO_2 thin films [52]. As can be seen from Fig. 6c, doping of $SnO_{2-\delta}$ nanocrystals with Co ions causes an increase of the charge carriers concentration and shift of the optical absorption edge toward UV region, making the investigated material more conductive and at the same time more transparent.

It is well known that large number of defects, such as oxygen vacancies or vacancy clusters, can be formed at the SnO_2 nanoparticles surface and subsurface [21]. Intrinsic oxygen vacancies can be of three types: in-plane (V_{Oin}), bridging (V_{OB}) and subbridging (V_{OSB}) vacancies [36,38]. These vacancies can be in different charge states, i.e. vacancies which trap one, two or none electrons, so called F^+, F^0 and F^{++} centres, and they can form defect levels inside the $SnO_{2-\delta}$ gap [53]. Among the optical spectroscopy methods, photoluminescence (PL) spectroscopy is convenient method to investigate the defect structure of the pure and Co-doped $SnO_{2-\delta}$ samples.

Room temperature PL spectra of the $SnO_{2-\delta}$, $Sn_{0.99}Co_{0.01}O_{2-\delta}$ and $Sn_{0.95}Co_{0.05}O_{2-\delta}$ samples using a wavelength of 380 nm for excitation are presented in Fig. 7a. The PL spectrum of $SnO_{2-\delta}$ is deconvoluted into four Gaussian peaks centred at 510, 575, 470 and 446 nm (inset of Fig. 7a). In the deconvoluted PL spectrum of the undoped $SnO_{2-\delta}$ two bands dominate: broad intense band centred at around 510 nm and another band of lower intensity at around 575 nm. Since the excitation and emissions are both lower than the band gap of $SnO_{2-\delta}$, neither of these PL bands can be ascribed to the recombination of the Sn $4p$ conduction electrons with a holes from a O $2p$ band. The broad green luminescence around 510 nm is already seen in SnO_2 thin films [10] and nanoparticles [36] and it was attributed to the in-plane oxygen vacancy defects [36]. Therefore, the strong PL peak at 510 nm (2.45 eV) is ascribed to V_{Oin} defects. This finding is in accordance with corresponding Raman spectrum in which the most prominent Raman mode originates from in-plane oxygen vacancies. Another PL band at 575 nm (2.15 eV) can be ascribed to the isolated bridging oxygen vacancy defects, i.e. singly ionized F^+ defects [53]. The PL bands around 470 and 440 nm were seen in SnO_2 nanopowders [54]. These PL bands obtained with similar excitation line as in our case were ascribed to have excitonic origin [54]. It is well known that excitonic bands are formed near the band edge and they are usually of much narrower bandwidth than PL bands which originate from defect structures. As the band gap of the $SnO_{2-\delta}$ sample is around 4 eV, it can be concluded that PL bands at 446 and 470 nm lie deeper in the gap. Hence, it is unlikely that these two bands originate from some excitonic states. Performing density functional calculation for defective $SnO_{2-\delta}$ nanocrystals, Liu *et al.* [38] have shown that PL peaks at 446 and 470 nm originate from the subbridging oxygen vacancies, V_{OSB}. Schematic model for different relaxation processes in the $SnO_{2-\delta}$ nanocrystals is presented in Fig. 7b.

Co-doping induced complete reduction of PL intensity. Even the smallest percent of Co-doping (see Fig. 7a) almost completely quenched the luminescence. By integrating the spectra of the $Sn_{1-x}Co_xO_{2-\delta}$ samples from Fig. 7a, the areas within the boundary of emission were calculated for both undoped and doped samples in order to compare the quantum efficiencies. As the spectra were recorded under the identical excitation/absorption

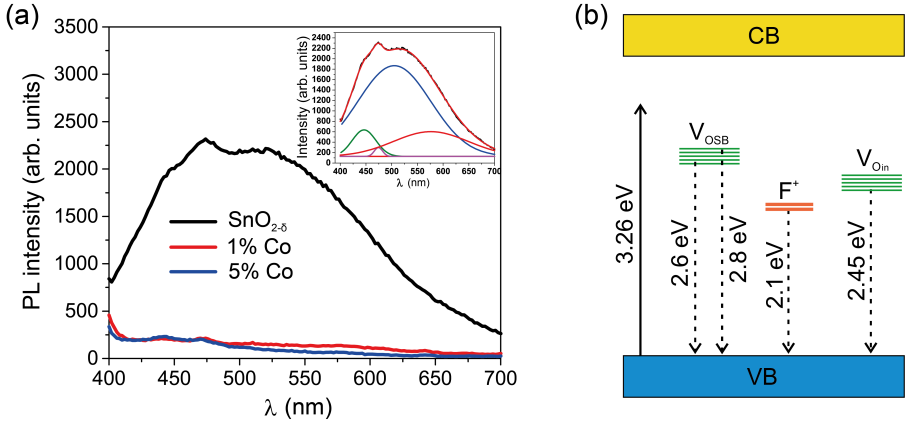

Figure 7. Room-temperature PL spectra of $Sn_{1-x}Co_xO_{2-\delta}$ nanoparticles (a) and the schematic of relaxation mechanism (b)

[7]

conditions, the drop in quantum yield value was estimated to be nearly 93%, which evidently implies that cobalt doping drastically quenches the photoluminescence of $SnO_{2-\delta}$. It has been already demonstrated that Co ions act as luminescence quenchers for metal oxides like TiO_2 or ZnO, decreasing the intensity of PL emission by forming the large number of nonradiative centres [55,56]. Therefore, it can be inferred that Co-doping of the $SnO_{2-\delta}$ nanocrystals increases the nonradiative recombination processes.

3.4. Photocatalytic performances

The degradation of MB under the UV light in the presence of the $Sn_{1-x}Co_xO_{2-\delta}$ samples is shown in Fig. 8a. The blank experiment in the absence of the catalyst (black curve) displayed almost no photocatalytic degradation of MB under UV irradiation. The $SnO_{2-\delta}$ nanoparticles exhibited high photocatalytic activity as the degradation of MB was completed after 6 h. The photocatalytic efficiency of the $SnO_{2-\delta}$ nanoparticles is much better than the ones of bulk SnO_2 [53] and is comparable to other reported works on SnO_2 nanoparticles [24,57]. Photoinduced degradation of MB was significantly slower in the presence of Co-doped samples. After 6 h, the MB degradation of 50% was obtained in the presence of the $Sn_{0.99}Co_{0.01}O_{2-\delta}$ catalyst, whereas significant decrease of photocatalytic activity was registered for the $Sn_{0.97}Co_{0.03}O_{2-\delta}$ and $Sn_{0.95}Co_{0.05}O_{2-\delta}$ samples. The obtained results are in accordance with the solitary work of Entradas *et al.* [22] who showed that increased Co-doping resulted in the decreased photocatalytic activity of SnO_2. The experimental kinetic data for $SnO_{2-\delta}$ catalyst were fitted to the rate equation of a pseudo first-order reaction $\ln(C/C_0) = kt$, where k is the rate constant and C_0 and C are the initial dye concentration and that at time t. The reaction kinetics for the $SnO_{2-\delta}$ catalyst (inset of Fig. 8a) follows the first order and the reaction rate constant estimated from the slope of the linear fit is 0.323 h^{-1}. The degradation process of MB is initiated when the electron-hole pairs are formed on the $SnO_{2-\delta}$ surface under the UV irradiation. Photogenerated electrons and holes, if not recombined, can migrate to the catalyst surface and react with adsorbed oxygen, water molecules or hydroxyl anions generating hydroxyl ($OH^\bullet$), superoxide ($O_2^{\bullet-}$) or ($HO_2^\bullet$) radicals. These reactions can be presented by Eq. 4–8:

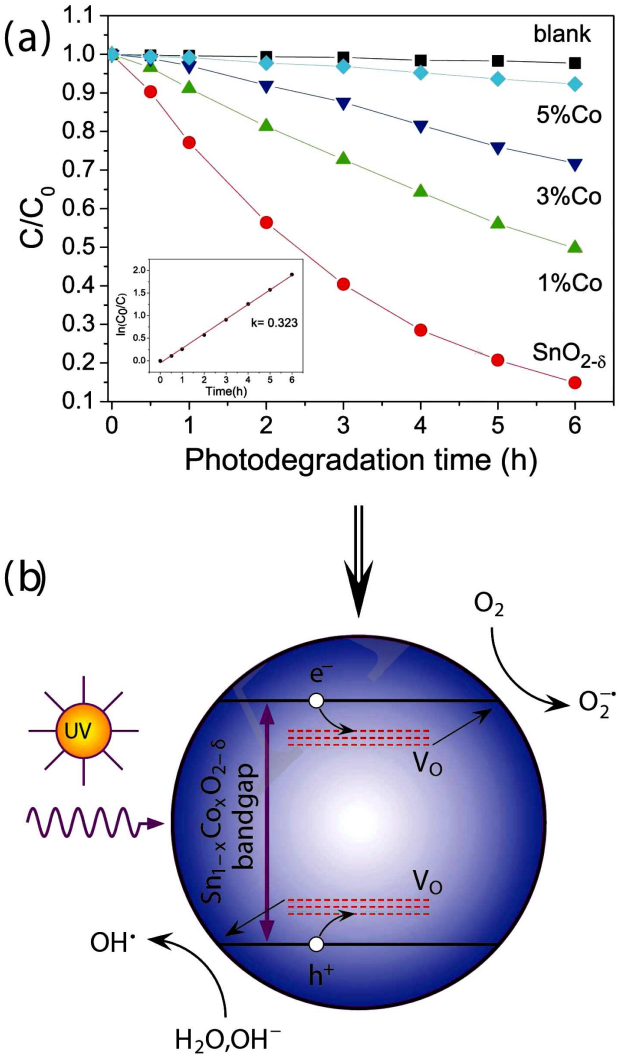

Figure 8. Photocatalytic degradation of MB in the presence of $Sn_{1-x}Co_xO_{2-\delta}$ samples (inset: pseudo first-order reaction kinetics of $SnO_{2-\delta}$ sample) (a) and illustration of proposed photodegradation mechanism under UV light illumination (b)

$$SnO_2 + h\nu \longrightarrow SnO_2(e^-_{cb} + h^+_{vb}) \quad (4)$$

$$e^-_{cb} + O_{2ads} \longrightarrow O_2^{\bullet-} \quad (5)$$

$$h^+_{vb} + H_2O \longrightarrow H^+ + OH^\bullet \quad (6)$$

$$h^+_{vb} + OH^- \longrightarrow OH^\bullet \quad (7)$$

$$O_2^{\bullet-} + H^+ \longrightarrow HO_2^\bullet \quad (8)$$

The photocatalytic efficiency of semiconductors like SnO_2 can be enhanced by introducing lattice defects such as oxygen vacancies because these defects can be active sites on the photocatalyst surface and delay the recombination of photogenerated electrons and holes [21,58]. The as-prepared $SnO_{2-\delta}$ nanopowders are very much oxygen deficient as confirmed by Raman results. The oxygen vacancies can form defect states inside the gap influencing the electronic structure of $SnO_{2-\delta}$ nanoparticles, as already seen from PL spectrum. By applying complementary techniques such as ultraviolet photoelectron spectroscopy and ion-scattering spectroscopy, Cox *et al.* [59] analysed oxygen vacancy electronic states on the SnO_2 surface and they showed that in-plane oxygen vacancies V_{Oin} form defect electronic states inside the SnO_2 gap near the conduction band behaving like F^+ centre donor states. Bridging/subbridging oxygen vacancies form states near the valence band [59] playing the role of hole acceptors. These donor/acceptor states can serve as carrier traps for electrons and holes ensuring better charge separation efficiency and suppression of *e-h* recombination process. Besides, doubly ionized (F^{++}) or singly ionized (F^+)

[7]

in-plane or subbridging vacancies formed at the surface of the catalyst facilitate charge transfer to adsorption species like H_2O or O_2, forming reactive radicals responsible for dye degradation. The holes, h^+_{vb}, trapped by oxygen vacancies at the nanoparticle surface react with adsorbed H_2O or OH^- groups to form $OH^\bullet$ radicals (Eqs. 6 and 7). Besides, electrons, e^-_{cb}, can be trapped by surface F^{++} vacancies which convert to F^+. Molecular oxygen adsorbed on the $SnO_{2-\delta}$ surface can capture electrons located on F^+ states [58] to form $O_2^{\bullet-}$ radicals:

$$e^-_{cb} + F^{++} \longrightarrow F^+ \quad (9)$$

$$F^+ + O_2 \longrightarrow O_2^{\bullet-} + F^{++} \quad (10)$$

Therefore, it is reasonable to assume that in-plane and subbridging/bridging oxygen vacancies in different charge states play significant role in enhancing the photocatalytic efficiency of $SnO_{2-\delta}$. The proposed mechanism of photodegradation process is presented in Fig. 8b.

Among the reactive radicals, $OH^\bullet$ radicals are considered to be the most important oxidative agent in photocatalytic reactions on metal-oxide nanostructures. They have one of the highest oxidation potentials among the oxidizing species (2.8 V) and can rapidly attack pollutants on the semiconductor surface. These radicals are considered as non-selective oxidizing species, since they can oxidize almost all electron rich organic molecules because of its electrophilic nature. $OH^\bullet$ radicals are usually formed by the reaction between the holes and OH^- or water molecules present on the surface of the catalyst (Eqs. 6 and 7). The formation of $OH^\bullet$ radicals on the surface of UV-illuminated $SnO_{2-\delta}$ was tested by performing the experiment with terephthalic acid, described in detail in section 2.3. The concentration of $OH^\bullet$ radicals was estimated from the intensity change of the PL peak attributed to 2-hydroxyterephtalic acid which is known to be proportional to the amount of $OH^\bullet$ radicals formed [30,31]. Figure 9 showed that intensity of PL peak at around 430 nm gradually increased with the prolonged irradiation time pointing to the higher formation rate of hydroxyl radicals. This result indicates that increased formation of $OH^\bullet$ radicals has a great effect on the photocatalytic activity of $SnO_{2-\delta}$. Further investigations will be directed to the estimation of the optimal SnO_2 concentration and the influence of solution pH on the SnO_2 photocatalytic properties. In that sense, more detailed mechanism study needs to be performed.

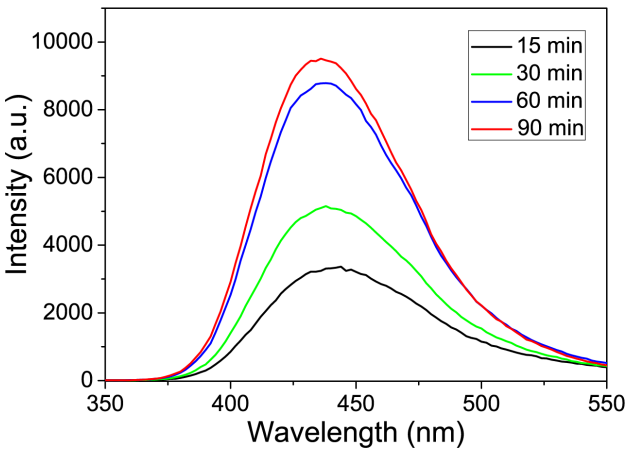

Figure 9. PL intensity change of 430 nm peak observed during UV illumination of $SnO_{2-\delta}$ sample in the solution of terephthalic acid and recorded at different time

With Co-doping the photocatalytic performances of $SnO_{2-\delta}$ were deteriorated. The reasons can be found in increased number of nonradiative centres with increasing cobalt concentration which act as trapping centres, immobilizing the fast transfer of photo-generated electrons to the nanoparticle surface. However, one of the main reasons can be found in the decreased concentration of oxygen vacancies which promotes the charge separation enhancing at the same time the photocatalytic activity. Also, the increased band gap of the Co-doped samples decreases the number of photons with sufficient energy to initiate photocatalytic processes, i.e. less UV energy is absorbed.

IV. Conclusions

Single phase ultrafine $Sn_{1-x}Co_xO_{2-\delta}$ nanocrystals, of a tetragonal (cassiterite-type) crystal structure, were prepared using a simple microwave-assisted hydrothermal synthesis at low temperature without the addition of any surfactant. Rietveld refinement of the XRD data showed that Co cations entered substitutionally into $SnO_{2-\delta}$ lattice and the unit cell volume increased up to $x = 0.05$. The slight shrinkage of the unit cell of the $Sn_{0.95}Co_{0.05}O_{2-\delta}$ sample was ascribed to the increased amount of Co^{3+} cations. The average crystallite size of the $SnO_{2-\delta}$ nanocrystals was less than Bohr exciton radius and it was found to decrease with increasing Co-doping level. UV-Vis absorption measurements confirmed that Co cations entered into the $SnO_{2-\delta}$ lattice in mixed valence state for higher dopant content ($x > 0.01$) and the concentration of Co^{3+} cations increased in the $Sn_{0.95}Co_{0.05}O_{2-\delta}$ sample. Raman spectra revealed oxygen deficient structure of the $SnO_{2-\delta}$ nanocrystals, whereas the oxygen vacancy concentration decreased with increased Co-doping. Further, Co-doping brought significant changes in the optical and electronic properties of tin oxide. $SnO_{2-\delta}$ nanocrystals exhibited blue shift of the band gap energy, compared to the bulk counterpart, due to the combined phonon confinement and the Burstein-Moss effects. The optical band gap energy increased with increasing Co concentration. The luminescence process in $SnO_{2-\delta}$ nanocrystals mainly originated from oxygen vacancy related defects and it was completely quenched in the Co-doped nanocrystals due to the increased nonradiative recombination processes. The oxygen-deficient $SnO_{2-\delta}$ was efficient for the light-induced degradation of methylene blue. Enhanced photocatalytic activity of $SnO_{2-\delta}$ can be ascribed to the

[7]

oxygen vacancies-assisted better charge separation and faster charge transport to adsorbed species. On the other hand, deteriorated photocatalytic performances of Co-doped $SnO_{2-\delta}$ nanopowders can be ascribed to the decreased oxygen vacancy concentration and less amount of absorbed UV light because of the band gap widening.

Acknowledgement: The authors acknowledge funding by the Institute of Physics Belgrade, through the grant by the Serbian Ministry of Education, Science and Technological Development. V.D. Araújo and M.I.B. Bernardi wish to thank Brazilian agencies FAPESP, FACEPE and CNPq for financial support.

References

1. H. Park, S. Alhammadi, K. Bouras, G. Schmerber, F. Gérald, D. Aziz, S. Abdelilah, J. Chan-Wook, P. Chinho, K. Woo Kyoung, "Nd-doped SnO_2 and ZnO for application in Cu(InGa)Se_2 solar cells", *Sci. Adv. Mater.*, **9** (2017) 2114–2120.
2. J. Lee, N.H. Kim, Y.S. Park, "Characteristics of SnO_2:Sb films as transparent conductive electrodes of flexible inverted organic solar cells", *J. Nanosci. Nanotechnol.*, **16** (2016) 4973–4977.
3. Y. Chen, J. Lu, S. Wen, L. Lu, J. Xue, "Synthesis of SnO_2/MoS_2 composites with different component ratios and their applications as lithium ion battery anodes", *J. Mater. Chem. A*, **2** (2014) 17857–17866.
4. M. Batzill, U. Diebold, "The surface and materials science of tin oxide", *Prog. Surf. Sci.*, **79** (2005) 47–154.
5. K. Singh, R. Malakar, R. Narzary, K. Priyanka, M. Biplob, "Hydrogen sensing properties of pure and composites of ZnO and SnO_2 particles: Understanding sensing mechanism", *Sens. Lett.*, **15** (2017) 771–778.
6. Z. Zhao, B. Wang, J. Ma, W. Zhan, L. Wang, Y. Guo, Y. Guo, G. Lu, "Catalytic combustion of methane over Pd/SnO_2 catalysts", *Chinese J. Catal.*, **38** (2017) 1322–1329.
7. J.T. Wiswall, M.S. Wooldridge, H.G. Im, "An experimental investigation of catalytic oxidation of propane using temperature controlled Pt, Pd, SnO_2, and 90% SnO_2–10% Pt catalysts", *Catal. Sci. Technol.*, **3** (2013) 618–625.
8. J.S. Chen, X.W.D. Lou, "SnO_2-based nanomaterials: synthesis and application in lithium-Ion batteries", *Small*, **9** (2013) 1877–1893.
9. M.O. Orlandi, A.J. Ramirez, E.R. Leite, E. Longo, "Morphological evolution of tin oxide nanobelts after phase transition", *Cryst. Growth Des.*, **8** (2008) 1067–1072.
10. J. Jeong, S.-P. Choi, C.I. Chang, D.C. Shin, J.S. Park, B.-T. Lee, Y.-J. Park, H.-J. Song, "Photoluminescence properties of SnO_2 thin films grown by thermal CVD", *Solid State Commun.*, **127** (2003) 595–597.
11. Y. Wang, M.H. Wu, Z. Jiao, J.Y. Lee, "One-dimensional SnO_2 nanostructures: facile morphology tuning and lithium storage properties", *Nanotechnology*, **20** (2009) 345704.
12. Z.R. Dai, Z.W. Pan, Z.L. Wang, "Growth and structure evolution of novel tin oxide diskettes", *J. Am. Chem. Soc.*, **124** (2002) 8673–8680.
13. X. Li, Q. Yu, C. Yu, Y. Huang, R. Li, J. Wang, F. Guo, Y. Zhang, S. Gao, L. Zhao, "Zinc-doped SnO_2 nanocrystals as photoanode materials for highly efficient dye-sensitized solar cells", *J. Mater. Chem. A*, **3** (2015) 8076–8082.
14. Y. Liu, F. Yang, X. Yang, "Size-controlled synthesis and characterization of quantum-size SnO_2 nanocrystallites by a solvothermal route", *Colloid Surf. A*, **312** (2008) 219–225.
15. Y.K. Liu, C.L. Zheng, W.Z. Wang, Y.J. Zhan, G.H. Wang, "Production of SnO_2 nanorods by redox reaction", *J. Cryst. Growth*, **233** (2001) 8–12.
16. J.Q. Hu, Y. Bando, Q.L. Liu, D. Golberg, "Laser-ablation growth and optical properties of wide and long single-crystal SnO_2 ribbons", *Adv. Funct. Mater.*, **13** (2003) 493–496.
17. H.Q. Cao, X.Q. Qiu, Y. Liang, L. Zhang, M.J. Zhao, Q.M. Zhu, "Sol-gel template synthesis and photoluminescence of n- and p-type semiconductor oxide nanowires", *Chem. Phys. Chem.*, **7** (2006) 497–501.
18. Y.K. Liu , C.L. Zheng , W.Z. Wang , C.R. Yin , G.H. Wang, "Synthesis and characterization of rutile SnO_2 nanorods", *Adv. Mater.*, **13** (2001) 1883–1887.
19. D. Chen, S. Huang, R. Huang, Q. Zhang, T.-T. Lee, E. Cheng, Z. Hu, Z. Chen, "Highlights on advances in SnO_2 quantum dots: insights into synthesis strategies, modifications and applications", *Mater. Res. Lett.*, **6** (2018) 462–488.
20. P.G. Mendes, M.L. Moreira, S.M. Tebcherani, M.O. Orlandi, J. Andrés, M.S. Li, N. Diaz-Mora. J.A. Varela. E. Longo, "SnO_2 nanocrystals synthesized by microwave-assisted hydrothermal method: towards a relationship between structural and optical properties", *J. Nanopart. Res.*, **14** (2012) 750–13.
21. A.M. Al-Hamdi, U. Rinner, M. Sillanpää, "Tin dioxide as a photocatalyst for water treatment: A review", *Process Saf. Environ.*, **107** (2017) 190–205.
22. T. Entradas, J.F. Cabrita, S. Dalui, M.R. Nunes, O.C. Monteiro, A.J. Silvestre, "Synthesis of sub-5 nm Co-doped SnO_2 nanoparticles and their structural, microstructural, optical and photocatalytic properties", *Mater. Chem. Phys.*, **147** (2014) 563–571.
23. R. Mani, K. Vivekanandan, K. Vallalperuman, "Synthesis of pure and cobalt (Co) doped SnO_2 nanoparticles and its structural, optical and photocatalytic properties", *J. Mater. Sci. Mater. Electron.*, **28** (2017) 4396–4402.
24. D. Chandran, L.S. Nair, S. Balachandran, K. Rajendra Babu, M. Deepa, "Structural, optical, photocatalytic, and antimicrobial activities of cobalt-doped tin oxide nanoparticles", *J. Sol-Gel Sci. Technol.*, **76** (2015) 582–591.
25. Y. Cao, L. Huang, Y. Bai, K. Jermsittiparsert, R. Hosseinzadeh, H. Rasoulnezhad, G. Hosseinzadeh, "Synergic effect of oxygen vacancy defect and shape on the photocatalytic performance of nanostructured TiO_2 coating", *Polyhedron*, **175** (2020) 114214.
26. X. Xu, X. Ding, X. Yang, P. Wang, S. Li, Z. Lu, H. Chen, "Oxygen vacancy boosted photocatalytic decomposition of ciprofloxacin over Bi_2MoO_6: Oxygen vacancy engineering, biotoxicity evaluation and mechanism study", *J. Hazar. Mater.*, **364** (2019) 691–699.
27. Q. Zhang, X. Zhao, L. Duan, H. Shen, R. Liu, "Controlling oxygen vacancies and enhanced visible light photocatalysis of CeO_2/ZnO nanocomposites", *J. Photoch. Photobio. A*, **392** (2020) 112156.
28. B. Matovic, J. Lukovic, B. Stojadinović, S. Aškrabić, A. Zarubica, B. Babic, Z. Dohčević-Mitrović, "Influence of Mg doping on structural, optical and photocatalytic performances of ceria nanopowders", *Process. Appl. Ceram.*,

[7]

11 (2017) 304–310.
29. Z. Dohčević-Mitrović, S. Stojadinović, L. Lozzi, S. Aškrabić, M. Rosić, N. Tomić, N. Paunović, S. Lazović, M.G. Nikolić, S. Santucci, "WO_3/TiO_2 composite coatings: Structural, optical and photocatalytic properties", *Mater. Res. Bull.*, **83** (2016) 217–224.
30. T.M. Su, Z.L. Liu, Y. Liang, Z.Z. Qin, J. Liu, Y.Q. Huang, "Preparation of PbYO composite photocatalysts for degradation of methyl orange under visible-light irradiation", *Catal. Comm.*, **18** (2012) 93–97.
31. K. Ishibashi, A. Fujishima, T. Watanabe, K. Hashimoto, "Detection of active oxidative species in TiO_2 photocatalysis using the fluorescence technique", *Electrochem. Commun.*, **2** (2000) 207–210.
32. D. Menzel, A. Awada, H. Dierke, J. Schoenes, F. Ludwig, M. Schilling, "Free-carrier compensation in ferromagnetic ion-implanted SnO_2:Co", *J. Appl. Phys.*, **103** (2008) 07D106.
33. E.J.H. Lee, C. Ribeiro, T.R. Giraldi, E. Longo, E.R. Leite, J.A. Varela, "Photoluminescence in quantum-confined SnO_2 nanocrystals: Evidence of free exciton decay", *Appl. Phys. Lett.*, **84** (2004) 1745–1747.
34. B. Babu, Ch.V. Reddy, J. Shim, R.V.S.S.N. Ravikumar, J. Park, "Effect of cobalt concentration on morphology of Co-doped SnO_2 nanostructures synthesized by solution combustion method", *J. Mater. Sci. Mater. Electron.*, **27** (2016) 5197–5203.
35. P.S. Peercy, B. Morosin, "Pressure and temperature dependences of the Raman-active phonons in SnO_2", *Phys. Rev. B*, **7** (1973) 2779–2786.
36. V. Bonu, A. Das, S. Amirthapandian, S. Dhara, A.K. Tyagi, "Photoluminescence of oxygen vacancies and hydroxyl group surface functionalized SnO_2 nanoparticles", *Phys. Chem. Chem. Phys.*, **17** (2015) 9794–9801.
37. A. Diéguez, A. Romano-Rodríguez, A. Vilà, J.R. Morante, "The complete Raman spectrum of nanometric SnO_2 particles", *J. Appl. Phys.*, **90** (2001) 1550–1557.
38. L.Z. Liu, J.K. Xu, X.L. Wu, T.H. Li, J.C. Shen, P.K. Chu, "Optical identification of oxygen vacancy types in SnO_2 nanocrystals", *Appl. Phys. Lett.*, **102** (2013) 031916.
39. K.N. Yu, Y. Xiong, Y. Liu, C. Xiong, "Microstructural change of nano-SnO_2 grain assemblages with the annealing temperature", *Phys. Rev. B*, **55** (1997) 2666–2671.
40. Y. Liu, M. Liu, "Growth of aligned square-shaped SnO_2 tube arrays", *Adv. Funct. Mater.*, **15** (2005) 57–62.
41. F. Wang, X. Zhou, J. Zhou, T.-K. Sham, Z. Ding, "Observation of single tin dioxide nanoribbons by confocal Raman microspectroscopy", *J. Phys. Chem. C*, **111** (2007) 18839–18843.
42. C. Van Komen, A. Thurber, K.M. Reddy, J. Hays, A. Punnoose, "Structure-magnetic property relationship in transition metal (M = V, Cr, Mn, Fe, Co, Ni) doped SnO_2 nanoparticles", *J. Appl. Phys.*, **103** (2008) 07D141.
43. D.A. Popescu, J.-M. Herrmann, A. Ensuque, F. Bozon-Verduraz, "Nanosized tin dioxide: Spectroscopic (UV-VIS, NIR, EPR) and electrical conductivity studies", *Phys. Chem. Chem. Phys.*, **3** (2001) 2522–2530.
44. I. Rossetti, B. Bonelli, G. Ramis, E. Bahadori, R. Nasi, A. Aronne, S. Esposito, "New insights into the role of the synthesis procedure on the performance of Co-based catalysts for ethanol steam reforming", *Top. Catal.*, **61** (2018) 734–1745.
45. Y. Brik, M. Kacimi, M. Ziyad, F. Bozon-Verduraz, "Titania-supported cobalt and cobalt-phosphorus catalysts: Characterization and performances in ehane oxidative dehydrogenation", *J. Catal.*, **202** (2001) 118–128.
46. S. Roy, A.G. Joshi, S. Chatterjee, A.K. Ghosh, "Local symmetry breaking in SnO_2 nanocrystals with cobalt doping and its effect on optical properties", *Nanoscale*, **10** (2018) 10664–10682.
47. A.S. Ferlauto, G.M. Ferreira, J.M. Pearce, C.R. Wronski, R.W. Collins, X. Deng, G. Ganguly, "Analytical model for the optical functions of amorphous semiconductors from the near-infrared to ultraviolet: Applications in thin film photovoltaics", *J. Appl. Phys.*, **92** (2002) 2424–2436.
48. P.D. Borges, L.M.R. Scolfaro, H.W. Leite Alves, E.F. da Silva Jr., "DFT study of the electronic, vibrational, and optical properties of SnO_2", *Theor. Chem. Acc.*, **126** (2010) 39–44.
49. L. Brus, "Electronic wave functions in semiconductor clusters: experiment and theory", *J. Phys. Chem.*, **90** (1986) 2555–2560.
50. S. Dalui, S. Rout, A.J. Silvestre, G. Lavareda, L.C.J. Pereira, P. Brogueira, O. Conde, "Structural, electrical and magnetic studies of Co:SnO_2 and (Co,Mo):SnO_2 films prepared by pulsed laser deposition", *Appl. Surf. Sci.*, **278** (2013) 127–131.
51. H.S. So, J.-W. Park, D.H. Jung, K.H. Ko, H. Lee, "Optical properties of amorphous and crystalline Sb-doped SnO_2 thin films studied with spectroscopic ellipsometry: Optical gap energy and effective mass", *J. Appl. Phys.*, **118** (2015) 085303.
52. A. Oprea, E. Moretton, N. Bârsan, W.J. Becker, J. Wöllenstein, U. Weimar, "Conduction model of SnO_2 thin films based on conductance and Hall effect measurements", *J. Appl. Phys.*, **100** (2006) 033716.
53. A. Kar, M.A. Stroscio, M. Dutta, J. Kumari, M. Meyyappan, "Growth and properties of tin oxide nanowires and the effect of annealing conditions", *Semicond. Sci. Technol.*, **25** (2010) 024012.
54. I.I. Gontia, M. Baibarac, I. Baltog, "Photoluminescence and Raman studies on tin dioxide powder and tin dioxide/single-walled carbon-nanotube composites", *Phys. Status Solidi B*, **248** (2011) 1494–1498.
55. B. Choudhury, A. Choudhury, "Luminescence characteristics of cobalt doped TiO_2 nanoparticles", *J. Lumin.*, **132** (2012) 178–184.
56. S. Yamamoto, "Photoluminescence quenching in cobalt doped ZnO nanocrystals", *J. Appl. Phys.*, **111** (2012) 094310.
57. S.P. Kim, M.Y. Choi, H.C. Choi, "Photocatalytic activity of SnO_2 nanoparticles in methylene blue degradation", *Mater. Res. Bull.*, **74** (2016) 85–89.
58. X. Pan, M.-Q. Yang, X. Fu, N. Zhang, Y.-J. Xu, "Defective TiO_2 with oxygen vacancies: synthesis, properties and photocatalytic applications", *Nanoscale*, **5** (2013) 3601–3614.
59. D.F. Cox, T.B. Fryberger, S. Semancik, "Oxygen vacancies and defect electronic states on the SnO_2(110)-1 × 1", *Phys. Rev. B*, **38** (1988) 2072–2083.

The Physics Teacher

Dry Friction Camouflaged in Viscous Drag

Cite as: Phys. Teach. **58**, 340 (2020); https://doi.org/10.1119/1.5145531
Published Online: 14 May 2020

Dejan M. Djokić

[8] Dry Friction Camouflaged in Viscous Drag

Dejan M. Djokić, Nanostructured Matter Laboratory, Institute of Physics Belgrade, University of Belgrade, Pregrevica 118, Republic of Serbia

Here is presented an interesting problem that can be used to introduce students to a variety of physics topics including non-inertial frames and frictional forces, rotational dynamics, and damped oscillations; the normal force also appears, but not in its usual guises. The problem is a generalized version of problem 3.34 presented in the "Oscillations and Waves," part of the collection of problems in general physics by I. E. Irodov.[1] The formulation of the problem, now extended by the kinetic friction inclusion, is given in what follows. In the setup shown in Fig. 1, a massive sleeve is fixed between two long identical massless springs. The sleeve can slide over a long horizontal bar against the dry friction of kinetic friction coefficient μ, which emerges to oppose to the relative lateral motion of the two solid surfaces in contact. The horizontal bar rotates at a constant angular velocity about a vertical axis passing through the middle. Above what critical value of the angular velocity ($\omega_C^* = ?$) will there no longer be oscillations of the sleeve if in the absence of the friction that value amounts to ω_C? Initially, the sleeve is given a velocity to start its motion from the center along the rotating bar. Gravitational effects are considered negligible here, but we do use N for the normal force of contact that the bar exerts on the sleeve in the x-y plane. The original problem by Irodov illustrates the same example in order to determine the critical value of angular velocity ω_C, but specifically disregards friction ($\mu = 0$).

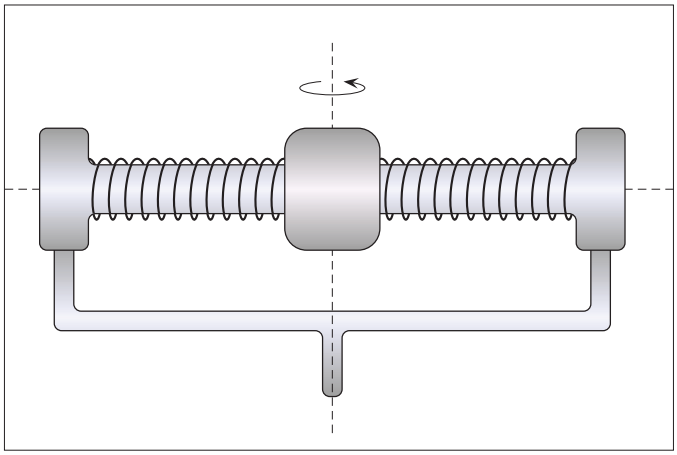

Fig. 1. Massive rotating sleeve fixed between two long identical massless springs.

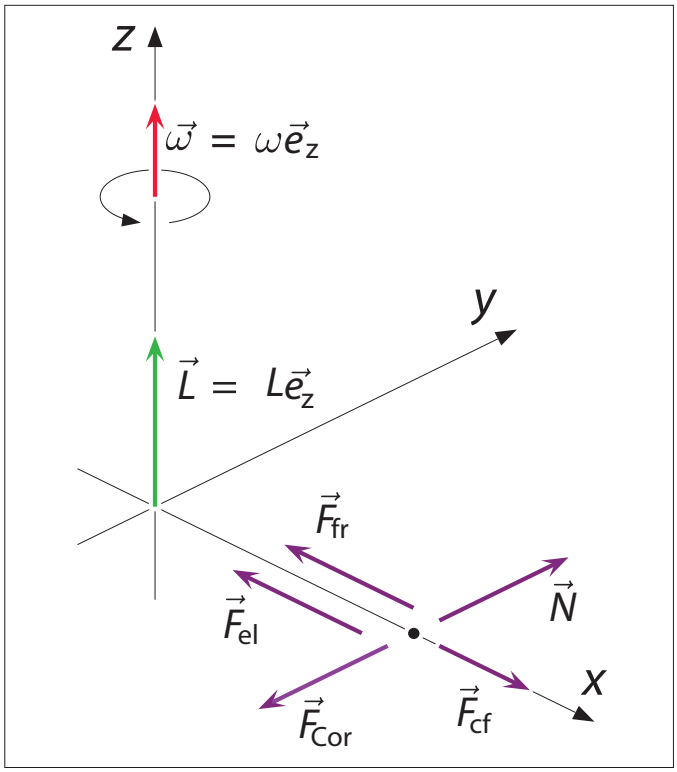

Fig. 2. Relevant forces (purple arrows) acting on the sleeve in the rotating frame, including the fictional forces associated with the fact that the rotating frame is not an inertial frame.

Proposed solution

Let the mass of the sleeve be m and let the elastic constant of each spring be κ. Newton's second law projected onto $\boldsymbol{e}_x$ within the viewpoint of the non-inertial reference frame rotating with uniform angular velocity ω reads as

$$m\ddot{x} = -2\kappa x + m\omega^2 x - \mu N(\dot{x}), \qquad (1)$$

where $-2\kappa x\boldsymbol{e}_x$ stands for the elastic restitutional force F_{el} always pointing opposite to the displacement vector $x\boldsymbol{e}_x$, whereas $m\omega^2 x\boldsymbol{e}_x$ is a fictitious or inertial force, familiarly known as centrifugal F_{cf} acting alongside the displacement to depress the restitutional capacity of the oscillator. See Fig. 2 for clarification where the dot delineates the sleeve moving at an instant in the sense of $\boldsymbol{e}_x$. Moreover, there is yet another force experienced by the sleeve—the kinetic friction force $F_{fr} = -\mu N(\dot{x})\boldsymbol{e}_x$, which is purely dry. This force may not always be directed oppositely to $\boldsymbol{e}_x$. Namely, it will be shortly demonstrated that the normal reaction force N due to the immediate contact with the bar depends linearly on the radial velocity of the sleeve ($\dot{x}$), which is relative to the rotational frame. In other words, the algebraic value of $-\mu N(\dot{x})$ may well be positive. This is controlled by the sign of $N(\dot{x})$. However, where does the normal reaction force come from since no gravity is present? To answer this, it proves rather expedient to look at the rotational motion of the sleeve in the inertial laboratory frame, which accommodates no fictitious forces. Explicitly, the angular momentum with respect to this frame, $L(t) = mx(t)^2$, is not conserved as $x(t)$ and consequently the moment of inertia are functions of time. The torque acting on the sleeve is given by $N(\dot{x})x(t)$, coming from the real force N, and is equivalent to a change in angular momentum by analogy with the change in impulse due to variable-mass uniform translatory motions. In fact, the sleeve moving outward/inward along the rotating bar enters the region in which its tangential velocity (x along e_y) increases/decreases linearly with position x. The change in this velocity takes place due to the force N acting sidewise to the bar, therefore, along the z-axis. Thus the rotational version of Newton's second law is

 DOI: 10.1119/1.5145531

[8]

$$\frac{dL}{dt} = N(\dot{x})x. \tag{2}$$

Since $dL = d(m\omega x^2) = 2m\omega x dx$, the normal reaction force becomes $\dot{x}$ dependent (directly proportional to $\dot{x}$) as $N(\dot{x}) = 2m\omega\dot{x}$. If the algebraic value of $\dot{x}$ is ± by sign, then the sense of $N(\dot{x})$ is along $\pm(\boldsymbol{e}_z \times \boldsymbol{e}_x)$ or alternatively $\pm\boldsymbol{e}_y$. Moreover, in the rotational frame the sleeve remains stationary along the direction perpendicular to the x-axis. So, there must be a fictitious force other than centrifugal to balance against the real force $\boldsymbol{N}(\dot{x})$. This force is known as the inertial Coriolis force $\boldsymbol{F}_{\text{Cor}}$ and is equal to $-\boldsymbol{N}(\dot{x}) = 2m(\dot{x})\boldsymbol{e}_x) \times (\omega\boldsymbol{e}_z)$, more details about which can be found elsewhere.[2] In such a way, the dry kinetic friction formally manifests itself as a laminar drag[3] force through the velocity-dependent normal reaction. This considerably eases finding the straightforward analytic solution to the equation of motion in Eq. (1). It ultimately boils down to

$$\ddot{x} + 2\beta\dot{x} + \omega_0^2 x = 0, \tag{3}$$

where $\beta \equiv \mu\omega$ (β as effective damping factor) and $\omega_0^2 \kappa/m - \omega^2$ (ω_0 as effective natural oscillator frequency). The equation of motion in Eq. (3) describes a motion of a damped oscillator, which becomes underdamped only when $\omega_0^2 - \beta^2 > 0$. Otherwise, the motion is non-oscillatory. This means that the critical value of the angular velocity beyond which there is no longer oscillatory motion is

$$\omega_c^* = \sqrt{\frac{2\kappa}{m(1+\mu^2)}}$$

in the case of friction, i.e., $\omega_C = \sqrt{\frac{2\kappa}{m}}$ in its absence. At last,

$$\omega_c^* = \frac{\omega_c}{\sqrt{1+\mu^2}}. \tag{4}$$

Acknowledgments

The author would like to thank Dimitrije Stepanenko for his constructive criticism. Support by the Serbian Ministry of Education, Science, and Technological Development through project OI 171032 is greatly acknowledged.

References

1. I. E. Irodov, *Problems in General Physics*, 10th ed. (CBS Publishers and Distributors Pvt Ltd, New Delhi, 2015 & BKL Publishers Binom, Moscow, 2014).
2. D. Kleppner and R. Kolenkow, *An Introduction to Mechanics*, 2nd ed. (Cambridge University Press, Cambridge, 2013).
3. In general, the immediate origin of a drag is internal friction. However, the turbulent drag is viscosity independent and proportional to squared velocity as contrary to the laminar flow case.

Dejan M. Djokić, scientific collaborator, Institute of Physics Belgrade (University of Belgrade), Nanostructured Matter Laboratory Pregrevica 118, 11 080 Belgrade, Republic of Serbia; djokic@ipb.ac.rs

[9]

QUANTUM YIELD COMPUTATION IN POLYMER-WRAPPED CARBON NANOTUBES

Dejan M. Djokić

Center for Solid State Physics and New Materials, Institute of Physics Belgrade, University of Belgrade, Belgrade, Serbia;
Institute of Chemical Sciences and Engineering, Ecole Polytechnique Fédérale de Lausanne (EPFL), Lausanne, Switzerland

Quantum yield in polymer-wrapped carbon nanotubes can be estimated using a 2D model of exciton decay with non-radiative channels as a result of the diffusive motion across the nanotube surface. Its ends act as exciton quenchers, while the influence of the wrapping polymer is exerted through its chemistry and wrapping angle. The model was solved analytically for zero-angle wrapping, a particular case when polymer interfaces the nanotube alongside. The general case was treated numerically and it was concluded that the wrapping angle has no significant impact on quantum yield values that are experimentally purposeful. An extensive range of quantum yield values was calculated to help us understand potentially accessible photoluminescence data of carbon nanotubes wrapped with a diversity of polymer families.

5. F. Cordero, F. Trequattrini, F. Craciun, et al., *Phys. Rev. B*, **99** (2019) 064106
6. F. Cordero, F. Craciun, F. Trequattrini, et al., *J. Phys. Chem. Lett.*, **9** (2018) 4401

I-23

VARIABLE RANGE HOPPING MECHANISM OF CARRIER TRANSPORT IN $BiFeO_3$ NANO-PARTICLES REVEALED VIA RAMAN SCATTERING TECHNIQUE

Dejan M. Djokić, Bojan Stojadinović, Dimitrije Stepanenko, Sonja Aškrabić, Zorana Dohčević-Mitrović

Nanostructured Matter Laboratory, Institute of Physics Belgrade, University of Belgrade, Pregrevica 118, 11 080 Belgrade, Serbia

Single-phase multiferroic $BiFeO_3$ compound has recently captivated much attention because of its desirably high ferroelectric Curie temperature of ~1100 K and antiferromagnetic Néel temperature T_N of ~640 K, which both slightly decrease with decreasing crystallite size. As such, $BiFeO_3$ at nanoscale proves to be promising for prospective applications in memory smart devices, satellite communications, novel sensing technologies, and spintronics. In order to meet these industrial requirements, the electric resistance of $BiFeO_3$ nanopowders must far exceed low insulation electric transport values, of which mechanism is hard to capture using contact probes. As highly informative experimental tool, Raman spectroscopy demonstrates ability to assess the nature and dynamics of charge carriers in conductive systems in a contactless indirect manner. In the present study we have analyzed broad electronic Raman scattering response of $BiFeO_3$ nanoparticles as a function of temperature (80–723 K) from which the carrier scattering rate can be estimated [1]. Two different 3D phonon-assisted Variable Range Hopping (VRH) electron transport mechanisms have been detected. VRH model due to Mott [2] is accompanied with the high-temperature paramagnetic phase (above T_N), whereas the VRH mechanism based on Efross & Shklovskii model [3] has been revealed in the strongly correlated low-temperature phase (below T_N). Our preliminary estimation of the electronic density of states above T_N exceeds number of 10^{19} electron states per (eV cm^3), which is in agreement with the finding by Ruby & Inbanathan [4] obtained directly from DC electrical resistivity measurements in doped $BiFeO_3$ thin films. In both cases the electron localization length has been found to closely match the average nanoparticle size of few tens of nanometers. This finding indicates that the system is disordered enough to localize the charge-carrier states within the nanoparticles.

1. A. Zawadowski, M. Cardona, *Phys. Rev. B*, **42** (1990) 10732
2. N.F. Mott, *Electronic Processes in Non-Crystalline Materials*, Oxford Univ. Press, 1979
3. A.L. Efros, B.I. Shklovskii, *J. Phys. C: Solid State Phys.*, **8** (1975) L49
4. S. Ruby, S.S.R. Inbanathan, *Appl. Surf. Sci.*, **449** (2018) 10